Space-Time Discontinuous Galerkin Methods for Convection-Diffusion Problems

Application to Wet-Chemical Etching

The research described in this thesis was undertaken at the Group of Numerical Analysis and Computational Mechanics, Department of Applied Mathematics, Faculty EWI, Universiteit Twente, Enschede.

The funding of the research was provided by the Dutch Technology Foundation STW through research project TWI. 5453 (Analysis and control of transport phenomena in wet-chemical etching processes).

Printed by Wöhrmann Printing Service, Zutphen, The Netherlands
The summary in Dutch was done by Ruud van Damme

ISBN 90-365-2287-0

SPACE-TIME DISCONTINUOUS GALERKIN METHODS FOR CONVECTION-DIFFUSION PROBLEMS

APPLICATION TO WET-CHEMICAL ETCHING

DISSERTATION

to obtain
the doctor's degree at the University of Twente,
on the authority of the rector magnificus,
prof. dr. W.H.M. Zijm,
on account of the decision of the graduation committee,
to be publicly defended
on Thursday 8 December 2005 at 15.00

by

Janivita Joto Sudirham
born on 24 May 1974
in Jakarta, Indonesia

This dissertation has been approved by the promoter
Prof. dr. ir. J.J.W. van der Vegt
and the assistant promoter
dr. R.M.J. van Damme

Praise be to Allah, who hath guided us to this work:
never could we have found guidance,
had it not been for the guidance of Allah. (Q.S. 7:43)

with the power and skill did We construct the firmament,
for it is We who create the vastness of space. (Q.S. 51:47)

this thesis is dedicated
to my mother and my father
to my husband

Summary

Etching is an important step in the fabrication of microstructures, during which a pattern is transferred onto the background material by etching away part of the material. In industrial applications, an acid fluid is used to dissolve the material and it is therefore called wet-chemical etching. The transport of the acid fluid and etching products during wet-chemical etching is important to obtain the desired patterns. However, it is generally complicated to control the process. Numerical simulations are then used to study transport phenomena during etching. Due to the complexity of the phenomena and the geometry of the structures, wet-chemical etching processes require numerical techniques which can deal with deforming elements to accommodate the movement of the etching cavity boundary.

In this thesis we discuss space-time discontinuous Galerkin (DG) finite element methods for transport phenomena in incompressible flows. The methods, which simultaneously discretize the equations in space and time, provide the necessary flexibility to deal with time deforming meshes and mesh adaptation. In particular, we discuss space-time DG methods for the advection-diffusion equation, which governs the concentration of the acid fluid, and for the incompressible Navier-Stokes equations to model the flow of the acid fluid inside and outside the etching cavity. We provide a detailed theoretical analysis of the stability of the newly developed methods, as well as some simple numerical tests to investigate the accuracy of the methods.

We demonstrate the capabilities of the newly developed methods to wet-chemical etching processes. Two cases of diffusion-controlled etching are discussed: etching of a slit, which can be considered as a two dimensional problem, and etching of a circular hole. The latter we solve without using the fact that the problem has a rotational symmetry, this we have done in order to show that a fully three dimensional simulation is indeed possible. For simple cases, the numerical results show good agreement with the predictions obtained with an analytical approach. Moreover, the numerical simulations can give a complete description of the time evolution of the shape of the etching cavity. The numerical simulations of convection-dominated etching of a slit coupled with the Stokes equations give a detailed description of the transport phenomena in wet-chemical etching inside the cavity.

Samenvatting

Het etsproces is een essentieel onderdeel in het fabricatieproces van microstructuren. Er wordt in dit proces als het ware een zeker patroon, dat vastgelegd is in het zogenaamde masker, gecopieerd op het materiaal door dit materiaal weg te etsen op de plaatsen waar het masker het materiaal *niet* beschermt. In industriële toepassingen wordt een zure vloeistof gebruikt om het materiaal op te lossen, en deze manier van etsen wordt daarom nat-chemisch etsen genoemd. Het transport van de zure vloeistof en het ets-materiaal bepaalt in hoge mate het uiteindelijke patroon. Het is echter zo, dat dit proces moeilijk te beheersen is. Daarom worden numerieke simluaties gebruikt om de transportfenomenen beter te begrijpen. Door de complexiteit van alle fenomenen alsook de geometrie van de structuren, is het noodzakelijk dat deze numerieke simulaties kunnen omgaan met deformerende elementen om de beweging van het scheidingsoppervlak tussen daar waar wél en waar niet ge-etst is, nauwkeurig te kunnen volgen.

In dit proefschrift bediscussiëren we Galerkin methoden waarvan de basisfuncties zowel in de ruimtelijke richting als in de tijdrichting discontinu mogen zijn (DG). Doel is om met deze methoden transportproblemen van incompressibele vloeistoffen te beschrijven. Deze methoden, die tegelijkertijd de vergelijkingen in de ruimte en in tijd discretizeren, staan garant voor de noodzakelijke flexibiliteit die nodig is om bewegende roosters en ook topologisch veranderende roosters, aan te kunnen. In het bijzonder bespreken we DG methoden, in plaats en in tijd, voor de advectie-diffusievergelijking – deze bepaalt de concentratie van de zure vloeistof – en voor de Navier-Stokesvergelijkingen. Deze laatste zijn nodig om de beweging van de zure vloeistof in het hele domein nauwkeurig te beschrijven. We geven in dit proefschrift ook een gedetailleerde theoretische analyse van de stabiliteit van de ontworpen numerieke methoden. Voorts voeren we enkele eenvoudige numerieke tests uit om de nauwkeurigheid van de methoden te onderzoeken en de methoden te valideren.

We demonstreren de mogelijkheden van deze nieuwe methoden aan de hand van nat-chemisch etsprocessen. Twee gevallen van etsen, waarbij diffusie het etsproces domineeert, worden besproken. Op de eerste plaats een etsprobleem waarbij het masker een (zeer lange) spleet heeft, die overal even breed is. Dit geval kunnen we effectief beschouwen als een tweedimensionaal probleem in de ruimte. Op de tweede

plaats bekijken we het proces waarbij het masker precies één cirkelvormig gaatje bevat. Dit probleem hebben we door kunnen rekenen zonder gebruik te maken van de cirkelsymmetrie die het probleem in zich heeft – dit hebben we gedaan om aan te tonen dat berekeningen in drie ruimtedimensies inderdaad tot de mogelijkheden behoren. De numerieke resultaten laten in alle gevallen een zeer goede overeenkomst zien met de analytische voorspellingen. Sterker nog, de numerieke simulaties geven een beschrijving van de verandering van de etsholte als functie van de tijd. De numerieke simulaties van de vergelijkingen waarin de vloeistofbeweging wordt beschreven door de zogenaamde vergelijkingen van Stokes, zijn ook uitgevoerd voor het nat-chemisch etsen met een masker met een zeer lange spleet en geven een nauwkeurige beschrijving van de transportverschijnselen in de etsholte.

Contents

Chapter 1

Introduction

1.1 The etching process

Nowadays, many devices are assembled from large numbers of small but important components. These components contain extremely small features and are produced with special fabrication techniques. One of these techniques is photolithography in which a pattern with small features is transferred onto a photosensitive substrate and the background material is chemically etched away to produce the desired pattern. An important step in photolithography, which is called etching, is widely used in integrated circuit technology where a circuit pattern of great complexity is transferred onto a circuit board, see Fig. 1.1.

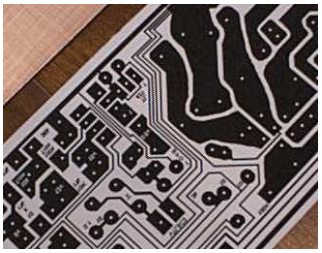

(a) Patterns in the design

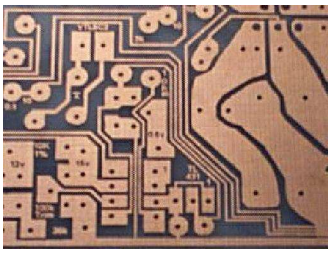

(b) Patterns on the circuit board after etching

Figure 1.1: Electronic circuit board. Source: Easy PCB Fabrication.

Etching is also applied in the fabrication of microstructures, and this technique is called micromachining. One example of micromachining is the fabrication of nanochannels and tubes, which are used for many applications, such as fluidic delivery systems, biochemical reaction chambers, fluid pumps and valves. An impression of a typical nanochannel is shown in Fig 1.2.

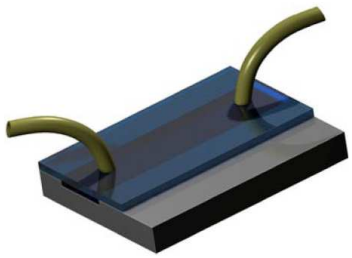

(a) Nanochannel in silicon with glass cover

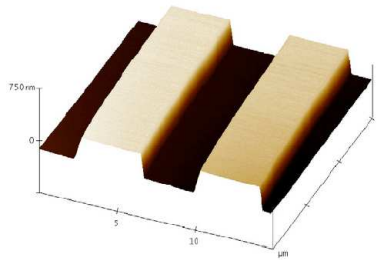

(b) View of nanochannel in silicon after etching

Figure 1.2: Fluidic 1D Nanochannels. Source : Haneveld et. al (2003) [37].

Another example is the fabrication of small holes on which artificial hairs in flow sensors stand on, see Fig. 1.3. For this application, the small holes are made by deep ion etching.

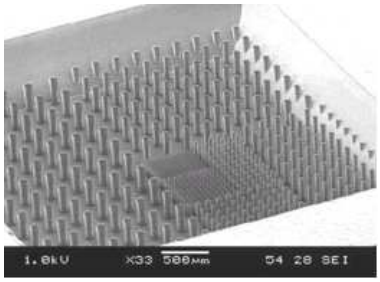

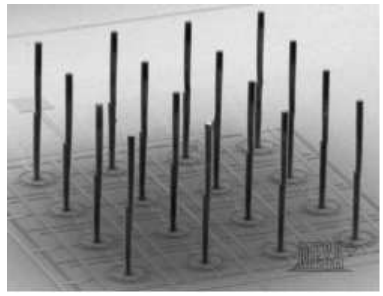

Figure 1.3: Artificial hairs made by micromachining. Source : Chair Transducers Science and Technology, University of Twente.

Besides those two examples, many other objects are also made with etching techniques, such as lead frames, encoder discs, microfluidic parts, valve springs, connectors and optical parts, see for instance Fig. 1.4.

One of the primary reasons to use etching in microfabrication is that an etching process is independent of the complexity of the pattern design. Etching also has many other advantages, such as no deformation of the material, the final product is free of burrs, the process is independent of the thickness of the material, and economical for the production of large numbers of tools and parts.

An illustration of the etching process in the fabrication of microstructures is shown in Fig. 1.5. First, a photosensitive material is deposited in thin films. This photosensitive material will act as the mask during the etching process. Part of the photo-

Figure 1.4: Different objects made by etching. Source: Stork Veco.

sensitive material is then exposed to light. After light exposure, the desired pattern is transferred to the exposed material, as the material properties of the exposed and unexposed regions differ. The unexposed photosensitive material is then removed by rinsing and the part of the material which is not covered by the mask is subsequently removed by etching. After the etching process is finished, the desired pattern or structure is obtained.

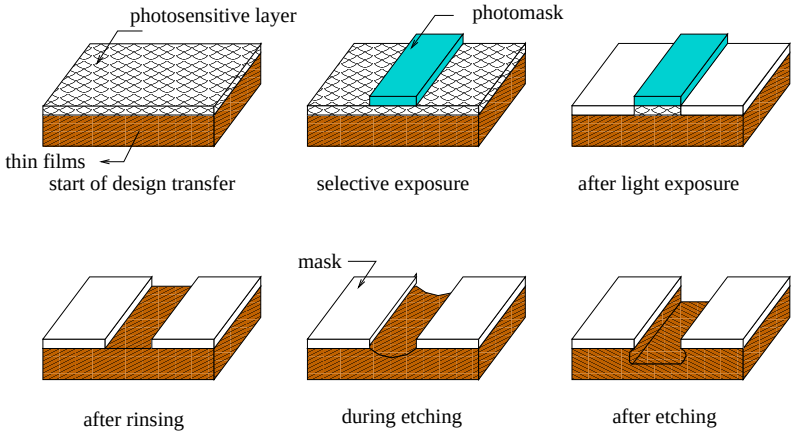

Figure 1.5: Etching process. Source: Driesen (1999) [29].

In general, there are two classes of etching processes [47, 48]: wet-chemical etching and dry etching. In wet-chemical etching an acid fluid is used to dissolve the material

which is not protected by a mask. This process is influenced by the transport of the fluid flowing into and out of the etching cavity. Wet-chemical etching is widely used for etching on thin films and for mass production. Dry etching is more recently developed compared to wet-chemical etching. In dry etching, the solid material is dissolved using reactive ions or a vapor phase etchant. This technique is expensive compared to wet-chemical etching. It gives, however, high resolution for etching small features on thin films. In this thesis we consider wet-chemical etching as it is widely used in industrial applications.

The quality of an etched object depends on the process control during etching. Many problems can occur during etching, resulting in an inaccurate shape of the etched object. The first problem is the underetching effect, see Fig. 1.6(a) as an illustration. Since the size of this underetching has approximately the same length as the depth of the etching cavity, the resulting etched object will have an opening larger than the desired size on the mask. Another problem one has to deal with is the influence of neighboring holes and cavities, see Fig. 1.6(b). Assuming that the acid fluid flow comes from the left, the resulting cavities in the middle and on the right are smaller than the one on the left as the concentration of the etchant changes downstream because of the chemical reaction with the solid. Since etching is largely used in mass production with complicated mask designs consisting of tightly packed structures, it is important to understand the flow of the acid fluid in the cavities, and the resulting changes in the chemical composition of the etching fluid and shape of the etching cavity boundary.

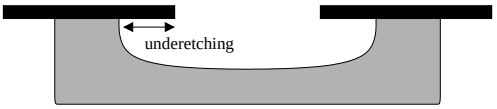

(a) Underetching

(b) Neighboring holes

Figure 1.6: Underetching and effect of neighboring holes in etching.

Other important parameters which influence the shape of the etched object are the material properties of the acid fluid and the solid materials, see Fig. 1.7 as an illustration. For example, the use of an acid fluid that has different rates for the chemical reaction with the solid material in different directions, results in anisotropic etching. Also, a different crystal orientation of the uncovered surface will result in anisotropic

effects on the shape of the object. In some applications this anisotropic phenomenon is to be avoided, such as for biomedical devices, while for other applications, such as deep channels, this phenomenon is needed.

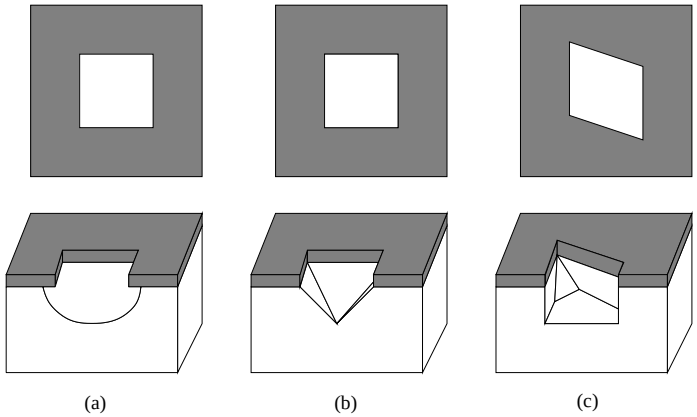

Figure 1.7: Anisotropic etched features [47]. (a.) isotropic etching, (b.) anisotropy due to the etchant, (c.) anisotropy due to crystal orientation.

Due to these problems, designing a mask that can give accurate results and to control the etching process is generally complicated. Numerous redesigns and trial-and-error experiments are frequently conducted to obtain a suitable mask design and process control for different types of etching processes, which is costly and time-consuming.

Mathematical models offer the possibility to improve the understanding of important physical phenomena in the etching process, to predict the shape of the etched object, and to obtain a suitable mask design, without the need of having to make and test each individual design experimentally. This will reduce the cost of designing accurate masks for industrial processes and reduce the time necessary to develop new products.

1.2 Overview of mathematical models for wet-chemical etching

Many attempts have been made to use mathematical models, both analytical approaches and numerical simulations, to study important mechanisms in wet-chemical etching. Here we mention several of them.

A description of mathematical models using an analytical approach and a prediction of the shape of the etched surface during diffusion-controlled etching of semi-infinite masks can be found in [42, 44, 45]. Here the following modeling assumptions

are made to simplify the problem: diffusion is the only process that controls etching, the diffusion coefficient of the acid fluid is constant, and the surface reaction between the acid fluid and the solid material is very fast compared to the transport of the etchant and reaction products. A prediction of the shape of the etched surface during time evolution for diffusion-controlled etching of a slit and a circular hole, is discussed in [43] and [46], respectively. These studies show that the shape of the etched objects is symmetric with respect to the center line, and there is a strong influence of the mask on the shape of the etching cavity near the edge of the mask. The analytical approach presented in [43, 46] also provides some simple rules to predict the etch rate and the amount of underetching.

Besides the analytical approaches, numerical simulations are used for predicting the shape of the etched surface. For the case of diffusion-controlled etching of a slit, [66] presents simulation results on the shape of the etched surface for different types of etching processes: a fast versus slow chemical reaction on the surface and fast versus slow movement of the surface. These simulations are conducted using continuous finite element methods. The results for the case of a fast surface reaction that are presented in [66] agree well with the analytical results from [43]. In real applications, the wet-chemical etching process is, however, frequently dominated by the convection of the acid fluid flowing into and out of the cavity. The mathematical models then should also include the governing equations for the fluid flow. Studies for the case of convection-dominated etching which involve solving the Stokes or the incompressible Navier-Stokes equations are conducted in [29, 56, 57].

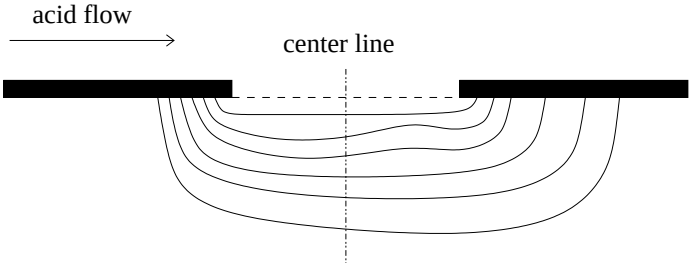

Figure 1.8: Shape of a slit during convection-dominated etching.

Since the inclusion of the equations for the fluid flow increases the complexity of the problems, numerical techniques are applied to study these models. A continuous finite element method is used in [56, 57], while a boundary element method is used in [29]. All numerical studies conducted so far consider the etching of a slit. The results in [29, 56, 57] assume a quasi steady-state problem, which means that the physical variables relevant to the wet-chemical etching process do not change much due to the

change of the position of the etched surface.

Convection also influences the shape of the cavity which is no longer symmetric with respect to the center line of the slit since the concentration of the etchant in the cavity is influenced by the convection. A sketch of the shape of a slit during convection-dominated etching is given in Fig. 1.8.

1.3 Approach

Mathematical models offer the possibility to study the physical phenomena during etching and to predict the shape of an etched object. For relatively simple models analytical techniques can be used to predict the final shape of an etched object, but when the transport phenomena in the wet-chemical etching processes or the shape of the object become more complex, then numerical simulations are more useful since they require less modeling assumptions.

The numerical simulation of wet-chemical etching is, however, a non-trivial task. The numerical method should be able to compute the fluid flow and transport phenomena in complex and time-dependent geometries. The numerical technique should also be able to adapt the computational mesh locally in order to capture small structures, such as boundary layers and singularities accurately and efficiently. One of the techniques that has these features is the discontinuous Galerkin (DG) finite element method.

The DG method is a class of finite element methods that uses basis functions that are discontinuous across the element boundary. This has several important benefits, in particular, DG methods can achieve higher order accuracy on unstructured meshes, are suitable for local adaptation, and efficient on parallel computers. These features make DG methods an excellent numerical technique for the simulation of wet-chemical etching.

An important aspect in the simulation of wet-chemical etching is that we need to perform computations on time-dependent flow domains where the shape of the domain is part of the solution. This requires the use of moving and deforming elements which is greatly facilitated by the use of a space-time discretization.

In a space-time discretization, there is no separation between the space and time variables. This discretization technique is beneficial for problems defined on time-dependent domains, such as occur in fluid-solid interaction problems and other problems with moving interfaces. The space-time DG method is proposed in [41], together with a theoretical analysis of this technique for multidimensional scalar conservation laws (see also [15]). In [64, 65], the space-time DG method is extended to nonlinear hyperbolic systems in particular the Euler equations of gas dynamics. The space-time DG method provides optimal efficiency to adapt and deform the mesh to accommodate for the changes in the domain boundaries, while maintaining a conservative numerical discretization. Since simulations of wet-chemical etching processes

require a numerical technique that can deal with the movement of the etching cavity boundary, space-time DG methods are well suited for the simulation of wet-chemical etching. In this thesis we consider the development and analysis of space-time DG methods for the advection-diffusion equation and the incompressible (Navier)-Stokes equations and we apply these techniques to the simulation of wet-chemical etching.

1.4 Objectives

The research documented in this thesis has two main objectives: the development of a space-time discontinuous Galerkin finite element method for the simulation of transport phenomena in incompressible flow and the application and demonstration of this technique to wet-chemical etching of different objects.

The first objective requires the development of a space-time DG method suitable for solving: (a) the advection-diffusion equation for an active etching component in a time-dependent domain and (b) the incompressible (Navier)-Stokes equations which control the fluid flow inside and outside the etching cavity. Also, a detailed theoretical analysis is necessary to investigate the accuracy, stability, and convergence of the numerical methods, which is essential to obtain a robust and accurate numerical technique.

The second objective focusses on the simulation of wet-chemical etching processes. The capability of the newly developed method to simulate different types of etching processes will be investigated using a sequence of increasingly more complicated model problems. First, simulations of diffusion-controlled etching will be conducted to study the potential of the space-time DG method for this type of etching. These simulations are also used to investigate the accuracy of the computed shape of the moving boundary by comparing them with analytical approximations and other numerical results. Next, simulations of convection-dominated etching are conducted to study the transport phenomena in wet-chemical etching in a more realistic model by including the velocity field of the acid fluid into the model. This is intended to study the influence of the convection of the acid fluid on the shape of the cavity.

1.5 Outline of the thesis

The outline of this thesis is as follows.

In Chapter 2 the governing equations relevant for wet-chemical etching processes are presented. First, the equations are formulated in their usual form. Next, we introduce reference values for wet-chemical etching processes and use these values to write the equations in dimensionless form.

The next three chapters will be devoted to the development and analysis of DG methods suitable for the simulation of wet-chemical etching. First, the discretization of elliptic partial differential equations with DG methods is discussed in Chapter

3, which serves as an introduction to DG discretizations for second-order partial differential equations. We also present some simple one dimensional numerical tests to demonstrate the accuracy of the DG methods, in particular their suitability for *hp*-adaptation.

In Chapter 4, we discuss the space-time DG discretization for the convection-diffusion equation in time-dependent flow domains and give a complete derivation of this numerical method. A detailed theoretical analysis of the stability and error estimates is also given. This chapter is completed with some simple numerical tests to verify the theoretical analysis of the convergence rate of the space-time DG method.

The space-time DG discretization for time-dependent incompressible flows is discussed in Chapter 5. Special attention is given to the extension of the DG techniques developed for steady-state problems to problems on time-dependent domains. The theoretical analysis of the stability of the method is given, as well as some simple tests to investigate the accuracy of the method.

Simulation results for different types of wet-chemical etching processes are presented in Chapter 6. First, we describe the DG discretization for an equation governing the movement of the etching surface together with the construction of an initial space-time mesh for the computations.

For the etching simulations we consider both diffusion and convection-dominated etching. For diffusion-controlled etching, two cases are discussed: the etching of a slit, which can be seen as a two dimensional problem, and the etching of a circular hole, as an example of a three dimensional problem. For convection-dominated etching, we consider the etching of a slit. First, we only consider the case when the velocity field of the etchant concentration throughout the computational domain is given. Next, the computations of the transport of the etchant are fully coupled with the computation of the velocity field using the time-dependent Stokes equations.

Finally, conclusions and recommendations for future research are presented in Chapter 7.

Chapter 2

Mathematical Modeling of Wet-Chemical Etching Processes

2.1 Introduction

In this chapter we discuss the main transport phenomena involved in wet-chemical etching processes and describe the governing equations.

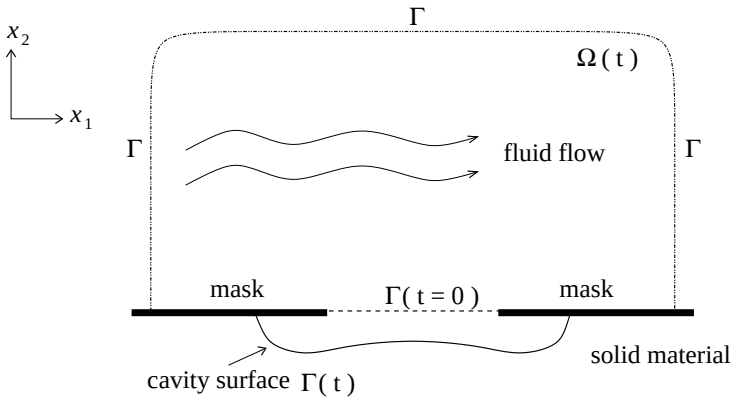

Figure 2.1: Schematic of flow transport in etching process.

A schematic of the system is shown in Fig. 2.1. The wet-chemical etching process can be described by the following steps. A solid material such as a thin film, which is partially covered by a mask, is placed in an acid fluid which flows past the material. The acid fluid contains an etchant which can react with the solid material. The mask

is made of a different material that does not react with the acid. The etchant is transported by convection and diffusion to the uncovered part of the solid material where it reacts, thereby dissolving the unprotected part of the material, and develops a small cavity. As etching proceeds, the shape of the cavity evolves with time according to the etch rate distribution along the cavity, which depends on the concentration of the etchant inside the flow domain. In the next sections, we discuss in more detail the governing equations which describe wet-chemical etching processes.

2.2 Governing equations for wet-chemical etching processes

In this section we discuss the governing equations for each subproblem in wet-chemical etching.

1. Concentration of the etchant

   For many applications we can assume that only one species in the acid fluid, which is the etchant, is important in the etching process. The distribution of the concentration of the etchant c in a domain $\Omega \subset \mathbb{R}^d$, with $d = 2$ or 3, is governed by a scalar advection-diffusion equation

   $$\frac{\partial c}{\partial t} + \sum_{i=1}^{d} \frac{\partial}{\partial x_i}\big(u_i c\big) - D \sum_{i=1}^{d} \frac{\partial^2 c}{\partial x_i^2} = 0, \tag{2.1}$$

   with u_i the Cartesian components of the velocity vector u, and D the diffusion coefficient, which is assumed to be constant throughout the flow domain. The governing equation (2.1) has to be completed with initial and boundary conditions, which are related to the type of process we consider.

   The boundary condition at the etching surface needs to be discussed in more detail, as it is related to the chemical reaction between the etchant and the solid material. First, some chemical background information is described, which is taken from [29, 45]. We consider as an example metallic iron (Fe) to be etched with ferric chloride (FeCl3)

   $$\mathrm{Fe}_{(s)} + 2\mathrm{FeCl3}_{(aq)} \rightleftharpoons 3\mathrm{FeCl2}_{(aq)}, \tag{2.2a}$$

   where (s) means solid and (aq) means that the species is dissolved in water. The process in (2.2a) shows that two molecules of ferric chloride are needed to dissolve one molecule of iron

   $$2\mathrm{Fe}^{3+} + \mathrm{Fe} \rightarrow 3\mathrm{Fe}^{2+}, \tag{2.2b}$$

   where Fe^{3+} means a molecule of iron that misses three electrons. As shown in [45], assuming that there is only one active component, the amount of etchant disappearing at the surface is: $k\,c$, with k the surface reaction constant of the

dissolution process and c the concentration at the surface. The amount of solid dissolved by the reaction is then equal to: $k\,c/m$, with m a constant which follows from the chemical reaction (for a reaction such as (2.2b) the constant m is equal to 2). This phenomenon tends to lower the concentration of the active component at the surface and a diffusion process is then initiated. The amount of etchant that is reacted away at the surface is balanced by a diffusive transport of etchant towards the surface. This leads to the following mass-transfer balance:

$$D \sum_{i=1}^{d} n_i \frac{\partial c}{\partial x_i} = -k\,c, \tag{2.3}$$

with n_i the i-th component of outward normal vector $\bar{n}$ at the boundary $\partial\Omega$ of Ω.

2. Movement of the cavity boundary

   The movement of the boundary of the etching cavity depends on the chemical reaction between the etchant and the solid material at the surface. This movement is obtained from the consideration that for the amount of etchant used in the reaction, m times the amount of solid material will dissolve into the fluid. Based on a mass balance, the velocity of the cavity boundary in the direction of the outward normal then is linearly proportional to the normal derivative of the concentration at the boundary in the opposite direction. Denoting the points on the cavity surface as $\bar{x}_s = (x_{s,1}, \ldots, x_{s,d})$, each Cartesian component of $\bar{x}_s$ moves according to the following equation

$$\frac{dx_{s,i}}{dt} = -\sigma_s n_i \sum_{j=1}^{d} \frac{\partial c}{\partial x_j} n_j, \quad \text{for } j = 1, \ldots, d, \tag{2.4}$$

   with constant σ_s given by

$$\sigma_s = \frac{D\,M_s}{m\,\rho_s}. \tag{2.5}$$

   This constant σ represents the rate of the chemical reaction between the solid material and the acid fluid on the etching surface. Here M_s is the molecular weight of the solid material and ρ_s its density.

3. Fluid flow inside the etching cavity

   When the distribution of the concentration is convection-dominated we need to model the flow of the acid fluid coming into and going out of the etching cavity. This flow is, in a very good approximation, an incompressible flow. The velocity field $u = \{u_i\}$, $i = 1, \ldots, d$ of the acid fluid and its kinematic pressure p are

therefore governed by the incompressible Navier-Stokes equations

$$\frac{\partial u_i}{\partial t} + \sum_{j=1}^{d} u_j \frac{\partial u_i}{\partial x_j} - \nu \sum_{j=1}^{d} \frac{\partial^2 u_i}{\partial x_j^2} + \frac{\partial p}{\partial x_i} = 0, \tag{2.6a}$$

$$\sum_{i=1}^{d} \frac{\partial u_i}{\partial x_i} = 0, \tag{2.6b}$$

with $\nu > 0$ the kinematic viscosity.

2.3 Dimensionless form of the governing equations

In the experiments and in the numerical simulations, it is useful to introduce dimensionless variables. A key benefit of this approach is that the dimensional analysis will provide the similarity variables which are the independent variables, describing the physical processes. Therefore, in this section the governing equations will be presented in dimensionless form. First, we introduce reference values for the variables relevant in wet-chemical etching processes.

Table 2.1: Reference values for etching process.

characteristic variable	symbol
length	L
concentration of etchant	C
fluid velocity	U
time	L^2/D
kinematic pressure	$1/U^2$

Here L is a representative length scale, C a reference concentration, for instance the initial etchant concentration, U a reference velocity, and D the diffusion coefficient of the etchant.

Using these reference variables, the governing equation (2.1) for the etchant concentration can be written in dimensionless form as follows:

$$\frac{\partial c}{\partial t} + \mathrm{Pe} \sum_{i=1}^{d} \frac{\partial}{\partial x_i}\big(u_i c\big) - \sum_{i=1}^{d} \frac{\partial^2 c}{\partial x_i^2} = 0, \tag{2.7}$$

with the Péclet number Pe defined as

$$\mathrm{Pe} = \frac{U\,L}{D}. \tag{2.8}$$

The Péclet number gives the ratio between convection and diffusion processes of the etchant concentration in the acid fluid. The value of the Péclet number indicates the

type of the etching process we consider. A small Péclet number means that the transport of the etchant is caused by the diffusion process and is called diffusion-controlled etching, whereas for large Péclet numbers the concentration is influenced by the fluid flow and is considered convection-dominated etching. In industrial applications, the Péclet number is generally large: $\mathrm{Pe} \sim 10^4$ and the convection dominates the transport of the etchant. The diffusion process is, however, dominant in thin layers close to the etched surface. For small values of the Péclet number we can neglect the convection term in (2.7).

In dimensionless form, the boundary condition (2.3) becomes

$$\sum_{i=1}^{d} n_i \frac{\partial c}{\partial x_i} = -\mathrm{Sh}\, c, \tag{2.9}$$

with the Sherwood number Sh defined as

$$\mathrm{Sh} = \frac{k\,L}{D}. \tag{2.10}$$

Here k is the surface reaction constant of the dissolution process. The Sherwood number represents the ratio between the amount of etchant that reacts at the surface and the amount of etchant transported by the diffusion process towards the surface. In wet-chemical etching processes the Sherwood number can cover a wide range of values for different applications, ranging from zero to infinity, and has a significant effect on the shape of the surface. A small Sherwood number means that the etchant which has reacted on the surface is immediately transported away from the surface, and the concentration of the etchant near the surface will be the same as the concentration away from the surface. A large Sherwood number means that the transport of the etchant away from the surface is slow compared to the dissolution process of the etchant at the surface. The etching process is controlled by the mass transfer to and from the surface and the final shape of the surface depends on a combination of the fluid velocity field and the concentration of the etchant on the surface.

Next, we consider the governing equation for the movement of the boundary described by (2.4). Using the reference values in Table 2.1, we can write (2.4) in dimensionless form as follows:

$$\frac{dx_{s,i}}{dt} = -\frac{1}{\beta} n_i \sum_{j=1}^{d} \frac{\partial c}{\partial x_j} n_j, \quad \text{for } j = 1, \ldots, d, \tag{2.11}$$

with the parameter β defined as

$$\beta = \frac{D}{\sigma_s\, C}. \tag{2.12}$$

Here σ_s is the constant defined in (2.5). The parameter β is a measure for the velocity by which the etched surface moves. When β is very large ($\beta \gg 1$) the surface moves very slowly. Typical values of β for a few well-known etching systems are

listed in [44]. It was shown in [44] that β is usually a very large parameter (between $100 \sim 50000$). When β goes to infinity, the velocity of the etched surface becomes very small, which means that the displacement of the etched surface is small compared to the convection-diffusion process of the etchant concentration and we can consider a quasi-steady-state process.

The incompressible Navier-Stokes equations (2.6) that govern the acid fluid flow can be written in dimensionless form as follows:

$$\frac{1}{\mathrm{Pe}}\frac{\partial u_i}{\partial t} + \sum_{j=1}^{d} u_j \frac{\partial u_i}{\partial x_j} - \frac{1}{\mathrm{Re}} \sum_{j=1}^{d} \frac{\partial^2 u_i}{\partial x_j^2} + \frac{\partial p}{\partial x_i} = 0, \tag{2.13a}$$

$$\sum_{i=1}^{d} \frac{\partial u_i}{\partial x_i} = 0, \tag{2.13b}$$

where the Reynolds number Re is defined as

$$\mathrm{Re} = \frac{U\,L}{\nu}. \tag{2.14}$$

Here ν is the kinematic viscosity. The Reynolds number represents the balance between the inertia and viscous forces on a fluid particle, thus characterizes the fluid flow problem under consideration. For small Reynolds numbers, the fluid flow is dominated by viscosity and we can consider laminar flows. A large Reynolds number indicates a dominance of inertial forces which may lead to turbulent flows.

For wet-chemical etching problems, the Reynolds number of the flow inside the cavity resulting from the etching process is relatively small: $\mathrm{Re} \sim 10^{-1}$ to 10^2 and the flow field is laminar. Inside the cavity, the inertial forces then can be neglected from (2.13), resulting in the Stokes equations:

$$\frac{1}{\mathrm{Pe}}\frac{\partial u_i}{\partial t} - \frac{1}{\mathrm{Re}} \sum_{j=1}^{d} \frac{\partial^2 u_i}{\partial x_j^2} + \frac{\partial p}{\partial x_i} = 0, \tag{2.15a}$$

$$\sum_{i=1}^{d} \frac{\partial u_i}{\partial x_i} = 0. \tag{2.15b}$$

Outside the cavity the Reynolds number is generally much larger and this has a significant influence on the mass transport outside the cavity.

Chapter 3

Discontinuous Galerkin Methods for Elliptic Equations

3.1 Introduction

Discontinuous Galerkin (DG) methods have a number of interesting features which make them attractive for the solution of the transport equations describing wet-chemical etching. As outlined in Chapter 1, in particular space-time DG methods are promising and will receive significant attention in the next two chapters. The key feature of DG methods is that they use basis functions which are only weakly coupled to the basis functions in neighboring elements. This makes DG methods ideally suited for higher order accurate discretizations on unstructured meshes, mesh adaptation and parallel computing. In this chapter, we will provide an introduction to the main aspects of DG methods using second-order elliptic partial differential equations as an example. We will introduce the main techniques frequently used in the subsequent chapters and also discuss some simple model problems to highlight certain features of DG methods, including their usefulness for adaptation.

DG methods have been around for quite some time. The first DG method was introduced in 1973 by Reed and Hill [51] for hyperbolic equations, and since then there have been major developments in DG methods for first-order hyperbolic partial differential equations. In particular, the work of Cockburn and Shu has been of great importance. For a survey, see [18, 19]. At the same time DG methods were independently proposed for elliptic and parabolic partial differential equations, see for example [3, 28, 67]. Based on the term added to stabilize the discretization, these DG methods were usually called interior penalty (IP) methods. The interior penalty method has, however, a mesh dependent constant which needs to be properly chosen to ensure stability and is considerably more complicated than continuous Galerkin (CG) methods, which initially have been applied much more frequently.

In recent years, DG methods have attracted significant attention resulting in many applications. At first, many researches were dedicated to the development of DG methods for nonlinear hyperbolic equations, especially for dealing with discontin-

uous solutions and shock capturing [17]. The excellent results obtained with DG methods for hyperbolic problems drew the attention from several researchers which extended the DG discretizations to the more complex fluid flow problems in which, although the convection still dominates the problem, diffusion should also be taken into account. An important step forward in combining convection and diffusion in a DG discretization were the results of Bassi and Rebay [6] for the compressible Navier-Stokes equations. These equations are rewritten as a first-order system, after which the DG discretization technique is applied. The approach of Bassi and Rebay, however, suffered from a weak instability and during the same time several other approaches were put forward. Important contributions are from Baumann and Oden [9, 10] which proposed a DG algorithm without free parameters for elliptic partial differential equations and also applied this technique to the convection-diffusion equation and the compressible Navier-Stokes equations. This algorithm is, however, suboptimal in accuracy and not stable for linear polynomials. An alternative method is provided by the Local Discontinuous Galerkin (LDG) method, developed by Cockburn and Shu [16] as an extension to the method of Bassi and Rebay. This method is suitable for a wide range of partial differential equations and has gained considerable popularity in recent years. The convergence of the LDG method for elliptic problems on arbitrary and Cartesian meshes is studied in [14] and [20]. An overview of all DG methods developed so far for elliptic partial differential equations, together with a unified analysis, can be found in [4]. Motivated by the nice results obtained with DG methods for elliptic and hyperbolic problems, they have been recently extended to the incompressible Navier-Stokes equations. The LDG method is used in [21] for the Stokes equations, and subsequently extended to the Oseen equations in [23], and the incompressible Navier-Stokes equations in [24]. An analysis of several DG techniques applied to the Stokes equations is provided in [54, 55].

In the remaining part of this chapter we first introduce the div-grad equation as a model problem in Section 3.2 and the finite element spaces in Section 3.3. Next, we describe in Section 3.4 the main steps to derive a DG discretization for second-order elliptic partial differential equations. Finally, an adaptation technique applied to the DG discretization is discussed in Section 3.5. In addition, both in Sections 3.4 and 3.5, several aspects of DG methods will be demonstrated with some simple numerical experiments.

3.2 Model problem

As an introduction to the discontinuous Galerkin methods discussed in Chapters 4 and 5, we describe in this chapter the main steps of deriving a DG discretization for second order elliptic partial differential equations using the div-grad equation as a model problem.

Let $\Omega \subset \mathbb{R}^d$, $d = 1, 2$, or 3, be a computational domain with boundary $\partial\Omega$. The

boundary is partitioned as $\partial\Omega = \partial\Omega_D \cup \partial\Omega_N$, with $\partial\Omega_D \cap \partial\Omega_N = \emptyset$ and $\partial\Omega_D$ has a nonzero measure. Introducing the notation $\overline{\nabla}$ for the spatial gradient operator in $\mathbb{R}^d$, defined as $\overline{\nabla} = \left(\frac{\partial}{\partial x_1}, \ldots, \frac{\partial}{\partial x_d}\right)$, we consider the following boundary value problem

$$-\overline{\nabla} \cdot (a\overline{\nabla}\phi) = f \quad \text{in } \Omega, \tag{3.1}$$

with $a = \{a_{ij}\}_{i,j=1}^{d}$ a symmetric positive definite matrix and f a given function on Ω. We supplement (3.1) with the boundary conditions

$$\phi = b_D \quad \text{on } \partial\Omega_D, \qquad \bar{n} \cdot (a\overline{\nabla}\phi) = b_N \quad \text{on } \partial\Omega_N, \tag{3.2}$$

where b_D and b_N are given functions defined on $\partial\Omega_D$ and $\partial\Omega_N$, respectively, and $\bar{n}$ the unit outward normal vector on $\partial\Omega$. As discussed in [4], it is beneficial for the DG discretization to rewrite the second order partial differential equation (3.1) as a first order system of equations by introducing an auxiliary variable $\lambda = \overline{\nabla}\phi$, such that (3.1) is written as

$$\lambda = a\overline{\nabla}\phi, \tag{3.3a}$$

$$-\overline{\nabla} \cdot \lambda = f. \tag{3.3b}$$

3.3 Finite element spaces and trace operators

In this section we define the finite element spaces for the DG discretization for the elliptic equation (3.1) and the trace operators necessary to account for the discontinuity of the basis functions across the element faces. Before doing that, we first discuss the partitioning of the computational domain into elements.

The computational domain Ω is partitioned into N elements K. The tessellation $T_h = \{K\}$ of Ω is defined as

$$T_h := \{K_j \mid \bigcup_{j=1}^{N} K_j = \Omega \text{ and } K_j \cap K_{j'} = \emptyset \text{ if } j \neq j', \quad 1 \leq j, j' \leq N\}.$$

In this chapter we assume that each element $K \in T_h$ is an affine image of a fixed master element $\hat{K}$; i.e., $K = F_K(\hat{K})$ for all $K \in T_h$, where $\hat{K}$ is either the open unit simplex or the open unit hypercube in $\mathbb{R}^d$. This assumption can be relaxed by using a composition of two mappings discussed later in Chapter 4. The boundary of each element is denoted by ∂K, and the outward normal vector on ∂K is denoted by $\bar{n}_K$. The radius of the smallest sphere containing each element K is denoted by h_K.

We consider several sets of faces. The set of all faces S in $\bar{\Omega}$ is denoted with F, the set of all interior faces in Ω with F_I, and the set of all boundary faces on $\partial\Omega$ with F_{bnd}. Two sets of boundary faces are defined as follows. The set of faces with a Dirichlet boundary condition is denoted as F_D, while the set of faces with a Neumann

boundary condition is denoted with F_N. The sets F_I and F_D are grouped into the set F_{ID}.

For the definition of the weak formulation and the finite element discretization we need to introduce the following function spaces. First, we recall the standard definition of the Sobolev spaces $H^s(\mathcal{D})$ (see e.g. [11]), with s a non-negative integer, in a domain $\mathcal{D} \subset \mathbb{R}^d$:

$$H^s(\mathcal{D}) := \{\phi \in L^2(\mathcal{D}) : \partial^\gamma \phi \in L^2(\mathcal{D}) \text{ for } |\gamma| \leq s\},$$

where ∂^γ denotes the weak derivative (see [11]) and γ the multi-index symbol, $\gamma = (\gamma_1, \ldots, \gamma_d)$, with γ_i non-negative integers. The length of γ is given by $|\gamma| = \sum_{i=1}^d \gamma_i$. When $s = 0$ the space is denoted as $L^2(\mathcal{D})$, which is equipped with the standard inner-product and norm:

$$(\phi, \psi)_{\mathcal{D}} := \int_{\mathcal{D}} \phi\psi \, \mathrm{d}\mathcal{K}, \quad \|\phi\|_{0,\mathcal{D}} := (\phi, \phi)_{\mathcal{D}}^{1/2},$$

and for $s \geq 1$, the Sobolev norm and semi-norm are defined as:

$$\|\phi\|_{s,\mathcal{D}} := \left(\sum_{|\gamma| \leq s} \|\partial^\gamma \phi\|_{0,\mathcal{D}}^2 \right)^{\frac{1}{2}}, \; |\phi|_{s,\mathcal{D}} := \left(\sum_{|\gamma| = s} \|\partial^\gamma \phi\|_{0,\mathcal{D}}^2 \right)^{\frac{1}{2}}.$$

Next, we introduce the concept of broken Sobolev spaces, which is necessary since the DG method is a non-conforming method. To each element $K \in T_h$ we assign a nonnegative integer s_K and collect this into the vector $s = \{s_K, \forall K \in T_h\}$. We then assign to T_h the broken Sobolev space $H^s(\Omega, T_h) := \{\phi \in L^2(\Omega) : \phi\,|_K \in H^{s_K}, \forall K \in T_h\}$, with corresponding norm and seminorm defined as:

$$\|\phi\|_{s,T_h} := \left(\sum_{K \in T_h} \|\phi\|_{s,K}^2 \right)^{\frac{1}{2}}, \qquad |\phi|_{s,T_h} := \left(\sum_{K \in T_h} |\phi|_{s,K}^2 \right)^{\frac{1}{2}}.$$

The DG discretization requires the use of the broken gradient $\overline{\nabla}_h \phi$ for $\phi \in H^1(\Omega, T_h)$, which is denoted by $(\overline{\nabla}_h \phi)\,|_K := \overline{\nabla}(\phi_K)$, $\forall K \in T_h$.

To each $K \in T_h$ we assign a nonnegative integer p_K as local polynomial degree. We denote by $Q_{p_K}(\hat{K})$ the set of all tensor product polynomials on $\hat{K}$ of degree $p_K \geq 0$ in each coordinate direction. The finite element space is then defined as

$$\Phi_h^p := \{\phi \in L^2(\Omega) : \phi\,|_K \circ F_K \in Q_{p_K}(\hat{K}), \quad \forall K \in T_h\}.$$

In the derivation of the DG discretization we also make use of the auxiliary space Λ_h^p:

$$\Lambda_h^p := \{\lambda \in L^2(\Omega)^d : \lambda\,|_K \circ F_K \in [Q_{p_K}(\hat{K})]^d, \quad \forall K \in T_h\}.$$

The traces of $\phi \in \Phi_h^p$ on the element boundary ∂K are defined as $\phi_K^{\pm} = \lim_{\epsilon \downarrow 0} \phi(x \pm \epsilon \bar{n}_K)$. The traces of $\lambda \in \Lambda_h^p$ are defined similarly.

In the DG finite element discretization we also need the *average* $\{\!\{\cdot\}\!\}$ and *jump* $\langle\!\langle\cdot\rangle\!\rangle$ operators as trace operators for the sets F_I and F_{bnd}. Note that the functions $\phi \in \Phi_h^p$ and $\lambda \in \Lambda_h^p$ are, in general, multivalued on a face $S \in F_I$. Introducing functions $\phi_i := \phi\,|_{K_i}$, $\lambda_i := \lambda\,|_{K_i}$, $\bar{n}_i := \bar{n}_{K_i}$, the average operator on $S \in F_I$ is defined as

$$\{\!\{\phi\}\!\} = \frac{1}{2}(\phi_i^- + \phi_j^-), \quad \{\!\{\lambda\}\!\} = \frac{1}{2}(\lambda_i^- + \lambda_j^-), \quad \text{on } S \in F_I,$$

while the jump operator is defined as:

$$\langle\!\langle\phi\rangle\!\rangle = \phi_i^- \bar{n}_i + \phi_j^- \bar{n}_j, \quad \langle\!\langle\lambda\rangle\!\rangle = \lambda_i^- \cdot \bar{n}_i + \lambda_j^- \cdot \bar{n}_j, \quad \text{on } S \in F_I,$$

with i and j the indices of the elements K_i and K_j which connect to the face $S \in F_I$. On a face $S \in F_{\text{bnd}}$, the average and jump operators are defined as:

$$\{\!\{\phi\}\!\} = \phi^-, \quad \{\!\{\lambda\}\!\} = \lambda^-, \quad \langle\!\langle\phi\rangle\!\rangle = \phi^- \bar{n}, \quad \langle\!\langle\lambda\rangle\!\rangle = \lambda^- \cdot \bar{n}, \quad \text{on } S \in F_{\text{bnd}}.$$

Notice that the jump $\langle\!\langle\phi\rangle\!\rangle$ is a vector parallel to the normal vector $\bar{n}$ and the jump $\langle\!\langle\lambda\rangle\!\rangle$ is a scalar quantity.

3.4 DG weak formulations

In this section we present the weak formulations of DG methods for the elliptic problem (3.3a)-(3.3b) with general boundary conditions, citing the main results from [4]. We also give a list of choices of stable numerical fluxes, based on the analysis presented in [4].

We start by multiplying (3.3a) and (3.3b) by test functions $\kappa \in \Lambda_h^p$ and $\zeta \in \Phi_h^p$, respectively, and formally integrate by parts on an element K to obtain

$$\int_K \lambda \cdot \kappa \, \mathrm{d}K = -\int_K a\phi \overline{\nabla} \cdot \kappa \, \mathrm{d}K + \int_{\partial K} a\phi \, \bar{n}_K \cdot \kappa \, \mathrm{d}\partial K, \quad \forall \kappa \in \Lambda_h^p, \tag{3.4a}$$

$$\int_K \lambda \cdot \overline{\nabla}\zeta \, \mathrm{d}K = \int_K f\,\zeta \, \mathrm{d}K + \int_{\partial K} \lambda \cdot \bar{n}_K \zeta \, \mathrm{d}\partial K, \quad \forall \zeta \in \Phi_h^p. \tag{3.4b}$$

The DG finite element discretization is obtained by approximating the functions ϕ and λ in each element $K \in T_h$ with $\phi_h \in \Phi_h^p$ and $\lambda_h \in \Lambda_h^p$. Since the functions ϕ_h and λ_h are discontinuous functions across the element boundary ∂K, they are replaced with *numerical fluxes* $\hat{\phi}_h$ and $\hat{\lambda}_h$, which are the approximations to ϕ and λ on ∂K, respectively. Choosing appropriate numerical fluxes is an important topic in many articles discussing the DG method for elliptic problems, see for instance [4]. The general weak formulation can be expressed as:

Find $\phi_h \in \Phi_h^p$ and $\lambda_h \in \Lambda_h^p$, such that for all $K \in T_h$, we have

$$\int_\Omega \lambda_h \cdot \kappa \, \mathrm{d}K = -\int_\Omega a\phi_h \overline{\nabla}_h \cdot \kappa \, \mathrm{d}K + \sum_{K \in T_h} \int_{\partial K} a\hat{\phi}_h \, \bar{n}_K \cdot \kappa \, \mathrm{d}\partial K, \quad \forall \kappa \in \Lambda_h^p, \tag{3.5a}$$

$$\int_\Omega \lambda_h \cdot \overline{\nabla}_h \zeta \, \mathrm{d}K = \int_\Omega f\,\zeta \, \mathrm{d}K + \sum_{K\in T_h} \int_{\partial K} \hat{\lambda}_h \cdot \bar{n}_K \zeta \, \mathrm{d}\partial K, \quad \forall \zeta \in \Phi_h^p. \tag{3.5b}$$

Using the following relation (see [4]) for scalar functions ϕ and vectors κ:

$$\sum_{K\in T_h} \int_{\partial K} \phi\kappa \cdot \bar{n}_K \, \mathrm{d}\partial K = \sum_{S\in F} \int_S \langle\!\langle \phi \rangle\!\rangle \cdot [\![\kappa]\!] \, \mathrm{d}S + \sum_{S\in F_I} \int_S [\![\phi]\!] \langle\!\langle \kappa \rangle\!\rangle \, \mathrm{d}S, \tag{3.6}$$

we can transform the integrals over the element boundary into integrals over interior and boundary faces:

$$\int_\Omega \lambda_h \cdot \kappa \, \mathrm{d}K = -\int_\Omega a\phi_h \overline{\nabla}_h \cdot \kappa \, \mathrm{d}K + \sum_{S\in F} \int_S a \langle\!\langle \hat{\phi}_h \rangle\!\rangle \cdot [\![\kappa]\!] \, \mathrm{d}S + \sum_{S\in F_I} \int_S a [\![\hat{\phi}_h]\!] \langle\!\langle \kappa \rangle\!\rangle \, \mathrm{d}S, \tag{3.7a}$$

$$\int_\Omega \lambda_h \cdot \overline{\nabla}_h \zeta \, \mathrm{d}K = \int_\Omega f\,\zeta \, \mathrm{d}K + \sum_{S\in F} \int_S [\![\hat{\lambda}_h]\!] \cdot \langle\!\langle \zeta \rangle\!\rangle \, \mathrm{d}S + \sum_{S\in F_I} \int_S \langle\!\langle \hat{\lambda}_h \rangle\!\rangle [\![\zeta]\!] \, \mathrm{d}S. \tag{3.7b}$$

Using integration by parts and (3.6), we can transform (3.7a) into

$$\begin{aligned} \int_\Omega \lambda_h \cdot \kappa \, \mathrm{d}K = \int_\Omega a\overline{\nabla}_h \phi_h \cdot \kappa \, \mathrm{d}K - \sum_{S\in F} \int_S a \langle\!\langle \phi_h - \hat{\phi}_h \rangle\!\rangle \cdot [\![\kappa]\!] \, \mathrm{d}S \\ - \sum_{S\in F_I} \int_S a [\![\phi_h - \hat{\phi}_h]\!] \langle\!\langle \kappa \rangle\!\rangle \, \mathrm{d}S. \end{aligned} \tag{3.8}$$

The next step is to eliminate the auxiliary variable λ_h from the weak formulation (3.5a). If we define lifting operators $r : (L^2(S))^d \to \Lambda_h^p$, $\forall S \in F$, and $l : L^2(S) \to \Lambda_h^p$, $\forall S \in F_I$, by

$$\int_\Omega r(v) \cdot \kappa \, \mathrm{d}K = -\sum_{S\in F} \int_S v \cdot [\![\kappa]\!] \, \mathrm{d}S, \tag{3.9}$$

$$\int_\Omega l(q) \cdot \kappa \, \mathrm{d}K = -\sum_{S\in F_I} \int_S q \langle\!\langle \kappa \rangle\!\rangle \, \mathrm{d}S, \tag{3.10}$$

for all $\kappa \in \Lambda_h^p$, we can write (3.8) as

$$\int_\Omega \lambda_h \cdot \kappa \, \mathrm{d}K = \int_\Omega a\overline{\nabla}_h \phi_h \cdot \kappa \, \mathrm{d}K + \int_\Omega ar(\langle\!\langle \phi_h - \hat{\phi}_h \rangle\!\rangle) \cdot \kappa \, \mathrm{d}K + \int_\Omega al([\![\phi_h - \hat{\phi}_h]\!]) \cdot \kappa \, \mathrm{d}K. \tag{3.11}$$

From the last equation, we obtain

$$\lambda_h = a\overline{\nabla}_h \phi_h + ar(\langle\!\langle \phi_h - \hat{\phi}_h \rangle\!\rangle) + al([\![\phi_h - \hat{\phi}_h]\!]) \qquad \text{a.e. } \forall x \in \Omega. \tag{3.12}$$

Inserting (3.12) into (3.7b), we obtain

$$\begin{aligned} \int_\Omega a\big(\overline{\nabla}_h \phi_h + r(\langle\!\langle \phi_h - \hat{\phi}_h \rangle\!\rangle) + l([\![\phi_h - \hat{\phi}_h]\!])\big) \cdot \overline{\nabla}_h \zeta \, \mathrm{d}K = \\ \int_\Omega f\,\zeta \, \mathrm{d}K + \sum_{S\in F} \int_S [\![\hat{\lambda}_h]\!] \cdot \langle\!\langle \zeta \rangle\!\rangle \, \mathrm{d}S + \sum_{S\in F_I} \int_S \langle\!\langle \hat{\lambda}_h \rangle\!\rangle [\![\zeta]\!] \, \mathrm{d}S. \end{aligned} \tag{3.13}$$

The DG weak formulation for the div-grad equation (3.1) then can be written as:

Find a $\phi_h \in \Phi_h^p$, such that the following relation is satisfied for all $\zeta \in \Phi_h^p$:

$$B(\phi_h, \zeta) = \int_\Omega f\,\zeta \,\mathrm{d}K, \tag{3.14}$$

where using (3.9)-(3.10), $B(\phi_h, \zeta)$ are defined as:

$$\begin{aligned} B(\phi_h, \zeta) := &\int_\Omega a\overline{\nabla}_h\phi_h \cdot \overline{\nabla}_h\zeta \,\mathrm{d}K - \sum_{S\in F}\int_S \left(a\langle\!\langle \phi_h - \hat{\phi}_h\rangle\!\rangle \cdot \{\!\{\overline{\nabla}_h\zeta\}\!\} + \{\!\{\hat{\lambda}_h\}\!\} \cdot \langle\!\langle\zeta\rangle\!\rangle\right) \mathrm{d}S \\ &- \sum_{S\in F_I}\int_S \left(a\{\!\{\phi_h - \hat{\phi}_h\}\!\}\langle\!\langle\overline{\nabla}_h\zeta\rangle\!\rangle + \langle\!\langle\hat{\lambda}_h\rangle\!\rangle\{\!\{\zeta\}\!\}\right) \mathrm{d}S. \end{aligned} \tag{3.15}$$

In [4] all the choices for the numerical fluxes $\hat{\phi}_h$ and $\hat{\lambda}_h$ that have been proposed so far are listed. The consistency and stability of all methods is also analyzed in this reference, including the optimality of the error bounds. In Table 3.1 we list all consistent and stable methods analyzed in [4], together with the choice of the numerical fluxes on the interior faces $S \in F_I$.

Table 3.1: Consistent and stable DG methods for elliptic problems.

Method	$\hat{\phi}_h \mid_{F_I}$	$\hat{\lambda}_h \mid_{F_I}$	L^2-norm
1. Brezzi et al. [12]	$\{\!\{\phi_h\}\!\}$	$\{\!\{\lambda_h\}\!\} - \alpha_r(\langle\!\langle\phi_h\rangle\!\rangle)$	$h_K^{p_K+1}$
2. LDG [16]	$\{\!\{\phi_h\}\!\} - \beta\cdot\langle\!\langle\phi_h\rangle\!\rangle$	$\{\!\{\lambda_h\}\!\} + \beta\langle\!\langle\lambda_h\rangle\!\rangle - \alpha_j(\langle\!\langle\phi_h\rangle\!\rangle)$	$h_K^{p_K+1}$
3. IP [28]	$\{\!\{\phi_h\}\!\}$	$\{\!\{\overline{\nabla}_h\phi_h\}\!\} - \alpha_j(\langle\!\langle\phi_h\rangle\!\rangle)$	$h_K^{p_K+1}$
4. Bassi et al. [5]	$\{\!\{\phi_h\}\!\}$	$\{\!\{\overline{\nabla}_h\phi_h\}\!\} - \alpha_r(\langle\!\langle\phi_h\rangle\!\rangle)$	$h_K^{p_K+1}$
5. NIPG [52]	$\{\!\{\phi_h\}\!\} + \bar{n}_K\cdot\langle\!\langle\phi_h\rangle\!\rangle$	$\{\!\{\overline{\nabla}_h\phi_h\}\!\} - \alpha_j(\langle\!\langle\phi_h\rangle\!\rangle)$	$h_K^{p_K}$

All numerical fluxes $\hat{\lambda}_h$ in Table 3.1 contain either the operators $\alpha_j(\langle\!\langle\phi_h\rangle\!\rangle)$ or $\alpha_r(\langle\!\langle\phi_h\rangle\!\rangle)$. Here we explain briefly the formulation for these operators, which are called local lifting operators.

- The operator α_j, is defined as $\alpha_j(v) = \mu v$ with $\mu \in \mathbb{R}^+$. This operator comes from the interior penalty (IP) term

$$\alpha^j(\phi, \zeta) = \sum_{S\in F}\int_S \mu\langle\!\langle\phi\rangle\!\rangle \cdot \langle\!\langle\zeta\rangle\!\rangle \,\mathrm{d}S, \tag{3.16}$$

  where the penalty weighting function $\mu : S \in F \to \mathbb{R}^+$ is given by $\mu = \eta_S h_S^{-1}$, with η_S a positive number and h_S the mesh size perpendicular to the face S.

- The operator $\alpha_r(v)$, is defined as $\alpha_r(v) = -\eta_S \{\!\{ r_S(v) \}\!\}$ on a face $S \in F_I$ and as $\alpha_r(v) = -\eta_S r_S(v) + \eta_S r_S(b_D \bar{n})$ on a face $S \in F_D$. On a face $S \in F_N$ this operator $\alpha_r(v)$ is equal to zero. For all $\kappa \in \Lambda_h^p$, the local lifting operator $r_S : (L^2(S))^d \to \Lambda_h^p$ is given by

$$\int_\Omega r_S(v) \cdot \kappa \, \mathrm{d}K = -\int_S v \cdot \{\!\{ \kappa \}\!\} \, \mathrm{d}S, \quad \text{on } S \in F_I, \tag{3.17}$$

$$\int_\Omega r_S(v) \cdot \kappa \, \mathrm{d}K = -\int_S v \cdot \kappa \, \mathrm{d}S, \qquad \text{on } S \in F_D. \tag{3.18}$$

  Note that $r_S(v)$ vanishes outside the union of the one or two elements connected to the face S and that $r(v) = \sum_{S \in F} r_S(v)$ for any $K \in T_h$.

We state here the main conclusions based on the analysis given in [4]. The Methods 1-4 in Table 3.1 are consistent, adjoint consistent, stable (under certain conditions on the parameters μ and η_s) and have optimal rates of convergence $h_K^{p_K+1}$ in the L^2-norm. Method 5 is consistent and stable (under similar conditions on μ, η_S), but is not adjoint consistent and has suboptimal rates of convergence $h_K^{p_K}$ in the L^2-norm. All methods in Table 3.1 have a local lifting operator in their formulation, either of the form α_j or α_r. This fact indicates that the lifting operator plays an important role in the DG method (more precisely to the stability of the methods). It is also concluded in [4] that DG methods whose numerical fluxes $\hat{\lambda}_h$ are independent of λ_h (Methods 3-5 in Table 3.1) produce stiffness matrices with a smaller number of non-zero entries. This makes that matrices resulting from the DG discretization with Methods 3-5 are more sparse than the matrices resulting from the DG discretization with Methods 1-2.

Considering several aspects of the numerical discretization, such as consistency, stability, optimal convergence, and sparsity of the resulting matrices, Methods 3-4 in Table 3.1 are good candidates for further study. Method 3, however, uses the local lifting operator α_j and the parameter μ in this operator depends on h_S^{-1}, the mesh size perpendicular to the face S on which this operator acts, which is not easy to define on general anisotropic meshes. Method 4, meanwhile, uses the local lifting operator α_r, and this operator only depends on a parameter η_S which is independent of the element size. Based on this fact, we choose Method 4 for the extension of the DG formulation to space-time problems, which will be discussed in Chapters 4 and 5.

We discuss now in detail the bilinear form $B(\cdot, \cdot)$ for Method 4, which is first introduced in [5], and later discussed in [7, 12]. For the general boundary conditions (3.2), the Bassi et al. method [5] uses the following numerical fluxes:

$$\begin{aligned} \hat{\phi}_h &= \{\!\{ \phi_h \}\!\} && \text{on } S \in F_I, \\ \hat{\phi}_h &= b_D && \text{on } S \in F_D, \\ \hat{\phi}_h &= \phi_h && \text{on } S \in F_N, \end{aligned} \tag{3.19}$$

and:

$$\begin{aligned} \hat{\lambda}_h &= \{\!\{\overline{\nabla}_h \phi_h\}\!\} + \eta_S \{\!\{ r_S(\langle\!\langle \phi_h \rangle\!\rangle) \}\!\} && \text{on } S \in F_I, \\ \hat{\lambda}_h &= \overline{\nabla}_h \phi_h + \eta_S r_S(\langle\!\langle \phi_h \rangle\!\rangle) - \eta_S r_S(b_D \bar{n}) && \text{on } S \in F_D, \\ \hat{\lambda}_h \cdot \bar{n} &= b_N && \text{on } S \in F_N. \end{aligned} \tag{3.20}$$

Substituting (3.19)-(3.20) into (3.15), we obtain

$$\begin{aligned} B(\phi_h, \zeta) := & \int_\Omega a \overline{\nabla}_h \phi_h \cdot \overline{\nabla}_h \zeta \, \mathrm{d}K \\ & - \sum_{S \in F_{ID}} \int_S a \big(\langle\!\langle \phi_h \rangle\!\rangle \cdot \{\!\{ \overline{\nabla}_h \zeta \}\!\} + \{\!\{ \overline{\nabla}_h \phi_h \}\!\} \cdot \langle\!\langle \zeta \rangle\!\rangle + \eta_S \{\!\{ r_S(\langle\!\langle \phi_h \rangle\!\rangle) \}\!\} \cdot \langle\!\langle \zeta \rangle\!\rangle \big) \, \mathrm{d}S \\ & + \sum_{S \in F_D} \int_S a \big(b_D \bar{n} \cdot \overline{\nabla}_h \zeta + \eta_S r_S(b_D \bar{n}) \cdot \bar{n} \zeta \big) \, \mathrm{d}S - \sum_{S \in F_N} \int_S b_N \zeta \, \mathrm{d}S. \end{aligned} \tag{3.21}$$

It is shown in [4, 12] that the bilinear form (3.21) is stable when the constant parameter η_S is chosen such that $\eta_S > N_S$, with N_S the number of faces on each element.

We complete this section with presenting some simple numerical experiments in one spatial dimension to demonstrate theoretically predicted rate of convergence of the DG discretization Method 4, $O(h_K^{p_K+1})$ in the L^2-norm (see the last column in Table 3.1).

We consider the elliptic equation (3.1) in $\Omega = (0, 1)$ with $a = 1$. The right hand side f and the Dirichlet boundary condition b_D are chosen such that the exact solution is:

$$\phi(x) = \sin(2\pi x).$$

We show the rates of convergence of the error in the L^2-norm for successively finer meshes and increasing polynomial degrees. The results are given in Fig. 3.1. This figure shows that the error in the L^2-norm converges at the optimal rate $h_K^{p_K+1}$, which is predicted by the theoretical estimates given in the last column in Table 3.1.

3.5 Adaptation

One of features of DG methods is their suitability for adaptation. In the field of adaptation several different strategies are distinguished: *h*-refinement by locally refining the mesh size, *p*-refinement by locally increasing the polynomial degree, and *hp*-refinement, which is a combination of *h* and *p*-refinement.

The search for optimal adaptation strategies has a long history in the development of finite element methods. A series of memorable papers on *h*-adaptivity, *p*-adaptivity, and *hp*-adaptivity has been written by Babuška and Gui in 1986, see [34, 35, 36].

In general, the construction of an adaptive strategy involves three main steps [39]. The first one is the derivation of a sharp *a posteriori* error bound for the finite

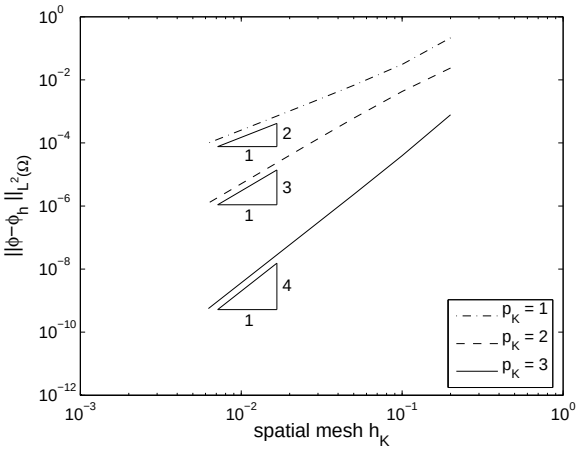

Figure 3.1: Elliptic equation, convergence with h-refinement.

element approximation of the partial differential equation under consideration. This error bound is then used as a stopping criteria to terminate the adaptive algorithm once the desired accuracy is achieved. The second step is the design of an appropriate refinement indicator to identify regions where adaptation is needed. The third step is the application of a local mesh modification strategy to improve the discretization within the regions where adaptation is needed.

Most of the development in adaptive methods concern the first and the second steps of the adaptive strategy, see [2, 50] for continuous Galerkin (CG) methods, and [39, 40, 53] for DG methods. Not so many studies are conducted in the field of the mesh modification strategy, which is important for practical implementation. Recently, an interesting paper on *hp*-refinement strategies for continuous Galerkin methods is proposed in [26]. The strategy described in [26] is the basic strategy we are going to pursue in this section. In one spatial dimension the method can be easily extended to a DG discretization, arriving at an almost optimal efficiency, as we will discuss in Section 3.5.2. The strategy in more spatial dimensions is described in [25].

3.5.1 Adaptation algorithms

A method that automatically provides (almost) optimal solutions is constructed by Demkowicz, Rachowicz, Devloo [26, 27, 49]. A solution at some stage is used as the starting point of the adaptive algorithm. In one spatial dimension, this input consists of a series of points $x_i, i = 0, \ldots, N$ and the degree of polynomials p_i in every element $[x_i, x_{i+1}]$ for $i = 0, \ldots, N-1$. The Galerkin method provides the coefficients

of each individual polynomial. The adaptive algorithm for one spatial dimension can be summarized in the following algorithm.

Algorithm 3.1 1D Adaptive algorithm from [26].

(1) Compute the solution u^* on a globally refined *hp* grid, i.e., the solution on a twice finer grid, with the polynomial degree in every element raised by one. So within an old element $[x_i, x_{i+1}]$, u^* can be represented by two polynomials of degree $p_i + 1$, namely on the element $[x_i, (x_i + x_{i+1})/2]$ and on $[(x_i + x_{i+1})/2, x_{i+1}]$. Hence the total number of the degrees of freedom on a refined grid becomes $2(p_i + 2)$.

(2) Solve the following (equidistant) interpolation problems in each old element $[x_i, x_{i+1}]$:

   (i) interpolate u^* on $[x_i, x_{i+1}]$ with *one* polynomial of degree $p_i + 1$, i.e., the number of the degrees of freedom is equal to $p_i + 2$.

   (ii) interpolate u^* on both elements $[x_i, (x_i + x_{i+1})/2]$ and $[(x_i + x_{i+1})/2, x_{i+1}]$ with *two* polynomials whose degrees add up to p_i, i.e. the number of the degrees of freedom equals $p_{i,1} + 1 + p_{i,2} + 1 = p_i + 2$, with $p_{i,1}, p_{i,2}$ are the polynomial degrees of the two subintervals. The choice for a pair of polynomial degrees is: $(p_i - 1, 1), (p_i - 2, 2), ..., (1, p_i - 1)$.

(3) For each choice in Steps (2.i) and (2.ii), we compute the error ϵ_i, defined as:

$$\epsilon_i = \|u^* - u_{\text{choice}}\|_{0,K},$$

   and the best choice is the one that gives minimal ϵ_i. This choice is stored, together with the corresponding ϵ_i.

(4) The elements i with error ϵ_i larger than a given tolerance are refined with the adaptation technique (h or p-refinement) chosen in Step (3).

There are several remarks regarding Algorithm 3.1. First, the strategy requires first finding a much better reference solution u^* of the problem, and then locally in every element the best approximation of u^* is constructed using interpolation with a smaller number of coefficients. Indeed, in element i, the solution u^* has $2(p_i + 2)$ degrees of freedom, whereas each approximation in Step (2) has $p_i + 2$ degrees of freedom. The degrees of freedom on a refined element are increased by one, no matter what choice has been made in Step (2).

For the DG discretization the basic strategy is slightly modified. The interpolation and the L^2-norm computations are replaced with the computation of the L^2-norm of the approximation. (Using Legendre polynomials as basis functions, Step (2) reduces to taking a few inner-products). The following algorithm is then applied for the DG discretization.

Algorithm 3.2 Modified 1D adaptation algorithm.

(1) Compute the solution u^* on a globally refined *hp* grid. Within an old element $[x_i, x_{i+1}]$, u^* can be represented by two polynomials of degree $p_i + 1$, namely on the element $[x_i, (x_i + x_{i+1})/2]$ and on $[(x_i + x_{i+1})/2, x_{i+1}]$.

(2) In each old element $[x_i, x_{i+1}]$ compute the following approximation errors:

  (i) The L^2-approximation of u^* on $[x_i, x_{i+1}]$ with *one* polynomial of degree $p_i + 1$.

  (ii) The L^2-approximation of u^* on both elements $[x_i, (x_i + x_{i+1})/2]$ and $[(x_i + x_{i+1})/2, x_{i+1}]$ with *two* polynomials whose degrees add up to p_i. The choice for a pair of the polynomial degrees is: $(p_i, 0), ..., (0, p_i)$.

(3) In each element determine the best approximation from Steps (2.i) and (2.ii), that is the one with the smallest ϵ_i, with ϵ_i defined in Algorithm 3.1.

(4) The elements i with the error ϵ_i larger than a given tolerance are refined with the adaptation technique (either h or $-p$ refinement) chosen in Step (3).

3.5.2 The efficiency of the method

We test the described method on the following model problem:

$$\frac{d}{dx}\Big(x^\beta \frac{d\phi(x)}{dx}\Big) = 2 - \beta, \quad \phi(0) = 0, \phi(1) = 1, \tag{3.22}$$

which has the analytic solution: $\phi(x) = x^{2-\beta}$. This solution is chosen based on the discussion in [34, 35, 36] which specifies theoretically the results of an optimal *hp*-refinement strategy. This theoretical result therefore provides a benchmark for every *hp*-adaptive method. The characterization of an optimal solution to problem (3.22) discussed in [34, 35, 36] can be summarized as follows:

- The error ϵ as a function of N, with N the total degrees of freedom, shows an exponential decay:
$$\epsilon \leq Ce^{-\gamma\sqrt{N}} \tag{3.23}$$
with γ a positive constant.

- The optimal mesh is a graded one, i.e.,
$$h_{i+1} = \lambda h_i, \tag{3.24}$$
with i the mesh index counted from $x = 0$, which means that away from the singularity the mesh stretches with a factor of λ. The optimal value for λ is given as: $\lambda = \lambda^* = 1/(\sqrt{2} - 1)^2 \approx 6$.

- The polynomial degree increases away from the singularity with the following formula:

$$p_i = \lceil \mu i \rceil, \tag{3.25}$$

with i the mesh index counted from $x = 0$ and μ a positive constant.

The adaptive method described in Algorithm 3.2 is implemented for problem (3.22) with $\beta = 1/3$, and the results show a very good approximation of the optimal solution and the final grid resulting from the adaptation. The local degree of the polynomials in each element is shown in Fig. 3.2.

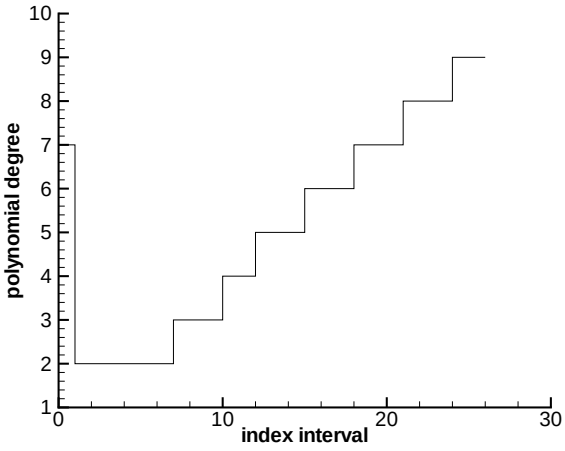

Figure 3.2: Local polynomial degree for problem (3.22) with $\beta = 1/3$, using Algorithm 3.2.

Since Gui and Babuška have theoretically predicted the optimal solution and the grid for (3.22), we can compute the optimal error curve as a function of the total number of the degrees of freedom, which is shown in Fig. 3.3. The results for the adaptive method using Algorithm 3.1 with a continuous Galerkin (CG) method lie in Fig. 3.3 on top of the optimal solution and the grid, while the results for the DG discretization are slightly higher. In multiple dimensions the DG algorithm is, however, much more flexible to deal with *hp*-adaptation than a CG algorithm, which easily compensates the slightly larger number of degrees of freedom required by the DG method. The adaptation algorithm is robust and results in (nearly) optimal meshes. Using for instance an additional criterion which consists of a combination of ϵ_i and the absolute value of the jumps of the current solution at left and right face of the element does not give a better solution, as shown in Fig. 3.4.

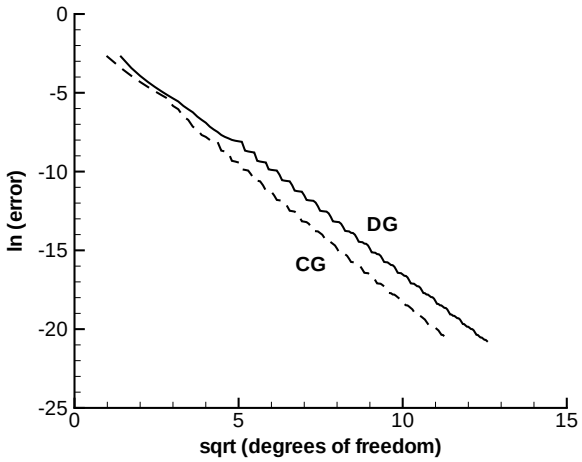

Figure 3.3: Error as function of the number of degrees of freedom for problem (3.22) with $\beta = 1/3$ using Algorithm 3.2, compare with (3.23).

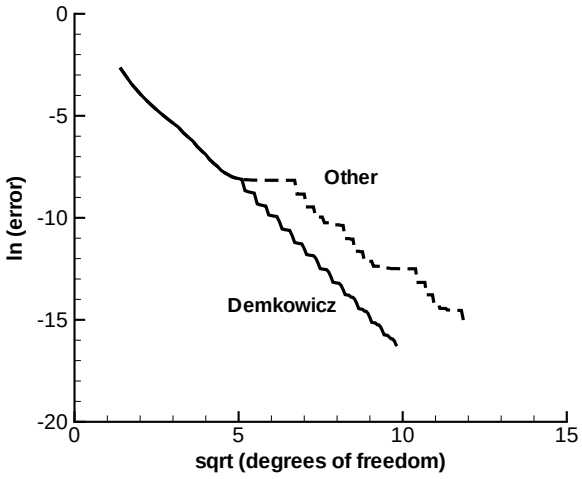

Figure 3.4: Error as function of the number of degrees of freedom for problem (3.22) with $\beta = 1/3$, including the jump of the solution (Other).

3.6 Concluding remarks

In this chapter, we discuss DG methods for the div-grad equation with general boundary conditions. Based on the analysis presented in [4] the DG method developed in [5] has been chosen for further study because the method is stable, consistent, gives optimal convergence, produces a sparse matrix, and its stabilization parameter is independent from the mesh size. The numerical experiments verify the optimality of the rate of convergence which will be further investigated in the subsequent chapters.

Also, a mesh adaptation technique has been studied to obtain optimal discretizations using both h and p adaptation. We applied a basic adaptation strategy that is originally developed in [26] for standard (continuous) Galerkin methods, to DG methods. The algorithm has been modified such that it combines well with the DG discretization. We show numerical experiments in one dimension which compare well with the theoretically predicted results.

Chapter 4

A Space-Time Discontinuous Galerkin Method for the Advection-Diffusion Equation in Time-Dependent Domains

4.1 Introduction

Wet-chemical etching processes require a finite element method which can efficiently deal with deforming elements to accommodate for the movement of the etching cavity boundary. In addition, thin boundary layers and singularities must be captured which can be done efficiently with mesh adaptation using either mesh refinement (h-adaptation) or adjustment of the polynomial degree (p-refinement). The space-time DG method, which simultaneously discretizes the equations in space and time, provides the necessary flexibility to deal both with time deforming meshes and hp-adaptation, and is an excellent technique for this type of problems. In this chapter we discuss the space-time DG discretization for the advection-diffusion equation in a time-dependent domain, which is the governing equation for the concentration of the etchant (2.1). The material is taken from [61].

First, the advection-diffusion equation is transformed to the space-time framework in a rather general setting. This will allow the extension of the mathematical model to anisotropic etching processes. After a description of the construction of space-time elements and the introduction of the function spaces and trace operators in Section 4.3, we give a complete derivation of the space-time DG discretization for the advection-diffusion equation in Section 4.4. This section is completed with the Arbitrary Lagrangian Eulerian (ALE) formulation of the space-time DG discretization as the latter formulation is useful for actual implementation of the discretization.

We then analyze the stability and the uniqueness of the numerical solution of the space-time DG discretization in Section 4.5. We also give error estimates and prove hp convergence of the space-time DG discretization in Section 4.6. Some simple numerical experiments are presented in Section 4.7 to verify the analysis.

4.2 The advection-diffusion equation

In this section we consider the advection-diffusion equation in the usual form and in the space-time framework. Let Ω_t be an open, bounded domain in $\mathbb{R}^d$, with d the number of spatial dimensions. The closure of Ω_t is $\overline{\Omega}_t$ and the boundary of Ω_t is denoted by $\partial\Omega_t$. The subscript t denotes the domain at time t as we consider the geometry of the spatial domain to be time-dependent. The outward normal vector to $\partial\Omega_t$ is denoted by $\bar{n} = (n_1, \ldots, n_d)$. Denoting $\bar{x} = (x_1, \ldots, x_d)$ as the spatial variables, we consider the time-dependent advection-diffusion equation:

$$\frac{\partial c}{\partial t} + \sum_{i=1}^{d} \frac{\partial}{\partial x_i}\big(u_i(t,\bar{x})c\big) - \sum_{i,j=1}^{d} \frac{\partial}{\partial x_j}\Big(D_{ij}(t,\bar{x})\frac{\partial c}{\partial x_i}\Big) = 0, \quad \text{in } \Omega_t, \tag{4.1}$$

where $u = (u_1, \ldots, u_d)$ is a vector field whose entries are continuous real-valued functions on $\bar{\Omega}_t$. Furthermore, $D \in \mathbb{R}^{d\times d}$ is a symmetric matrix of diffusion coefficients on $\bar{\Omega}_t$ whose entries are continuous real-valued functions. This matrix is positive definite in Ω_t and positive semi-definite on $\partial\Omega_t$. Then there exists a symmetric matrix $D^\star \in \mathbb{R}^{d\times d}$, the matrix square root $D^\star = D^{1/2}$, such that

$$D = D^\star\, D^\star. \tag{4.2}$$

In the space-time discretization we directly consider a domain in $\mathbb{R}^{d+1}$. A point $x \in \mathbb{R}^{d+1}$ has coordinates $(x_0, \bar{x})$, with $x_0 = t$ representing time. We then define the space-time domain $\mathcal{E} \subset \mathbb{R}^{d+1}$. The boundary of the space-time domain $\partial\mathcal{E}$ consists of the hypersurfaces $\Omega_0 := \{x \in \partial\mathcal{E} \mid x_0 = 0\}$, $\Omega_T := \{x \in \partial\mathcal{E} \mid x_0 = T\}$, and $\mathcal{Q} := \{x \in \partial\mathcal{E} \mid 0 < x_0 < T\}$. We reformulate the advection-diffusion equation now in the space-time framework. First, we introduce the vector function $B \in \mathbb{R}^{d+1}$ and the symmetric matrix $A \in \mathbb{R}^{(d+1)\times(d+1)}$ as:

$$B = \big(1, u\big), \qquad A = \begin{pmatrix} 0 & 0 \\ 0 & D \end{pmatrix}.$$

Then the advection-diffusion equation (4.1) can be transformed into a space-time formulation as:

$$-\nabla \cdot (-Bc + A\nabla c) = 0 \quad \text{in} \quad \mathcal{E}, \tag{4.3}$$

where $\nabla = \big(\frac{\partial}{\partial x_0}, \frac{\partial}{\partial x_1}, \ldots, \frac{\partial}{\partial x_d}\big)$ denotes the gradient operator in $\mathbb{R}^{d+1}$. Later we will also use the notation $\overline{\nabla}$ to denote the spatial gradient operator in $\mathbb{R}^d$, defined as $\overline{\nabla} = \big(\frac{\partial}{\partial x_1}, \ldots, \frac{\partial}{\partial x_d}\big)$. The unit outward normal vector at $\partial\mathcal{E}$ is denoted with n.

As different boundary conditions are imposed on $\partial\mathcal{E}$, we discuss in more detail the subdivision of $\partial\mathcal{E}$ into different parts. The boundary $\partial\mathcal{E}$ is divided into disjoint boundary subsets Γ_S, Γ_-, and Γ_+, where each subset is defined as follows:

$$\Gamma_S := \{x \in \partial\mathcal{E} : \bar{n}^T D\bar{n} > 0\},$$
$$\Gamma_- := \{x \in \partial\mathcal{E} \setminus \Gamma_S : B \cdot n < 0\}, \qquad \Gamma_+ := \{x \in \partial\mathcal{E} \setminus \Gamma_S : B \cdot n \geq 0\}.$$

The subscript S denotes the part of $\partial\mathcal{E}$ where matrix D is symmetric positive definite, while the subscripts $-$ and $+$ denote the inflow and outflow boundaries, respectively. We assume that Γ_S has a non-zero surface measure. Note that $\partial\mathcal{E} = \Gamma_S \cup \Gamma_- \cup \Gamma_+$. We subdivide Γ_S further into two sets: $\Gamma_S = \Gamma_{DS} \cup \Gamma_M$, with Γ_{DS} the part of Γ_S with a Dirichlet boundary condition and Γ_M the part of Γ_S with a mixed boundary condition. We also subdivide Γ_- into two parts: $\Gamma_- = \Gamma_{DB} \cup \Omega_0$, with Γ_{DB} the part of Γ_- with a Dirichlet boundary condition and Ω_0 the part of Γ_- with the initial condition. Note that $\Gamma_D = \Gamma_{DS} \cup \Gamma_{DB} \subset \partial\mathcal{E}$ is the part of the space-time domain boundary with a Dirichlet boundary condition. The boundary conditions on different parts of $\partial\mathcal{E}$ are written as

$$\begin{aligned} c &= c_0 \quad \text{on } \Omega_0, \\ c &= g_D \quad \text{on } \Gamma_D, \\ \alpha c + n \cdot (A\nabla c) &= g_M \quad \text{on } \Gamma_M, \end{aligned} \tag{4.4}$$

with $\alpha \geq 0$ and c_0, g_D, g_M given functions defined on the boundary. There is no boundary condition imposed on Γ_+.

4.3 Space-time description, finite element spaces and trace operators

4.3.1 Definition of space-time slabs, elements and faces

In this section we give a description of the space-time slabs, elements and faces used in the DG discretization. First, consider the time interval $\mathcal{I} = [0, T]$, partitioned by an ordered series of time levels $t_0 = 0 < t_1 < \ldots < t_{N_t} = T$. Denoting the nth time interval as $I_n = (t_n, t_{n+1})$, we have $\mathcal{I} = \cup_n \bar{I}_n$. The length of I_n is defined as $\triangle_n t = t_{n+1} - t_n$. Let Ω_{t_n} be an approximation to the spatial domain Ω at t_n for each $n = 0, \ldots, N_t$. A space-time slab is defined as the domain $\mathcal{E}^n = \mathcal{E} \cap (I_n \times \mathbb{R}^d)$ with boundaries Ω_{t_n}, $\Omega_{t_{n+1}}$ and $\mathcal{Q}^n = \partial\mathcal{E}^n \setminus (\Omega_{t_n} \cup \Omega_{t_{n+1}})$.

We now describe the construction of the space-time elements $\mathcal{K}$ in the space-time slab $\mathcal{E}^n$. Let the domain Ω_{t_n} be divided into N_n non-overlapping spatial elements K^n. At t_{n+1} the spatial elements K^{n+1} are obtained by mapping the elements K^n to their new position. Each space-time element $\mathcal{K}$ is obtained by connecting elements K^n and K^{n+1} using linear interpolation in time. A sketch of the space-time slab $\mathcal{E}^n$ and element $\mathcal{K}$ for two spatial dimensions is shown in Fig. 4.1. We denote by $h_\mathcal{K}$ the radius of the smallest sphere containing each element $\mathcal{K}$. The element boundary $\partial\mathcal{K}$ is the union of open faces of $\mathcal{K}$, which contains three parts K^n, K^{n+1}, and $\mathcal{Q}^n_\mathcal{K} = \partial\mathcal{K} \setminus (K^n \cup K^{n+1})$. We denote by $n_\mathcal{K}$ the unit outward space-time normal vector on $\partial\mathcal{K}$. The definition of the space-time domain is completed with the tessellation $\mathcal{T}_h^n$, which consists of all space-time elements in $\mathcal{E}^n$, and $\mathcal{T}_h = \cup_n \mathcal{T}_h^n$, which consists of all space-time elements in $\mathcal{E}$.

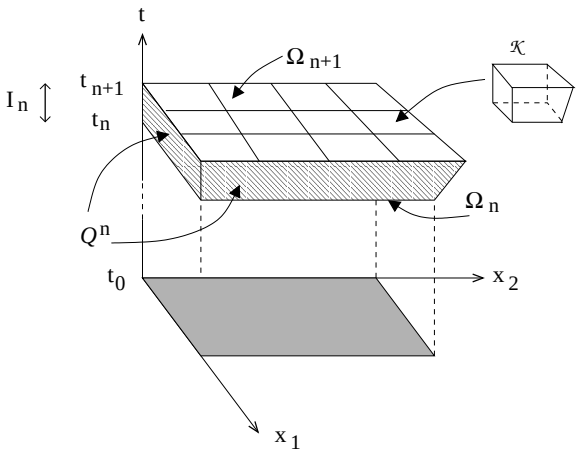

Figure 4.1: Space-time slab $\mathcal{E}^n$ with space-time element $\mathcal{K}$.

Next, we consider several sets of faces S. The set of all faces in $\bar{\mathcal{E}}$ is denoted with $\mathcal{F}$, the set of all interior faces in $\mathcal{E}$ with $\mathcal{F}_{\text{int}}$, and the set of all boundary faces on $\partial\mathcal{E}$ with $\mathcal{F}_{\text{bnd}}$. In the space-time slab $\mathcal{E}^n$ we denote the set of all faces with $\mathcal{F}^n$ and the set of all interior faces with $\mathcal{S}_I^n$. The faces separating two space-time slabs are denoted as $\mathcal{S}_S^n$. Several sets of boundary faces are defined as follows. The set of faces on Γ_{DS} and Γ_{DB} are denoted with $\mathcal{S}_{DS}^n$ and $\mathcal{S}_{DB}^n$, respectively. These sets are grouped into $\mathcal{S}_D^n$. The set of faces with a mixed boundary condition is denoted with $\mathcal{S}_M^n$. The set of faces with either a Dirichlet or a mixed boundary condition is denoted as $\mathcal{S}_{DM}^n$. The sets $\mathcal{S}_I^n$ and $\mathcal{S}_D^n$ are grouped into $\mathcal{S}_{ID}^n$.

Depending on whether the advective flux on $\mathcal{S}_{DS}^n$ is inflow or outflow, we subdivide further $\mathcal{S}_{DS}^n$ into $\mathcal{S}_{DSm}^n$ and $\mathcal{S}_{DSp}^n$, where $B \cdot n < 0$ on $\mathcal{S}_{DSm}^n$ and $B \cdot n \geq 0$ on $\mathcal{S}_{DSp}^n$. The sets $\mathcal{S}_{DB}^n$ and $\mathcal{S}_{DSm}^n$ are grouped into $\mathcal{S}_{DBSm}^n$ while the sets $\mathcal{S}_M^n$ and $\mathcal{S}_{DSp}^n$ are grouped into $\mathcal{S}_{MDSp}^n$. These sets are important when we discuss the advective flux in Section 4.4.2.

4.3.2 Finite element spaces and trace operators

This section starts with the introduction of anisotropic Sobolev spaces, such as in [31], on the domain $\mathcal{D} \subset \mathbb{R}^{d+1}$. The definition of the (standard) Sobolev spaces follows the definition in Section 3.3 for function spaces in $\mathbb{R}^{d+1}$. Here we restrict the definition of anisotropy to the case where the Sobolev index can be different for the temporal and spatial variables. All spatial variables have, however, the same index. Let (s_t, s_s) be a pair of non-negative integers, with s_t, s_s corresponds to temporal and spatial Sobolev index, respectively. For $\gamma_t, \gamma_s \geq 0$, the anisotropic Sobolev space of order (s_t, s_s) on

$\mathcal{D}$ is defined by

$$H^{(s_t,s_s)}(\mathcal{D}) := \{w \in L^2(\mathcal{D}) : \partial^{\gamma_t}\partial^{\gamma_s} w \in L^2(\mathcal{D}) \text{ for } \gamma_t \leq s_t, |\gamma_s| \leq s_s\},$$

with associated norm and semi-norm:

$$\|w\|_{s_t,s_s,\mathcal{D}} := \Bigg(\sum_{\substack{\gamma_t \leq s_t \\ |\gamma_s| \leq s_s}} \|\partial^{\gamma_t}\partial^{\gamma_s} w\|^2_{0,\mathcal{D}} \Bigg)^{\frac{1}{2}}, \quad |w|_{s_t,s_s,\mathcal{D}} := \Bigg(\sum_{\substack{\gamma_t = s_t \\ |\gamma_s| = s_s}} \|\partial^{\gamma_t}\partial^{\gamma_s} w\|^2_{0,\mathcal{D}} \Bigg)^{\frac{1}{2}}.$$

We now introduce mappings of the space-time elements. Following the discussion in [31], we assume that each element $\mathcal{K} \in \mathcal{T}_h$ is an image of a fixed master element $\hat{\mathcal{K}}$, with $\hat{\mathcal{K}}$ an open unit hypercube in $\mathbb{R}^{d+1}$, constructed via two mappings $Q_\mathcal{K} \circ F_\mathcal{K}$, where $F_\mathcal{K} : \hat{\mathcal{K}} \to \tilde{\mathcal{K}}$ is an affine mapping and $Q_\mathcal{K} : \tilde{\mathcal{K}} \to \mathcal{K}$ is a (regular enough) diffeomorphism (see Fig. 4.2). The definition of the Sobolev space $H^{(s_t,s_s)}(\tilde{\mathcal{K}})$ on $\tilde{\mathcal{K}}$ follows the definition of the anisotropic Sobolev space, while the Sobolev space $H^{(s_t,s_s)}(\mathcal{K})$ is defined as follows:

$$H^{(s_t,s_s)}(\mathcal{K}) := \{w \in L^2(\mathcal{K}) : w \circ Q_\mathcal{K} \in H^{(s_t,s_s)}(\tilde{\mathcal{K}})\}.$$

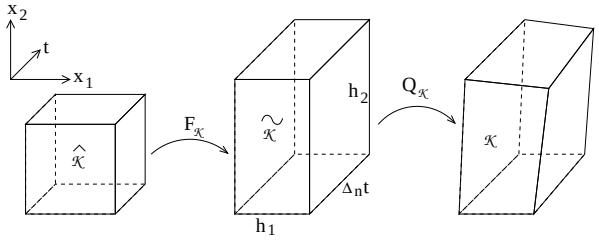

Figure 4.2: Construction of elements $\mathcal{K}$ via composition of affine maps and diffeomorphisms (for $d = 2$).

Since the DG method is a non-conforming method, it is necessary to introduce the concept of a broken anisotropic Sobolev space. To each element $\mathcal{K}$ we assign a pair of nonnegative integers $(s_{t,\mathcal{K}}, s_{s,\mathcal{K}})$ and collect them in the vectors $s_t = \{s_{t,\mathcal{K}} : \mathcal{K} \in \mathcal{T}_h\}$ and $s_s = \{s_{s,\mathcal{K}} : \mathcal{K} \in \mathcal{T}_h\}$. Then we assign to $\mathcal{T}_h$ the broken Sobolev space $H^{(s_t,s_s)}(\mathcal{E}, \mathcal{T}_h) := \{w \in L^2(\mathcal{E}) : w|_\mathcal{K} \in H^{(s_{t,\mathcal{K}},s_{s,\mathcal{K}})}(\mathcal{K}), \forall \mathcal{K} \in \mathcal{T}_h\}$, equipped with the broken Sobolev norm and corresponding semi-norm, respectively,

$$\|w\|_{s_t,s_s,\mathcal{T}_h} := \Bigg(\sum_{\mathcal{K}\in\mathcal{T}_h} \|w\|^2_{s_{t,\mathcal{K}},s_{s,\mathcal{K}},\mathcal{K}} \Bigg)^{\frac{1}{2}}, \qquad |w|_{s_t,s_s,\mathcal{T}_h} := \Bigg(\sum_{\mathcal{K}\in\mathcal{T}_h} |w|^2_{s_{t,\mathcal{K}},s_{s,\mathcal{K}},\mathcal{K}} \Bigg)^{\frac{1}{2}}.$$

For $w \in H^{(1,1)}(\mathcal{E}, \mathcal{T}_h)$, we define the broken gradient $\nabla_h w$ of w by $(\nabla_h w)|_{\mathcal{K}} := \nabla(w|_{\mathcal{K}})$, $\forall \mathcal{K} \in \mathcal{T}_h$.

Now we introduce the finite element spaces associated with the tessellation $\mathcal{T}_h$ that will be used in this chapter. To each element $\mathcal{K}$ we assign a pair of nonnegative integers $(p_{t,\mathcal{K}}, p_{s,\mathcal{K}})$ as local polynomial degrees, where the subscripts t and s denote time and space, and collect them into vectors $p_t = \{p_{t,\mathcal{K}} : \mathcal{K} \in \mathcal{T}_h\}$ and $p_s = \{p_{s,\mathcal{K}} : \mathcal{K} \in \mathcal{T}_h\}$. Defining $\mathcal{Q}_{p_{t,\mathcal{K}}, p_{s,\mathcal{K}}}(\hat{\mathcal{K}})$ as the set of all tensor-product polynomials on $\hat{\mathcal{K}}$ of degree $p_{t,\mathcal{K}}$ in the time direction and degree $p_{s,\mathcal{K}}$ in each spatial coordinate direction, we then introduce the finite element space of discontinuous piecewise polynomial functions as

$$\mathcal{W}_h^{(p_t,p_s)} := \{w \in L^2(\mathcal{E}) : w|_{\mathcal{K}} \circ Q_{\mathcal{K}} \circ F_{\mathcal{K}} \in \mathcal{Q}_{(p_{t,\mathcal{K}}, p_{s,\mathcal{K}})}(\hat{\mathcal{K}}), \forall \mathcal{K} \in \mathcal{T}_h\}.$$

In the derivation and analysis of the numerical discretization we also make use of the auxiliary space $\Upsilon_h^{(p_t,p_s)}$:

$$\Upsilon_h^{(p_t,p_s)} = \{\varphi \in L^2(\mathcal{E})^{d+1} : \varphi|_{\mathcal{K}} \circ Q_{\mathcal{K}} \circ F_{\mathcal{K}} \in [\mathcal{Q}_{(p_{t,\mathcal{K}}, p_{s,\mathcal{K}})}(\hat{\mathcal{K}})]^{d+1}, \forall \mathcal{K} \in \mathcal{T}_h\}.$$

The so called traces of $w \in \mathcal{W}_h^{(p_t,p_s)}$ on $\partial\mathcal{K}$ are defined as: $w_{\mathcal{K}}^{\pm} = \lim_{\epsilon \downarrow 0} w(x \pm \epsilon n_{\mathcal{K}})$. The traces of $\varphi \in \Upsilon_h^{(p_t,p_s)}$ are defined similarly.

Next, we define the *average* $\{\!\{\cdot\}\!\}$ and *jump* $[\![\cdot]\!]$ operators as trace operators for the sets $\mathcal{F}_{\text{int}}$ and $\mathcal{F}_{\text{bnd}}$. Note that functions $w \in \mathcal{W}_h^{(p_t,p_s)}$ and $\varphi \in \Upsilon_h^{(p_t,p_s)}$ are in general multivalued on a face $S \in \mathcal{F}_{\text{int}}$. Introducing the functions $w_i := w|_{\mathcal{K}_i}$, $\varphi_i := \varphi|_{\mathcal{K}_i}$, $n_i := n|_{\partial\mathcal{K}_i}$, we define the average operator on $S \in \mathcal{F}_{\text{int}}$ as:

$$\{\!\{w\}\!\} = \frac{1}{2}(w_i^- + w_j^-), \quad \{\!\{\varphi\}\!\} = \frac{1}{2}(\varphi_i^- + \varphi_j^-), \quad \text{on } S \in \mathcal{F}_{\text{int}},$$

while the jump operator is defined as:

$$[\![w]\!] = w_i^- \, n_i + w_j^- \, n_j, \quad [\![\varphi]\!] = \varphi_i^- \cdot n_i + \varphi_j^- \cdot n_j, \text{ on } S \in \mathcal{F}_{\text{int}},$$

with i and j the indices of the elements $\mathcal{K}_i$ and $\mathcal{K}_j$ which connect to the face $S \in \mathcal{F}_{\text{int}}$. On a face $S \in \mathcal{F}_{\text{bnd}}$, the average and jump operators are defined as:

$$\{\!\{w\}\!\} = w^-, \quad \{\!\{\varphi\}\!\} = \varphi^-, \quad [\![w]\!] = w^- \, n, \quad [\![\varphi]\!] = \varphi^- \cdot n, \quad \text{on } S \in \mathcal{F}_{\text{bnd}}.$$

Note that the jump $[\![w]\!]$ is a vector parallel to the normal vector n and the jump $[\![\varphi]\!]$ is a scalar quantity. We also need the spatial jump operator $\langle\!\langle \cdot \rangle\!\rangle$ for functions $w \in \mathcal{W}_h^{(p_t,p_s)}$, which is defined as:

$$\langle\!\langle w \rangle\!\rangle = w_i^- \, \bar{n}_i + w_j^- \, \bar{n}_j, \quad \text{on } S \in \mathcal{F}_{\text{int}}, \qquad \langle\!\langle w \rangle\!\rangle = w^- \, \bar{n}, \quad \text{on } S \in \mathcal{F}_{\text{bnd}}.$$

This spatial jump operator is similar to the jump operator in Section 3.3.

4.3.3 Lifting operators

In this section we introduce several lifting operators. The lifting operators discussed in this section are similar to the ones introduced in [4, 12]. These operators are required for the derivation of the space-time DG formulation in Section 4.4 and also for the analysis in Sections 4.5 and 4.6.

First, we introduce the local lifting operator $r_S : (L^2(S))^{d+1} \to \Upsilon_h^{(p_t,p_s)}$ as:

$$\int_{\mathcal{E}} r_S(\kappa) \cdot \varphi \, \mathrm{d}\mathcal{E} = -\int_S \kappa \cdot \{\!\{\varphi\}\!\} \, \mathrm{d}S, \quad \forall \varphi \in \Upsilon_h^{(p_t,p_s)}, \forall S \in \cup_n \mathcal{S}_{ID}^n. \tag{4.5}$$

The support of the operator r_S is limited to the element(s) that share the face S. Then we introduce the global lifting operator $R : (L^2(\cup_n \mathcal{S}_{ID}^n))^{d+1} \to \Upsilon_h^{(p_t,p_s)}$ as:

$$\int_{\mathcal{E}} R(\kappa) \cdot \varphi \, \mathrm{d}\mathcal{E} = \sum_{S \in \cup_n \mathcal{S}_{ID}^n} \int_{\mathcal{E}} r_S(\kappa) \cdot \varphi \, \mathrm{d}\mathcal{E}, \quad \forall \varphi \in \Upsilon_h^{(p_t,p_s)}. \tag{4.6}$$

We specify the above lifting operators for the Dirichlet boundary condition. Let $\mathcal{P}$ be the L^2 projection on $\Upsilon_h^{(p_t,p_s)}$, and replace κ by $\mathcal{P}g_D n$ in (4.5). Then on faces $S \in \cup_n \mathcal{S}_D^n$ we have

$$\int_{\mathcal{E}} r_S(\mathcal{P}g_D n) \cdot \varphi \, \mathrm{d}\mathcal{E} = -\int_S g_D n \cdot \varphi \, \mathrm{d}S, \quad \forall \varphi \in \Upsilon_h^{(p_t,p_s)}, \forall S \in \cup_n \mathcal{S}_D^n. \tag{4.7}$$

For the global lifting operators, we proceed in a similar way. Using the projection operator $\mathcal{P}$, we replace κ by $\mathcal{P}g_D n$ in (4.6) and (4.5) to have:

$$\int_{\mathcal{E}} R(\mathcal{P}g_D n) \cdot \varphi \, \mathrm{d}\mathcal{E} = -\sum_{S \in \cup_n \mathcal{S}_D^n} \int_S g_D n \cdot \varphi \, \mathrm{d}S, \quad \forall \varphi \in \Upsilon_h^{(p_t,p_s)}. \tag{4.8}$$

Using (4.6) and (4.8), we then introduce $R_{ID} : (L^2(\cup_n \mathcal{S}_{ID}^n))^{d+1} \to \Upsilon_h^{(p_t,p_s)}$ as:

$$R_{ID}(\kappa) = R(\kappa) - R(\mathcal{P}g_D n). \tag{4.9}$$

The spatial part of the lifting operators R and r_S, denoted by $\bar{R}$ and $\bar{r}_S$, are obtained by eliminating the first component of R and r_S, respectively.

4.4 Space-time DG discretization for the advection-diffusion

In this section, we describe the derivation of the space-time DG weak formulation for the advection-diffusion equation. As shown in e.g. [4, 12], it is beneficial for a DG discretization to rewrite the second order partial differential equation (4.3) into a system of first order equations. Following the same approach, we introduce an auxiliary variable $\upsilon = A\nabla c$ to obtain the following system of first order equations:

$$\upsilon = A\nabla c, \tag{4.10a}$$

$$-\nabla \cdot (-Bc + v) = 0. \tag{4.10b}$$

We discuss the derivation of the weak formulation of (4.10a)-(4.10b) in the following sections.

4.4.1 Weak formulation for the auxiliary variable

First, we consider the auxiliary equation (4.10a). By multiplying this equation with an arbitrary test function $\varphi \in \Upsilon_h^{(p_t,p_s)}$ and integrating over an element $\mathcal{K} \in \mathcal{T}_h$, we obtain:

$$\int_{\mathcal{K}} v \cdot \varphi \, \mathrm{d}\mathcal{K} = \int_{\mathcal{K}} A\nabla c \cdot \varphi \, \mathrm{d}\mathcal{K}, \quad \forall \varphi \in \Upsilon_h^{(p_t,p_s)}.$$

Next, we substitute v and c with their numerical approximations $v_h \in \Upsilon_h^{(p_t,p_s)}$ and $c_h \in \mathcal{W}_h^{(p_t,p_s)}$. After integration by parts twice and summation over all elements, we have for all $\varphi \in \Upsilon_h^{(p_t,p_s)}$ the following formulation:

$$\int_{\mathcal{E}} v_h \cdot \varphi \, \mathrm{d}\mathcal{E} = \int_{\mathcal{E}} A\nabla_h c_h \cdot \varphi \, \mathrm{d}\mathcal{E} + \sum_{\mathcal{K}\in\mathcal{T}_h} \int_{\partial\mathcal{K}} A(\hat{c}_h - c_h^-)n \cdot \varphi^- \, \mathrm{d}\partial\mathcal{K}. \tag{4.11}$$

The variable $\hat{c}_h$ is the *numerical flux* that must be introduced to account for the multivalued trace on $\partial\mathcal{K}$.

We recall the following relation (see [4], relation (3.3)), which holds for vectors φ and scalars q, piecewise smooth on $\mathcal{T}_h$:

$$\sum_{\mathcal{K}\in\mathcal{T}_h} \int_{\partial\mathcal{K}} (\varphi \cdot n)q \, \mathrm{d}\partial\mathcal{K} = \sum_{S\in\mathcal{F}} \int_S \{\!\{\varphi\}\!\} \cdot [\![q]\!] \, \mathrm{d}S + \sum_{S\in\mathcal{F}_{\mathrm{int}}} \int_S [\![\varphi]\!]\{\!\{q\}\!\} \, \mathrm{d}S. \tag{4.12}$$

When applied to the last contribution in (4.11) and using the symmetry of the matrix A, this results in

$$\begin{aligned} &\sum_{\mathcal{K}\in\mathcal{T}_h} \int_{\partial\mathcal{K}} A(\hat{c}_h - c_h^-)n \cdot \varphi^- \, \mathrm{d}\partial\mathcal{K} \\ &\quad = \sum_{S\in\mathcal{F}} \int_S [\![\hat{c}_h - c_h]\!] \cdot \{\!\{A\varphi\}\!\} \, \mathrm{d}S + \sum_{S\in\mathcal{F}_{\mathrm{int}}} \int_S \{\!\{\hat{c}_h - c_h\}\!\}[\![A\varphi]\!] \, \mathrm{d}S. \end{aligned} \tag{4.13}$$

We consider now the choice for the numerical flux $\hat{c}_h$. Several stable numerical fluxes for elliptic problems are listed in Table 3.1. Based on the discussion in Section 3.4 concerning the consistency, conservation properties, and matrix sparsity of those numerical fluxes in Table 3.1, we choose the following numerical flux, which is similar to the choices in [5, 12]:

$$\hat{c}_h = \{\!\{c_h\}\!\} \text{ on } S \in \mathcal{F}_{\mathrm{int}}, \quad \hat{c}_h = g_D \text{ on } S \in \cup_n \mathcal{S}_D^n, \quad \hat{c}_h = c_h^- \text{ elsewhere.} \tag{4.14}$$

Note that on faces $S \in \mathcal{S}_S^n$, which are the element boundaries K^n and K^{n+1}, the normal vector n has values $n = (\pm 1, \underbrace{0, \ldots, 0}_{d\times})$ and thus $An = (\underbrace{0, \ldots, 0}_{(d+1)\times})$. Hence there is no coupling between the space-time slabs. Substituting the choices for the numerical flux (4.14) into (4.13) and using the fact that entries of the matrix A are continuous functions, we obtain for each space-time slab $\mathcal{E}^n$:

$$\begin{aligned}\sum_{\mathcal{K}\in\mathcal{T}_h^n} \int_{\partial\mathcal{K}} A(\hat{c}_h - c_h^-)n \cdot \varphi^- \,\mathrm{d}\partial\mathcal{K} \\ = -\sum_{S\in\mathcal{S}_{ID}^n} \int_S [\![c_h]\!] \cdot A\{\!\{\varphi\}\!\} \,\mathrm{d}S + \sum_{S\in\mathcal{S}_D^n} \int_S g_D n \cdot A\varphi \,\mathrm{d}S. \end{aligned} \tag{4.15}$$

After summation over all space-time slabs, and using the symmetry of matrix A we can introduce the lifting operator (4.9) into (4.15) to obtain

$$\sum_{\mathcal{K}\in\mathcal{T}_h} \int_{\partial\mathcal{K}} A(\hat{c}_h - c_h^-)n \cdot \varphi^- \,\mathrm{d}\partial\mathcal{K} = \int_{\mathcal{E}} AR_{ID}([\![c_h]\!]) \cdot \varphi \,\mathrm{d}\mathcal{E}. \tag{4.16}$$

Introducing (4.16) into (4.11), we obtain for all $\varphi \in \Upsilon_h^{(p_t,p_s)}$:

$$\int_{\mathcal{E}} \upsilon_h \cdot \varphi \,\mathrm{d}\mathcal{E} = \int_{\mathcal{E}} A\nabla_h c_h \cdot \varphi \,\mathrm{d}\mathcal{E} + \int_{\mathcal{E}} AR_{ID}([\![c_h]\!]) \cdot \varphi \,\mathrm{d}\mathcal{E},$$

which implies that we can express $\upsilon_h \in \Upsilon_h^{(p_t,p_s)}$ as:

$$\upsilon_h = A\nabla_h c_h + AR_{ID}([\![c_h]\!]) \quad \text{a.e. } \forall x \in \mathcal{E}. \tag{4.17}$$

4.4.2 Weak formulation for the primal variable

The weak formulation for the advection-diffusion equation is obtained if we multiply (4.10b) with arbitrary test functions $w \in \mathcal{W}_h^{(p_t,p_s)}$, integrate by parts over element $\mathcal{K}$, and then substitute c, υ with their numerical approximations $c_h \in \mathcal{W}_h^{(p_t,p_s)}, \upsilon_h \in \Upsilon_h^{(p_t,p_s)}$:

$$\int_{\mathcal{E}} (-Bc_h + \upsilon_h) \cdot \nabla_h w \,\mathrm{d}\mathcal{E} - \sum_{\mathcal{K}\in\mathcal{T}_h} \int_{\partial\mathcal{K}} (-B\hat{c}_h + \hat{\upsilon}_h) \cdot n w^- \,\mathrm{d}\partial\mathcal{K} = 0. \tag{4.18}$$

Here we replaced c_h, υ_h on $\partial\mathcal{K}$ with the numerical fluxes $\hat{c}_h$, $\hat{\upsilon}_h$, to account for the multivalued traces on $\partial\mathcal{K}$.

The next step is to find appropriate choices for the numerical fluxes. We separate the numerical fluxes into an *advective flux* $B\hat{c}_h$ and a *diffusive flux* $\hat{\upsilon}_h$. For the advective flux, the obvious choice is an upwind flux, as described in [64]. However, for simplicity of proving the stability of the discretization, the upwind flux is written

as the sum of an average plus a jump penalty, as suggested in [13]. Thus, we write the numerical flux $B\,\hat{c}_h$ as:

$$B\hat{c}_h = \{\!\{Bc_h\}\!\} + C_S[\![c_h]\!]. \tag{4.19}$$

The parameter C_S is chosen as:

$$C_S = \frac{1}{2}|B \cdot n| \quad \text{on } S \in \mathcal{F}_{\text{int}}. \tag{4.20}$$

For conciseness of the proofs discussed later in Sections 4.5 and 4.6 we extend the definition of C_S to the boundary of the space-time domain as:

$$C_S = \begin{cases} -B \cdot n/2, & \text{on } S \in (\cup_n \mathcal{S}^n_{DBSm} \cup \Omega_0), \\ +B \cdot n/2, & \text{on } S \in (\cup_n \mathcal{S}^n_{MDSp} \cup \Gamma_+). \end{cases} \tag{4.21}$$

If we substitute φ and q in relation (4.12) with $\{\!\{Bc_h\}\!\} + C_S[\![c_h]\!]$ and w, respectively, the summation over the boundaries $\partial\mathcal{K}$ can be written as a sum over all faces:

$$\begin{aligned} &\sum_{\mathcal{K}\in\mathcal{T}_h} \int_{\partial\mathcal{K}} (\{\!\{Bc_h\}\!\} + C_S[\![c_h]\!]) \cdot nw^- \,\mathrm{d}\partial\mathcal{K} \\ &\quad = \sum_{S\in\mathcal{F}_{\text{int}}} \int_S (\{\!\{Bc_h\}\!\} + C_S[\![c_h]\!]) \cdot [\![w]\!] \,\mathrm{d}S + \sum_{S\in\mathcal{F}_{\text{bnd}}} \int_S Bc_h \cdot nw \,\mathrm{d}S. \end{aligned} \tag{4.22}$$

Now we consider the numerical flux $\hat{v}_h$. From [4], we have several options for this numerical flux. For similar reason as in Section 4.4.1, we choose $\hat{v}_h = \{\!\{v_h\}\!\}$, which is the same as in [5, 12]. By replacing $\hat{v}_h$ with $\{\!\{v_h\}\!\}$, then using (4.12), the contribution with $\hat{v}_h$ in (4.18) can also be written as a sum over all faces $S \in \mathcal{F}$:

$$\sum_{\mathcal{K}\in\mathcal{T}_h} \int_{\partial\mathcal{K}} \{\!\{\hat{v}_h\}\!\} \cdot nw^- \,\mathrm{d}\partial\mathcal{K} = \sum_{S\in\mathcal{F}} \int_S \{\!\{v_h\}\!\} \cdot [\![w]\!] \,\mathrm{d}S. \tag{4.23}$$

Using (4.22)-(4.23) and (4.17) (to eliminate v_h), the primal formulation for c_h is obtained:

$$\begin{aligned} &\int_{\mathcal{E}} \big(-Bc_h + A\nabla_h c_h + AR_{ID}([\![c_h]\!])\big) \cdot \nabla_h w \,\mathrm{d}\mathcal{E} \\ &+ \sum_{S\in\mathcal{F}_{\text{int}}} \int_S (\{\!\{Bc_h\}\!\} + C_S[\![c_h]\!]) \cdot [\![w]\!] \,\mathrm{d}S + \sum_{S\in\mathcal{F}_{\text{bnd}}} \int_S Bc_h \cdot nw \,\mathrm{d}S \\ &- \sum_{S\in\mathcal{F}} \int_S \big(A\{\!\{\nabla_h c_h\}\!\} + A\{\!\{R_{ID}([\![c_h]\!])\}\!\}\big) \cdot [\![w]\!] \,\mathrm{d}S = 0. \end{aligned} \tag{4.24}$$

This relation can be simplified using the following steps. Due to the symmetry of the matrix A and using the lifting operator R_{ID} (4.9) we have the relation

$$\begin{aligned} &\int_{\mathcal{E}} AR_{ID}([\![c_h]\!]) \cdot \nabla_h w \,\mathrm{d}\mathcal{E} \\ &\quad = -\sum_{S\in\cup_n\mathcal{S}^n_{ID}} \int_S A[\![c_h]\!] \cdot \{\!\{\nabla_h w\}\!\} \,\mathrm{d}S + \sum_{S\in\cup_n\mathcal{S}^n_D} \int_S Ag_D n \cdot \nabla_h w \,\mathrm{d}S. \end{aligned} \tag{4.25}$$

Further, the lifting operator R_{ID} has nonzero values only on faces $S \in \mathcal{S}_{ID}^n$. Using R, R_{ID} (see (4.6) and (4.9)) we obtain the following relation

$$\begin{aligned} &- \sum_{S\in\mathcal{F}} \int_S A\{\!\{R_{ID}([\![c_h]\!])\}\!\} \cdot [\![w]\!] \,\mathrm{d}S \\ &\quad = \int_{\mathcal{E}} AR([\![c_h]\!]) \cdot R([\![w]\!]) \,\mathrm{d}\mathcal{E} - \int_{\mathcal{E}} AR(\mathcal{P}g_D n) \cdot R([\![w]\!]) \,\mathrm{d}\mathcal{E}. \end{aligned} \tag{4.26}$$

Following a similar approach as in [12], we replace each term in (4.26) with the local lifting operator r_S, defined in Section 4.3.3, and make the following simplifications:

$$\int_{\mathcal{E}} AR([\![c_h]\!]) \cdot R([\![w]\!]) \,\mathrm{d}\mathcal{E} \cong \sum_{S\in\cup_n \mathcal{S}_{ID}^n} \sum_{\mathcal{K}\in\mathcal{T}_h} \eta_{\mathcal{K}} \int_{\mathcal{K}} Ar_S([\![c_h]\!]) \cdot r_S([\![w]\!]) \,\mathrm{d}\mathcal{K}, \tag{4.27}$$

$$\int_{\mathcal{E}} AR(\mathcal{P}g_D n) \cdot R([\![w]\!]) \,\mathrm{d}\mathcal{E} \cong \sum_{S\in\cup_n \mathcal{S}_{D}^n} \sum_{\mathcal{K}\in\mathcal{T}_h} \eta_{\mathcal{K}} \int_{\mathcal{K}} Ar_S(\mathcal{P}g_D n) \cdot r_S([\![w]\!]) \,\mathrm{d}\mathcal{K}. \tag{4.28}$$

In Section 4.5 we will derive a sufficient condition for the constant $\eta_{\mathcal{K}} > 0$ to guarantee a stable and unique solution. The advantage of this replacement is that the stiffness matrix in the weak formulation using the local lifting operators is considerably sparser than the stiffness matrix resulting from the weak formulation with global lifting operators. We refer to [4, 12] for a further explanation.

Substituting relations (4.25)-(4.26) into (4.24), using relations (4.27)-(4.28), and considering the structure of matrix A, we then obtain:

$$\begin{aligned} &- \int_{\mathcal{E}} Bc_h \cdot \nabla_h w \,\mathrm{d}\mathcal{E} + \int_{\mathcal{E}} D\overline{\nabla}_h c_h \cdot \overline{\nabla}_h w \,\mathrm{d}\mathcal{E} \\ &- \sum_{S\in\cup_n \mathcal{S}_{ID}^n} \int_S D\langle\!\langle c_h \rangle\!\rangle \cdot \{\!\{\overline{\nabla}_h w\}\!\} \,\mathrm{d}S + \sum_{S\in\cup_n \mathcal{S}_{D}^n} \int_S g_D D\bar{n} \cdot \overline{\nabla}_h w \,\mathrm{d}S \\ &+ \sum_{S\in\mathcal{F}_{\mathrm{int}}} \int_S (\{\!\{Bc_h\}\!\} + C_S[\![c_h]\!]) \cdot [\![w]\!] \,\mathrm{d}S + \sum_{S\in\mathcal{F}_{\mathrm{bnd}}} \int_S Bc_h \cdot nw \,\mathrm{d}S \\ &- \sum_{S\in\cup_n \mathcal{S}_{ID}^n} \int_S D\{\!\{\overline{\nabla}_h c_h\}\!\} \cdot \langle\!\langle w \rangle\!\rangle \,\mathrm{d}S - \sum_{S\in\mathcal{F}_{\mathrm{bnd}}\setminus\cup_n \mathcal{S}_{D}^n} \int_S D\overline{\nabla}_h c_h \cdot \bar{n}w \,\mathrm{d}S \\ &+ \sum_{S\in\cup_n \mathcal{S}_{ID}^n} \sum_{\mathcal{K}\in\mathcal{T}_h} \eta_{\mathcal{K}} \int_{\mathcal{K}} D\bar{r}_S([\![c_h]\!]) \cdot \bar{r}_S([\![w]\!]) \,\mathrm{d}\mathcal{K} \\ &- \sum_{S\in\cup_n \mathcal{S}_{D}^n} \sum_{\mathcal{K}\in\mathcal{T}_h} \eta_{\mathcal{K}} \int_{\mathcal{K}} D\bar{r}_S(\mathcal{P}g_D n) \cdot \bar{r}_S([\![w]\!]) \,\mathrm{d}\mathcal{K} = 0. \end{aligned} \tag{4.29}$$

Here we used the spatial gradient operator $\overline{\nabla}$, the spatial jump operator $\langle\!\langle \cdot \rangle\!\rangle$ (see Section 4.3.2) and the spatial lifting operator $\bar{r}_S$ (see Section 4.3.3). Next, we substitute

the following boundary and initial conditions:

$$\begin{aligned} D\overline{\nabla}_h c_h \cdot \bar{n} &= g_M - \alpha c_h \quad && \text{on } S \in \cup_n \mathcal{S}_M^n, \\ c_h &= g_D && \text{on } S \in \cup_n \mathcal{S}_{DBSm}^n, \\ c_h &= c_0 && \text{on } \Omega_0, \end{aligned}$$

into (4.29). We introduce now the bilinear form $a : \mathcal{W}_h^{(p_t,p_s)} \times \mathcal{W}_h^{(p_t,p_s)} \to \mathbb{R}$:

$$a(c_h, w) = a_a(c_h, w) + a_d(c_h, w), \tag{4.30}$$

with $a_a : \mathcal{W}_h^{(p_t,p_s)} \times \mathcal{W}_h^{(p_t,p_s)} \to \mathbb{R}$, $a_d : \mathcal{W}_h^{(p_t,p_s)} \times \mathcal{W}_h^{(p_t,p_s)} \to \mathbb{R}$ defined as:

$$\begin{aligned} a_a(c_h, w) = &- \int_{\mathcal{E}} Bc_h \cdot \nabla_h w \, \mathrm{d}\mathcal{E} + \sum_{S \in \mathcal{F}_{\text{int}}} \int_S (\{\!\{Bc_h\}\!\} + C_S [\![c_h]\!]) \cdot [\![w]\!] \, \mathrm{d}S \\ &+ \sum_{S \in (\cup_n \mathcal{S}_{MDSp}^n \cup \Gamma_+)} \int_S B \cdot n c_h w \, \mathrm{d}S, \end{aligned} \tag{4.31}$$

$$\begin{aligned} a_d(c_h, w) = &\int_{\mathcal{E}} D\overline{\nabla}_h c_h \cdot \overline{\nabla}_h w \, \mathrm{d}\mathcal{E} \\ &- \sum_{S \in \cup_n \mathcal{S}_{ID}^n} \int_S \left(D\langle\!\langle c_h \rangle\!\rangle \cdot \{\!\{\overline{\nabla}_h w\}\!\} + D\{\!\{\overline{\nabla}_h c_h\}\!\} \cdot \langle\!\langle w \rangle\!\rangle \right) \mathrm{d}S \\ &+ \sum_{S \in \cup_n \mathcal{S}_{ID}^n} \sum_{\mathcal{K} \in \mathcal{T}_h} \eta_{\mathcal{K}} \int_{\mathcal{K}} D\bar{r}_S([\![c_h]\!]) \cdot \bar{r}_S([\![w]\!]) \, \mathrm{d}\mathcal{K} + \sum_{S \in \cup_n \mathcal{S}_M^n} \int_S \alpha c_h w \, \mathrm{d}S, \end{aligned} \tag{4.32}$$

and the linear form $\ell : \mathcal{W}_h^{(p_t,p_s)} \to \mathbb{R}$ defined as:

$$\begin{aligned} \ell(w) = &- \sum_{S \in \cup_n \mathcal{S}_D^n} \int_S g_D D\bar{n} \cdot \overline{\nabla}_h w \, \mathrm{d}S + \sum_{S \in \cup_n \mathcal{S}_D^n} \sum_{\mathcal{K} \in \mathcal{T}_h} \eta_{\mathcal{K}} \int_{\mathcal{K}} D\bar{r}_S(\mathcal{P} g_D n) \cdot \bar{r}_S([\![w]\!]) \, \mathrm{d}\mathcal{K} \\ &+ \sum_{S \in \cup_n \mathcal{S}_M^n} \int_S g_M w \, \mathrm{d}S - \sum_{S \in \cup_n \mathcal{S}_{DBSm}^n} \int_S B g_D \cdot n w \, \mathrm{d}S + \int_{\Omega_0} c_0 w \, \mathrm{d}\Omega. \end{aligned} \tag{4.33}$$

Note that the term $\sum_{S \in \mathcal{F}_{\text{bnd}} \setminus \cup_n \mathcal{S}_{DM}^n} \int_S D\overline{\nabla}_h c_h \cdot \bar{n} w \, \mathrm{d}S$ is dropped from the bilinear form $a_d(\cdot,\cdot)$ since on $S \in \mathcal{F}_{\text{bnd}} \setminus \cup_n \mathcal{S}_{DM}^n$ the matrix D is zero. The space-time DG discretization for (4.1) can now be formulated as follows.

Find a $c_h \in \mathcal{W}_h^{(p_t,p_s)}$ such that:

$$a(c_h, w) = \ell(w), \qquad \forall w \in \mathcal{W}_h^{(p_t,p_s)}. \tag{4.34}$$

This formulation is the most straightforward for the analysis discussed in Sections 4.5 and 4.6, but for practical implementations, an arbitrary Lagrangian Eulerian (ALE) formulation is preferable. Therefore, in this paper, we also present the ALE

form of the space-time weak formulation (4.34). The relation between the space-time and ALE formulation discussed here follows the derivation in [64].

Using a result from [64], the space-time normal vector n can be split into two parts: $n = (n_t, \bar{n})$, with n_t the temporal part and $\bar{n}$ the spatial part of space-time normal vector n. Next, we consider the normal vector n on the faces $S \in \mathcal{F}_{\text{int}}$, which consist of two sets: $\mathcal{F}_{\text{int}} = \cup_n(\mathcal{S}_I^n \cup \mathcal{S}_S^n)$. On $S \in \mathcal{S}_S^n$, the space-time normal vector is $n = (\pm 1, \underbrace{0, \ldots, 0}_{d\times})$ and is not affected by the mesh velocity. On the faces $S \in \mathcal{S}_I^n$ the space-time normal vector depends on the mesh velocity u_g:

$$n = (-u_g \cdot \bar{n}, \bar{n}), \tag{4.35}$$

which also holds on the boundary faces $S \in \mathcal{F}_{\text{bnd}} \setminus (\Omega_0 \cup \Omega_T)$.

If we recall the bilinear and linear forms in (4.31)-(4.33), then only $a_a(\cdot,\cdot)$ and $\ell(\cdot)$ are needed to be rewritten into the ALE formulation by splitting the normal vector n into a temporal and spatial part. The bilinear form a_d in (4.32) remains valid for the ALE formulation since it does not depend on n_t. We now consider the contribution $\{\!\{Bc_h\}\!\} \cdot [\![w]\!]$ in (4.31). On $S \in \cup_n \mathcal{S}_I^n$, this contribution can be written in the ALE formulation using (4.35) as:

$$\{\!\{Bc_h\}\!\} \cdot [\![w]\!] = \{\!\{c_h\}\!\}(u - u_g) \cdot \langle\!\langle w \rangle\!\rangle,$$

while on $S \in \mathcal{S}_S^n$ this term does not change. Next, consider the term $[\![c_h]\!] \cdot [\![w]\!]$. Since the normal vector n has length one, we immediately obtain

$$[\![c_h]\!] \cdot [\![w]\!] = (c_h^+ - c_h^-)(w^+ - w^-),$$

and thus this contribution also does not depend on the mesh velocity u_g. The bilinear form $a_a(\cdot,\cdot)$ and linear functional $\ell(\cdot)$ in the ALE formulation are now equal to:

$$\begin{aligned}
a_a(c_h, w) = &- \int_{\mathcal{E}} Bc_h \cdot \nabla_h w \ \mathrm{d}\mathcal{E} + \sum_{S \in \cup_n \mathcal{S}_I^n} \int_S (\{\!\{c_h\}\!\}(u - u_g) \cdot \langle\!\langle w \rangle\!\rangle + C_S [\![c_h]\!] \cdot [\![w]\!]) \ \mathrm{d}S \\
&+ \sum_{S \in \cup_n \mathcal{S}_S^n} \int_S (\{\!\{Bc_h\}\!\} + C_S [\![c_h]\!]) \cdot [\![w]\!] \ \mathrm{d}S \\
&+ \sum_{S \in (\cup_n \mathcal{S}_{MDSp}^n \cup \Gamma_+)} \int_S (u - u_g) \cdot \bar{n} c_h w \ \mathrm{d}S, \qquad (4.36) \\
\ell(w) = &- \sum_{S \in \cup_n \mathcal{S}_D^n} \int_S g_D D\bar{n} \cdot \overline{\nabla}_h w \ \mathrm{d}S \\
&+ \sum_{S \in \cup_n \mathcal{S}_D^n} \sum_{\mathcal{K} \in \mathcal{T}_h} \eta_{\mathcal{K}} \int_{\mathcal{K}} D\bar{r}_S(\mathcal{P} g_D n) \cdot \bar{r}_S([\![w]\!]) \ \mathrm{d}\mathcal{K} + \sum_{S \in \cup_n \mathcal{S}_M^n} \int_S g_M w \ \mathrm{d}S \\
&- \sum_{S \in \cup_n \mathcal{S}_{DBSm}^n} \int_S g_D (u - u_g) \cdot \bar{n} w \ \mathrm{d}S + \int_{\Omega_0} c_0 w \ \mathrm{d}\Omega. \qquad (4.37)
\end{aligned}$$

4.5 Consistency, coercivity, and stability

In this section we present an analysis of the consistency, coercivity and stability of the space time discontinuous Galerkin formulation (4.30)-(4.34). This section is divided into two subsections, Section 4.5.1 concerns with the main results while detailed proofs can be found in Section 4.5.2.

4.5.1 Main results

The analysis of the space-time discontinuous Galerkin formulation is considerably simplified by the introduction of a so called DG norm, which is closely related to the bilinear form (4.30).

Definition 4.1 The DG norm $|||\cdot|||_{\mathrm{DG}}$ corresponding to the bilinear form (4.30) can be defined on $H^{(0,1)}(\mathcal{E}) + \mathcal{W}_h^{(p_t,p_s)}$, with $H^{(0,1)}(\mathcal{E})$ the anisotropic Sobolev space defined in Section 4.3.2, $\alpha \geq 0$ and $D^\star$ a symmetric positive semi-definite matrix, as:

$$|||w|||_{\mathrm{DG}}^2 = \sum_{\mathcal{K}\in\mathcal{T}_h} \|w\|_{0,\mathcal{K}}^2 + \sum_{\mathcal{K}\in\mathcal{T}_h} \|D^\star \overline{\nabla}_h w\|_{0,\mathcal{K}}^2 + \sum_{S\in\cup_n \mathcal{S}_{ID}^n} \sum_{\mathcal{K}\in\mathcal{T}_h} \|D^\star \bar{r}_S([\![w]\!])\|_{0,\mathcal{K}}^2 + \sum_{S\in\cup_n \mathcal{S}_M^n} \|\sqrt{\alpha} w\|_{0,S}^2 + \sum_{S\in\mathcal{F}} \|C_S^{1/2} |[\![w]\!]|\|_{0,S}^2.$$

First, we discuss the consistency of the space-time DG method (4.34). This formulation is consistent when (4.34) is also satisfied by $c \in H^2(\mathcal{E})$, the solution of (4.3)-(4.4):

$$a(c, w) = \ell(w), \qquad \forall w \in H^{(1,1)}(\mathcal{E}, \mathcal{T}_h). \tag{4.38}$$

The proof for consistency is straightforward. We replace c_h in (4.30) by c. Since c solves (4.3)-(4.4), we have $\{\!\{Bc\}\!\} = Bc$ on $S \in \mathcal{F}$, $[\![c]\!] = 0$ and $[\![\nabla_h c]\!] = 0$ on $S \in \mathcal{F}_{\mathrm{int}}$, $[\![c]\!] = g_D n$ on $S \in \mathcal{S}_D^n$, and $\{\!\{\nabla_h c\}\!\} = \nabla c$ on $S \in \mathcal{S}_{ID}^n$. If we use these relations into (4.30), perform integration by parts, and use the boundary conditions (4.4), we obtain $\ell(w)$. Subtracting (4.34) from (4.38) yields the Galerkin orthogonality property

$$a(c - c_h, w) = 0, \qquad \forall w \in \mathcal{W}_h^{(p_t,p_s)}. \tag{4.39}$$

The next result concerns the coercivity of the bilinear form $a(\cdot,\cdot)$. In order to prove the coercivity, we first introduce the following inequality, which is a direct extension of the one discussed in [4], p.1763, to the space-time discretization,

$$\|v\|_{0,\mathcal{E}} \leq C_p \Big(\sum_{\mathcal{K}\in\mathcal{T}_h} \|D^\star \overline{\nabla}_h v\|_{0,\mathcal{K}}^2 + \sum_{S\in\cup_n \mathcal{S}_{ID}^n} \sum_{\mathcal{K}\in\mathcal{T}_h} \|D^\star \bar{r}_S([\![v]\!])\|_{0,\mathcal{K}}^2 \Big)^{1/2}. \tag{4.40}$$

The constant C_p in this inequality follows from the discrete Poincaré inequality in [3], Lemma 2.1. We then prove the coercivity in the following lemma.

Lemma 4.2 *Let $\eta_0 = \min_{\mathcal{K}\in\mathcal{T}_h} \eta_{\mathcal{K}}$. Assume that $\eta_0 > N_f$, with N_f the number of faces of each element $\mathcal{K} \in \mathcal{T}_h$. Then, if*

$$\frac{\beta_c}{C_p^2} + \inf_{x\in\mathcal{E}} \overline{\nabla} \cdot u(x) \geq b_0 > 0, \tag{4.41}$$

with $\beta_c = \min(1-\epsilon, \eta_0 - \frac{N_f}{\epsilon}) > 0$ for $\epsilon \in (\frac{N_f}{\eta_0}, 1)$, there exists a constant $\beta_a > 0$, independent of the mesh size $h = \max_{\mathcal{K}\in\mathcal{T}_h} h_{\mathcal{K}}$, such that

$$a(w,w) \geq \beta_a |||w|||_{\mathrm{DG}}^2, \quad \forall w \in \mathcal{W}_h^{(p_t,p_s)}, \tag{4.42}$$

for $0 \leq p_t \leq 1$ and $p_s \geq 0$, with $\beta_a = \min(\frac{b_0}{2}, \frac{\beta_c}{2})$.

The proof, which is given in Section 4.5.2, is an extension to the space-time framework of the analysis given in [12, 13]. The condition $\overline{\nabla} \cdot u \geq 0$ for $\forall x \in \mathcal{E}$ such as in [38] is relaxed using the assumption (4.41).

The next result shows that the solution to (4.34) is bounded by known data.

Lemma 4.3 *Assume that the parameters $\eta_0, \beta_a, \beta_c, b_0$ are such that Lemma 4.2 is satisfied and let $\eta_m = \max_{\mathcal{K}\in\mathcal{T}_h} \eta_{\mathcal{K}}$. Then the solution to the weak formulation* (4.34) *satisfies the following upper bound:*

$$\begin{aligned}\beta_a^2 |||c_h|||_{\mathrm{DG}}^2 \leq & \sum_{\mathcal{K}\in\mathcal{T}_h} \|D^\star \bar{R}(\mathcal{P} g_D n)\|_{0,\mathcal{K}}^2 + \eta_m^2 \sum_{S\in\cup_n \mathcal{S}_D^n} \sum_{\mathcal{K}\in\mathcal{T}_h} \|D^\star \bar{r}_S(\mathcal{P} g_D n)\|_{0,\mathcal{K}}^2 \\ & + \sum_{S\in\cup_n \mathcal{S}_M^n} \|\alpha^{-1/2} g_M\|_{0,S}^2 + 4 \sum_{S\in\cup_n \mathcal{S}_{DB}^n} \|C_S^{1/2} g_D\|_{0,S}^2 \\ & + 4\|C_S^{1/2} c_0\|_{0,\Omega_0}^2.\end{aligned}$$

The proof, given in Section 4.5.2, is an extension to space-time framework of the analysis given in [38]. It mainly consists of applying the Schwarz and arithmetic-geometric mean inequalities to linear form $\ell(\cdot)$ and making use of the result from Lemma 4.2.

The upper bound for the solution given by Lemma 4.3 is independent of $h_{\mathcal{K}}$, the radius of the smallest sphere containing each space-time element, hence also from the time step $\triangle_n t$ since $\triangle_n t \leq h_{\mathcal{K}}$. This result shows that the space-time DG discretization is unconditionally stable when the proper stabilization coefficient η_0 is chosen.

The next result states the existence of a unique solution of (4.34). Its proof, which is discussed in Section 4.5.2, is obtained by using the coercivity in Lemma 4.2.

Theorem 4.4 *Assume that $\eta_0 > N_f$, with N_f the number of faces of each element $\mathcal{K} \in \mathcal{T}_h$, and the parameters β_a, β_c are chosen such that Lemma 4.2 is satisfied. Then the space-time discontinuous Galerkin discretization given by* (4.34) *is unconditionally stable and has a unique solution for basis functions which are constant or linear in time.*

4.5.2 Detailed proofs

Proof of coercivity in Lemma 4.2

To prove Lemma 4.2, we first consider $a_a(c_h, w)$. Take $c_h = w$ in (4.31), use the relation: $wB \cdot \nabla_h w = -\frac{1}{2}(\nabla_h \cdot B)w^2 + \frac{1}{2}\nabla_h \cdot (Bw^2)$, and apply Gauss' Theorem for $a_a(w, w)$ to obtain the following relation:

$$\begin{aligned} a_a(w,w) =& \frac{1}{2}\int_{\mathcal{E}} (\nabla_h \cdot B)w^2 \ \mathrm{d}\mathcal{E} - \frac{1}{2}\sum_{\mathcal{K}\in\mathcal{T}_h}\int_{\partial\mathcal{K}} (B\cdot n)w^2 \ \mathrm{d}\partial\mathcal{K} \\ &+ \sum_{S\in\mathcal{F}_{\mathrm{int}}}\int_S (\{\!\{Bw\}\!\} + C_S[\![w]\!])\cdot[\![w]\!] \ \mathrm{d}S + \sum_{S\in(\cup_n \mathcal{S}^n_{MDSp}\cup\Gamma_+)}\int_S B\cdot n w^2 \ \mathrm{d}S. \end{aligned}$$

Using the identity (4.12) and the fact that vector B is a continuous function, the last equation is written further as

$$\begin{aligned} a_a(w,w) =& \frac{1}{2}\int_{\mathcal{E}} (\nabla\cdot B)w^2 \ \mathrm{d}\mathcal{E} - \frac{1}{2}\sum_{S\in\mathcal{F}_{\mathrm{int}}}\int_S B\cdot[\![w^2]\!] \ \mathrm{d}S \\ &- \frac{1}{2}\sum_{S\in(\cup_n \mathcal{S}^n_{DBSm}\cup\Omega_0)}\int_S B\cdot n w^2 \ \mathrm{d}S + \sum_{S\in\mathcal{F}_{\mathrm{int}}}\int_S \{\!\{Bw\}\!\}\cdot[\![w]\!] \ \mathrm{d}S \\ &+ \frac{1}{2}\sum_{S\in(\cup_n \mathcal{S}^n_{MDSp}\cup\Gamma_+)}\int_S B\cdot n w^2 \ \mathrm{d}S + \sum_{S\in\mathcal{F}_{\mathrm{int}}}\int_S C_S[\![w]\!]\cdot[\![w]\!] \ \mathrm{d}S. \end{aligned} \tag{4.43}$$

Due to the continuity of vector B, on faces $S \in \mathcal{F}_{\mathrm{int}}$ we have:

$$\int_S \{\!\{Bw\}\!\}\cdot[\![w]\!] \ \mathrm{d}S = \frac{1}{2}\int_S B\cdot[\![w^2]\!] \ \mathrm{d}S. \tag{4.44}$$

As a consequence of (4.44) and using the definition of C_S in (4.20)-(4.21), we can write the final form of $a_a(w, w)$ as:

$$a_a(w,w) = \frac{1}{2}\int_{\mathcal{E}} (\nabla\cdot B)w^2 \ \mathrm{d}\mathcal{E} + \sum_{S\in\mathcal{F}} \|C_S^{1/2}|[\![w]\!]|\|^2_{0,S}. \tag{4.45}$$

Next, we consider $a_d(w, w)$ in (4.32) with $c_h = w$. Using the global lifting operator $\bar{R}$, which is the spatial part of the lifting operator R defined in (4.6), and the fact that matrix $D^\star$ is symmetric, we can write $a_d(w, w)$ as:

$$\begin{aligned} a_d(w,w) =& \sum_{\mathcal{K}\in\mathcal{T}_h} \|D^\star\overline{\nabla}_h w\|^2_{0,\mathcal{K}} + 2\sum_{\mathcal{K}\in\mathcal{T}_h}\int_{\mathcal{K}} D^\star\overline{\nabla}_h w\cdot D^\star\bar{R}([\![w]\!]) \ \mathrm{d}\mathcal{K} \\ &+ \sum_{S\in\cup_n\mathcal{S}^n_{ID}}\sum_{\mathcal{K}\in\mathcal{T}_h}\eta_{\mathcal{K}}\|D^\star\bar{r}_S([\![w]\!])\|^2_{0,\mathcal{K}} + \sum_{S\in\cup_n\mathcal{S}^n_M}\|\sqrt{\alpha}w\|^2_{0,S}. \end{aligned} \tag{4.46}$$

Using the Schwarz and arithmetic-geometric mean inequalities we obtain

$$2\int_{\mathcal{K}} D^\star\overline{\nabla}_h w \cdot D^\star\bar{R}([\![w]\!])\ \mathrm{d}\mathcal{K} \geq -\epsilon\|D^\star\overline{\nabla}_h w\|^2_{0,\mathcal{K}} - \frac{1}{\epsilon}\|D^\star\bar{R}([\![w]\!])\|^2_{0,\mathcal{K}}, \tag{4.47a}$$

with $\epsilon > 0$. As a consequence of (4.6) and the fact that the local lifting operator $\bar{r}_S$ is only non-zero in the elements connected to the face S, we also have

$$\|D^\star\bar{R}([\![w]\!])\|^2_{0,\mathcal{K}} \leq N_f \sum_{S\in\cup_n\mathcal{S}^n_{ID}} \|D^\star\bar{r}_S([\![w]\!])\|^2_{0,\mathcal{K}}, \tag{4.47b}$$

with N_f the number of faces of each element $\mathcal{K} \in \mathcal{T}_h$. Introducing (4.47a)-(4.47b) into (4.46) and combining with (4.45), we deduce

$$\begin{aligned} a(w,w) \geq \frac{1}{2}\int_{\mathcal{E}} (\overline{\nabla}\cdot u)w^2\ \mathrm{d}\mathcal{E} + \big(1-\epsilon\big) \sum_{\mathcal{K}\in\mathcal{T}_h} \|D^\star\overline{\nabla}_h w\|^2_{0,\mathcal{K}} \\ + \big(\eta_0 - \frac{N_f}{\epsilon}\big) \sum_{S\in\cup_n\mathcal{S}^n_{ID}} \sum_{\mathcal{K}\in\mathcal{T}_h} \|D^\star\bar{r}_S([\![w]\!])\|^2_{0,\mathcal{K}} \\ + \sum_{S\in\cup_n\mathcal{S}^n_M} \|\sqrt{\alpha}w\|^2_{0,S} + \sum_{S\in\mathcal{F}} \|C_S^{1/2}|[\![w]\!]|\|^2_{0,S}, \end{aligned} \tag{4.48}$$

with η_0 defined as $\eta_0 = \min_{\mathcal{K}\in\mathcal{T}_h}\eta_{\mathcal{K}}$. If we take $\eta_0 > N_f$ and $\epsilon \in (\frac{N_f}{\eta_0}, 1)$, and choosing $\beta_c = \min(1-\epsilon, \eta_0 - \frac{N_f}{\epsilon}) > 0$, we obtain

$$\begin{aligned} a(w,w) \geq & \frac{1}{2}\int_{\mathcal{E}} (\overline{\nabla}\cdot u)w^2\ \mathrm{d}\mathcal{E} + \beta_c \sum_{\mathcal{K}\in\mathcal{T}_h} \|D^\star\overline{\nabla}_h w\|^2_{0,\mathcal{K}} + \beta_c \sum_{S\in\cup_n\mathcal{S}^n_{ID}} \sum_{\mathcal{K}\in\mathcal{T}_h} \|D^\star\bar{r}_S([\![w]\!])\|^2_{0,\mathcal{K}} \\ & + \sum_{S\in\cup_n\mathcal{S}^n_M} \|\sqrt{\alpha}w\|^2_{0,S} + \sum_{S\in\mathcal{F}} \|C_S^{1/2}|[\![w]\!]|\|^2_{0,S}. \end{aligned} \tag{4.49}$$

Making use inequality (4.40) into (4.49) and assuming the existence of $b_0 > 0$ that satisfies (4.41), we then obtain:

$$\begin{aligned} a(w,w) \geq & \frac{b_0}{2}\|w\|^2_{0,\mathcal{E}} + \frac{\beta_c}{2} \sum_{\mathcal{K}\in\mathcal{T}_h} \|D^\star\overline{\nabla}_h w\|^2_{0,\mathcal{K}} + \frac{\beta_c}{2} \sum_{S\in\cup_n\mathcal{S}^n_{ID}} \sum_{\mathcal{K}\in\mathcal{T}_h} \|D^\star\bar{r}_S([\![w]\!])\|^2_{0,\mathcal{K}} \\ & + \sum_{S\in\cup_n\mathcal{S}^n_M} \|\sqrt{\alpha}w\|^2_{0,S} + \sum_{S\in\mathcal{F}} \|C_S^{1/2}|[\![w]\!]|\|^2_{0,S}. \end{aligned} \tag{4.50}$$

Since $\beta_c/2$ is always less than one, choosing $\beta_a = \min(\frac{b_0}{2}, \frac{\beta_c}{2})$ completes the proof of the coercivity. □

Proof of boundedness in Lemma 4.3

To prove Lemma 4.3, we take $w = c_h$ in (4.34), which results in the relation:

$$a(c_h, c_h) = \ell(c_h). \tag{4.51}$$

Using the lifting operator R in (4.8), the symmetry of matrix D, and the definition of C_S on $S \in \mathcal{F}_{\text{bnd}}$ given by (4.21), the linear functional $\ell(c_h)$ can be written as:

$$\begin{aligned}\ell(c_h) = &\sum_{\mathcal{K}\in\mathcal{T}_h}\int_{\mathcal{K}} D^\star \bar{R}(\mathcal{P}g_D n)\cdot D^\star\overline{\nabla}_h c_h \,\mathrm{d}\mathcal{K}\\ &+\sum_{S\in\cup_n\mathcal{S}_D^n}\sum_{\mathcal{K}\in\mathcal{T}_h}\eta_{\mathcal{K}}\int_{\mathcal{K}} D^\star\bar{r}_S(\mathcal{P}g_D n)\cdot D^\star\bar{r}_S([\![c_h]\!])\,\mathrm{d}\mathcal{K}+\sum_{S\in\cup_n\mathcal{S}_M^n}\int_S g_M c_h\,\mathrm{d}S\\ &+2\sum_{S\in\cup_n\mathcal{S}_{DBSm}^n}\int_S C_S g_D c_h\,\mathrm{d}S+2\int_{\Omega_0} C_S c_0 c_h\,\mathrm{d}\Omega. \end{aligned}\tag{4.52}$$

Applying the Schwarz and arithmetic-geometric mean inequalities on each term in (4.52) and combining this result with (4.51) and Lemma 4.2 using $w = c_h$, we obtain the inequality

$$\begin{aligned}&\beta_a\|c_h\|_{0,\mathcal{E}}^2+\big(\beta_a-\frac{\epsilon_1}{2}\big)\sum_{\mathcal{K}\in\mathcal{T}_h}\|D^\star\overline{\nabla}_h c_h\|_{0,\mathcal{K}}^2+\big(\beta_a-\frac{\eta_m\epsilon_2}{2}\big)\sum_{S\in\cup_n\mathcal{S}_{ID}^n}\sum_{\mathcal{K}\in\mathcal{T}_h}\|D^\star\bar{r}_S([\![c_h]\!])\|_{0,\mathcal{K}}^2\\ &+\big(\beta_a-\frac{\epsilon_3}{2}\big)\sum_{S\in\cup_n\mathcal{S}_M^n}\|\sqrt{\alpha}c_h\|_{0,S}^2+\big(\beta_a-\epsilon_4\big)\sum_{S\in\mathcal{F}}\|C_S^{1/2}|[\![c_h]\!]|\|_{0,S}^2\\ &\le\ \frac{1}{2\epsilon_1}\sum_{\mathcal{K}\in\mathcal{T}_h}\|D^\star\bar{R}(\mathcal{P}g_D n)\|_{0,\mathcal{K}}^2+\frac{\eta_m}{2\epsilon_2}\sum_{S\in\cup_n\mathcal{S}_D^n}\sum_{\mathcal{K}\in\mathcal{T}_h}\|D^\star\bar{r}_S(\mathcal{P}g_D n)\|_{0,\mathcal{K}}^2\\ &\quad+\frac{1}{2\epsilon_3}\sum_{S\in\cup_n\mathcal{S}_M^n}\|\alpha^{-1/2}g_M\|_{0,S}^2+\frac{1}{\epsilon_4}\sum_{S\in\cup_n\mathcal{S}_{DBSm}^n}\|C_S^{1/2}g_D\|_{0,S}^2+\frac{1}{\epsilon_4}\|C_S^{1/2}c_0\|_{0,\Omega_0}^2,\end{aligned}\tag{4.53}$$

with $\epsilon_1,\ldots,\epsilon_4 > 0$ and $\eta_m = \max_{\mathcal{K}\in\mathcal{T}_h}\eta_{\mathcal{K}}$. Next, we substitute the following coefficients: $\epsilon_1 = \beta_a, \epsilon_2 = \frac{\beta_a}{\eta_m}, \epsilon_3 = \beta_a$, and $\epsilon_4 = \frac{\beta_a}{2}$ into (4.53) and multiply the result with $2\beta_a$ to complete the proof. □

Proof of the uniqueness in Theorem 4.4

To prove the uniqueness of the solution it is sufficient to show that the following homogeneous equation:
Find a $c_h \in \mathcal{W}_h^{(p_t,p_s)}$ such that:

$$a(c_h, w) = 0, \quad \forall w \in \mathcal{W}_h^{(p_t,p_s)}, \qquad \text{with } c_h(0,\bar{x}) = 0, \tag{4.54}$$

has only the trivial solution $c_h = 0$ for all $t > 0$.

We proceed as follows. Assume that c_h is a solution of (4.54) and take $w = c_h$ in (4.30). Then we rewrite (4.42) as:

$$\begin{aligned}a(c_h,c_h)\ge\beta_a\sum_{n=0}^{N_t-1}\Big(&\sum_{\mathcal{K}\in\mathcal{T}_h^n}\|c_h\|_{0,\mathcal{K}}^2+\sum_{\mathcal{K}\in\mathcal{T}_h^n}\|D^\star\overline{\nabla}_h c_h\|_{0,\mathcal{K}}^2+\sum_{S\in\mathcal{S}_{ID}^n}\sum_{\mathcal{K}\in\mathcal{T}_h^n}\|D^\star\bar{r}_S([\![c_h]\!])\|_{0,\mathcal{K}}^2\\ &+\sum_{S\in\mathcal{S}_M^n}\|\sqrt{\alpha}c_h\|_{0,S}^2+\sum_{S\in\mathcal{F}^n}\|C_S^{1/2}|[\![c_h]\!]|\|_{0,S}^2\Big).\end{aligned}$$

Consider now the space-time slab for $n = 0$. The coercivity condition, in combination with the initial condition $c_h^+ = 0$ at $t = 0$ and (4.54), implies that $c_h = 0$ in the first space-time slab when constant or linear polynomials in time are used. We can continue this argument to the other space-time slabs and obtain that $c_h = 0$ is the only solution possible for the homogeneous equation. Hence the DG algorithm has a unique solution c_h for constant or linear basis functions in time. The unconditional stability of the DG algorithm is a direct consequence of Lemma 4.3.

4.6 Error estimates and *hp*-convergence

First, let us define the projection $\mathcal{P} : L^2(\mathcal{E}) \to \mathcal{W}_h^{(p_t,p_s)}$ as:

$$\sum_{\mathcal{K}\in\mathcal{T}_h} (\mathcal{P}c, w)_{\mathcal{K}} = \sum_{\mathcal{K}\in\mathcal{T}_h} (c, w)_{\mathcal{K}}, \quad \forall w \in \mathcal{W}_h^{(p_t,p_s)}, \tag{4.55}$$

which can be used to decompose the global error $c - c_h$ as:

$$c - c_h = (c - \mathcal{P}c) + (\mathcal{P}c - c_h) \equiv \rho + \theta, \tag{4.56}$$

with ρ the interpolation error and θ the discretization error. In the next section we discuss the upper bounds for the interpolation error ρ.

4.6.1 Bounds for the interpolation error

In this section we present the upper bounds for the interpolation error $\rho = c - \mathcal{P}c$. These estimates are an extension of the bounds for the interpolation error derived in [31] to general dimensions. We restrict the derivations for a separate polynomial degree $p_{t,\mathcal{K}}$ in time and a polynomial degree $p_{s,\mathcal{K}}$ in each spatial variable.

Lemma 4.5 *Assume that $\mathcal{K}$ is a space-time element in $\mathbb{R}^{d+1}$ constructed via two mappings $Q_{\mathcal{K}}$, $F_{\mathcal{K}}$, with $F_{\mathcal{K}} : \hat{\mathcal{K}} \to \tilde{\mathcal{K}}$ and $Q_{\mathcal{K}} : \tilde{\mathcal{K}} \to \mathcal{K}$. Assume also that $h_{i,\mathcal{K}}, i = 1, \ldots, d$ is the edge length of $\tilde{\mathcal{K}}$ in the x_i direction, and $\triangle_n t$ the edge length in the x_0 direction (see illustration in Fig. 4.2 for $d = 2$). Let $c|_{\mathcal{K}} \in H^{(k_{t,\mathcal{K}}+1,k_{s,\mathcal{K}}+1)}(\mathcal{K})$, with $k_{t,\mathcal{K}}, k_{s,\mathcal{K}} \geq 0$. Let $\mathcal{P}$ denote the L^2 projection of c onto the finite element space $\mathcal{W}_h^{(p_t,p_s)}$. Then the projection error $\rho = c - \mathcal{P}c$ in $\mathcal{K}$ and its trace at the boundary $\partial\mathcal{K}$ obey the error bounds:*

$$\|\rho\|_{0,\mathcal{K}}^2 \leq CZ_{\mathcal{K}}, \tag{4.57}$$

$$\|\overline{\nabla}_h\rho\|_{0,\mathcal{K}}^2 \leq CN_{\mathcal{K}}, \tag{4.58}$$

$$\|\rho\|_{0,\partial\mathcal{K}}^2 \leq C(A_{\mathcal{K}} + B_{\mathcal{K}}), \tag{4.59}$$

where

$$
\begin{aligned}
Z_{\mathcal{K}} &= \sum_{i=1}^{d} \Big(\frac{h_{i,\mathcal{K}}}{p_{s,\mathcal{K}}}\Big)^{2s_{\mathcal{K}}} \|\tilde{\partial}_i^{s_{\mathcal{K}}} c\|_{0,\tilde{\mathcal{K}}}^2 + \Big(\frac{\triangle_n t}{p_{t,\mathcal{K}}}\Big)^{2s_{0,\mathcal{K}}} \|\tilde{\partial}_0^{s_{0,\mathcal{K}}} c\|_{0,\tilde{\mathcal{K}}}^2,\\
N_{\mathcal{K}} &= \sum_{i=1}^{d} \frac{h_{i,\mathcal{K}}^{2t_{\mathcal{K}}}}{p_{s,\mathcal{K}}^{2t_{\mathcal{K}}-1}} \|\tilde{\partial}_i^{t_{\mathcal{K}}+1} c\|_{0,\tilde{\mathcal{K}}}^2 + \sum_{i=1}^{d}\sum_{j\neq i} \frac{h_{j,\mathcal{K}}^{2t_{\mathcal{K}}+2}}{p_{s,\mathcal{K}}^{2t_{\mathcal{K}}}} \|\tilde{\partial}_j^{t_{\mathcal{K}}+1}\tilde{\partial}_i c\|_{0,\tilde{\mathcal{K}}}^2\\
&\quad + \sum_{i=1}^{d} \frac{(\triangle_n t)^{2t_{0,\mathcal{K}}+2}}{p_{t,\mathcal{K}}^{2t_{0,\mathcal{K}}}} \|\tilde{\partial}_0^{t_{0,\mathcal{K}}+1}\tilde{\partial}_i c\|_{0,\tilde{\mathcal{K}}}^2,\\
A_{\mathcal{K}} &= \sum_{i=1}^{d} \Big(\frac{h_{i,\mathcal{K}}}{p_{s,\mathcal{K}}}\Big)^{2t_{\mathcal{K}}+1} \|\tilde{\partial}_i^{t_{\mathcal{K}}+1} c\|_{0,\tilde{\mathcal{K}}}^2 + \sum_{i=1}^{d}\sum_{j\neq i} \frac{1}{h_{i,\mathcal{K}}}\Big(\frac{h_{j,\mathcal{K}}}{p_{s,\mathcal{K}}}\Big)^{2s_{\mathcal{K}}} \|\tilde{\partial}_j^{s_{\mathcal{K}}} c\|_{0,\tilde{\mathcal{K}}}^2\\
&\quad + \sum_{i=1}^{d}\sum_{j\neq i} \frac{h_{i,\mathcal{K}}}{p_{s,\mathcal{K}}}\Big(\frac{h_{j,\mathcal{K}}}{p_{s,\mathcal{K}}}\Big)^{2q_{\mathcal{K}}} \|\tilde{\partial}_j^{q_{\mathcal{K}}}\tilde{\partial}_i c\|_{0,\tilde{\mathcal{K}}}^2,\\
B_{\mathcal{K}} &= \sum_{i=1}^{d} \frac{1}{h_{i,\mathcal{K}}}\Big(\frac{\triangle_n t}{p_{t,\mathcal{K}}}\Big)^{2s_{0,\mathcal{K}}} \|\tilde{\partial}_0^{s_{0,\mathcal{K}}} c\|_{0,\tilde{\mathcal{K}}}^2 + \sum_{i=1}^{d} \frac{h_{i,\mathcal{K}}}{p_{s,\mathcal{K}}}\Big(\frac{\triangle_n t}{p_{t,\mathcal{K}}}\Big)^{2q_{0,\mathcal{K}}} \|\tilde{\partial}_0^{q_{0,\mathcal{K}}}\tilde{\partial}_i c\|_{0,\tilde{\mathcal{K}}}^2\\
&\quad + \Big(\frac{\triangle_n t}{p_{t,\mathcal{K}}}\Big)^{2t_{0,\mathcal{K}}+1} \|\tilde{\partial}_0^{t_{0,\mathcal{K}}+1} c\|_{0,\tilde{\mathcal{K}}}^2 + \frac{1}{\triangle_n t}\sum_{i=1}^{d} \Big(\frac{h_{i,\mathcal{K}}}{p_{s,\mathcal{K}}}\Big)^{2s_{\mathcal{K}}} \|\tilde{\partial}_i^{s_{\mathcal{K}}} c\|_{0,\tilde{\mathcal{K}}}^2\\
&\quad + \frac{\triangle_n t}{p_{t,\mathcal{K}}}\sum_{i=1}^{d} \Big(\frac{h_{i,\mathcal{K}}}{p_{s,\mathcal{K}}}\Big)^{2q_{\mathcal{K}}} \|\tilde{\partial}_i^{q_{\mathcal{K}}}\tilde{\partial}_0 c\|_{0,\tilde{\mathcal{K}}}^2,
\end{aligned}
$$

with $p_{t,\mathcal{K}}$ and $p_{s,\mathcal{K}}$ the local polynomial degree in time and space, respectively, on element $\mathcal{K}$, $0 < s_{0,\mathcal{K}} \leq \min(p_{t,\mathcal{K}}+1, k_{t,\mathcal{K}}+1)$, $0 < s_{\mathcal{K}} \leq \min(p_{s,\mathcal{K}}+1, k_{s,\mathcal{K}}+1)$, $0 < q_{0,\mathcal{K}} \leq \min(p_{t,\mathcal{K}}+1, k_{t,\mathcal{K}})$, $0 < q_{\mathcal{K}} \leq \min(p_{s,\mathcal{K}}+1, k_{s,\mathcal{K}})$, $0 < t_{0,\mathcal{K}} \leq \min(p_{t,\mathcal{K}}, k_{t,\mathcal{K}})$, and $0 < t_{\mathcal{K}} \leq \min(p_{s,\mathcal{K}}, k_{s,\mathcal{K}})$. The constant C has a positive value that depends only on the spatial dimension d and the mapping $Q_{\mathcal{K}}$.

Remark 4.6 In particular, when c is sufficiently smooth and the spatial shape of element $\mathcal{K}$ is regular: $h_{\mathcal{K}} = h_{i,\mathcal{K}}, i = 1, \ldots, d$, we obtain the following leading terms for each estimate given in Lemma 4.5:

$$
\begin{aligned}
\|\rho\|_{0,\mathcal{K}}^2 &\leq C\Big(\frac{h_{\mathcal{K}}^{2p_{s,\mathcal{K}}+2}}{p_{s,\mathcal{K}}^{2p_{s,\mathcal{K}}+2}} + \frac{\triangle_n t^{2p_{t,\mathcal{K}}+2}}{p_{t,\mathcal{K}}^{2p_{t,\mathcal{K}}+2}}\Big)|c|_{p_{t,\mathcal{K}}+1,p_{s,\mathcal{K}}+1,\mathcal{K}}^2,\\
\|\overline{\nabla}_h\rho\|_{0,\mathcal{K}}^2 &\leq C\Big(\frac{h_{\mathcal{K}}^{2p_{s,\mathcal{K}}}}{p_{s,\mathcal{K}}^{2p_{s,\mathcal{K}}-1}} + \frac{\triangle_n t^{2p_{t,\mathcal{K}}+2}}{p_{t,\mathcal{K}}^{2p_{t,\mathcal{K}}}}\Big)|c|_{p_{t,\mathcal{K}}+1,p_{s,\mathcal{K}}+1,\mathcal{K}}^2,\\
\|\rho\|_{0,\partial\mathcal{K}}^2 &\leq C\Big(\frac{h_{\mathcal{K}}^{2p_{s,\mathcal{K}}+1}}{p_{s,\mathcal{K}}^{2p_{s,\mathcal{K}}+1}} + \frac{\triangle_n t^{2p_{t,\mathcal{K}}+1}}{p_{t,\mathcal{K}}^{2p_{t,\mathcal{K}}+1}}\Big)|c|_{p_{t,\mathcal{K}}+1,p_{s,\mathcal{K}}+1,\mathcal{K}}^2.
\end{aligned}
$$

The proof for Lemma 4.5 is a straightforward extension of Lemmas 3.13 and 3.17 in [31] to general dimensions and therefore only the main steps are summarized. The details are derived in Appendix B. The first bound (4.57) follows directly from Lemma 3.13 in [31]. The second bound (4.58) is obtained as follows. First, the bound for the partial derivative in each spatial variable in Lemma 3.13 [31] is extended to general dimensions. The upper bound for the gradient is then obtained by adding all the bounds for partial derivatives in the spatial variables. The third bound (4.59) is obtained in similar way. First, the bound of the interpolation error at each boundary of $\mathcal{K}$ is derived, which is an extension of Lemma 3.17 in [31] to general dimensions. Then the upper bounds at each part of boundary $\partial\mathcal{K}$ are added up.

We also need an upper bound for the following term:

$$\sum_{S\in\cup_n\mathcal{S}_{ID}^n} \|D^\star \bar{r}_S([\![\rho]\!])\|_{0,\mathcal{E}}^2. \tag{4.60}$$

The upper bound for this term is obtained through the following technique. First, we use a similar derivation as in ([54], Lemma 7.2) to express an upper bound of (4.60) in terms of the interpolation error ρ at the boundary:

$$\sum_{S\in\cup_n\mathcal{S}_{ID}^n} \|D^\star \bar{r}_S([\![\rho]\!])\|_{0,\mathcal{E}}^2 \leq C\bar{D}\sum_{\mathcal{K}}\sum_{i=1}^{d} h_{i,\mathcal{K}}^{-1} p_{s,\mathcal{K}}^2 \|\rho\|_{0,\partial\mathcal{K}_i}^2, \tag{4.61}$$

with $\bar{D} = \max_{\mathcal{K}\in\mathcal{T}_h} \|D\|_{0,\infty,\mathcal{K}}$, $\partial\mathcal{K}_i$ the boundary of $\mathcal{K}$ in the x_i direction, $i = 1,\ldots,d$, and the constant C depends on the mapping $Q_\mathcal{K}$. After that the upper bound for ρ on each $\partial\mathcal{K}_i$ (an extension of Lemma 3.17 in [31] to general dimensions) is used. The result is shown in the following Lemma.

Lemma 4.7 *Assume that $\mathcal{K}$ is a space-time element in $\mathbb{R}^{d+1}$ constructed via two mappings $Q_\mathcal{K}$, $F_\mathcal{K}$, with $F_\mathcal{K} : \hat{\mathcal{K}} \to \tilde{\mathcal{K}}$ and $Q_\mathcal{K} : \tilde{\mathcal{K}} \to \mathcal{K}$. Assume also that $h_{i,\mathcal{K}}, i = 1,\ldots,d$ is the edge length of $\tilde{\mathcal{K}}$ in the x_i direction, and $\triangle_n t$ the edge length in the x_0 direction. Let $c|_\mathcal{K} \in H^{(k_{t,\mathcal{K}}+1,k_{s,\mathcal{K}}+1)}(\mathcal{K})$, with $k_{t,\mathcal{K}}, k_{s,\mathcal{K}} \geq 0$. Let $\mathcal{P}$ denote the L^2 projection of c onto the finite element space $\mathcal{W}_h^{(p_t,p_s)}$. Then the following estimate holds:*

$$\sum_{S\in\cup_n\mathcal{S}_{ID}^n} \|D^\star \bar{r}_S([\![\rho]\!])\|_{0,\mathcal{E}}^2 \leq C\bar{D}\sum_{\mathcal{K}\in\mathcal{T}_h}(R_\mathcal{K} + T_\mathcal{K}),$$

with $\bar{D} = \max_{\mathcal{K}\in\mathcal{T}_h} \|D\|_{0,\infty,\mathcal{K}}$ and

$$R_\mathcal{K} = \sum_{i=1}^{d} \frac{p_{s,\mathcal{K}}^2}{h_{i,\mathcal{K}}}\Big(\frac{h_{i,\mathcal{K}}}{p_{s,\mathcal{K}}}\Big)^{2t_\mathcal{K}+1} \|\tilde{\partial}_i^{t_\mathcal{K}+1} c\|_{0,\tilde{\mathcal{K}}}^2 + \sum_{i=1}^{d}\sum_{j\neq i}\Big(\frac{p_{s,\mathcal{K}}}{h_{i,\mathcal{K}}}\Big)^2\Big(\frac{h_{j,\mathcal{K}}}{p_{s,\mathcal{K}}}\Big)^{2s_\mathcal{K}} \|\tilde{\partial}_j^{s_\mathcal{K}} c\|_{0,\tilde{\mathcal{K}}}^2$$
$$+ \sum_{i=1}^{d}\sum_{j\neq i} p_{s,\mathcal{K}}\Big(\frac{h_{j,\mathcal{K}}}{p_{s,\mathcal{K}}}\Big)^{2q_\mathcal{K}} \|\tilde{\partial}_j^{q_\mathcal{K}}\tilde{\partial}_i c\|_{0,\tilde{\mathcal{K}}}^2,$$

$$T_{\mathcal{K}} = \sum_{i=1}^{d} \frac{p_{s,\mathcal{K}}^2}{h_{i,\mathcal{K}} \triangle_n t} \Big(\frac{\triangle_n t}{p_{t,\mathcal{K}}} \Big)^{2s_{0,\mathcal{K}}} \|\tilde{\partial}_0^{s_{0,\mathcal{K}}} c\|_{0,\tilde{\mathcal{K}}}^2 + \sum_{i=1}^{d} p_{s,\mathcal{K}} \Big(\frac{\triangle_n t}{p_{t,\mathcal{K}}} \Big)^{2q_{0,\mathcal{K}}} \|\tilde{\partial}_0^{q_{0,\mathcal{K}}} \tilde{\partial}_i c\|_{0,\tilde{\mathcal{K}}}^2,$$

with $p_{t,\mathcal{K}}$ and $p_{s,\mathcal{K}}$ the local polynomial degree in time and space, respectively, on element $\mathcal{K}$, $0 < s_{0,\mathcal{K}} \leq \min(p_{t,\mathcal{K}} + 1, k_{t,\mathcal{K}} + 1)$, $0 < s_{\mathcal{K}} \leq \min(p_{s,\mathcal{K}} + 1, k_{s,\mathcal{K}} + 1)$, $0 < q_{0,\mathcal{K}} \leq \min(p_{t,\mathcal{K}} + 1, k_{t,\mathcal{K}})$, $0 < q_{\mathcal{K}} \leq \min(p_{s,\mathcal{K}} + 1, k_{s,\mathcal{K}})$, $0 < t_{0,\mathcal{K}} \leq \min(p_{t,\mathcal{K}}, k_{t,\mathcal{K}})$, and $0 < t_{\mathcal{K}} \leq \min(p_{s,\mathcal{K}}, k_{s,\mathcal{K}})$. The constant C has a positive value that depends only on the spatial dimension d and the mapping $Q_{\mathcal{K}}$.

Remark 4.8 In particular, when c is sufficiently smooth and the spatial shape of element $\mathcal{K}$ is regular: $h_{\mathcal{K}} = h_{i,\mathcal{K}}, i = 1, \ldots, d$, we obtain the following leading term for the estimate given in Lemma 4.7:

$$\sum_{S \in \cup_n \mathcal{S}_{ID}^n} \|D^\star \bar{r}_S([\![\rho]\!])\|_{0,\mathcal{E}}^2 \leq C\bar{D} \sum_{\mathcal{K} \in \mathcal{T}_h} \Big(\frac{h_{\mathcal{K}}^{2p_{s,\mathcal{K}}}}{p_{s,\mathcal{K}}^{2p_{s,\mathcal{K}}-1}} + \frac{p_{s,\mathcal{K}}^2}{h_{\mathcal{K}}} \frac{\triangle_n t^{2p_{t,\mathcal{K}}+1}}{p_{t,\mathcal{K}}^{2p_{t,\mathcal{K}}+2}} \Big) |c|_{p_{t,\mathcal{K}}+1, p_{s,\mathcal{K}}+1, \mathcal{K}}^2.$$

4.6.2 Global estimates

As a first step in obtaining global estimates, we need an estimate for θ in terms of ρ, which is given by the following Lemma.

Lemma 4.9 *There exists a constant $\beta_a > 0$, defined in Lemma 4.2, independent of the mesh size $h = \max_{\mathcal{K} \in \mathcal{T}_h} h_{\mathcal{K}}$, such that the function θ defined in* (4.56) *satisfies the inequality*

$$\begin{aligned}
\frac{1}{4}\beta_a^2 |||\theta|||_{\mathrm{DG}}^2 \leq & \sum_{\mathcal{K} \in \mathcal{T}_h} \|(D^\star)^{-1} u\|_{0,\infty,\mathcal{K}}^2 \|\rho\|_{0,\mathcal{K}}^2 + (N_f + 1) \sum_{\mathcal{K} \in \mathcal{T}_h} \|D^\star \overline{\nabla}_h \rho\|_{0,\mathcal{K}}^2 \\
& + (N_f + \eta_m^2) \sum_{S \in \cup_n \mathcal{S}_{ID}^n} \sum_{\mathcal{K} \in \mathcal{T}_h} \|D^\star \bar{r}_S([\![\rho]\!])\|_{0,\mathcal{K}}^2 \\
& + \frac{1}{2} \sum_{S \in \cup_n \mathcal{S}_M^n} \|\sqrt{\alpha}\rho\|_{0,S}^2 + 2 \sum_{S \in \mathcal{F}_{\mathrm{int}}} \|C_S^{1/2} \{\!\{\rho\}\!\}\|_{0,S}^2 \\
& + \sum_{S \in \mathcal{F}_{\mathrm{int}}} \|C_S^{1/2} |[\![\rho]\!]|\|_{0,S}^2 + \sum_{S \in (\cup_n \mathcal{S}_{MDSp}^n \cup \Gamma_+)} 2\|C_S^{1/2} |[\![\rho]\!]|\|_{0,S}^2,
\end{aligned}$$

with $\beta_a = \min(\frac{b_0}{2}, \frac{\beta_c}{2})$, $0 < \beta_c = \min(1 - \epsilon, \eta_0 - \frac{N_f}{\epsilon})$, for $\epsilon \in (\frac{N_f}{\eta_0}, 1)$, and b_0 satisfies (4.41).

The proof for this lemma is given in Section 4.6.4.

Applying the triangle inequality to (4.56), we obtain the following bound on the global error $c - c_h$ in the DG norm:

$$|||c - c_h|||_{\mathrm{DG}} \leq |||\rho|||_{\mathrm{DG}} + |||\theta|||_{\mathrm{DG}}. \tag{4.62}$$

Using Lemma 4.9, the error in the DG norm can now be expressed solely in terms of the projection error ρ. Introducing the estimates for ρ given by Lemmas 4.5 and 4.7, the error bound can be formulated in the next theorem.

Theorem 4.10 *Suppose that $\mathcal{K}$ is a space-time element in $\mathbb{R}^{d+1}$ constructed via two mappings $Q_\mathcal{K} \circ F_\mathcal{K}$, with $F_\mathcal{K} : \hat{\mathcal{K}} \to \tilde{\mathcal{K}}$ and $Q_\mathcal{K} : \tilde{\mathcal{K}} \to \mathcal{K}$. Suppose also that $h_{i,\mathcal{K}}, i = 1, \ldots, d$ is the edge length of $\tilde{\mathcal{K}}$ in the x_i direction, and $\triangle_n t$ the edge length in the x_0 direction. Let $c|_\mathcal{K} \in H^{(k_{t,\mathcal{K}}+1, k_{s,\mathcal{K}}+1)}(\mathcal{K})$, with $k_{t,\mathcal{K}}, k_{s,\mathcal{K}} \geq 0$, and $c_h \in \mathcal{W}_h^{(p_t,p_s)}$ be the discontinuous Galerkin approximation to c defined by (4.34). Then, the following error bound holds:*

$$|||c - c_h|||_{\mathrm{DG}}^2 \leq \mathcal{C}\Big(a_1 \sum_\mathcal{K} Z_\mathcal{K} + a_2 \sum_\mathcal{K} N_\mathcal{K} + a_3 \sum_\mathcal{K} \big(R_\mathcal{K} + T_\mathcal{K}\big) + a_4 \sum_\mathcal{K} \big(A_\mathcal{K} + B_\mathcal{K}\big)\Big),$$

with $Z_\mathcal{K}, N_\mathcal{K}, A_\mathcal{K}, B_\mathcal{K}$ defined in Lemma 4.5, $R_\mathcal{K}, T_\mathcal{K}$ in Lemma 4.7, β_a in Lemma 4.9,

$$\begin{aligned} a_1 &= 1 + 4u_D^2/\beta_a^2, & a_2 &= (1 + 4(N_f + 1)/\beta_a^2)\bar{D}, \\ a_3 &= (1 + 4(N_f + \eta_m^2)/\beta_a^2)\bar{D}, & a_4 &= (1 + 2/\beta_a^2)\bar{\alpha} + (1 + 20/\beta_a^2)\bar{C}_S, \end{aligned}$$

and

$$\begin{aligned} \bar{D} &= \max_{\mathcal{K}\in\mathcal{T}_h} \|D\|_{0,\infty,\mathcal{K}}, & \bar{\alpha} &= \max_{\mathcal{K}\in\mathcal{T}_h} \|\alpha\|_{0,\infty,\mathcal{K}}, \\ \bar{C}_S &= \max_{\mathcal{K}\in\mathcal{T}_h} \|C_S\|_{0,\infty,\mathcal{K}}, & u_D &= \max_{\mathcal{K}\in\mathcal{T}_h} \|(D^\star)^{-1}u\|_{0,\infty,\mathcal{K}}. \end{aligned}$$

The constant $\mathcal{C}$ has a positive constant that depends on the spatial dimension d and the mapping $Q_\mathcal{K}$.

Corollary 4.11 *When c is sufficiently smooth, the spatial shapes of all elements $\mathcal{K} \in \mathcal{T}_h$ are regular: $h = h_\mathcal{K}, \forall \mathcal{K} \in \mathcal{T}_h$, and uniform polynomial degrees (p_t, p_s) are used for all elements $\mathcal{K} \in \mathcal{T}_h$, then we obtain the error bound*

$$\begin{aligned} |||c - c_h|||_{\mathrm{DG}}^2 \leq \mathcal{C}\Big(& a_1\Big(\frac{h^{2p_s+2}}{p_s^{2p_s+2}} + \frac{\triangle_n t^{2p_t+2}}{p_t^{2p_t+2}}\Big) + a_2\Big(\frac{h^{2p_s}}{p_s^{2p_s-1}} + \frac{\triangle_n t^{2p_t+2}}{p_t^{2p_t}}\Big) \\ & + a_3\Big(\frac{h^{2p_s}}{p_s^{2p_s-1}} + \frac{p_s^2}{h}\frac{\triangle_n t^{2p_t+1}}{p_t^{2p_t+2}}\Big) + a_4\Big(\frac{h^{2p_s+1}}{p_s^{2p_s+1}} + \frac{\triangle_n t^{2p_t+1}}{p_t^{2p_t+1}}\Big)\Big)\times \\ & |c|_{p_t+1,p_s+1,\mathcal{E}}^2. \end{aligned}$$

4.6.3 Error estimates at specific time levels

The error estimate given by Theorem 4.10 is useful to determine the dependence of the error in the complete space-time domain on the spatial mesh size, time step and the polynomial degrees. It is, however, also important to know the error at a specific time level. In this section we provide an error estimate in the L^2 norm in the domain

Ω_T at time T. Following a similar procedure as in [63], we consider the following *backward problem* in time, related to (4.1):

$$-\frac{\partial z}{\partial t}+\sum_{i=1}^{d}\frac{\partial}{\partial x_i}\big(u_i(t,\bar{x})z\big)-\sum_{i,j=1}^{d}\frac{\partial}{\partial x_j}\Big(D_{ij}(t,\bar{x})\frac{\partial z}{\partial x_i}\Big)=0,\quad \text{for } t<T, \tag{4.63}$$

with homogeneous boundary conditions at $\partial\mathcal{E}\setminus(\Omega_0\cup\Omega_T)$ and the following initial condition:

$$z=\phi \quad \text{at } \Omega_T, \tag{4.64}$$

with $\phi\in L^2(\Omega_T)$. Replacing t by $t_{N_t}+0-t$, the analogue of the weak formulation (4.34) for (4.63) is as follows.

Find a $z_h\in\mathcal{W}_h^{(p_t,p_s)}$, such that for all $w\in\mathcal{W}_h^{(p_t,p_s)}$, the following relation is satisfied:

$$a(w,z_h)=\ell^\star(w), \tag{4.65}$$

with

$$\ell^\star(w)=\sum_{S\subset\Omega_T}\int_S B\phi\cdot nw\;\mathrm{d}S=(\phi,w)_{\Omega_T}, \tag{4.66}$$

where the bilinear form $a(\cdot,\cdot)$ is defined in (4.30). Note that by replacing t by $t_{N_t}+0-t$, the definitions of the inflow-outflow boundaries and the DG norm remain the same. In addition, the backward problem has a unique solution and other results obtained for the original problem can be translated to this case, such as the orthogonality relation. We start with an estimate for the discretization error $\theta=\mathcal{P}c-c_h$ at time T.

Lemma 4.12 *Assume that the conditions of Lemma 4.2 are satisfied. Let c_h be the solution of* (4.34)*, z_h the solution of* (4.65)*, and $\theta=\mathcal{P}c-c_h$. The following inequality then holds:*

$$(\phi,\theta)_{\Omega_T}\leq\Big(C_e|||\rho|||_{\mathrm{DG}}+\big(2\sum_{S\in\mathcal{F}_{\mathrm{int}}}\|C_S^{1/2}\{\!\{\rho\}\!\}\|_{0,S}^2\big)^{1/2}\Big)|||z_h|||_{\mathrm{DG}}, \tag{4.67}$$

with $C_e=5+2\sqrt{N_f}+\eta_m+u_D$ and $u_D=\max_{\mathcal{K}\in\mathcal{T}_h}\|(D^\star)^{-1}u\|_{0,\infty,\mathcal{K}}$.

The proof is given in Section 4.6.4. An estimate for the DG norm of the solution z_h of the backward problem is provided by the next lemma.

Lemma 4.13 *The solution z_h to* (4.65) *satisfies the following upper bound:*

$$\frac{1}{2}\beta_a^2|||z_h|||_{\mathrm{DG}}^2\leq(\phi,\phi)_{\Omega_T},$$

with $\beta_a>0$ satisfies Lemma 4.2.

The proof is given in Section 4.6.4. Using Lemma 4.13, the estimate given by (4.67) can further be written as

$$(\phi,\theta)_{\Omega_T} \leq \frac{\sqrt{2}}{\beta_a}\Big(C_e|||\rho|||_{\mathrm{DG}} + \big(2\sum_{S\in\mathcal{F}_{\mathrm{int}}}\|C_S^{1/2}\{\!\{\rho\}\!\}\|_{0,S}^2\big)^{1/2}\Big)\|\phi\|_{0,\Omega_T}.$$

After using the relation

$$\|\theta\|_{0,\Omega_T} = \sup_{0\neq\phi\in L^2(\Omega_T)}\frac{(\phi,\theta)_{\Omega_T}}{\|\phi\|_{0,\Omega_T}},$$

we then have

$$\|\theta\|_{0,\Omega_T} \leq \frac{\sqrt{2}}{\beta_a}\Big(C_e|||\rho|||_{\mathrm{DG}} + \big(2\sum_{S\in\mathcal{F}_{\mathrm{int}}}\|C_S^{1/2}\{\!\{\rho\}\!\}\|_{0,S}^2\big)^{1/2}\Big). \tag{4.68}$$

Using the *hp*-estimates for ρ in Lemma 4.5, we obtain the following bound.

Theorem 4.14 *Suppose that $\mathcal{K}$ is a space-time element in $\mathbb{R}^{d+1}$ constructed via two mappings $Q_\mathcal{K}\circ F_\mathcal{K}$, with $F_\mathcal{K}:\hat{\mathcal{K}}\to\tilde{\mathcal{K}}$ and $Q_\mathcal{K}:\tilde{\mathcal{K}}\to\mathcal{K}$. Suppose also that $h_{i,\mathcal{K}}, i=1,\ldots,d$ is the edge length of $\tilde{\mathcal{K}}$ in the x_i direction, and $\triangle_n t$ the edge length in the x_0 direction. Let $c|_\mathcal{K}\in H^{(k_{t,\mathcal{K}}+1,k_{s,\mathcal{K}}+1)}(\mathcal{K})$, with $k_{t,\mathcal{K}},k_{s,\mathcal{K}}\geq 0$ and $c_h\in\mathcal{W}_h^{(p_t,p_s)}$ be the discontinuous Galerkin approximation to c defined by* (4.34)*. Then the following error bound holds:*

$$\|c-c_h\|_{0,\Omega_T}^2 \leq \mathcal{C}\bigg(\sum_\mathcal{K}\Big(b_1 Z_\mathcal{K} + b_2\big(N_\mathcal{K}+R_\mathcal{K}+T_\mathcal{K}\big) + (b_3+b_4)\big(A_\mathcal{K}+B_\mathcal{K}\big)\Big)\bigg),$$

with $Z_\mathcal{K}, N_\mathcal{K}, A_\mathcal{K}, B_\mathcal{K}$ defined in Lemma 4.5, $R_\mathcal{K}, T_\mathcal{K}$ in Lemma 4.7,

$$\begin{aligned} b_1 &= 2C_e^2/\beta_a^2, \qquad & b_2 &= \big(2C_e^2/\beta_a^2\big)\bar{D},\\ b_3 &= \big(2C_e^2/\beta_a^2\big)\bar{\alpha}, & b_4 &= \big(2C_e^2/\beta_a^2+4/\beta_a^2+1\big)\bar{C}_S, \end{aligned}$$

the coefficients $\bar{D},\bar{\alpha},\bar{C}_S$ given in Theorem 4.10, C_e in Lemma 4.12, and β_a satisfies Lemma 4.2. The constant $\mathcal{C}$ has a positive value that depends only on the spatial dimension d and the mapping $Q_\mathcal{K}$.

The proof of this theorem is immediate using (4.68) and Lemma 4.5.

Corollary 4.15 *When c is sufficiently smooth, the spatial shapes of all elements $\mathcal{K}\in\mathcal{T}_h$ are regular: $h=h_\mathcal{K}, \forall\mathcal{K}\in\mathcal{T}_h$, and uniform polynomial degrees (p_t,p_s) are used for all elements $\mathcal{K}\in\mathcal{T}_h$, then we obtain the error bound*

$$\begin{aligned}\|c-c_h\|_{0,\Omega_T}^2 \leq \mathcal{C}\bigg(&b_1\Big(\frac{h^{2p_s+2}}{p_s^{2p_s+2}}+\frac{\triangle_n t^{2p_t+2}}{p_t^{2p_t+2}}\Big)+b_2\Big(2\frac{h^{2p_s}}{p_s^{2p_s-1}}+\frac{\triangle_n t^{2p_t+2}}{p_t^{2p_t}}+\frac{p_s^2}{h}\frac{\triangle_n t^{2p_t+2}}{p_t^{2p_t}}\Big)\\ &+(b_3+b_4)\Big(\frac{h^{2p_s+1}}{p_s^{2p_s+1}}+\frac{\triangle_n t^{2p_t+1}}{p_t^{2p_t+1}}\Big)\bigg)|c|^2_{p_t+1,p_s+1,\mathcal{E}}.\end{aligned}$$

4.6.4 Proofs

Proof of the upper bound for the discretization error θ in Lemma 4.9

The proof of Lemma 4.9 starts with the orthogonality relation (4.39) and the decomposition of the error (4.56), which imply that

$$a(\theta+\rho,w)=0,\quad \forall w\in\mathcal{W}_h^{(p_t,p_s)}. \tag{4.69}$$

Taking $w=\theta$, we obtain $a(\theta,\theta)=-a(\rho,\theta)$. We continue with the derivation of an estimate for $|a(\rho,\theta)|$. First, we consider the bilinear form $a_a(\rho,\theta)$. Since $\theta\in\mathcal{W}_h^{(p_t,p_s)}$, which is a polynomial function, we have $\frac{\partial\theta}{\partial t}\in\mathcal{W}_h^{(p_t,p_s)}$ and we can use the L^2 orthogonality relation for the projection $\mathcal{P}$, given by (4.55), to obtain:

$$\begin{aligned}a_a(\rho,\theta)=&-\sum_{\mathcal{K}\in\mathcal{T}_h}\int_{\mathcal{K}}(D^\star)^{-1}u\rho\cdot D^\star\overline{\nabla}_h\theta\,\mathrm{d}\mathcal{K}+\sum_{S\in\mathcal{F}_{\text{int}}}\int_S\{\!\{B\rho\}\!\}\cdot[\![\theta]\!]\,\mathrm{d}S\\&+\sum_{S\in\mathcal{F}_{\text{int}}}\int_S C_S[\![\rho]\!]\cdot[\![\theta]\!]\,\mathrm{d}S+\sum_{S\in(\cup_n\mathcal{S}^n_{MDSp}\cup\Gamma_+)}\int_S B\cdot n\rho\theta\,\mathrm{d}S.\end{aligned} \tag{4.70}$$

Using the same argument as in [13], that is by using (4.20) and the continuity property of B, we have: $|\{\!\{B\rho\}\!\}\cdot n|=|B\cdot n||\{\!\{\rho\}\!\}|=2C_S|\{\!\{\rho\}\!\}|$. Then, by using the Schwarz inequality together with the arithmetic-geometric mean inequality in the form: $pq\le\frac{p^2}{\beta}+\frac{\beta q^2}{4}$, we have the following estimate:

$$\begin{aligned}|a_a(\rho,\theta)|\le&\frac{1}{\beta}\sum_{\mathcal{K}\in\mathcal{T}_h}\|(D^\star)^{-1}u\|^2_{0,\infty,\mathcal{K}}\|\rho\|^2_{0,\mathcal{K}}+\frac{2}{\beta}\sum_{S\in\mathcal{F}_{\text{int}}}\|C_S^{1/2}\{\!\{\rho\}\!\}\|^2_{0,S}\\&+\frac{1}{\beta}\sum_{S\in\mathcal{F}_{\text{int}}}\|C_S^{1/2}|[\![\rho]\!]|\|^2_{0,S}+\frac{2}{\beta}\sum_{S\in(\cup_n\mathcal{S}^n_{MDSp}\cup\Gamma_+)}\|C_S^{1/2}|[\![\rho]\!]|\|^2_{0,S}\\&+\frac{1}{4}\beta\sum_{\mathcal{K}\in\mathcal{T}_h}\|D^\star\overline{\nabla}_h\theta\|^2_{0,\mathcal{K}}+\frac{3}{4}\beta\sum_{S\in\mathcal{F}_{\text{int}}}\|C_S^{1/2}|[\![\theta]\!]|\|^2_{0,S}\\&+\frac{1}{2}\beta\sum_{S\in(\cup_n\mathcal{S}^n_{MDSp}\cup\Gamma_+)}\|C_S^{1/2}|[\![\theta]\!]|\|^2_{0,S}.\end{aligned} \tag{4.71}$$

Next, we consider the bilinear form $a_d(\rho,\theta)$. Using the lifting operator R, the bilinear form can be written as:

$$\begin{aligned}a_d(\rho,\theta)=&\sum_{\mathcal{K}\in\mathcal{T}_h}\int_{\mathcal{K}}D\overline{\nabla}_h\rho\cdot\overline{\nabla}_h\theta\,\mathrm{d}\mathcal{K}+\sum_{\mathcal{K}\in\mathcal{T}_h}\int_{\mathcal{K}}\bar{R}([\![\rho]\!])\cdot D\overline{\nabla}_h\theta\,\mathrm{d}\mathcal{K}+\sum_{\mathcal{K}\in\mathcal{T}_h}\int_{\mathcal{K}}D\overline{\nabla}_h\rho\cdot\bar{R}([\![\theta]\!])\,\mathrm{d}\mathcal{K}\\&+\sum_{S\in\cup_n\mathcal{S}^n_{ID}}\sum_{\mathcal{K}\in\mathcal{T}_h}\eta_{\mathcal{K}}\int_{\mathcal{K}}D\bar{r}_S([\![\rho]\!])\cdot\bar{r}_S([\![\theta]\!])\,\mathrm{d}\mathcal{K}+\sum_{S\in\cup_n\mathcal{S}^n_M}\int_S\alpha\rho\theta\,\mathrm{d}S.\end{aligned} \tag{4.72}$$

Applying the Schwarz' inequality, inequality (4.47b) and arithmetic-geometric mean inequality yields:

$$\begin{aligned}|a_d(\rho,\theta)| \leq & \frac{N_f+1}{\beta}\sum_{\mathcal{K}\in\mathcal{T}_h}\|D^\star\overline{\nabla}_h\rho\|_{0,\mathcal{K}}^2+\frac{N_f+\eta_m^2}{\beta}\sum_{S\in\cup_n\mathcal{S}_{ID}^n}\sum_{\mathcal{K}\in\mathcal{T}_h}\|D^\star\bar{r}_S([\![\rho]\!])\|_{0,\mathcal{K}}^2\\ &+\frac{1}{2\beta}\sum_{S\in\cup_n\mathcal{S}_M^n}\|\sqrt{\alpha}\rho\|_{0,S}^2+\frac{\beta}{2}\sum_{\mathcal{K}\in\mathcal{T}_h}\|D^\star\overline{\nabla}_h\theta\|_{0,\mathcal{K}}^2\\ &+\frac{\beta}{2}\sum_{S\in\cup_n\mathcal{S}_{ID}^n}\sum_{\mathcal{K}\in\mathcal{T}_h}\|D^\star\bar{r}_S([\![\theta]\!])\|_{L^2(\mathcal{K})}^2+\frac{\beta}{2}\sum_{S\in\cup_n\mathcal{S}_M^n}\|\sqrt{\alpha}\theta\|_{0,S}^2, \end{aligned}\tag{4.73}$$

with $\eta_m=\max_{\mathcal{K}\in\mathcal{T}_h}\eta_{\mathcal{K}}$. Adding (4.71) and (4.73) and combining the result with the coercivity estimate (4.42) for $w=\theta$, and taking $\beta=\beta_a$, with β_a defined in Lemma 4.2, we deduce:

$$\begin{aligned}\frac{\beta_a}{4}|||\theta|||_{\mathrm{DG}}^2 \leq & \frac{1}{\beta_a}\sum_{\mathcal{K}\in\mathcal{T}_h}\|(D^\star)^{-1}u\|_{0,\infty,\mathcal{K}}^2\|\rho\|_{0,\mathcal{K}}^2+\frac{N_f+1}{\beta_a}\sum_{\mathcal{K}\in\mathcal{T}_h}\|D^\star\overline{\nabla}_h\rho\|_{0,\mathcal{K}}^2\\ &+\frac{N_f+\eta_m^2}{\beta_a}\sum_{S\in\cup_n\mathcal{S}_{ID}^n}\sum_{\mathcal{K}\in\mathcal{T}_h}\|D^\star\bar{r}_S([\![\rho]\!])\|_{0,\mathcal{K}}^2\\ &+\frac{1}{2\beta_a}\sum_{S\in\cup_n\mathcal{S}_M^n}\|\sqrt{\alpha}\rho\|_{0,S}^2+\frac{2}{\beta_a}\sum_{S\in\mathcal{F}_{\mathrm{int}}}\|C_S^{1/2}\{\!\{\rho\}\!\}\|_{0,S}^2\\ &+\frac{1}{\beta_a}\sum_{S\in\mathcal{F}_{\mathrm{int}}}\|C_S^{1/2}|[\![\rho]\!]|\|_{0,S}^2+\frac{2}{\beta_a}\sum_{S\in(\cup_n\mathcal{S}_{MDSp}^n\cup\Gamma_+)}\|C_S^{1/2}|[\![\rho]\!]|\|_{0,S}^2. \end{aligned}\tag{4.74}$$

Multiplying the last equation with β_a completes the proof of Lemma 4.9. □

Proof of the upper bound for ϕ in Lemma 4.12

The proof of Lemma 4.12 starts with introducing $w=\theta$ in (4.65) and using (4.69):

$$(\phi,\theta)_{\Omega_T}=a_a(\theta,z_h)+a_d(\theta,z_h)\leq|a_a(\rho,z_h)|+|a_d(\rho,z_h)|.$$

We estimate now each term separately. First, we derive an estimate for the bilinear form $a_a(\rho,z_h)$. Since $\frac{\partial z_h}{\partial t}\in\mathcal{W}_h^{(p_t,p_s)}$, the contribution $\int_{\mathcal{K}}\rho\frac{\partial z_h}{\partial t}\,\mathrm{d}\mathcal{K}$ is zero due to the orthogonality relation (4.55) and hence the bilinear form a_a is similar to (4.70). Using the Schwarz' inequality, we can estimate a_a as:

$$|a_a(\rho,z_h)|\leq\Big(C_c|||\rho|||_{\mathrm{DG}}+\big(2\sum_{S\in\mathcal{F}_{\mathrm{int}}}\|C_S^{1/2}\{\!\{\rho\}\!\}\|_{0,S}^2\big)^{1/2}\Big)|||z_h|||_{\mathrm{DG}},$$

with $C_c=3+u_D$ and $u_D=\max_{\mathcal{K}\in\mathcal{T}_h}\|(D^\star)^{-1}u\|_{0,\infty,\mathcal{K}}$. Next, we consider $a_d(\rho,z_h)$, which is of the form (4.72). Using inequality (4.47b), we obtain the upper bound for the bilinear form a_d as follows:

$$|a_d(\rho,z_h)|\leq C_d|||\rho|||_{\mathrm{DG}}|||z_h|||_{\mathrm{DG}},$$

with $C_d = 2 + 2\sqrt{N_f} + \eta_m$. Collecting all the terms, we obtain the estimate

$$(\phi, \theta)_{\Omega_T} \leq \Big(C_e |||\rho|||_{\mathrm{DG}} + \big(2 \sum_{S \in \mathcal{F}_{\mathrm{int}}} \|C_S^{1/2} \{\!\{\rho\}\!\}\|_{0,S}^2\big)^{1/2} \Big) |||z_h|||_{\mathrm{DG}},$$

with $C_e = C_c + C_d$. □

Proof of the upper bound for z_h in Lemma 4.13

To prove Lemma 4.13 we proceed as follows. First, we take $w = z_h$ in (4.65). Then we use the Schwarz and arithmetic-geometric mean inequalities and the definition of C_S on $S \in \mathcal{F}_{\mathrm{bnd}}$ (4.21) to obtain:

$$a(z_h, z_h) \leq \frac{1}{2\alpha_1} (\phi, \phi)_{\Omega_T} + \alpha_1 \sum_{S \in \mathcal{F}} \|C_S^{1/2} |[\![z_h]\!]|\|_{0,S}^2, \tag{4.75}$$

with $\alpha_1 > 0$ an arbitrary constant. Since Lemma 4.2 also applies to the backward problem, we can state that

$$a(z_h, z_h) \geq \beta_a |||z_h|||_{\mathrm{DG}}^2, \tag{4.76}$$

with $\beta_a > 0$ defined in Lemma 4.2. Combining (4.75) and (4.76) and choosing $\alpha_1 = \frac{\beta_a}{2}$, we obtain:

$$\frac{1}{2} \beta_a |||z_h|||_{\mathrm{DG}}^2 \leq \frac{1}{\beta_a} (\phi, \phi)_{\Omega_T}.$$

Multiplying the last equation with β_a completes the proof. □

4.7 Numerical results

In this section we present a number of numerical experiments in two spatial dimensions in order to verify the error analysis discussed in the previous sections. We provide results for the following time-dependent advection-diffusion equation:

$$\frac{\partial c}{\partial t} + u \sum_{i=1}^{2} \frac{\partial c}{\partial x_i} - D \sum_{i=1}^{2} \frac{\partial^2 c}{\partial x_i^2} = 0, \quad (0,1)^2, \tag{4.77}$$

with u and $D \geq 0$ constants. The initial condition is

$$c(0, x_1, x_2) = \sin(\pi x_1) \sin(\pi x_2),$$

and the boundary conditions are chosen so that the analytical solution is given by

$$c(t, x_1, x_2) = \sin(\pi(x_1 - ut)) \sin(\pi(x_2 - ut)) \exp(-2D\pi^2 t).$$

We consider three cases: (1) advection problem ($u = 1, D = 0$), (2) advection-diffusion problem ($u = 1, D = 1$), and (3) diffusion problem ($u = 0, D = 1$).

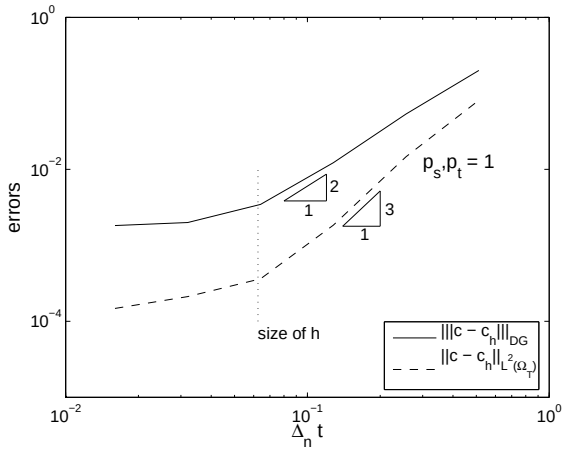

Figure 4.3: Convergence of space-time DG method when $u = 1, D = 0$ under $\triangle_n t$-refinement.

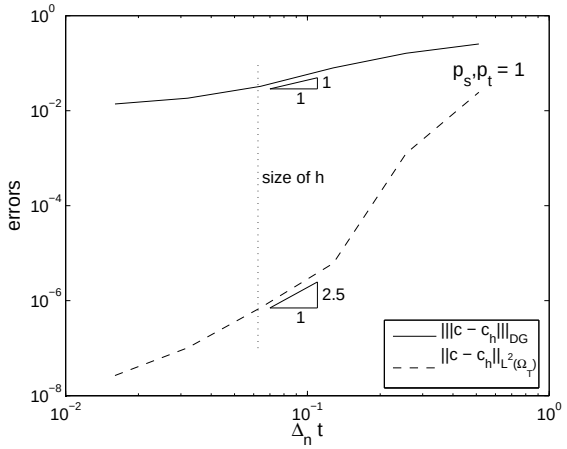

Figure 4.4: Convergence of space-time DG method when $u = 1, D = 1$ under $\triangle_n t$-refinement.

First, we investigate the behavior of the space-time DG discretization on a sequence of successively finer time intervals with a fixed number of elements in space and linear polynomial degrees: $p_{t,\mathcal{K}}, p_{s,\mathcal{K}} = 1$. We perform computations from $t = 0$

until the final time $T = 0.5$. The results are given in 4.3-4.5. When there is no diffusion process ($D = 0$), Fig. 4.3 shows that the error in the DG-norm as a function of the time step converges at the rate $O(\triangle_n t^2)$ when $\triangle_n t \geq h$, with h the spatial mesh size. This rate of convergence is better than the theoretical estimates presented in Theorem 4.10. This means that the errors in the DG-norm are dominated by the L^2-norm contribution (the first term in Theorem 4.10), while the contributions due to the jumps at the element boundaries are negligible. When there is also diffusion process present ($D = 1$), the errors in the DG-norm are dominated by the L^2-norm of the derivatives (the second term in Theorem 4.10), see Fig. 4.4-4.5. The errors in the DG-norm converge then at the rate $O(\triangle_n t)$, verifying the theoretical estimates in Theorem 4.10. At the final time $T = 0.5$, the rates of the convergence of the space-time DG discretization are better than the theoretical estimates given in Theorem 4.14.

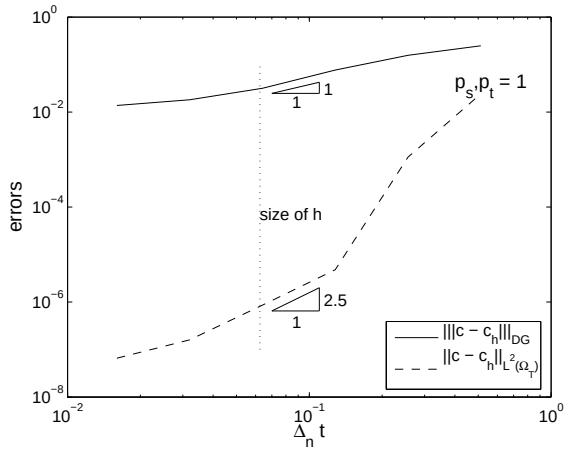

Figure 4.5: Convergence of space-time DG method when $u = 0, D = 1$ under $\triangle_n t$-refinement.

Next, we study the rates of convergence on meshes with a different spatial mesh size and increasing polynomial degrees. We compare the error for equal polynomial degrees: $p_{t,\mathcal{K}} = p_{s,\mathcal{K}}$ and also for linear polynomials in time: $p_{t,\mathcal{K}} = 1$. The results are shown in Fig. 4.6-4.8. When there is no diffusion ($D = 0$) and equal polynomial degrees in time and space are used, Fig. 4.6 shows that the error in the DG-norm converges at the rate h^{p_s+1}. This rate is better than is obtained in the theoretical estimates Theorem 4.10. This indicates that the errors in the DG-norm are dominated by the L^2-norm contribution and we can neglect contribution from the L^2-norm on the boundary $\partial\mathcal{K}$. However, when diffusion is also present ($D = 1$), from Fig. 4.7-4.8

we can conclude that the errors in the DG-norm are also influenced by L^2-norm of the derivatives and hence the errors converge at the rate h^{p_s} as we expect from Theorem 4.10.

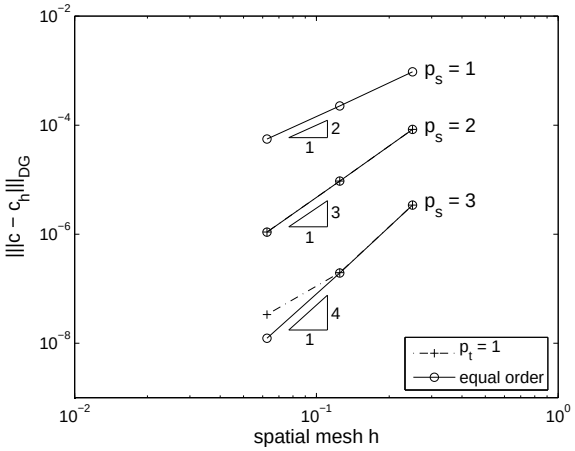

Figure 4.6: Convergence of space-time DG method when $u = 1, D = 0$ under h-refinement.

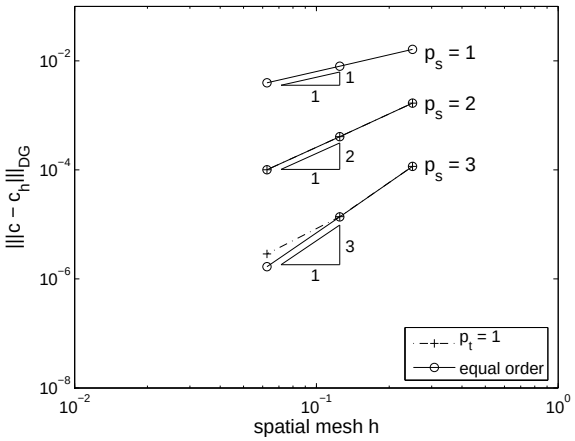

Figure 4.7: Convergence of space-time DG method when $u = 1, D = 1$ under h-refinement.

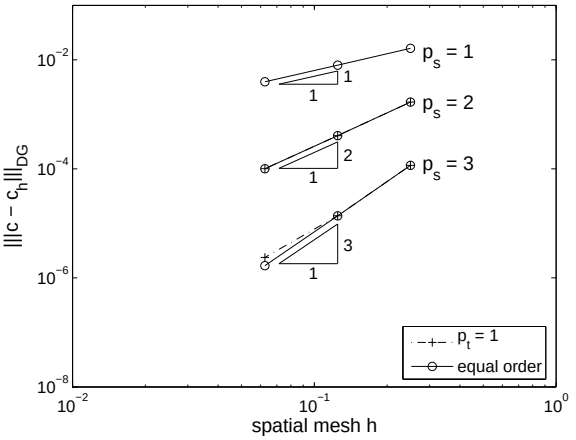

Figure 4.8: Convergence of space-time DG method when $u = 0, D = 1$ under h-refinement.

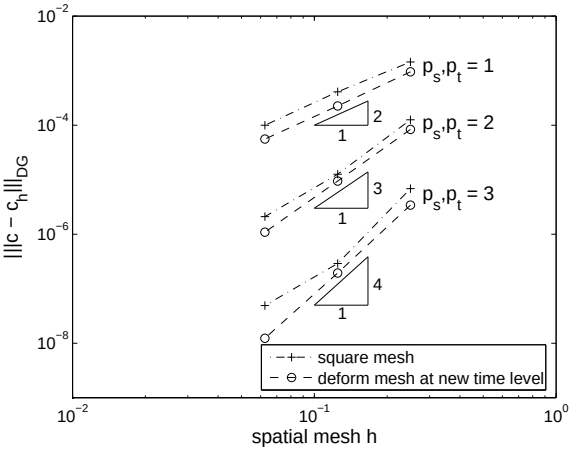

Figure 4.9: Convergence of space-time DG method when $u = 1, D = 0$ under h-refinement for square and deformed mesh.

Using linear polynomials in time, we observe that as the mesh becomes finer, then the error is dominated by the error in time, but this only occurs at relatively small error levels. The tests with linear polynomials in time were performed since the

analysis presented in Section 4.5 could only prove a unique solution for polynomials linear in time and we want to investigate the effect of restricting the polynomial degree in time on the accuracy.

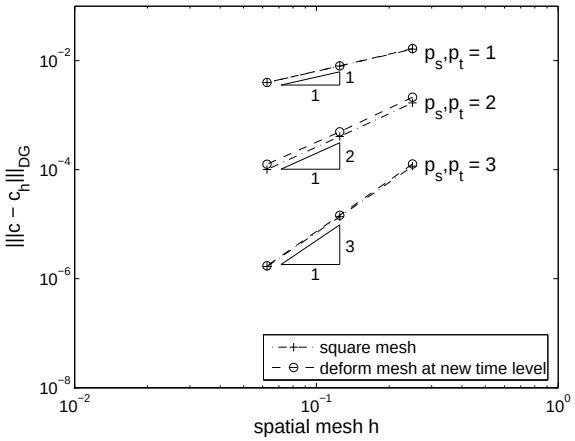

Figure 4.10: Convergence of space-time DG method when $u = 1, D = 1$ under h-refinement for square and deformed mesh.

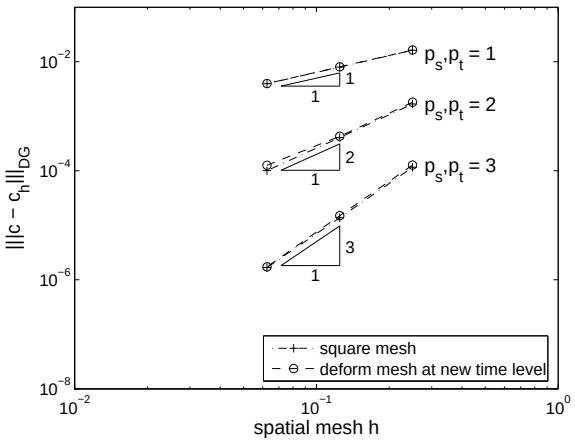

Figure 4.11: Convergence of space-time DG method when $u = 0, D = 1$ under h-refinement for square and deformed mesh.

We also investigate the effect of the mesh movement on the accuracy. We construct the mesh movement as follows. At t_n we have a uniform square mesh. At t_{n+1}, the uniform mesh is deformed by randomly perturbing the interior nodes. Thus the meshes at t_n and at t_{n+1} are not identical, and the mesh velocity (discussed in Section 4.4.2) is present. The plots of the errors in the DG-norm on time deforming meshes are shown in Fig. 4.9-4.11. The figures show that the errors in the DG-norm on a square mesh and on a time deforming mesh converge at the same rate.

Finally, we investigate the convergence of the space-time DG method with p-refinement and the results are shown in Fig. 4.12-4.14. Here we only study the p-refinement for equal polynomial degrees in time and space: $p_{t,\mathcal{K}} = p_{s,\mathcal{K}}$ on a square mesh. We observe that on a linear-log scale, the errors in the DG-norm for all three cases become straight lines which indicate exponential convergence in p.

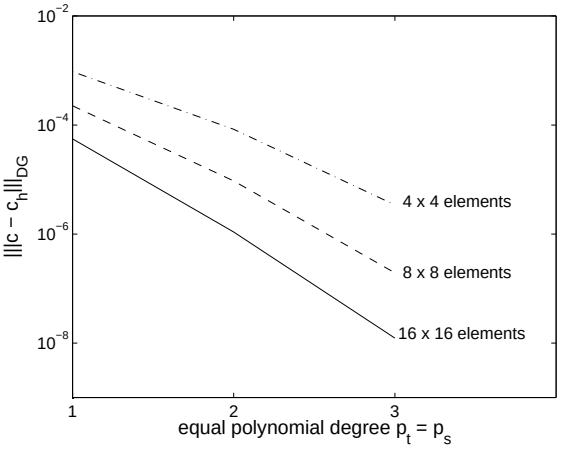

Figure 4.12: Convergence of space-time DG method when $u = 1, D = 0$ under p-refinement.

4.8 Concluding remarks

In this chapter we present a new space-time DG method for the advection-diffusion equation in time-dependent domains. We study and prove the coercivity, stability and the existence of a unique solution of the method. We also present an error estimate in the DG-norm on the space-time domain and in the L^2-norm at a specific time level.

The numerical results show that for pure advection problems, the space-time DG discretization with h-refinement converges in the DG-norm faster than the theoretical estimate in Theorem 4.10. For the case when diffusion is present the convergence

of the space-time DG discretization with h-refinement is numerically observed to be optimal in the DG norm, thus verifies the theoretical estimates. The use of a time deforming mesh does not influence the rates of convergence.

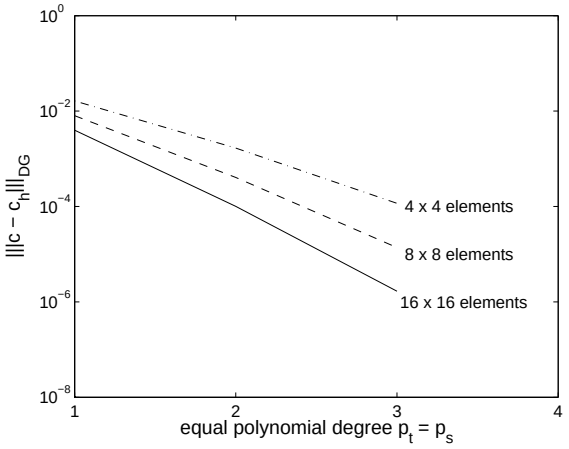

Figure 4.13: Convergence of space-time DG method when $u = 1, D = 1$ under p-refinement.

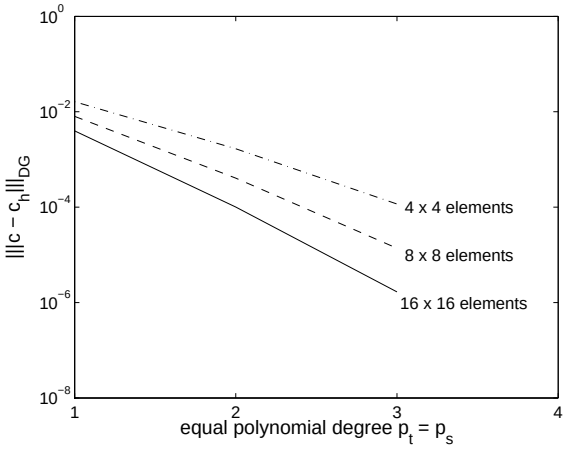

Figure 4.14: Convergence of space-time DG method when $u = 0, D = 1$ under p-refinement.

The rates of convergence with p-refinement is numerically observed to be optimal in the DG-norm for all three cases. Further, although the space-time DG discretization was only proven to be stable for the linear polynomials in time, in the numerical simulations the algorithm performs also well for higher polynomial degrees in time.

As the space-time DG discretization is unconditionally stable, gives a unique solution and optimal convergence for high-order polynomial degrees, the governing equations (2.1) for the concentration of the etchant will be discretized with this method in Chapter 6.

Chapter 5

A Space-Time Discontinuous Galerkin Method for Incompressible Flows

5.1 Introduction

In this chapter we discuss a space-time DG discretization for the incompressible Navier-Stokes equations, which are the governing equations for the velocity and pressure field in the acid fluid, see (2.6). The algorithm is closely related to the DG discretization developed by Cockburn, Kanschat, and Schötzau, which is discussed in a series of papers [21, 22, 23, 24]. Also, the analysis in [54, 55] provides important information on the construction of DG algorithms for incompressible flows. A different approach using approximate Riemann solvers for the artificial compressibility pertubation of the incompressible Navier-Stokes equations is provided in [8], but this technique only applies to steady flows.

There are four important points that have to be considered in the development of a DG discretization for the incompressible Navier-Stokes equations. Each one is shortly discussed here together with what has been studied in the literature for the steady-state case.

The first issue is the treatment of the nonlinearity in the convective term. There are several ways to deal with this nonlinear term. In [24] the nonlinear incompressible Navier-Stokes equations are linearized by applying a Picard linearization to obtain a sequence of Oseen equations. This sequence of Oseen equations is then solved iteratively. An alternative technique is to solve the nonlinear equations directly using a Newton method, such as done in [8]. This requires, however, a careful linearization of all terms which is non-trivial when the solution of the Navier-Stokes equations must be coupled with more complicated models for the chemical reactions in the wet-chemical etching process.

The second issue is the DG discretization of the viscous terms. The obvious choice is to discretize the viscous terms in a similar way as done for elliptic equations

(see Chapter 3), but now extended to vector functions. In [8], the Bassi and Rebay method (Method 4 in Table 3.1) is used, while the LDG method (Method 2 in Table 3.1) is used in [21, 22, 23, 24]. Based on our experience with the advection-diffusion equation, discussed in Chapter 4, we will use the Bassi and Rebay method for the viscous contribution.

The third issue is the incompressibility constraint imposed by the continuity equation. In [24], the mean values are chosen as the numerical flux at the element faces in the continuity equation. In order to have a globally divergence-free velocity field, a post processing operator is then used to project the velocity field onto the space of globally divergence-free functions. Another approach, presented in [8], is to add an artificial compressibility term to the continuity equation. The numerical flux at the element faces is provided by the solution of a Riemann problem. This algorithm is, however, limited to steady flows.

The fourth issue is the pressure stabilization. The analysis presented in [54, 55] discusses the importance of the pressure stabilization operator for the choice of the polynomial degrees in the approximations of the velocity and pressure. Without a stabilization term, the DG method can only be proven stable when the polynomial degree used in the approximation of the pressure is one less than the polynomial degree for the approximation of the velocity. By adding a stabilization term similar to the one used for the elliptic equations, stability is proven when equal polynomial degrees are used for both the velocity and the pressure.

The above issues are also of direct interest for a space-time DG discretization of the incompressible Navier-Stokes equations. To deal with the nonlinear term, we follow the approach in which the nonlinear problem is linearized as an Oseen equation. This is discussed in Section 5.2. After the introduction of the finite element spaces and trace operators in Section 5.3, we give the derivation of the space-time DG weak formulation for the Oseen equations in time-dependent domains in Section 5.4. The discretization of the viscous terms follows the space-time DG discretization in Chapter 4. Two approaches for the stabilization term are considered, which are similar to the stabilization operators for the elliptic equations discussed in Chapter 3. The analysis of the stability of the space-time DG discretization for the Oseen equations is presented in Section 5.5. Some numerical experiments are given in Section 5.6.

5.2 The incompressible flows

In this section we recapitulate the Navier-Stokes equations given for incompressible flows and set some notations. We follow the description given in [32].

Let Ω_t be an open, bounded, time-dependent domain in $\mathbb{R}^d$ at time t, where d is the number of spatial dimensions. The closure of Ω_t is $\bar{\Omega}_t$ and the boundary of Ω_t is denoted by $\partial\Omega_t$. Denoting $\bar{x} = (x_1, \ldots, x_d)$ as the spatial variables, we consider the

time-dependent incompressible Navier-Stokes equations for the velocity field $u \in \mathbb{R}^d$ and the kinematic pressure $p := p/\rho \in \mathbb{R}$ in the domain Ω_t:

$$\frac{\partial u}{\partial t} + \overline{\nabla} \cdot (u \otimes u) - \nu \overline{\nabla} \cdot \overline{\nabla} u + \overline{\nabla} p = f, \quad \text{in } \Omega_t, \tag{5.1a}$$

$$\overline{\nabla} \cdot u = 0, \quad \text{in } \Omega_t, \tag{5.1b}$$

where $\nu \in \mathbb{R}^+$ is the kinematic viscosity and $f \in \mathbb{R}^d$ the force vector. We introduce the product between two vectors $a \in \mathbb{R}^m, b \in \mathbb{R}^n$ as $a \otimes b \in \mathbb{R}^{m \times n}$ with elements $(a \otimes b)_{ij} = a_i b_j$. The notation $\overline{\nabla}$ is used for the spatial gradient operator in $\mathbb{R}^d$, and defined as $\overline{\nabla} = \left(\frac{\partial}{\partial x_1}, \ldots, \frac{\partial}{\partial x_d}\right)$. We also define the divergence of a tensor $A \in \mathbb{R}^{m \times n}$ as: $\overline{\nabla} \cdot A = \sum_j \frac{\partial}{\partial x_j} A_{ij}$.

As mentioned in the introduction, we linearize (5.1) using a Picard linearization. This results in the Oseen equations:

$$\frac{\partial u}{\partial t} + \overline{\nabla} \cdot (u \otimes w) - \nu \overline{\nabla} \cdot \overline{\nabla} u + \overline{\nabla} p = f, \quad \text{in } \Omega_t, \tag{5.2a}$$

$$\overline{\nabla} \cdot u = 0, \quad \text{in } \Omega_t, \tag{5.2b}$$

with $w \in \mathbb{R}^d$ a given convective divergence free velocity field.

For the space-time discretization, we consider the Oseen equations directly in a domain in $\mathbb{R}^{d+1}$. A point $x \in \mathbb{R}^{d+1}$ has coordinates $(x_0, \bar{x})$, with $x_0 = t$ representing time. We define the space-time domain $\mathcal{E} \subset \mathbb{R}^{d+1}$. The boundary of the space-time domain $\partial\mathcal{E}$ consists of the hypersurfaces $\Omega_0 := \{x \in \partial\mathcal{E} \mid x_0 = 0\}$, $\Omega_T := \{x \in \partial\mathcal{E} \mid x_0 = T\}$, and $\mathcal{Q} := \{x \in \partial\mathcal{E} \mid 0 < x_0 < T\}$. Introducing the gradient operator in $\mathbb{R}^{d+1}$ as $\nabla = \left(\frac{\partial}{\partial x_0}, \frac{\partial}{\partial x_1}, \ldots, \frac{\partial}{\partial x_d}\right)$ and the vector $\mathbb{C} = (1, w)$, the Oseen equations (5.2) can be transformed into a space-time formulation as:

$$\nabla \cdot (u \otimes \mathbb{C}) - \nu \overline{\nabla} \cdot \overline{\nabla} u + \overline{\nabla} \cdot (\mathbb{I}_d\, p) = f, \quad \text{in } \mathcal{E}, \tag{5.3a}$$

$$\overline{\nabla} \cdot u = 0, \quad \text{in } \mathcal{E}, \tag{5.3b}$$

with $\mathbb{I}_d$ the $d \times d$ identity matrix.

Since different boundary conditions are imposed on $\partial\mathcal{E}$, we discuss the subdivision of $\partial\mathcal{E}$ into different parts. The boundary $\partial\mathcal{E}$ is divided into disjoint subsets Γ_m and Γ_p, with:

$$\Gamma_m := \{x \in \partial\mathcal{E} : \mathbb{C} \cdot n < 0\}, \quad \Gamma_p := \{x \in \partial\mathcal{E} : \mathbb{C} \cdot n \geq 0\}.$$

The subscripts m and p denote the inflow and outflow boundaries, respectively. We subdivide Γ_m further into two sets: Γ_{Dm} and Ω_0, with Γ_{Dm} the part of Γ_m with a Dirichlet boundary condition and Ω_0 the part of Γ_m with the initial condition. The part Γ_p is divided into three sets: Ω_T, Γ_{Dp} and Γ_N, with Ω_T the part of $\partial\mathcal{E}$ at the final time T, Γ_{Dp} the part of Γ_p with a Dirichlet boundary condition and Γ_N the part of Γ_p with a Neumann boundary condition. Note that $\Gamma_D = \Gamma_{Dm} \cup \Gamma_{Dp}$ is the

part of the space-time boundary with a Dirichlet boundary condition. The boundary conditions on different parts of $\partial\mathcal{E}$ are written as

$$u = u_0 \quad \text{on } \Omega_0, \tag{5.4a}$$
$$u = g_D \quad \text{on } \Gamma_D, \tag{5.4b}$$
$$\bar{n} \cdot \overline{\nabla} u = g_N \quad \text{on } \Gamma_N, \tag{5.4c}$$
$$p = p_N \quad \text{on } \Gamma_N, \tag{5.4d}$$

with u_0 a given initial function and g_D, g_N, p_N given functions defined on the boundary. There is no boundary condition imposed on Ω_T.

5.3 Space-time elements, finite element spaces and trace operators

5.3.1 Definition of space-time slabs, elements and faces

The description of the space-time slabs and the construction of the space-time elements in this section follows the definitions given in Section 4.3.1. As already introduced in the previous section, we consider the problem in a space-time domain $\mathcal{E}$. The nth time interval is denoted by I_n, with its length defined as $\triangle_n t = t_{n+1} - t_n$. A space-time slab is defined as the domain $\mathcal{E}^n = \mathcal{E} \cap (I_n \times \mathbb{R}^d)$ with boundaries Ω_{t_n}, $\Omega_{t_{n+1}}$ and $\mathcal{Q}^n = \partial\mathcal{E}^n \setminus (\Omega_{t_n} \cup \Omega_{t_{n+1}})$.

The space-time element is denoted by $\mathcal{K}$, with $h_\mathcal{K}$ the radius of the smallest sphere containing each element $\mathcal{K}$. The element boundary $\partial\mathcal{K}$ is the union of open faces of $\mathcal{K}$, which contains three parts K^n, K^{n+1}, and $\mathcal{Q}^n_\mathcal{K} = \partial\mathcal{K} \setminus (K^n \cup K^{n+1})$. We denote by $n_\mathcal{K}$ the unit outward space-time normal vector on $\partial\mathcal{K}$. The definition of the space-time domain is completed with the tessellation $\mathcal{T}_h^n$ in each space-time slab and $\mathcal{T}_h = \cup_n \mathcal{T}_h^n$ in the space-time domain.

We consider several sets of faces S. The set of all faces in $\mathcal{E}$ is denoted with $\mathcal{F}$, the set of all interior faces in $\mathcal{E}$ with $\mathcal{F}_{\text{int}}$, and the set of all boundary faces on $\partial\mathcal{E}$ with $\mathcal{F}_{\text{bnd}}$. In the space-time slab $\mathcal{E}^n$ we denote the set of all faces with $\mathcal{F}^n$ and the set of all interior faces with $\mathcal{S}_I^n$. The faces separating two space-time slabs are denoted as $\mathcal{S}_S^n$. Several sets of boundary faces are defined as follows. The set of faces with a Dirichlet boundary condition is denoted with $\mathcal{S}_D^n$. This set can be divided further into sets $\mathcal{S}_{Dm}^n$ and $\mathcal{S}_{Dp}^n$, which correspond to the faces with a Dirichlet boundary condition on Γ_m and Γ_p, respectively. The set of faces with a Neumann boundary condition is denoted with $\mathcal{S}_N^n$. Further, the sets $\mathcal{S}_I^n$ and $\mathcal{S}_D^n$ are grouped into $\mathcal{S}_{ID}^n$ and the sets $\mathcal{S}_I^n, \mathcal{S}_D^n$ and $\mathcal{S}_N^n$ are grouped into $\mathcal{S}_{IDN}^n$.

5.3.2 Finite element spaces and trace operators

The definitions of the anisotropic Sobolev spaces and the broken Sobolev spaces which are given in Section 4.3.2, with their corresponding norms and semi-norms, can be

straightforwardly extended to vector and tensor functions. For simplicity then the anisotropic Sobolev spaces that we discuss in this chapter follow the definition in Section 4.3.2.

We now discuss the finite element spaces associated with the tessellation $\mathcal{T}_h$ that will be used in this chapter. To each element $\mathcal{K}$ we assign a pair of nonnegative integers $(p_{t,\mathcal{K}}, p_{s,\mathcal{K}})$ as local polynomial degrees, where the subscripts t and s denote time and space, respectively, and collect them into vectors $p_t = \{p_{t,\mathcal{K}} : \mathcal{K} \in \mathcal{T}_h\}$ and $p_s = \{p_{s,\mathcal{K}} : \mathcal{K} \in \mathcal{T}_h\}$. We define $\mathcal{Q}_{p_{t,\mathcal{K}},p_{s,\mathcal{K}}}(\hat{\mathcal{K}})$ as the set of all tensor-product polynomials on $\hat{\mathcal{K}}$ of degree $p_{t,\mathcal{K}}$ in the time direction and degree $p_{s,\mathcal{K}}$ in each spatial coordinate direction. The finite element spaces of discontinuous polynomial functions are defined as follows

$$V_h^{(p_t,p_s)} := \{v \in L^2(\mathcal{E})^d : v|_{\mathcal{K}} \circ Q_{\mathcal{K}} \circ F_{\mathcal{K}} \in [\mathcal{Q}_{(p_{t,\mathcal{K}},p_{s,\mathcal{K}})}(\hat{\mathcal{K}})]^d, \forall \mathcal{K} \in \mathcal{T}_h\},$$
$$\mathcal{Q}_h^{(p_t,p_s)} := \{q \in L^2(\mathcal{E}) : q|_{\mathcal{K}} \circ Q_{\mathcal{K}} \circ F_{\mathcal{K}} \in \mathcal{Q}_{(p_{t,\mathcal{K}},p_{s,\mathcal{K}})}(\hat{\mathcal{K}}), \forall \mathcal{K} \in \mathcal{T}_h\}.$$

In the derivation and analysis of the numerical discretization we also make use of auxiliary spaces $\Sigma_h^{(p_t,p_s)}$ and $\bar{\Sigma}_h^{(p_t,p_s)}$:

$$\Sigma_h^{(p_t,p_s)} := \{\tau \in L^2(\mathcal{E})^{d\times(d+1)} : \tau|_{\mathcal{K}} \circ Q_{\mathcal{K}} \circ F_{\mathcal{K}} \in [\mathcal{Q}_{(p_{t,\mathcal{K}},p_{s,\mathcal{K}})}(\hat{\mathcal{K}})]^{d\times(d+1)}, \forall \mathcal{K} \in \mathcal{T}_h\},$$
$$\bar{\Sigma}_h^{(p_t,p_s)} := \{\bar{\tau} \in L^2(\mathcal{E})^{d\times d} : \bar{\tau}|_{\mathcal{K}} \circ Q_{\mathcal{K}} \circ F_{\mathcal{K}} \in [\mathcal{Q}_{(p_{t,\mathcal{K}},p_{s,\mathcal{K}})}(\hat{\mathcal{K}})]^{d\times d}, \forall \mathcal{K} \in \mathcal{T}_h\}.$$

The so called traces of $v \in V_h^{(p_t,p_s)}$ on $\partial\mathcal{K}$ are defined as: $v_{\mathcal{K}}^{\pm} = \lim_{\epsilon\downarrow 0} v(x \pm \epsilon n_{\mathcal{K}})$. The traces of $q \in \mathcal{Q}_h^{(p_t,p_s)}, \tau \in \Sigma_h^{(p_t,p_s)}$, and $\bar{\tau} \in \bar{\Sigma}_h^{(p_t,p_s)}$ are defined similarly.

Next, we define several trace operators for the sets $\mathcal{F}_{\text{int}}$ and $\mathcal{F}_{\text{bnd}}$. Note that functions $v \in V_h^{(p_t,p_s)}, q \in \mathcal{Q}_h^{(p_t,p_s)}, \tau \in \Sigma_h^{(p_t,p_s)}$ and $\bar{\tau} \in \bar{\Sigma}_h^{(p_t,p_s)}$ are in general multivalued on a face $S \in \mathcal{F}_{\text{int}}$. Introducing the functions $v_i := v|_{\mathcal{K}_i}$, $q_i := q|_{\mathcal{K}_i}$, $\tau_i := \tau|_{\mathcal{K}_i}$, $\bar{\tau}_i := \bar{\tau}|_{\mathcal{K}_i}$, we define the average operator $\{\!\{\cdot\}\!\}$ on $S \in \mathcal{F}_{\text{int}}$ as:

$$\{\!\{v\}\!\} = (v_i + v_j)/2, \quad \{\!\{q\}\!\} = (q_i + q_j)/2, \quad \{\!\{\tau\}\!\} = (\tau_i + \tau_j)/2, \quad \{\!\{\bar{\tau}\}\!\} = (\bar{\tau}_i + \bar{\tau}_j)/2,$$

while on $S \in \mathcal{F}_{\text{bnd}}$, we set accordingly

$$\{\!\{v\}\!\} = v, \quad \{\!\{q\}\!\} = q, \quad \{\!\{\tau\}\!\} = \tau, \quad \{\!\{\bar{\tau}\}\!\} = \bar{\tau}.$$

We also introduce the jump operators $[\![\cdot]\!]$ and $\langle\!\langle\cdot\rangle\!\rangle$. For functions $q \in \mathcal{Q}_h^{(p_t,p_s)}$, $\tau \in \Sigma_h^{(p_t,p_s)}$ and $\bar{\tau} \in \bar{\Sigma}_h^{(p_t,p_s)}$, the jump operators are defined on $S \in \mathcal{F}_{\text{int}}$ as:

$$[\![q]\!] = q_i n_i + q_j n_j, \quad [\![\tau]\!] = \tau_i \cdot n_i + \tau_j \cdot n_j,$$
$$\langle\!\langle q\rangle\!\rangle = q_i \bar{n}_i + q_j \bar{n}_j, \quad \langle\!\langle\bar{\tau}\rangle\!\rangle = \bar{\tau}_i \cdot \bar{n}_i + \bar{\tau}_j \cdot \bar{n}_j,$$

with $n_i, \bar{n}_i$ the outward normal vector on $\partial\mathcal{K}_i$ and its spatial part. For functions $v \in V_h^{(p_t,p_s)}$, we define the jump operators on $S \in \mathcal{F}_{\text{int}}$ as follows:

$$[\![v]\!] = v_i \otimes n_i + v_j \otimes n_j, \ \langle\!\langle v\rangle\!\rangle = v_i \otimes \bar{n}_i + v_j \otimes \bar{n}_j, \ \langle\!\langle v\rangle\!\rangle = v_i \cdot \bar{n}_i + v_j \cdot \bar{n}_j.$$

By taking all functions from the neighboring element equal to zero, the definitions of jump operators are also valid on boundary faces $S \in \mathcal{F}_{\text{bnd}}$. Note that $\langle\!\langle v \rangle\!\rangle$ is scalar, $[\![q]\!] \in \mathbb{R}^{d+1}$, $\langle\!\langle q \rangle\!\rangle \in \mathbb{R}^d$ are vectors, and $[\![v]\!] \in \mathbb{R}^{d\times(d+1)}$, $\langle\!\langle\!\langle v \rangle\!\rangle\!\rangle \in \mathbb{R}^{d\times d}$ are matrices. The jumps $[\![\tau]\!], \langle\!\langle \bar{\tau} \rangle\!\rangle \in \mathbb{R}^d$ are also vectors.

5.3.3 Lifting operators

The derivation of the space-time DG formulation in this chapter requires several lifting operators. In this section we introduce lifting operators for vector functions.

First, we introduce the lifting operator $\mathcal{L}_S : (L^2(S))^{d\times(d+1)} \to \Sigma_h^{(p_t,p_s)}$:

$$\int_{\mathcal{E}} \mathcal{L}_S(\vartheta) : \tau \, \mathrm{d}\mathcal{E} = \int_S \vartheta : \{\!\{\tau\}\!\} \, \mathrm{d}S, \ \forall \tau \in \Sigma_h^{(p_t,p_s)}, \forall S \in \cup_n \mathcal{S}_{ID}^n, \tag{5.5}$$

where the dyadic product between two matrices $A, B \in \mathbb{R}^{m\times n}$ is defined as: $A : B = \sum_{i=1}^m \sum_{j=1}^n A_{ij} B_{ij}$. The global lifting operator $\mathcal{L} : (L^2(\cup_n \mathcal{S}_{ID}^n))^{d\times(d+1)} \to \Sigma_h^{(p_t,p_s)}$ is then introduced as

$$\int_{\mathcal{E}} \mathcal{L}(\vartheta) : \tau \, \mathrm{d}\mathcal{E} = \sum_{S\in\cup_n \mathcal{S}_{ID}^n} \int_{\mathcal{E}} \mathcal{L}_S(\vartheta) : \tau \, \mathrm{d}\mathcal{E}, \ \forall \tau \in \Sigma_h^{(p_t,p_s)}. \tag{5.6}$$

We specify the above lifting operators for the Dirichlet boundary condition, using a similar argument as in Section 4.3.3. On faces $S \in \cup_n \mathcal{S}_D^n$ we have

$$\int_{\mathcal{E}} \mathcal{L}_S(\mathcal{P} g_D \otimes n) : \tau \, \mathrm{d}\mathcal{E} = \int_S g_D \otimes n : \tau \, \mathrm{d}S, \ \forall \tau \in \Sigma_h^{(p_t,p_s)}, \forall S \in \cup_n \mathcal{S}_D^n, \tag{5.7}$$

with $\mathcal{P}$ the L^2 projection on $\Sigma_h^{(p_t,p_s)}$. For the global lifting operators, we proceed also as in Section 4.3.3. We replace ϑ by $\mathcal{P} g_D \otimes n$ in (5.5) and (5.6) to obtain the following global lifting operator for the Dirichlet boundary:

$$\int_{\mathcal{E}} \mathcal{L}(\mathcal{P} g_D \otimes n) : \tau \, \mathrm{d}\mathcal{E} = \sum_{S\in\cup_n \mathcal{S}_D^n} \int_S g_D \otimes n : \tau \, \mathrm{d}S, \ \forall \tau \in \Sigma_h^{(p_t,p_s)}. \tag{5.8}$$

Using (5.6) and (5.8), we then introduce $\mathcal{L}_{ID} : (L^2(\cup_n \mathcal{S}_{ID}^n))^{d\times(d+1)} \to \Sigma_h^{(p_t,p_s)}$ as:

$$\mathcal{L}_{ID}(\vartheta) = -\mathcal{L}(\vartheta) + \mathcal{L}(\mathcal{P} g_D \otimes n). \tag{5.9}$$

Later in this chapter, we will also use the spatial part of the lifting operators, denoted by $\bar{\mathcal{L}}, \bar{\mathcal{L}}_S$, which are obtained by eliminating the first component of $\mathcal{L}, \mathcal{L}_S$, respectively.

5.4 Space-time DG discretization for the Oseen equations

In this section we give a derivation of the space-time DG weak formulation for the Oseen equations (5.3). As in Chapter 4, we introduce an auxiliary variable $\sigma = \overline{\nabla} u$,

to obtain the following system of first order equations:

$$\sigma = \overline{\nabla} u, \quad \text{in } \mathcal{E}, \tag{5.10a}$$

$$\nabla \cdot (u \otimes \mathbb{C}) - \nu \overline{\nabla} \cdot \sigma + \overline{\nabla} \cdot (\mathbb{I}_d\, p) = f, \quad \text{in } \mathcal{E}, \tag{5.10b}$$

$$\overline{\nabla} \cdot u = 0, \quad \text{in } \mathcal{E}, \tag{5.10c}$$

together with the boundary conditions (5.4a)-(5.4d). We assume that the convective velocity field w in the vector $\mathbb{C}$ is in the space:

$$\mathcal{J}_h := \{v \in L^2(\mathcal{E})^d, \overline{\nabla} \cdot v = 0 \,\text{and}\, v\,|_{\mathcal{K}} \in H^{0,1}(\mathcal{K})^d,\ \forall \mathcal{K} \in \mathcal{T}_h\}.$$

In the next three sections we give the derivation of the weak formulation for (5.10).

5.4.1 Weak formulation for the auxiliary variable

First, we consider the auxiliary variable (5.10a). Multiplying (5.10a) with an arbitrary test function $\bar{\tau} \in \bar{\Sigma}_h^{(p_t,p_s)}$ and integrating over an element $\mathcal{K} \in \mathcal{T}_h^n$, we obtain:

$$\int_{\mathcal{K}} \sigma : \bar{\tau}\ \mathrm{d}\mathcal{K} = \int_{\mathcal{K}} \overline{\nabla} u : \bar{\tau}\ \mathrm{d}\mathcal{K}, \quad \forall \bar{\tau} \in \bar{\Sigma}_h^{(p_t,p_s)}. \tag{5.11}$$

Next, we substitute σ, u with their approximations $\sigma_h \in \bar{\Sigma}_h^{(p_t,p_s)}, u_h \in V_h^{(p_t,p_s)}$ and perform integration by parts on the right hand side of (5.11) twice with respect to $x_1, \ldots, x_d$. After summation over all elements $\mathcal{K} \in \mathcal{T}_h^n$, we obtain for all $\bar{\tau} \in \bar{\Sigma}_h^{(p_t,p_s)}$:

$$\int_{\mathcal{E}^n} \sigma_h : \bar{\tau}\ \mathrm{d}\mathcal{E} = \int_{\mathcal{E}^n} \overline{\nabla}_h u_h : \bar{\tau}\ \mathrm{d}\mathcal{E} + \sum_{\mathcal{K} \in \mathcal{T}_h^n} \int_{\mathcal{Q}_{\mathcal{K}}^n} (\hat{u}_h^\sigma - u_h) \otimes \bar{n} : \bar{\tau}\ \mathrm{d}\partial\mathcal{K}. \tag{5.12}$$

The variable $\hat{u}_h^\sigma$ is the *numerical flux* that must be defined to account for the multivalued trace at $\mathcal{Q}_{\mathcal{K}}^n$. Note that since we perform the integration by parts on the spatial variables, we only have to consider the weak formulation in the space-time slab $\mathcal{E}^n$ since there are no fluxes between different space-time slabs.

We recall the following relation, which is an extension of the identity introduced in [4] for tensors $\bar{\tau}$ and vectors v, piecewise smooth on $\mathcal{T}_h$:

$$\sum_{\mathcal{K} \in \mathcal{T}_h^n} \int_{\mathcal{Q}_{\mathcal{K}}^n} v \otimes \bar{n} : \bar{\tau}\ \mathrm{d}\partial\mathcal{K} = \sum_{S \in \mathcal{S}_{IDN}^n} \int_S \langle\!\langle v \rangle\!\rangle : \{\!\{\bar{\tau}\}\!\}\ \mathrm{d}S + \sum_{S \in \mathcal{S}_I^n} \int_S \{\!\{v\}\!\} \cdot \langle\!\langle \bar{\tau} \rangle\!\rangle\ \mathrm{d}S, \tag{5.13}$$

and can be proved by a straightforward calculation. When applied to the last term in (5.12), this results in

$$\begin{aligned} \sum_{\mathcal{K} \in \mathcal{T}_h^n} \int_{\mathcal{Q}_{\mathcal{K}}^n} (\hat{u}_h^\sigma - u_h) \otimes \bar{n} : \bar{\tau}\ \mathrm{d}\partial\mathcal{K} = & \sum_{S \in \mathcal{S}_{IDN}^n} \int_S \langle\!\langle \hat{u}_h^\sigma - u_h \rangle\!\rangle : \{\!\{\bar{\tau}\}\!\}\ \mathrm{d}S \\ & + \sum_{S \in \mathcal{S}_I^n} \int_S \{\!\{\hat{u}_h^\sigma - u_h\}\!\} \cdot \langle\!\langle \bar{\tau} \rangle\!\rangle\ \mathrm{d}S. \end{aligned} \tag{5.14}$$

We consider now the choice for numerical flux $\hat{u}_h^\sigma$. We make a similar choice as in Section 4.4.1, but now applied to vector functions:

$$\hat{u}_h^\sigma = \{\!\{u_h\}\!\} \text{ on } \mathcal{S}_I^n, \quad \hat{u}_h^\sigma = g_D \text{ on } \mathcal{S}_D^n, \quad \hat{u}_h^\sigma = u_h \text{ on } \mathcal{S}_N^n. \tag{5.15}$$

Replacing $\hat{u}_h^\sigma$ in (5.14) with the choices for the numerical flux (5.15), we obtain:

$$\sum_{\mathcal{K}\in\mathcal{T}_h^n} \int_{\mathcal{Q}_\mathcal{K}^n} (\hat{u}_h^\sigma - u_h) \otimes \bar{n} : \bar{\tau} \, \mathrm{d}\partial\mathcal{K} = -\sum_{S\in\mathcal{S}_{ID}^n} \int_S \langle\!\langle u_h \rangle\!\rangle : \{\!\{\bar{\tau}\}\!\} \, \mathrm{d}S + \sum_{S\in\mathcal{S}_D^n} \int_S g_D \otimes \bar{n} : \bar{\tau} \, \mathrm{d}S. \tag{5.16}$$

The weak formulation (5.12) is now equal to:

Find a $\sigma_h \in \bar{\Sigma}_h^{(p_t,p_s)}$, such that for all $\bar{\tau} \in \bar{\Sigma}_h^{(p_t,p_s)}$, the following relation is satisfied:

$$\int_{\mathcal{E}^n} \sigma_h : \bar{\tau} \, \mathrm{d}\mathcal{E} = \int_{\mathcal{E}^n} \overline{\nabla}_h u_h : \bar{\tau} \, \mathrm{d}\mathcal{E} - \sum_{S\in\mathcal{S}_{ID}^n} \int_S \langle\!\langle u_h \rangle\!\rangle : \{\!\{\bar{\tau}\}\!\} \, \mathrm{d}S + \sum_{S\in\mathcal{S}_D^n} \int_S g_D \otimes \bar{n} : \bar{\tau} \, \mathrm{d}S. \tag{5.17}$$

We sum now (5.17) over all space-time slabs. The last two terms on the right hand side of (5.17) are then replaced with the spatial part of the lifting operator $\mathcal{L}_{ID}$, defined in (5.9), to obtain:

$$\int_{\mathcal{E}^n} \bar{\mathcal{L}}_{ID}(\langle\!\langle u_h \rangle\!\rangle) : \bar{\tau} \, \mathrm{d}\mathcal{E} = -\sum_{S\in\mathcal{S}_{ID}^n} \int_S \langle\!\langle u_h \rangle\!\rangle : \{\!\{\bar{\tau}\}\!\} \, \mathrm{d}S + \sum_{S\in\mathcal{S}_D^n} \int_S g_D \otimes \bar{n} : \bar{\tau} \, \mathrm{d}S. \tag{5.18}$$

Using (5.18) into (5.17), we can express $\sigma_h \in \bar{\Sigma}_h^{(p_t,p_s)}$ as

$$\sigma_h = \overline{\nabla}_h u_h + \bar{\mathcal{L}}_{ID}(\langle\!\langle u_h \rangle\!\rangle), \quad \text{a.e. } \forall\, x \in \mathcal{E}. \tag{5.19}$$

This relation will be used in the next section to eliminate the auxiliary variable from the DG discretization.

5.4.2 Weak formulation for the primal variables

In this section we derive the weak formulation for (5.10b). First we multiply (5.10b) with arbitrary test functions $v \in V_h^{(p_t,p_s)}$ and integrate over the element $\mathcal{K}$, such that for all $v \in V_h^{(p_t,p_s)}$ the following relation is satisfied:

$$\int_\mathcal{K} (\nabla \cdot (u \otimes \mathbb{C})) \cdot v \, \mathrm{d}\mathcal{K} - \int_\mathcal{K} (\nu \overline{\nabla} \cdot \sigma) \cdot v \, \mathrm{d}\mathcal{K} + \int_\mathcal{K} (\overline{\nabla} \cdot \mathbb{I}_d \, p) \cdot v \, \mathrm{d}\mathcal{K} = \int_\mathcal{K} f \cdot v \, \mathrm{d}\mathcal{K}. \tag{5.20}$$

The functions u, σ, p are then substituted by their approximations $u_h \in V_h^{(p_t,p_s)}, \sigma_h \in \bar{\Sigma}_h^{(p_t,p_s)}, p_h \in \mathcal{Q}_h^{(p_t,p_s)}$, respectively. Next, we integrate by parts each term on the left hand side of (5.20). For the first term, integration by parts is with respect to

$x_0, \dots, x_d$, while for the second and third term the integration by parts is with respect to $x_1, \dots, x_d$. After summation over all elements $\mathcal{K} \in \mathcal{T}_h$, we have for all $v \in V_h^{(p_t,p_s)}$:

$$\begin{aligned} -\int_{\mathcal{E}} (u_h \otimes \mathbb{C}) : \nabla_h v \,\mathrm{d}\mathcal{E} + \sum_{\mathcal{K}\in\mathcal{T}_h} \int_{\partial\mathcal{K}} (\hat{u}_h^c \otimes \mathbb{C}) : v \otimes n \,\mathrm{d}\partial\mathcal{K} \\ + \int_{\mathcal{E}} \nu\sigma_h : \overline{\nabla}_h v \,\mathrm{d}\mathcal{E} - \sum_{\mathcal{K}\in\mathcal{T}_h} \int_{\mathcal{Q}_{\mathcal{K}}^n} \nu\hat{\sigma}_h : v \otimes \bar{n} \,\mathrm{d}\partial\mathcal{K} \\ - \int_{\mathcal{E}} \mathbb{I}_d\, p_h : \overline{\nabla}_h v \,\mathrm{d}\mathcal{E} + \sum_{\mathcal{K}\in\mathcal{T}_h} \int_{\mathcal{Q}_{\mathcal{K}}^n} \mathbb{I}_d\, \hat{p}_h : v \otimes \bar{n} \,\mathrm{d}\partial\mathcal{K} = \int_{\mathcal{E}} f \cdot v \,\mathrm{d}\mathcal{E}. \end{aligned} \tag{5.21}$$

Here we replaced u_h, σ_h, p_h at $\partial\mathcal{K}$ with the numerical fluxes $\hat{u}_h^c, \hat{\sigma}_h, \hat{p}_h$, to account for the multivalued traces at $\partial\mathcal{K}$.

The next step is to find appropriate choices for the numerical fluxes. To simplify the derivation, the terms on the left-hand side in (5.21) are split into three parts,

$$T_c = -\int_{\mathcal{E}} u_h \otimes \mathbb{C} : \nabla_h v \,\mathrm{d}\mathcal{E} + \sum_{\mathcal{K}\in\mathcal{T}_h} \int_{\partial\mathcal{K}} \hat{u}_h^c \otimes \mathbb{C} : v \otimes n \,\mathrm{d}\partial\mathcal{K}, \tag{5.22a}$$

$$T_d = \int_{\mathcal{E}} \nu\sigma_h : \overline{\nabla}_h v \,\mathrm{d}\mathcal{E} - \sum_{\mathcal{K}\in\mathcal{T}_h} \int_{\mathcal{Q}_{\mathcal{K}}^n} \nu\hat{\sigma}_h : v \otimes \bar{n} \,\mathrm{d}\partial\mathcal{K}, \tag{5.22b}$$

$$T_p = -\int_{\mathcal{E}} \mathbb{I}_d p_h : \overline{\nabla}_h v \,\mathrm{d}\mathcal{E} + \sum_{\mathcal{K}\in\mathcal{T}_h} \int_{\mathcal{Q}_{\mathcal{K}}^n} \mathbb{I}_d \hat{p}_h : v \otimes \bar{n} \,\mathrm{d}\partial\mathcal{K}, \tag{5.22c}$$

related to the convective, diffusive, and pressure terms in (5.21). We discuss the derivation for each term separately.

First, we consider the convective term T_c (5.22a), which includes the *convective flux* $\hat{u}_h^c$. We decompose each element boundary $\partial\mathcal{K}$ into disjoint sets:

$$\partial\mathcal{K} = \partial_+\mathcal{K} \cup (\partial_-\mathcal{K} \setminus \Gamma_m) \cup (\partial_-\mathcal{K} \cap \Gamma_{Dm}) \cup (\partial_-\mathcal{K} \cap \Omega_0), \tag{5.23}$$

where:

$$\partial_-\mathcal{K} := \{x \in \partial\mathcal{K} : \mathbb{C} \cdot n_{\mathcal{K}} < 0\}, \qquad \text{and} \quad \partial_+\mathcal{K} := \{x \in \partial\mathcal{K} : \mathbb{C} \cdot n_{\mathcal{K}} \geq 0\}.$$

To ensure continuity and causality of the flux, on each boundary part we replace $\hat{u}_h^c$ with the following choice:

$$\hat{u}_h^c = \begin{cases} u_h^- & \text{on } \partial_+\mathcal{K}, \\ u_h^+ & \text{on } \partial_-\mathcal{K} \setminus \Gamma_m, \\ g_D & \text{on } \partial_-\mathcal{K} \cap \Gamma_{Dm}, \\ u_0 & \text{on } \partial_-\mathcal{K} \cap \Omega_0. \end{cases} \tag{5.24}$$

The term T_c then can be written as

$$\begin{aligned} T_c = &- \int_{\mathcal{E}} u_h \otimes \mathbb{C} : \nabla_h v \, \mathrm{d}\mathcal{E} + \sum_{\mathcal{K}\in\mathcal{T}_h} \int_{\partial_+\mathcal{K}} u_h^- \otimes \mathbb{C} : v \otimes n \, \mathrm{d}\partial\mathcal{K} \\ &+ \sum_{\mathcal{K}\in\mathcal{T}_h} \int_{\partial_-\mathcal{K}\setminus\Gamma_m} u_h^+ \otimes \mathbb{C} : v \otimes n \, \mathrm{d}\partial\mathcal{K} + \sum_{S\in\cup_n\mathcal{S}_{Dm}^n} \int_S g_D \otimes \mathbb{C} : v \otimes n \, \mathrm{d}S \\ &- \int_{\Omega_0} u_0 \cdot v \, \mathrm{d}S. \end{aligned} \tag{5.25}$$

Next, we consider the diffusive term T_d (5.22b). We recall the identity (5.13). When applied to the second term in (5.22b), we obtain:

$$\sum_{\mathcal{K}\in\mathcal{T}_h} \int_{\mathcal{Q}_\mathcal{K}^n} \nu\hat{\sigma}_h : v \otimes \bar{n} \, \mathrm{d}\partial\mathcal{K} = \sum_{S\in\cup_n\mathcal{S}_{IDN}^n} \int_S \nu\{\!\{\hat{\sigma}_h\}\!\} : \langle\!\langle v \rangle\!\rangle \, \mathrm{d}S + \sum_{S\in\cup_n\mathcal{S}_I^n} \int_S \nu\langle\!\langle\hat{\sigma}_h\rangle\!\rangle \cdot \{\!\{v\}\!\} \, \mathrm{d}S. \tag{5.26}$$

For the numerical flux $\hat{\sigma}_h$ we make the same choice as in Section 4.4.2, but now applied to tensor functions:

$$\hat{\sigma}_h = \{\!\{\sigma_h\}\!\} \text{ on } \mathcal{S}_I^n, \quad \hat{\sigma}_h = \sigma_h \text{ on } \mathcal{S}_D^n \cup \mathcal{S}_N^n. \tag{5.27}$$

Substituting (5.27) into (5.26), we obtain:

$$\sum_{\mathcal{K}\in\mathcal{T}_h} \int_{\mathcal{Q}_\mathcal{K}^n} \nu\hat{\sigma}_h : v \otimes \bar{n} \, \mathrm{d}\partial\mathcal{K} = \sum_{S\in\cup_n\mathcal{S}_{IDN}^n} \int_S \nu\{\!\{\sigma_h\}\!\} : \langle\!\langle v \rangle\!\rangle \, \mathrm{d}S. \tag{5.28}$$

The second term in (5.22b) is then replaced by (5.28) and we substitute also σ_h with (5.19). Finally, using the boundary condition (5.4c) on $S \in \cup_n\mathcal{S}_N^n$, which are equal to $\overline{\nabla}_h u_h \cdot \bar{n} = g_N$, the term T_d becomes:

$$\begin{aligned} T_d = &\int_{\mathcal{E}} \nu\overline{\nabla}_h u_h : \overline{\nabla}_h v \, \mathrm{d}\mathcal{E} + \int_{\mathcal{E}} \nu\bar{\mathcal{L}}_{ID}(\langle\!\langle u_h \rangle\!\rangle) : \overline{\nabla}_h v \, \mathrm{d}\mathcal{E} \\ &- \sum_{S\in\cup_n\mathcal{S}_{ID}^n} \int_S \nu\{\!\{\overline{\nabla}_h u_h\}\!\} : \langle\!\langle v \rangle\!\rangle \, \mathrm{d}S - \sum_{S\in\cup_n\mathcal{S}_{ID}^n} \int_S \nu\{\!\{\bar{\mathcal{L}}_{ID}(\langle\!\langle u_h \rangle\!\rangle)\}\!\} : \langle\!\langle v \rangle\!\rangle \, \mathrm{d}S \\ &- \sum_{S\in\cup_n\mathcal{S}_N^n} \int_S \nu g_N \cdot v \, \mathrm{d}S. \end{aligned} \tag{5.29}$$

We can further evaluate the second and fourth term in (5.29), by extending the derivation given in Section 4.4.2 to vector functions. Using the lifting operator $\bar{\mathcal{L}}_{ID}$ defined in (5.18) with $\bar{\tau} = \overline{\nabla}_h v$ we have the relation

$$\begin{aligned} \int_{\mathcal{E}} \nu\bar{\mathcal{L}}_{ID}(\langle\!\langle u_h \rangle\!\rangle) : \overline{\nabla}_h v \, \mathrm{d}\mathcal{E} = &- \sum_{S\in\cup_n\mathcal{S}_{ID}^n} \int_S \nu\langle\!\langle u_h \rangle\!\rangle : \{\!\{\overline{\nabla}_h v\}\!\} \, \mathrm{d}S \\ &+ \sum_{S\in\cup_n\mathcal{S}_D^n} \int_S \nu g_D \otimes \bar{n} : \overline{\nabla}_h v \, \mathrm{d}S, \end{aligned} \tag{5.30}$$

and by considering only the spatial part of the lifting operators $\mathcal{L}, \mathcal{L}_{ID}$, defined in (5.6) and (5.9), we obtain

$$\sum_{S\in\cup_n\mathcal{S}^n_{ID}}\int_S \nu\{\!\{\bar{\mathcal{L}}_{ID}(\langle\!\langle u_h\rangle\!\rangle)\}\!\} : \langle\!\langle v\rangle\!\rangle \,\mathrm{d}S = -\int_{\mathcal{E}} \nu\bar{\mathcal{L}}(\langle\!\langle u_h\rangle\!\rangle) : \bar{\mathcal{L}}(\langle\!\langle v\rangle\!\rangle)\,\mathrm{d}\mathcal{E} + \int_{\mathcal{E}} \nu\bar{\mathcal{L}}(\mathcal{P}g_D\otimes\bar{n}) : \bar{\mathcal{L}}(\langle\!\langle v\rangle\!\rangle)\,\mathrm{d}\mathcal{E}. \quad (5.31)$$

In order to ensure that only contributions from neighboring elements occur in the discretization, which improves both computational efficiency and memory use, the contributions from the global lifting operator $\bar{\mathcal{L}}$ in (5.31) are replaced with the local lifting operator $\bar{\mathcal{L}}_S$ (defined in (5.5) and (5.7)), using the following simplifications

$$\int_{\mathcal{E}} \nu\bar{\mathcal{L}}(\langle\!\langle u_h\rangle\!\rangle) : \bar{\mathcal{L}}(\langle\!\langle v\rangle\!\rangle)\,\mathrm{d}\mathcal{E} \cong \sum_{S\in\cup_n\mathcal{S}^n_{ID}}\sum_{\mathcal{K}\in\mathcal{T}_h}\eta^u_{\mathcal{K}}\int_{\mathcal{K}} \nu\bar{\mathcal{L}}_S(\langle\!\langle u_h\rangle\!\rangle) : \bar{\mathcal{L}}_S(\langle\!\langle v\rangle\!\rangle)\,\mathrm{d}\mathcal{K}, \quad (5.32a)$$

$$\int_{\mathcal{E}} \nu\bar{\mathcal{L}}(\mathcal{P}g_D\otimes\bar{n}) : \bar{\mathcal{L}}(\langle\!\langle v\rangle\!\rangle)\,\mathrm{d}\mathcal{E} \cong \sum_{S\in\cup_n\mathcal{S}^n_{D}}\sum_{\mathcal{K}\in\mathcal{T}_h}\eta^u_{\mathcal{K}}\int_{\mathcal{K}} \nu\bar{\mathcal{L}}_S(\mathcal{P}g_D\otimes\bar{n}) : \bar{\mathcal{L}}_S(\langle\!\langle v\rangle\!\rangle)\,\mathrm{d}\mathcal{K}, \quad (5.32b)$$

with the parameter $\eta^u_{\mathcal{K}}$ a positive constant. Later in Section 5.5 we discuss the minimum value for $\eta^u_{\mathcal{K}}$ in order to have a stable method. Introducing the relations (5.30)-(5.32b) into (5.29), the term T_d can be written in its final form

$$\begin{aligned} T_d = &\int_{\mathcal{E}} \nu\overline{\nabla}_h u_h : \overline{\nabla}_h v\,\mathrm{d}\mathcal{E} \\ &- \sum_{S\in\cup_n\mathcal{S}^n_{ID}}\int_S \nu\langle\!\langle u_h\rangle\!\rangle : \{\!\{\overline{\nabla}_h v\}\!\}\,\mathrm{d}S - \sum_{S\in\cup_n\mathcal{S}^n_{ID}}\int_S \nu\{\!\{\overline{\nabla}_h u_h\}\!\} : \langle\!\langle v\rangle\!\rangle\,\mathrm{d}S \\ &+ \sum_{S\in\cup_n\mathcal{S}^n_{ID}}\sum_{\mathcal{K}\in\mathcal{T}_h}\eta^u_{\mathcal{K}}\int_{\mathcal{K}} \nu\bar{\mathcal{L}}_S(\langle\!\langle u_h\rangle\!\rangle) : \bar{\mathcal{L}}_S(\langle\!\langle v\rangle\!\rangle)\,\mathrm{d}\mathcal{K} + \sum_{S\in\cup_n\mathcal{S}^n_{D}}\int_S \nu g_D\otimes\bar{n} : \overline{\nabla}_h v\,\mathrm{d}S \\ &- \sum_{S\in\cup_n\mathcal{S}^n_{D}}\sum_{\mathcal{K}\in\mathcal{T}_h}\eta^u_{\mathcal{K}}\int_{\mathcal{K}} \nu\bar{\mathcal{L}}_S(\mathcal{P}g_D\otimes\bar{n}) : \bar{\mathcal{L}}_S(\langle\!\langle v\rangle\!\rangle)\,\mathrm{d}\mathcal{K} \\ &- \sum_{S\in\cup_n\mathcal{S}^n_{N}}\nu g_N\cdot v\,\mathrm{d}S. \end{aligned} \quad (5.33)$$

Finally, we consider the last term T_p given by (5.22c). For simplicity, this term is written as:

$$T_p = -\int_{\mathcal{E}} p_h\overline{\nabla}_h\cdot v\,\mathrm{d}\mathcal{E} + \sum_{\mathcal{K}\in\mathcal{T}_h}\int_{\mathcal{Q}^n_{\mathcal{K}}}\hat{p}_h v\cdot\bar{n}\,\mathrm{d}\partial\mathcal{K}. \quad (5.34)$$

We recall again the relation (5.13), this time for vectors v and scalars q:

$$\sum_{\mathcal{K}\in\mathcal{T}_h}\int_{\mathcal{Q}^n_{\mathcal{K}}} v\cdot\bar{n}q\,\mathrm{d}\partial\mathcal{K} = \sum_{S\in\cup_n\mathcal{S}^n_{IDN}}\int_S \{\!\{v\}\!\}\cdot\langle\!\langle q\rangle\!\rangle\,\mathrm{d}S + \sum_{S\in\cup_n\mathcal{S}^n_{I}}\int_S \langle\!\langle v\rangle\!\rangle\{\!\{q\}\!\}\,\mathrm{d}S. \quad (5.35)$$

After applying (5.35) to the second term in (5.34), we find that

$$T_p = -\int_{\mathcal{E}} p_h \overline{\nabla}_h \cdot v \, \mathrm{d}\mathcal{E} + \sum_{S \in \cup_n \mathcal{S}_{IDN}^n} \int_S \langle\!\langle \hat{p}_h \rangle\!\rangle \cdot \{\!\{ v \}\!\} \, \mathrm{d}S + \sum_{S \in \cup_n \mathcal{S}_I^n} \int_S \{\!\{ \hat{p}_h \}\!\} \langle\!\langle v \rangle\!\rangle \, \mathrm{d}S. \tag{5.36}$$

We make the following choices to replace $\hat{p}_h$ in (5.36):

$$\hat{p}_h = \{\!\{ p_h \}\!\} \text{ on } \mathcal{S}_I^n, \quad \hat{p}_h = p_h \text{ on } \mathcal{S}_D^n, \quad \hat{p}_h = p_N \text{ on } \mathcal{S}_N^n. \tag{5.37}$$

Note that on faces $S \in \cup_n \mathcal{S}_{ID}^n$, we follow a similar approach as described in [24, 54]. The condition on $S \in \cup_n \mathcal{S}_N^n$ is required to have a well-posed problem for certain flow conditions. Introducing the numerical fluxes (5.37) into (5.36), we obtain the final form of T_p:

$$T_p = -\int_{\mathcal{E}} p_h \overline{\nabla}_h \cdot v \, \mathrm{d}\mathcal{E} + \sum_{S \in \cup_n \mathcal{S}_{ID}^n} \int_S \{\!\{ p_h \}\!\} \langle\!\langle v \rangle\!\rangle \, \mathrm{d}S + \sum_{S \in \cup_n \mathcal{S}_N^n} \int_S p_N v \cdot \bar{n} \, \mathrm{d}S. \tag{5.38}$$

Introducing all terms in (5.25), (5.33) and (5.38) into (5.21), we now obtain the weak formulation for the momentum equations in the space-time DG discretization of the Oseen equations (5.3):

Find $(u_h, p_h) \in V_h^{(p_t,p_s)} \times \mathcal{Q}_h^{(p_t,p_s)}$, such that the following relation is satisfied for all $(v, q) \in V_h^{(p_t,p_s)} \times \mathcal{Q}_h^{(p_t,p_s)}$:

$$\mathcal{O}_h(u_h, v; w) + \mathcal{A}_h(u_h, v) + \mathcal{B}_h(p_h, v) = N_h(v) + F_h(v) + G_h(v). \tag{5.39}$$

Here, the forms $\mathcal{O}_h : V_h^{(p_t,p_s)} \times V_h^{(p_t,p_s)} \times \mathcal{J}_h \to \mathbb{R}$, $\mathcal{A}_h : V_h^{(p_t,p_s)} \times V_h^{(p_t,p_s)} \to \mathbb{R}$, and $\mathcal{B}_h : V_h^{(p_t,p_s)} \times \mathcal{Q}_h^{(p_t,p_s)} \to \mathbb{R}$ are defined as:

$$\mathcal{O}_h(u_h, v; w) = -\int_{\mathcal{E}} u_h \otimes \mathbb{C} : \nabla_h v \, \mathrm{d}\mathcal{E} + \sum_{\mathcal{K} \in \mathcal{T}_h} \int_{\partial_+ \mathcal{K}} u_h^- \otimes \mathbb{C} : v \otimes n \, \mathrm{d}\partial\mathcal{K} + \sum_{\mathcal{K} \in \mathcal{T}_h} \int_{\partial_- \mathcal{K} \setminus \Gamma_m} u_h^+ \otimes \mathbb{C} : v \otimes n \, \mathrm{d}\partial\mathcal{K}, \tag{5.40}$$

$$\mathcal{A}_h(u_h, v) = \int_{\mathcal{E}} \nu \overline{\nabla}_h u_h : \overline{\nabla}_h v \, \mathrm{d}\mathcal{E} - \sum_{S \in \cup_n \mathcal{S}_{ID}^n} \int_S \nu \langle\!\langle\!\langle u_h \rangle\!\rangle\!\rangle : \{\!\{ \overline{\nabla}_h v \}\!\} \, \mathrm{d}S - \sum_{S \in \cup_n \mathcal{S}_{ID}^n} \int_S \nu \{\!\{ \overline{\nabla}_h u_h \}\!\} : \langle\!\langle\!\langle v \rangle\!\rangle\!\rangle \, \mathrm{d}S + \sum_{S \in \cup_n \mathcal{S}_{ID}^n} \sum_{\mathcal{K} \in \mathcal{T}_h} \eta_{\mathcal{K}}^u \int_{\mathcal{K}} \nu \bar{\mathcal{L}}_S(\langle\!\langle\!\langle u_h \rangle\!\rangle\!\rangle) : \bar{\mathcal{L}}_S(\langle\!\langle\!\langle v \rangle\!\rangle\!\rangle) \, \mathrm{d}\mathcal{K}, \tag{5.41}$$

$$\mathcal{B}_h(p_h, v) = -\int_{\mathcal{E}} p_h \overline{\nabla}_h \cdot v \, \mathrm{d}\mathcal{E} + \sum_{S \in \cup_n \mathcal{S}_{ID}^n} \int_S \{\!\{ p_h \}\!\} \langle\!\langle v \rangle\!\rangle \, \mathrm{d}S, \tag{5.42}$$

and the linear forms $N_h : V_h^{(p_t,p_s)} \to \mathbb{R}$, $F_h : V_h^{(p_t,p_s)} \to \mathbb{R}$, $G_h : V_h^{(p_t,p_s)} \to \mathbb{R}$ as:

$$N_h(v) = -\sum_{S\in\cup_n \mathcal{S}_{Dm}^n} \int_S g_D \otimes \mathbb{C} : v \otimes n \, \mathrm{d}S + \int_{\Omega_0} u_0 \cdot v \, \mathrm{d}S, \tag{5.43}$$

$$\begin{aligned} F_h(v) = &-\sum_{S\in\cup_n \mathcal{S}_D^n} \int_S \nu g_D \otimes \bar{n} : \overline{\nabla}_h v \, \mathrm{d}S \\ &+ \sum_{S\in\cup_n \mathcal{S}_D^n} \sum_{\mathcal{K}\in\mathcal{T}_h} \eta_{\mathcal{K}}^u \int_{\mathcal{K}} \nu \bar{\mathcal{L}}_S(\mathcal{P} g_D \otimes \bar{n}) : \bar{\mathcal{L}}_S(\langle\!\langle v \rangle\!\rangle) \, \mathrm{d}\mathcal{K} \\ &+ \sum_{S\in\cup_n \mathcal{S}_N^n} \int_S \nu g_N \cdot v \, \mathrm{d}S, \end{aligned} \tag{5.44}$$

$$G_h(v) = \int_{\mathcal{E}} f \cdot v \, \mathrm{d}\mathcal{E} - \sum_{S\in\cup_n \mathcal{S}_N^n} \int_S p_N v \cdot \bar{n} \, \mathrm{d}S. \tag{5.45}$$

5.4.3 Weak formulation for the continuity equation

In this section we derive the weak formulation for the continuity equation (5.10c). First we multiply (5.10c) with an arbitrary function $q \in \mathcal{Q}_h^{(p_t,p_s)}$ and integrate over element $\mathcal{K}$ to obtain:

$$\int_{\mathcal{K}} (\overline{\nabla} \cdot u) \, q \, \mathrm{d}\mathcal{K} = 0, \qquad \forall q \in \mathcal{Q}_h^{(p_t,p_s)}. \tag{5.46}$$

Next, we substitute u with $u_h \in V_h^{(p_t,p_s)}$ and integrate by parts twice with respect to $x_1, \ldots, x_d$. After summation over all elements $\mathcal{K} \in \mathcal{T}_h$ we obtain:

$$\int_{\mathcal{E}} (\overline{\nabla}_h \cdot u_h) q \, \mathrm{d}\mathcal{E} + \sum_{\mathcal{K}\in\mathcal{T}_h} \int_{\mathcal{Q}_{\mathcal{K}}^n} (\hat{u}_h^p - u_h) \cdot \bar{n} q \, \mathrm{d}\partial\mathcal{K} = 0, \quad \forall q \in \mathcal{Q}_h^{(p_t,p_s)}, \tag{5.47}$$

with $\hat{u}_h^p$ the numerical flux that has to be introduced to account for the multivalued traces on $\mathcal{Q}_{\mathcal{K}}^n$. Using (5.35), we can write (5.47) as

$$\int_{\mathcal{E}} \overline{\nabla}_h \cdot u_h \, q \, \mathrm{d}\mathcal{E} + \sum_{S\in\cup_n \mathcal{S}_{IDN}^n} \int_S \{\!\{ \hat{u}_h^p - u_h \}\!\} \cdot \langle\!\langle q \rangle\!\rangle \, \mathrm{d}S + \sum_{S\in\cup_n \mathcal{S}_I^n} \int_S \langle\!\langle \hat{u}_h^p - u_h \rangle\!\rangle \{\!\{ q \}\!\} \, \mathrm{d}S = 0. \tag{5.48}$$

The next step is to find appropriate numerical flux $\hat{u}_h^p$. Two approaches are considered for the numerical flux $\hat{u}_h^p$ on $S \in \cup_n \mathcal{S}_I^n$:

$$(1.) \quad \hat{u}_h^p = \{\!\{ u_h \}\!\} + \gamma \langle\!\langle p_h \rangle\!\rangle, \qquad (2.) \quad \hat{u}_h^p = \{\!\{ u_h \}\!\} + \alpha \{\!\{ \bar{\mathcal{L}}_S(\langle\!\langle p_h \rangle\!\rangle) \}\!\}, \tag{5.49}$$

with $\gamma, \alpha > 0$ and the lifting operator $\bar{\mathcal{L}}_S$ defined in Section 5.3.3, only now applied to scalar functions. The first approach is introduced in [22, 23], while the second

approach is similar to the technique used in [30]. The term containing the pressure in each approach is called the pressure stabilization. This stabilization has a similar form as the local lifting operators discussed in Section 3.4. On boundary faces we choose:

$$\hat{u}_h^p = g_D \text{ on } \mathcal{S}_D^n, \quad \hat{u}_h^p = u_h \text{ on } \mathcal{S}_N^n. \tag{5.50}$$

Introducing the numerical fluxes (5.49)-(5.50) into (5.48), we obtain the final form of the weak formulation for the continuity equation (5.10c):

Find $(u_h, p_h) \in V_h^{(p_t,p_s)} \times \mathcal{Q}_h^{(p_t,p_s)}$, such that the following relation is satisfied for all $q \in \mathcal{Q}_h^{(p_t,p_s)}$:

$$-\mathcal{B}_h(q, u_h) + \mathcal{C}_h^{(i)}(p_h, q) = H_h(q), \tag{5.51}$$

with $\mathcal{B}_h$ defined in (5.42), while $\mathcal{C}_h^{(i)} : \mathcal{Q}_h^{(p_t,p_s)} \times \mathcal{Q}_h^{(p_t,p_s)} \to \mathbb{R}$ and $H_h : \mathcal{Q}_h^{(p_t,p_s)} \to \mathbb{R}$ are defined as:

$$\mathcal{C}_h^{(1)}(p_h, q) = \sum_{S \in \cup_n \mathcal{S}_I^n} \int_S \gamma \langle\!\langle p_h \rangle\!\rangle \cdot \langle\!\langle q \rangle\!\rangle \, \mathrm{d}S, \tag{5.52}$$

$$\mathcal{C}_h^{(2)}(p_h, q) = \sum_{S \in \cup_n \mathcal{S}_I^n} \int_S \alpha \{\!\{ \bar{\mathcal{L}}_S(\langle\!\langle p_h \rangle\!\rangle) \}\!\} \cdot \langle\!\langle q \rangle\!\rangle \, \mathrm{d}S, \tag{5.53}$$

$$H_h(q) = -\sum_{S \in \cup_n \mathcal{S}_D^n} \int_S g_D \cdot \bar{n} q \, \mathrm{d}S. \tag{5.54}$$

The space-time DG weak formulation for the Oseen equations (5.10) can now be stated as:

Find $(u_h, p_h) \in V_h^{(p_t,p_s)} \times \mathcal{Q}_h^{(p_t,p_s)}$, such that for all $(v, q) \in V_h^{(p_t,p_s)} \times \mathcal{Q}_h^{(p_t,p_s)}$ the following relation is satisfied:

$$\begin{array}{rcccccccccc} \mathcal{O}_h(u_h, v; w) & + & \mathcal{A}_h(u_h, v) & + & \mathcal{B}_h(p_h, v) & = & N_h(v) & + & F_h(v) & + & G_h(v), \\ & - & \mathcal{B}_h(q, u_h) & + & \mathcal{C}_h^{(i)}(p_h, q) & = & H_h(q). & & & & \end{array} \tag{5.55}$$

5.5 Stability analysis

In this section we discuss the stability analysis of the bilinear forms in the space-time DG weak formulation (5.55).

The analysis of the weak formulation (5.55) is considerably simplified by the introduction of the following DG norm for vector functions given in Definition 5.1 and the boundary norm stated in Definition 5.2.

Definition 5.1 The DG norm $|||\cdot|||_{\mathrm{DG}}$ corresponding to the bilinear form (5.41) can be defined on $H^{(0,1)}(\mathcal{E}) + V_h^{(p_t,p_s)}$, with $H^{(0,1)}(\mathcal{E})$ the anisotropic Sobolev space defined in Section (4.3.2), as:

$$|||v|||_{\mathrm{DG}}^2 = \sum_{\mathcal{K} \in \mathcal{T}_h} \|v\|_{0,\mathcal{K}}^2 + \sum_{\mathcal{K} \in \mathcal{T}_h} \|\overline{\nabla}_h v\|_{0,\mathcal{K}}^2 + \sum_{S \in \cup_n \mathcal{S}_{ID}^n} \sum_{\mathcal{K} \in \mathcal{T}_h} \|\bar{\mathcal{L}}_S(\langle\!\langle v \rangle\!\rangle)\|_{0,\mathcal{K}}^2.$$

Definition 5.2 The boundary norm $\|\cdot\|_{\mathbb{C},S}$, with $S \subset \partial\mathcal{K}$, related to the vector $\mathbb{C} \in \mathbb{R}^{d+1}$ is defined as

$$(v,w)_{\mathbb{C},S} = \int_S |\mathbb{C}\cdot n| v\cdot w \ \mathrm{d}\partial\mathcal{K}.$$

A seminorm is defined on $\mathcal{Q}_h^{(p_t,p_s)}$ which is related to the bilinear form $\mathcal{C}_h^{(1)}$:

$$|q|^2_{\mathcal{S}_I^n} = \sum_{S\in\cup_n\mathcal{S}_I^n} \int_S \gamma |\langle\!\langle q \rangle\!\rangle|^2 \ \mathrm{d}S. \tag{5.56}$$

The first result in this section establishes the continuity properties of the bilinear form $\mathcal{A}_h$.

Lemma 5.3 *Let $\nu_m = \max_{x\in\mathcal{E}} \nu(x)$, $\eta_m^u = \max_{\mathcal{K}\in\mathcal{T}_h} \eta_{\mathcal{K}}^u$, and N_f be the number of faces of each element $\mathcal{K}\in\mathcal{T}_h$. Then there exists a constant $\alpha_{\mathcal{A}} = \eta_m^u + 2\sqrt{N_f}+1 > 0$, independent of the mesh size $h = \max_{\mathcal{K}\in\mathcal{T}_h} h_{\mathcal{K}}$, such that*

$$|\mathcal{A}_h(u_h,v)| \le \nu_m \alpha_{\mathcal{A}} |||u_h|||_{\mathrm{DG}} \ |||v|||_{\mathrm{DG}}, \quad \forall u_h, v \in V_h^{(p_t,p_s)}.$$

Proof . We consider bilinear form $\mathcal{A}_h$ in the form

$$\begin{aligned}\mathcal{A}_h(u_h,v) = &\sum_{\mathcal{K}\in\mathcal{T}_h}\int_{\mathcal{K}} \nu\overline{\nabla}_h u_h : \overline{\nabla}_h v \ \mathrm{d}\mathcal{K} - \sum_{\mathcal{K}\in\mathcal{T}_h}\int_{\mathcal{K}} \nu\overline{\nabla}_h u_h : \bar{\mathcal{L}}(\langle\!\langle v\rangle\!\rangle) \ \mathrm{d}\mathcal{K}\\ &- \sum_{\mathcal{K}\in\mathcal{T}_h}\int_{\mathcal{K}} \nu\bar{\mathcal{L}}(\langle\!\langle u_h\rangle\!\rangle) : \overline{\nabla}_h v \ \mathrm{d}\mathcal{K}\\ &+ \sum_{S\in\cup_n\mathcal{S}_{ID}^n}\sum_{\mathcal{K}\in\mathcal{T}_h} \eta_{\mathcal{K}}^u \int_{\mathcal{K}} \nu\bar{\mathcal{L}}_S(\langle\!\langle u_h\rangle\!\rangle) : \bar{\mathcal{L}}_S(\langle\!\langle v\rangle\!\rangle) \ \mathrm{d}\mathcal{K}.\end{aligned} \tag{5.57}$$

As a consequence of (5.6), we have

$$\|\bar{\mathcal{L}}(\langle\!\langle v\rangle\!\rangle)\|^2_{0,\mathcal{K}} \le N_f \sum_{S\in\cup_n\mathcal{S}_{ID}^n} \|\bar{\mathcal{L}}_S(\langle\!\langle v\rangle\!\rangle)\|^2_{0,\mathcal{K}}, \tag{5.58}$$

with N_f the number of faces of each element $\mathcal{K}\in\mathcal{T}_h$. Application of Schwarz' inequality on each term and the use of inequality (5.58) yields:

$$|\mathcal{A}_h(u_h,v)| \le \nu_m\alpha_{\mathcal{A}} |||u_h|||_{\mathrm{DG}} \ |||v|||_{\mathrm{DG}}, \tag{5.59}$$

with $\nu_m = \max_{x\in\mathcal{E}}\nu(x)$, $\eta_m^u = \max_{\mathcal{K}\in\mathcal{T}_h}\eta_{\mathcal{K}}^u$, and $\alpha_{\mathcal{A}} = \eta_m^u + 2\sqrt{N_f}+1$. □

The next result establishes the coercivity of $\mathcal{A}_h$.

Lemma 5.4 *Let $\nu_0 = \min_{x\in\mathcal{E}}\nu(x)$, $\eta_0^u = \min_{\mathcal{K}\in\mathcal{T}_h}\eta_{\mathcal{K}}^u$, and N_f be the number of faces of each element $\mathcal{K}\in\mathcal{T}_h$. Then there exists a constant $\bar{\beta}_{\mathcal{A}} > 0$, independent of the mesh size $h = \max_{\mathcal{K}\in\mathcal{T}_h} h_{\mathcal{K}}$, such that*

$$\mathcal{A}_h(v,v) \ge \nu_0\bar{\beta}_{\mathcal{A}} |||v|||^2_{\mathrm{DG}}, \quad \forall v \in V_h^{(p_t,p_s)},$$

with $\bar{\beta}_{\mathcal{A}} = \frac{\beta_{\mathcal{A}}}{2}\min(1, 1/C_p^2)$*, where* $\beta_{\mathcal{A}} = \min(1-\epsilon, \eta_0^u - \frac{N_f}{\epsilon})$ *for* $\epsilon \in (\frac{N_f}{\eta_0^u}, 1)$*, and* C_p^2 *the coefficient in the discrete Poincaré inequality ([3], Lemma 2.1).*

Proof . We start with replacing u_h in (5.57) with v:

$$\mathcal{A}_h(v,v) = \sum_{\mathcal{K}\in\mathcal{T}_h}\int_{\mathcal{K}} \nu\overline{\nabla}_h v : \overline{\nabla}_h v \,\mathrm{d}\mathcal{K} - 2\sum_{\mathcal{K}\in\mathcal{T}_h}\int_{\mathcal{K}} \nu\overline{\nabla}_h v : \bar{\mathcal{L}}(\langle\!\langle v\rangle\!\rangle)\,\mathrm{d}\mathcal{K} + \sum_{S\in\cup_n\mathcal{S}_{ID}^n}\sum_{\mathcal{K}\in\mathcal{T}_h}\eta_{\mathcal{K}}^u\int_{\mathcal{K}}\nu\bar{\mathcal{L}}_S(\langle\!\langle v\rangle\!\rangle) : \bar{\mathcal{L}}_S(\langle\!\langle v\rangle\!\rangle)\,\mathrm{d}\mathcal{K}. \tag{5.60}$$

Using the Schwarz and arithmetic-geometric mean inequalities we have the inequality:

$$2\int_{\mathcal{K}}\overline{\nabla}_h v : \bar{\mathcal{L}}(\langle\!\langle v\rangle\!\rangle)\,\mathrm{d}\mathcal{K} \le \epsilon\|\overline{\nabla}_h v\|_{0,\mathcal{K}}^2 + \frac{1}{\epsilon}\|\bar{\mathcal{L}}(\langle\!\langle v\rangle\!\rangle)\|_{0,\mathcal{K}}^2, \tag{5.61}$$

with $\epsilon > 0$. Introducing inequalities (5.58) and (5.61) into (5.60), we deduce

$$\mathcal{A}_h(v,v) \ge \nu_0(1-\epsilon)\sum_{\mathcal{K}\in\mathcal{T}_h}\|\overline{\nabla}_h v\|_{0,\mathcal{K}}^2 + \nu_0\Big(\eta_0 - \frac{N_f}{\epsilon}\Big)\sum_{S\in\cup_n\mathcal{S}_{ID}^n}\sum_{\mathcal{K}\in\mathcal{T}_h}\|\bar{\mathcal{L}}_S(\langle\!\langle v\rangle\!\rangle)\|_{0,\mathcal{K}}^2, \tag{5.62}$$

with $\nu_0 = \min_{x\in\mathcal{E}}\nu(x)$ and $\eta_0^u = \min_{\mathcal{K}\in\mathcal{T}_h}\eta_{\mathcal{K}}^u$. If we take the parameters $\eta_0^u > N_f$ and $\epsilon \in (\frac{N_f}{\eta_0^u}, 1)$, then for $0 < \beta_{\mathcal{A}} = \min(1-\epsilon, \eta_0^u - \frac{N_f}{\epsilon})$, we obtain

$$\mathcal{A}_h(v,v) \ge \nu_0\beta_{\mathcal{A}}\sum_{\mathcal{K}\in\mathcal{T}_h}\|\overline{\nabla}_h v\|_{0,\mathcal{K}}^2 + \nu_0\beta_{\mathcal{A}}\sum_{S\in\cup_n\mathcal{S}_{ID}^n}\sum_{\mathcal{K}\in\mathcal{T}_h}\|\bar{\mathcal{L}}_S(\langle\!\langle v\rangle\!\rangle)\|_{0,\mathcal{K}}^2. \tag{5.63}$$

Next, we recall the discrete inequality (4.40) in Section 4.5.1, but applied to vector functions:

$$\|v\|_{0,\mathcal{E}} \le C_p\Big(\sum_{\mathcal{K}\in\mathcal{T}_h}\|\overline{\nabla}_h v\|_{0,\mathcal{K}}^2 + \sum_{S\in\cup_n\mathcal{S}_{ID}^n}\sum_{\mathcal{K}\in\mathcal{T}_h}\|\bar{\mathcal{L}}_S(\langle\!\langle v\rangle\!\rangle)\|_{0,\mathcal{K}}^2\Big)^{1/2}. \tag{5.64}$$

Using (5.64) in (5.63), we then obtain:

$$\mathcal{A}_h(v,v) \ge \nu_0\Big(\frac{\beta_{\mathcal{A}}}{2C_p^2}\sum_{\mathcal{K}\in\mathcal{T}_h}\|v\|_{0,\mathcal{K}}^2 + \frac{\beta_{\mathcal{A}}}{2}\sum_{\mathcal{K}\in\mathcal{T}_h}\|\overline{\nabla}_h v\|_{0,\mathcal{K}}^2 + \frac{\beta_{\mathcal{A}}}{2}\sum_{S\in\cup_n\mathcal{S}_{ID}^n}\sum_{\mathcal{K}\in\mathcal{T}_h}\|\bar{\mathcal{L}}_S(\langle\!\langle v\rangle\!\rangle)\|_{0,\mathcal{K}}^2\Big). \tag{5.65}$$

Choosing $\bar{\beta}_{\mathcal{A}} = \frac{\beta_{\mathcal{A}}}{2}\min(1, 1/C_p^2)$ completes the proof. □

The next lemma shows that for $w \in \mathcal{J}_h$ the trilinear form $\mathcal{O}_h$ (5.40) satisfies a stability relation in the boundary norm.

Lemma 5.5 *For $w \in \mathcal{J}_h$ and $v \in V_h^{(p_t,p_s)}$, the trilinear form $\mathcal{O}_h$ (5.40) satisfies the following stability relation*

$$\begin{aligned}\mathcal{O}_h(v,v;w) =& \frac{1}{2}\sum_{\mathcal{K}\in\mathcal{T}_h} \|v^-\|^2_{\mathbb{C},\partial_+\mathcal{K}\cap\Gamma_p} + \frac{1}{2}\sum_{\mathcal{K}\in\mathcal{T}_h} \|v^-\|^2_{\mathbb{C},\partial_-\mathcal{K}\cap\Gamma_m} \\ &+ \frac{1}{2}\sum_{\mathcal{K}\in\mathcal{T}_h} \|v^- - v^+\|^2_{\mathbb{C},\partial_-\mathcal{K}\setminus\Gamma_m}, \quad \forall v \in V_h^{(p_t,p_s)}.\end{aligned}$$

Proof . First we replace u_h in (5.40) with v:

$$\begin{aligned}\mathcal{O}_h(v,v;w) =& -\int_{\mathcal{E}} v\otimes\mathbb{C} : \nabla_h v \,\mathrm{d}\mathcal{E} + \sum_{\mathcal{K}\in\mathcal{T}_h}\int_{\partial_+\mathcal{K}} (\mathbb{C}\cdot n)(v^-\cdot v^-)\,\mathrm{d}\partial\mathcal{K} \\ &+ \sum_{\mathcal{K}\in\mathcal{T}_h}\int_{\partial_-\mathcal{K}\setminus\Gamma_m} (\mathbb{C}\cdot n)(v^+\cdot v^-)\,\mathrm{d}\partial\mathcal{K}. \end{aligned} \tag{5.66}$$

Using the following relation

$$-v\otimes\mathbb{C} : \nabla_h v = \frac{1}{2}(\nabla_h\cdot\mathbb{C})(v\cdot v) - \frac{1}{2}\nabla_h\cdot((v\otimes\mathbb{C})\cdot v),$$

and applying the Gauss' theorem, the first term in (5.66) can be written for each element $\mathcal{K}\in\mathcal{T}_h$ as

$$-\int_{\mathcal{K}} v\otimes\mathbb{C} : \nabla_h v \,\mathrm{d}\mathcal{K} = \frac{1}{2}\int_{\mathcal{K}} (\nabla_h\cdot\mathbb{C})(v\cdot v)\,\mathrm{d}\mathcal{K} - \frac{1}{2}\int_{\partial\mathcal{K}} (\mathbb{C}\cdot n)(v^-\cdot v^-)\,\mathrm{d}\partial\mathcal{K}. \tag{5.67}$$

Substituting (5.67) into (5.66) yields:

$$\begin{aligned}\mathcal{O}_h(v,v;w) =& \frac{1}{2}\int_{\mathcal{E}} (\nabla_h\cdot\mathbb{C})(v\cdot v)\,\mathrm{d}\mathcal{E} + \frac{1}{2}\sum_{\mathcal{K}\in\mathcal{T}_h}\int_{\partial_+\mathcal{K}\cap\Gamma_p} (\mathbb{C}\cdot n)(v^-\cdot v^-)\,\mathrm{d}\partial\mathcal{K} \\ &+ \frac{1}{2}\sum_{\mathcal{K}\in\mathcal{T}_h}\int_{\partial_+\mathcal{K}\setminus\Gamma_p} (\mathbb{C}\cdot n)(v^-\cdot v^-)\,\mathrm{d}\partial\mathcal{K} \\ &- \frac{1}{2}\sum_{\mathcal{K}\in\mathcal{T}_h}\int_{\partial_-\mathcal{K}\cap\Gamma_m} (\mathbb{C}\cdot n)(v^-\cdot v^-)\,\mathrm{d}\partial\mathcal{K} \\ &+ \frac{1}{2}\sum_{\mathcal{K}\in\mathcal{T}_h}\int_{\partial_-\mathcal{K}\setminus\Gamma_m} (\mathbb{C}\cdot n)(v^-\cdot v^-)\,\mathrm{d}\partial\mathcal{K} \\ &- \sum_{\mathcal{K}\in\mathcal{T}_h}\int_{\partial_-\mathcal{K}\setminus\Gamma_m} (\mathbb{C}\cdot n)(v^- - v^+)\cdot v^-\,\mathrm{d}\partial\mathcal{K}. \end{aligned} \tag{5.68}$$

In the summation over all elements each interior face occurs twice with a boundary flux of opposite sign, hence

$$\sum_{\mathcal{K}\in\mathcal{T}_h}\int_{\partial_+\mathcal{K}\setminus\Gamma_p} (\mathbb{C}\cdot n)(v^-\cdot v^-)\,\mathrm{d}\partial\mathcal{K} + \sum_{\mathcal{K}\in\mathcal{T}_h}\int_{\partial_-\mathcal{K}\setminus\Gamma_m} (\mathbb{C}\cdot n)(v^+\cdot v^+)\,\mathrm{d}\partial\mathcal{K} = 0. \tag{5.69}$$

Introducing (5.69) into (5.68) and using the following relation

$$(v^- - v^+)\cdot v^- = \frac{1}{2}(v^-\cdot v^-) + \frac{1}{2}(v^- - v^+)\cdot(v^- - v^+) - \frac{1}{2}(v^+\cdot v^+), \tag{5.70}$$

the trilinear form $\mathcal{O}_h(v,v;w)$ can be written as

$$\begin{aligned}\mathcal{O}_h(v,v;w) = &\frac{1}{2}\int_{\mathcal{E}}(\nabla_h\cdot\mathbb{C})(v\cdot v)\ \mathrm{d}\mathcal{E} + \frac{1}{2}\sum_{\mathcal{K}\in\mathcal{T}_h}\int_{\partial_+\mathcal{K}\cap\Gamma_p}(\mathbb{C}\cdot n)(v^-\cdot v^-)\ \mathrm{d}\partial\mathcal{K}\\ &-\frac{1}{2}\sum_{\mathcal{K}\in\mathcal{T}_h}\int_{\partial_-\mathcal{K}\cap\Gamma_m}(\mathbb{C}\cdot n)(v^-\cdot v^-)\ \mathrm{d}\partial\mathcal{K}\\ &-\frac{1}{2}\sum_{\mathcal{K}\in\mathcal{T}_h}\int_{\partial_-\mathcal{K}\setminus\Gamma_m}(\mathbb{C}\cdot n)(v^- - v^+)\cdot(v^- - v^+)\ \mathrm{d}\partial\mathcal{K}.\end{aligned} \tag{5.71}$$

Using the boundary norm and the fact that $w\in\mathcal{J}_h$, we then obtain the stability property of $\mathcal{O}_h$ given in Lemma 5.5. □

In the next Lemma, we show that the bilinear form $\mathcal{B}_h$ (5.42) is continuous.

Lemma 5.6 *Let N_f be the number of faces of each element $\mathcal{K}\in\mathcal{T}_h$. Then there exists a constant $\alpha_{\mathcal{B}} = \sqrt{N_f}+1>0$, independent of the mesh size $h=\max_{\mathcal{K}\in\mathcal{T}_h}h_{\mathcal{K}}$, such that*

$$|\mathcal{B}_h(q,v)| \le \alpha_{\mathcal{B}}\|q\|_{0,0,\mathcal{T}_h}\,|||v|||_{\mathrm{DG}},\quad \forall (q,v)\in\mathcal{Q}_h^{(p_t,p_s)}\times V_h^{(p_t,p_s)},$$

with $\|\cdot\|_{0,0,\mathcal{T}_h}$ the broken Sobolev space norm defined in Section (4.3.2).

Proof . First, we consider the bilinear form $\mathcal{B}_h(q,v)$ in the form

$$\mathcal{B}_h(q,v) = -\sum_{\mathcal{K}\in\mathcal{T}_h}\int_{\mathcal{K}} I_d q : \overline{\nabla}_h v\ \mathrm{d}\mathcal{K} + \sum_{\mathcal{K}\in\mathcal{T}_h}\int_{\mathcal{K}} I_d q : \bar{\mathcal{L}}(\langle\!\langle v\rangle\!\rangle)\ \mathrm{d}\mathcal{K}. \tag{5.72}$$

Application of Schwarz' inequality on each term and inequality (5.58) yield:

$$|\mathcal{B}_h(q,v)| \le \|q\|_{0,0,\mathcal{T}_h}\,|||v|||_{\mathrm{DG}} + \sqrt{N_f}\|q\|_{0,0,\mathcal{T}_h}\,|||v|||_{\mathrm{DG}}, \tag{5.73}$$

with $\|\cdot\|_{0,0,\mathcal{T}_h}$ the broken Sobolev norm defined in Section 4.3.2. Choosing $\alpha_{\mathcal{B}} = \sqrt{N_f}+1$ completes the proof. □

For the stability proof we introduce the inf-sup condition for the Stokes equations in the domain Ω_t, for a proof see [32, 54], as follows:

$$\inf_{0\neq q\in L^2(\Omega_t)/\mathbb{R}}\ \sup_{0\neq v\in(H_0^1(\Omega_t))^d}\frac{-\int_{\Omega_t} q\overline{\nabla}_h\cdot v\ \mathrm{d}\Omega}{|v|_{1,\Omega_t}\|q\|_{0,\Omega_t}} \ge C_{\Omega_t} > 0, \tag{5.74}$$

with the constant C_{Ω_t} depending only on Ω_t. If we fix now $q\in\mathcal{Q}_h^{(p_t,p_s)}/\mathbb{R}$, then the inf-sup condition (5.74) guarantees that there exists a $w(t)\in(H_0^1(\Omega_t))^d$, with $t\in[0,T]$, such that:

$$-\int_{\Omega_t} q\overline{\nabla}_h\cdot w(t)\ \mathrm{d}\Omega = \|q\|_{0,\Omega_t}^2,\qquad \text{with}\quad |w(t)|_{1,\Omega_t}\le C_{\Omega_t}^{-1}\|q\|_{0,\Omega_t}, \tag{5.75}$$

where we use the Poincaré inequality to change $|w(t)|_{1,\Omega_t}$ into $\|w(t)\|_{1,\Omega_t}$. Integrating in time from $t = 0$ to $t = T$, then results in the relation:

$$-\int_{\mathcal{E}} q\overline{\nabla}_h \cdot w \, \mathrm{d}\mathcal{E} = \|q\|^2_{0,0,\mathcal{E}}, \qquad \text{with} \quad \|w\|_{0,1,\mathcal{E}} \leq C_{\mathcal{E}}^{-1}\|q\|_{0,0,\mathcal{E}}. \tag{5.76}$$

In the next lemma, we establish an inf-sup condition for the bilinear form $\mathcal{B}_h(\cdot,\cdot)$, defined in (5.42).

Lemma 5.7 *The following inf-sup condition holds for* $(q, v) \in \mathcal{Q}_h^{(p_t,p_s)} \times V_h^{(p_t,p_s)}$*:*

$$\mathcal{B}_h(q, v) \geq C\|q\|^2_{0,0,\mathcal{E}}\Big(1 - \frac{|q|_{\mathcal{S}_I^n}}{\|q\|_{0,0,\mathcal{E}}}\Big), \ \forall q \in \mathcal{Q}_h^{(p_t,p_s)}, \tag{5.77}$$

with $C > 0$ *solely depending on* $C_{\mathcal{E}}^{-1}$ *and the interpolation bounds.*

Proof . To prove the inf-sup condition, we follow similar steps as in [55]. First, we fix $q \in \mathcal{Q}_h^{(p_t,p_s)}$. Then we define the L^2-projection $\mathcal{P}_K : (L^2(K(t)))^d \to \bar{V}_h^{p_s}$, with $K(t) = \mathcal{K} \cap \{t\}$, and $\bar{V}_h^{p_s}$ equivalent to $V_h^{(p_t,p_s)}$ but now defined on Ω_t, as:

$$\sum_{\mathcal{K}\in\mathcal{T}_h} \int_{K(t)} (\mathcal{P}_K v)(t) \cdot \phi \, \mathrm{d}K = \sum_{\mathcal{K}\in\mathcal{T}_h} \int_{K(t)} v \cdot \phi \, \mathrm{d}K, \quad \forall \phi \in V_h^{(p_t,p_s)}, \tag{5.78}$$

hence $(\mathcal{P}_K v)(t) \in L^2([0, T]; \bar{V}_h^{p_s})$. For $q \in \mathcal{Q}_h^{(p_t,p_s)}/\mathbb{R}$, we consider the bilinear form $\mathcal{B}_h(q, w)$, with $w \in (H_0^1(\Omega_t))^d$, for $t \in (0, T)$:

$$\mathcal{B}_h(q, w) = -\int_{\mathcal{E}} q\overline{\nabla}_h \cdot w \, \mathrm{d}\mathcal{E} + \sum_{S\in\cup_n\mathcal{S}_{ID}^n} \int_S \{\!\{q\}\!\}\langle\!\langle w\rangle\!\rangle \, \mathrm{d}S.$$

Since $\langle\!\langle w\rangle\!\rangle = 0$, we can use (5.76) to obtain

$$\mathcal{B}_h(q, w) = \|q\|^2_{0,0,\mathcal{E}}. \tag{5.79}$$

Now we consider the bilinear form $\mathcal{B}_h(q, v)$, with $v = (\mathcal{P}_K w)(t)$:

$$\begin{aligned}
\mathcal{B}_h(q, v) =& \mathcal{B}_h(q, w) + \mathcal{B}_h(q, \mathcal{P}_K w - w),\\
=& \|q\|^2_{0,0,\mathcal{E}} - \int_{\mathcal{E}} q\overline{\nabla}_h \cdot (\mathcal{P}_K w - w) \, \mathrm{d}\mathcal{E} + \sum_{S\in\cup_n\mathcal{S}_{ID}^n} \int_S \{\!\{q\}\!\}\langle\!\langle \mathcal{P}_K w - w\rangle\!\rangle \, \mathrm{d}S,\\
=& \|q\|^2_{0,0,\mathcal{E}} + \int_{\mathcal{E}} \overline{\nabla}_h q \cdot (\mathcal{P}_K w - w) \, \mathrm{d}\mathcal{E} - \sum_{\mathcal{K}\in\mathcal{T}_h} \int_{\mathcal{Q}_{\mathcal{K}}^n} q\bar{n} \cdot (\mathcal{P}_K w - w) \, \mathrm{d}\partial\mathcal{K}\\
&+ \sum_{S\in\cup_n\mathcal{S}_{ID}^n} \int_S \{\!\{q\}\!\}\langle\!\langle \mathcal{P}_K w - w\rangle\!\rangle \, \mathrm{d}S.
\end{aligned} \tag{5.80}$$

The last equation is obtained using integration by parts and the fact that $\bar{n} = 0$ at Ω_0 and Ω_T. Applying identity (5.35) into (5.80), using the orthogonality property of the L^2-projection $\mathcal{P}_K$ and the fact that $w = 0$ at $\partial\Omega_t$, we then obtain:

$$\mathcal{B}_h(q,v) = \|q\|^2_{0,0,\mathcal{E}} - \sum_{S\in\cup_n\mathcal{S}_I^n}\int_S \langle\!\langle q\rangle\!\rangle \cdot \{\!\{\mathcal{P}_K w - w\}\!\}\ \mathrm{d}S,\ \forall q \in \mathcal{Q}_h^{(p_t,p_s)}/\mathbb{R}. \tag{5.81}$$

We estimate the second term on the right hand side in (5.81) as follows:

$$\begin{aligned}
|\sum_{S\in\cup_n\mathcal{S}_I^n}\int_S \langle\!\langle q\rangle\!\rangle \cdot \{\!\{\mathcal{P}_K w - w\}\!\}\ \mathrm{d}S| \leq & \Big(\sum_{S\in\cup_n\mathcal{S}_I^n}\int_S \gamma|\langle\!\langle q\rangle\!\rangle|^2\ \mathrm{d}S\Big)^{1/2}\times \\
& \Big(\sum_{S\in\cup_n\mathcal{S}_I^n}\frac{1}{\gamma}\int_S |\{\!\{\mathcal{P}_K w - w\}\!\}|^2\ \mathrm{d}S\Big)^{1/2}, \\
\leq & C|q|_{\mathcal{S}_I^n}\Big(\sum_{\mathcal{K}\in\mathcal{T}_h}\|\overline{\nabla}_h w\|^2_{0,\mathcal{K}}\Big)^{1/2},
\end{aligned} \tag{5.82}$$

using the seminorm defined in (5.56) for $\gamma \approx h$ and the anisotropic interpolation estimate given by Lemma B.14. Using (5.82), we obtain the following inequality for $\mathcal{B}_h(q,v)$:

$$\mathcal{B}_h(q,v) \geq \|q\|^2_{0,0,\mathcal{E}} - C|q|_{\mathcal{S}_I^n}\Big(\sum_{\mathcal{K}\in\mathcal{T}_h}\|\overline{\nabla}_h w\|^2_{0,\mathcal{K}}\Big)^{1/2} = C\|q\|^2_{0,0,\mathcal{E}}\Big(1 - \frac{|q|_{\mathcal{S}_I^n}\|w\|_{0,1,\mathcal{E}}}{\|q\|^2_{0,0,\mathcal{E}}}\Big), \tag{5.83}$$

and together with the fact that $\|w\|_{0,1,\mathcal{E}} \leq C_{\mathcal{E}}^{-1}\|q\|_{0,0,\mathcal{E}}$ this completes the proof. □

Using the results of the continuity and the coercivity of the bilinear forms $\mathcal{A}_h, \mathcal{B}_h$, and $\mathcal{O}_h$, we can obtain a global stability result. First, we define the product space $\mathcal{Z}_h^{(p_t,p_s)} = V_h^{(p_t,p_s)} \times \mathcal{Q}_h^{(p_t,p_s)}$, endowed with the norm:

$$|||(v,q)|||^2_{\mathrm{DG}} = |||v|||^2_{\mathrm{DG}} + \|q\|^2_{0,0,\mathcal{E}} + |q|^2_{\mathcal{S}_I^n}. \tag{5.84}$$

If we define the following forms $\tilde{\mathcal{A}}^{(i)} : \mathcal{Z}_h^{(p_t,p_s)} \times \mathcal{Z}_h^{(p_t,p_s)} \to \mathbb{R}$ and $\tilde{\mathcal{L}} : \mathcal{Z}_h^{(p_t,p_s)} \to \mathbb{R}$ as:

$$\tilde{\mathcal{A}}^{(i)}(u,p;v,q) = \mathcal{A}_h(u,v) + \mathcal{B}_h(p,v) - \mathcal{B}_h(q,u) + \mathcal{C}_h^{(i)}(p,q), \tag{5.85}$$

$$\tilde{\mathcal{L}}(v,q) = N_h(v) + F_h(v) + G_h(v) + H_h(q), \tag{5.86}$$

then (5.55) is equivalent with:

Find $(u_h, p_h) \in \mathcal{Z}_h^{(p_t,p_s)}$ such that:

$$\tilde{\mathcal{A}}^{(i)}(u_h,p_h;v,q) + \mathcal{O}_h(u_h,v;w) = \tilde{\mathcal{L}}(v,q), \quad \forall (v,q) \in \mathcal{Z}_h^{(p_t,p_s)}. \tag{5.87}$$

Using Lemma 7.2 from [54], there exists a constant $C_1 > 0$ which depends only on the shape regularity of the elements, such that for a face $S \in \cup_n\mathcal{S}_I^n$:

$$\|\bar{\mathcal{L}}_S(\langle\!\langle p\rangle\!\rangle)\|^2_{0,\mathcal{E}} \geq C_1 p_s^2 \int_S \gamma|\langle\!\langle p\rangle\!\rangle|^2\ \mathrm{d}S,$$

with p_s the polynomial degree of the spatial variables. Moreover, we have the following relation:

$$\mathcal{C}_h^{(2)}(p,p) = \sum_{S\in\cup_n \mathcal{S}_I^n} \alpha \|\bar{\mathcal{L}}_S(\langle\!\langle p \rangle\!\rangle)\|_{0,\mathcal{E}}^2 \geq C_1 \alpha_0 p_0^2 |p|_{\mathcal{S}_I^n}^2, \tag{5.88}$$

with $\alpha_0 = \min_{\mathcal{K}\in\mathcal{T}_h} \alpha$ and $p_0 = \min_{\mathcal{K}\in\mathcal{T}_h} p_{s,\mathcal{K}}$.

We can now state a global stability estimate for the Oseen equations discretized with the space-time DG method, given in (5.87).

Theorem 5.8 *There exists a constant $C_{\tilde{\mathcal{A}}} > 0$, only depending on the space-time domain $\mathcal{E}$, such that the following global stability estimate holds for all $(v,q) \in \mathcal{Z}_h^{(p_t,p_s)}$:*

$$\inf_{(0,0)\neq(u,p)\in\mathcal{Z}_h^{(p_t,p_s)}} \sup_{(0,0)\neq(v,q)\in\mathcal{Z}_h^{(p_t,p_s)}} \frac{\tilde{\mathcal{A}}(u,p;v,q)}{|||(u,p)|||_{\mathrm{DG}}|||(v,q)|||_{\mathrm{DG}}} \geq C_{\tilde{\mathcal{A}}}.$$

Proof . First, we fix $(0,0) \neq (u,p) \in V_h^{(p_t,p_s)} \times \mathcal{Q}_h^{(p_t,p_s)}$. We notice that using Lemma 5.4 and (5.88):

$$\begin{aligned}\tilde{\mathcal{A}}^{(i)}(u,p;u,p) =& \mathcal{A}_h(u,u) + \mathcal{C}_h^{(i)}(p,p),\\ \geq& \nu_0\bar{\beta}_{\mathcal{A}}|||u|||_{\mathrm{DG}}^2 + C^{(i)}|p|_{\mathcal{S}_I^n}^2,\end{aligned} \tag{5.89}$$

with $C^{(1)} = 1$ (related to the bilinear form $\mathcal{C}_h^{(1)}$) and $C^{(2)} = C_1\alpha_0 p_0^2$ (related to the bilinear form $\mathcal{C}_h^{(2)}$). From Lemma 5.7 and (5.76), we have:

$$\mathcal{B}_h(p,w) \geq C\|p\|_{0,0,\mathcal{E}}^2 - C|p|_{\mathcal{S}_I^n}\|p\|_{0,0,\mathcal{E}}, \quad \text{with } \|w\|_{0,1,\mathcal{E}} \leq C_{\mathcal{E}}^{-1}\|p\|_{0,0,\mathcal{E}}. \tag{5.90}$$

Using Lemma 5.3, (5.90), the arithmetic-geometric mean inequality, (5.76), and the fact that $|||w|||_{\mathrm{DG}} = \|w\|_{0,1,\mathcal{E}}$, we obtain:

$$\begin{aligned}\tilde{\mathcal{A}}(u,p;w,0) =& \mathcal{A}_h(u,w) + \mathcal{B}_h(p,w),\\ \geq& -\nu_m\alpha_{\mathcal{A}}\epsilon_1|||u|||_{\mathrm{DG}}^2 - \nu_m\alpha_{\mathcal{A}}\epsilon_1^{-1}|||w|||_{\mathrm{DG}}^2 + C\|p\|_{0,0,\mathcal{E}}^2\\ &- C\epsilon_2^{-1}\|p\|_{0,0,\mathcal{E}}^2 - C\epsilon_2|p|_{\mathcal{S}_I^n}^2,\\ \geq& (C - C\epsilon_2^{-1} - \nu_m\alpha_{\mathcal{A}}C_{\mathcal{E}}^{-2}\epsilon_1^{-1})\|p\|_{0,0,\mathcal{E}}^2\\ &- \nu_m\alpha_{\mathcal{A}}\epsilon_1|||u|||_{\mathrm{DG}}^2 - C\epsilon_2|p|_{\mathcal{S}_I^n}^2,\end{aligned} \tag{5.91}$$

with $\epsilon_1, \epsilon_2 > 0$ chosen such that $(C - C\epsilon_2^{-1} - \epsilon_1^{-1}\nu_m\alpha_{\mathcal{A}}C_{\mathcal{E}}^{-2}) > 0$.

If we choose $(v,q) = (u,p) + \epsilon_3(w,0)$ then

$$\begin{aligned}\tilde{\mathcal{A}}(u,p;v,q) =& \tilde{\mathcal{A}}^{(i)}(u,p;u,p) + \epsilon_3\tilde{\mathcal{A}}(u,p;w,0),\\ \geq& \epsilon_3(C - C\epsilon_2^{-1} - \epsilon_1^{-1}\nu_m\alpha_{\mathcal{A}}C_{\mathcal{E}}^{-2})\|p\|_{0,0,\mathcal{E}}^2\\ &+ (\nu_0\bar{\beta}_{\mathcal{A}} - \nu_m\alpha_{\mathcal{A}}\epsilon_1\epsilon_3)|||u|||_{\mathrm{DG}}^2 + (C^{(i)} - C\epsilon_2\epsilon_3)|p|_{\mathcal{S}_I^n}^2,\\ \geq& C_2|||(u,p)|||_{\mathrm{DG}}^2,\end{aligned} \tag{5.92}$$

with $C_2 = \min(\nu_0\bar{\beta}_{\mathcal{A}} - \nu_m\alpha_{\mathcal{A}}\epsilon_1\epsilon_3, \epsilon_3(C - C\epsilon_2^{-1} - \epsilon_1^{-1}\nu_m\alpha_{\mathcal{A}}C_{\mathcal{E}}^{-2}), C^{(i)} - C\epsilon_2\epsilon_3)$. Next, we have the following result:

$$\begin{aligned}
|||(v,q)|||_{\mathrm{DG}}^2 \leq & |||(u,p)|||_{\mathrm{DG}}^2 + \epsilon_3|||(w,0)|||_{\mathrm{DG}}^2, \\
\leq & |||(u,p)|||_{\mathrm{DG}}^2 + \epsilon_3\|w\|_{0,1,\mathcal{E}}^2, \\
\leq & |||(u,p)|||_{\mathrm{DG}}^2 + \epsilon_3 C_{\mathcal{E}}^{-2}\|p\|_{0,0,\mathcal{E}}^2, \\
\leq & |||(u,p)|||_{\mathrm{DG}}^2 + \epsilon_3 C_{\mathcal{E}}^{-2}|||(u,p)|||_{\mathrm{DG}}^2, \\
\leq & C_3|||(u,p)|||_{\mathrm{DG}}^2, \qquad (5.93)
\end{aligned}$$

with $C_3 = 1 + \epsilon_3 C_{\mathcal{E}}^{-2}$. Combining the results from (5.92)-(5.93) completes the proof. □

5.6 Numerical results

In this section we provide several numerical experiments in two spatial dimensions to investigate the order of accuracy of the space-time DG discretization given by (5.55). We consider the Stokes system, which is obtained by neglecting the convective term in (5.2). The initial and boundary conditions and the source vector f are chosen such that the analytical solution is given by:

$$\begin{aligned}
u_1(t,x_1,x_2) &= -\exp(x_1)(x_2\cos(x_2) + \sin(x_2))\exp(-t), \\
u_2(t,x_1,x_2) &= \exp(x_1)x_2\sin(x_2)\exp(-t), \\
p(t,x_1,x_2) &= 2\exp(x_1)\sin(x_2)\exp(-t).
\end{aligned}$$

The computational domain is taken to be $(-1,1)^2$ and Dirichlet boundary conditions are imposed on the boundary.

We first study the influence of the choice of the stabilization parameter γ in the bilinear form $\mathcal{C}_h^{(1)}$, defined in (5.52), on the accuracy of the DG solution. We conduct therefore simulations for different values of γ on a mesh with 8×8 elements and different polynomial degrees, both in space and time. The results are shown in Table 5.1. For each simulation, the polynomial degrees for p are taken the same as for u. The results show that the choice of the stabilization parameter γ does not influence the accuracy of u and p. The parameter γ does have, however, a significant influence on the conditioning of the matrix resulting from the discretization. Larger values of γ gives a better conditioning of the matrix.

We also study the influence of the choice of the stabilization parameter α in the bilinear form $\mathcal{C}_h^{(2)}$, defined in (5.53), on the accuracy of the DG solution. We conduct simulations for different values of α on a mesh with 8×8 elements and different polynomial degrees, both in space and time. The results are shown in Table 5.2. For each simulation, the polynomial degrees for p are taken the same as for u. The same as in the case of the parameter γ, the results show that the choice of the stabilization

parameter α also does not influence the accuracy of u and p. There is, however, no clear relation visible on the influence of the values of α on the conditioning of the matrix. Based on this fact, we use the stabilization term $\mathcal{C}_h^{(1)}$ in the remaining part of this thesis.

Table 5.1: L^2-norm of the error for u_1, u_2, and p for different values of the parameter γ.

(p_t, p_s)		$\gamma = 10$	$\gamma = 100$	$\gamma = 1000$	$\gamma = 10000$
$(1,2)$	u_1	$7.0907E-05$	$7.0909E-05$	$7.0909E-05$	$7.0909E-05$
	u_2	$5.1696E-05$	$5.1740E-05$	$5.1744E-05$	$5.1745E-05$
	p	$5.2061E-03$	$5.2036E-03$	$5.2034E-03$	$5.2033E-03$
$(2,2)$	u_1	$7.1004E-05$	$7.1006E-05$	$7.1006E-05$	$7.1006E-05$
	u_2	$5.2344E-05$	$5.2390E-05$	$5.2394E-05$	$5.2395E-05$
	p	$5.5020E-03$	$5.4999E-03$	$5.4997E-03$	$5.4997E-03$
$(1,3)$	u_1	$1.4069E-06$	$1.4069E-06$	$1.4069E-06$	$1.4069E-06$
	u_2	$9.3052E-07$	$9.3053E-07$	$9.3053E-07$	$9.3053E-07$
	p	$1.6467E-04$	$1.6467E-04$	$1.6467E-04$	$1.6467E-04$
$(3,3)$	u_1	$9.6206E-07$	$9.6206E-07$	$9.6206E-07$	$9.6207E-07$
	u_2	$7.0011E-07$	$7.0012E-07$	$7.0012E-07$	$7.0012E-07$
	p	$5.4017E-05$	$5.4006E-05$	$5.4005E-05$	$5.4007E-05$

Table 5.2: L^2-norm of the error for u_1, u_2, and p for different values of the parameter α.

(p_t, p_s)		$\alpha = 10$	$\alpha = 100$	$\alpha = 100$	$\alpha = 10000$
$(1,2)$	u_1	$7.0909E-05$	$7.0909E-05$	$7.0909E-05$	$7.0909E-05$
	u_2	$5.1738E-05$	$5.1738E-05$	$5.1738E-05$	$5.1738E-05$
	p	$5.2037E-03$	$5.2037E-03$	$5.2037E-03$	$5.2037E-03$
$(2,2)$	u_1	$7.1006E-05$	$7.1006E-05$	$7.1006E-05$	$7.1006E-05$
	u_2	$5.2388E-05$	$5.2388E-05$	$5.2388E-05$	$5.2388E-05$
	p	$5.5000E-03$	$5.5000E-03$	$5.5000E-03$	$5.5000E-03$
$(1,3)$	u_1	$1.4069E-06$	$1.4069E-06$	$1.4069E-06$	$1.4069E-06$
	u_2	$9.3053E-07$	$9.3053E-07$	$9.3053E-07$	$9.3053E-07$
	p	$1.6467E-04$	$1.6467E-04$	$1.6467E-04$	$1.6467E-04$
$(3,3)$	u_1	$9.6206E-07$	$9.6206E-07$	$9.6206E-07$	$9.6206E-07$
	u_2	$7.0012E-07$	$7.0012E-07$	$7.0012E-07$	$7.0012E-07$
	p	$5.4006E-05$	$5.4006E-05$	$5.4006E-05$	$5.4006E-05$

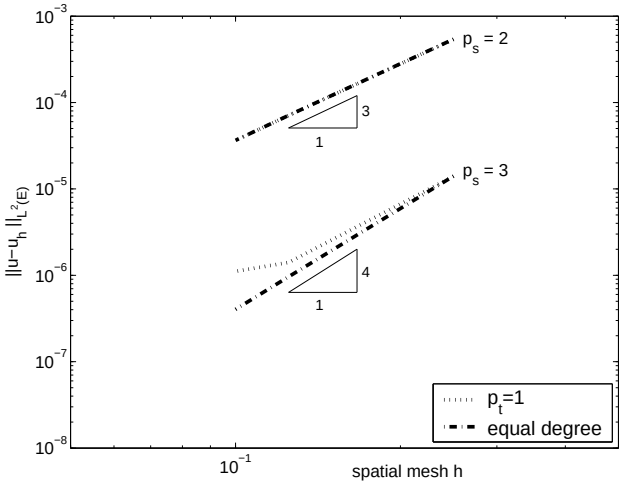

Figure 5.1: $L^2(\mathcal{E})$ error for the u_1 velocity component in the space-time DG discretization of the Stokes equations under h-refinement.

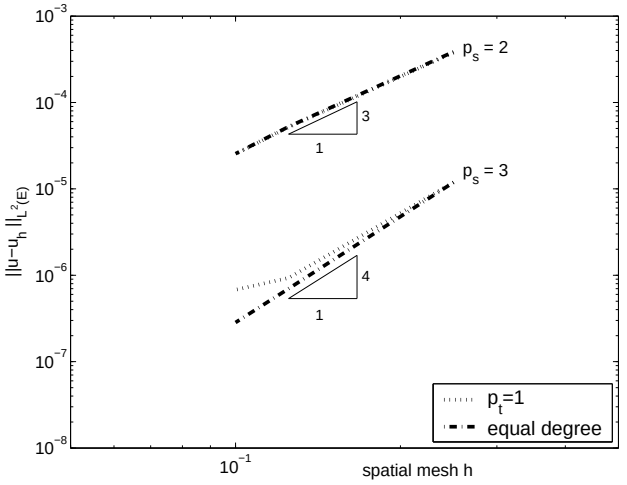

Figure 5.2: $L^2(\mathcal{E})$ error for the u_2 velocity component in the space-time DG discretization of the Stokes equations under h-refinement.

Next, we study the order of accuracy of the velocity field u and pressure p on meshes with different mesh sizes and increasing polynomial degrees. Here we use the

stabilization term $\mathcal{C}_h^{(1)}$ with $\gamma = 10000$. We first study the error in the L^2-norm in the whole space-time domain $\mathcal{E}$ for the velocity field u. The results are shown in Figs. 5.1-5.2. The plots show that the rate of convergence of the space-time DG method for the velocity field is optimal in the L^2-norm. Using linear polynomials in time and higher polynomial degrees in space we observe that, as the mesh becomes finer, the error is dominated by the error in time, but this only happens when the spatial error is already very small. We observed this also in Section 4.7 for the advection-diffusion equation.

We also consider the L^2-norm of error for the pressure p in Ω_T, the domain at the final time T of the simulation, both when equal polynomial degrees for u and p are used and also for different polynomial degrees. The results are shown in Figure 5.3. We observe that when equal polynomial degrees are used for u and p then the L^2-norm of the error of the pressure converges at the rate h^{p_s}, with p_s the polynomial degree of the pressure, while when the polynomial degrees for p are one less than the polynomial degrees for u, then the pressure converges at the rate $h^{p_s+1.5}$ for $p_s = 1$ and h^{p_s+1} for $p_s = 2$.

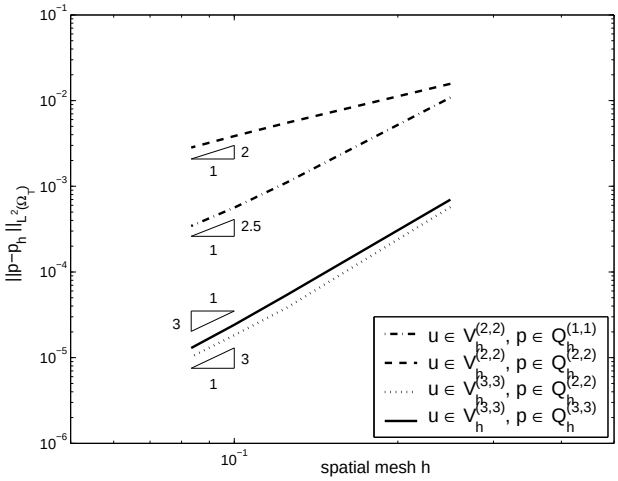

Figure 5.3: $L^2(\Omega_T)$ error for the pressure p in the space-time DG discretization of the Stokes equations under h-refinement.

5.7 Concluding remarks

In this chapter we present a space-time DG discretization for the Oseen equations in a time-dependent domain. We prove the continuity, coercivity and stability of the method and investigate the effect of the pressure stabilization operator on stability.

The simulations show that the values of the parameter γ in the pressure stabilization operator $\mathcal{C}_h^{(1)}$ do not influence the accuracy of the method. The values of γ have, however, a significant effect on the conditioning of the matrix resulting from the discretization. Larger values of γ give a better conditioning of the matrix. The values of the parameter α in the pressure stabilization operator $\mathcal{C}_h^{(2)}$ also does not influence the accuracy. Unfortunately, no conclusion can be obtained on the effect of α on the conditioning of the matrix.

The numerical experiments show that the convergence rate of the space-time DG solution for the velocity field is optimal in the L^2-norm, while the pressure converges at the rate h^{p_s} for equal polynomial degrees of the velocity and pressure, with p_s the polynomial degree of the pressure, and between h^{p_s+1} and $h^{p_s+1.5}$ for mixed polynomial degrees. The simulations show that the algorithm also performs well for higher polynomial degrees in time.

The space-time DG discretization in this chapter is limited to the Oseen equations, the extension to the incompressible Navier-Stokes equations which requires the use of a projection operator to ensure a divergence free velocity field will be discussed in [62].

Chapter 6

Simulation of Wet-Chemical Etching Processes

6.1 Introduction

In this chapter we present simulation results for different types of wet-chemical etching processes. The equations describing the transport phenomena in wet-chemical etching have been stated in Chapter 2, and consist of an advection-diffusion equation for the etchant concentration, the incompressible Navier-Stokes equations to model the flow of the etchant, and an equation for the movement of the etching surface.

A space-time DG discretization for the advection-diffusion equation has been developed in Chapter 4, while in Chapter 5 a space-time DG discretization for the incompressible Navier-Stokes equations has been worked out. In this chapter we will first discuss in Section 6.2 the DG discretization of the equation for the moving boundary of the etching surface. Next, a special technique to construct an initial space-time computational mesh is described in Section 6.3. These algorithms will be used to discretize the equations describing wet-chemical etching processes.

In the second part of this chapter simulation results using DG discretizations for different types of wet-chemical etching processes will be discussed. Part of these results have been presented in [60].

6.2 Discretization of the equation for the moving boundary

First, we recall the dimensionless form of the moving boundary equation (2.11) for each Cartesian component $x_{s,i}$ of a point $\bar{x}_s$ at the cavity surface:

$$\frac{dx_{s,i}}{dt} = -\frac{1}{\beta} n_i \sum_{j=1}^{d} \frac{\partial c}{\partial x_j} n_j, \quad j = 1, \ldots, d. \tag{6.1}$$

We consider the movement of the etching surface in a time interval $I_n = (t_n, t_{n+1})$. For each time interval we assume that I_n is an image of a reference interval $\hat{I} = (-1, 1)$

using a linear mapping F_I. Each component $x_{s,i}$ is approximated with functions from the finite element space Θ_h, which is defined as:

$$\Theta_h = \{\xi \in L^2(I_n) : \xi|_I \circ F_I \in P_{p_I}(\hat{I})\},$$

with $P_{p_I}(\hat{I})$ the set of polynomials on $\hat{I}$ of degree $p_I \geq 0$. The trace of functions $\xi \in \Theta_h$ at the boundary of the time interval is defined as: $\xi(t^{\pm}) = \lim_{\epsilon \to 0} \xi(t \pm \epsilon)$.

Denoting $x_{h,i}$ as an approximation to $x_{s,i}$ in Θ_h, the time DG method for (6.1) is defined as follows:

Within each time interval I_n, find $x_{h,i} \in \Theta_h$ such that the following relation holds for all $\xi \in \Theta_h$:

$$\xi(t_{n+1}^-)x_{h,i}(t_{n+1}^-) - \xi(t_n^+)x_{h,i}(t_n^-) - \int_{I_n} \frac{d\xi}{dt} x_{h,i} dt = -\frac{1}{\beta} \int_{I_n} n_i \xi \sum_{j=1}^{d} \frac{\partial c_s}{\partial x_j} n_j dt, \quad (6.2)$$

with c_s the concentration of the etchant at the point $\bar{x}_h$.

6.3 Construction of an initial computational mesh

In this section we discuss the construction of the space-time elements at the start of the etching process. Before the etching starts, the surface to be etched is generally flat. As soon as the etching process begins, the cavity boundary immediately moves downwards and under the mask at $t = t_1$, see Fig. 6.1 for an illustration of the etching of a slit. This makes the generation of an initial mesh complicated.

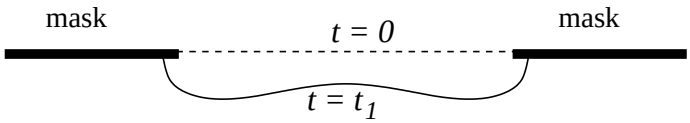

Figure 6.1: Time evolution of the moving boundary at the beginning of the etching process.

A special technique is therefore needed to create the computational mesh at the beginning of the etching process since in the space-time DG method we also need an estimate for the mesh position at $t = t_1$ to start the simulation. We describe now an algorithm to create the initial mesh, see Fig. 6.2 for an illustration in two-spatial dimensions. At $t = 0$ we divide the boundary on the slit into spatial elements K_j^0. Even though their coordinates in space at $t = 0$ are identical, these elements relate to different space-time elements (see Fig. 6.2(a)). At $t = t_1$ the computational domain is divided into spatial elements K_j^1. The space-time elements $\mathcal{K}_j^0$ are constructed by

connecting the elements K_j^0 and K_j^1, see Fig. 6.2(b). With this construction we can deal with the degenerated space elements at $t = 0$, since the space-time elements have a non-zero volume.

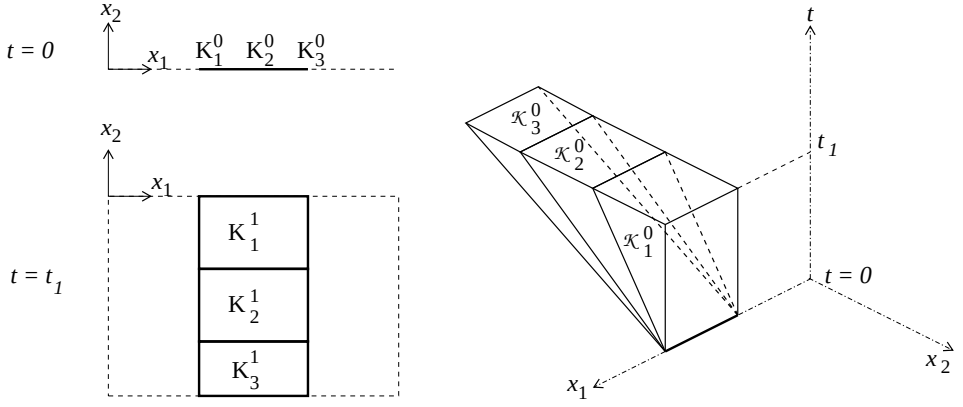

(a) Element construction at $t = 0$ and $t = t_1$.

(b) Construction of space-time elements in I_0.

Figure 6.2: Construction of space-time elements in the initial space-time slab.

Now that all DG discretizations for the equations used to model wet-chemical etching have been presented, including an algorithm for the construction of an initial computational mesh, we will discuss in the remaining parts of this chapter the algorithm and simulation results for different types of wet-chemical etching processes using the DG discretizations.

6.4 Diffusion-controlled wet-chemical etching

When the Péclet number Pe is small, the diffusion process controls the etchant concentration during etching, and we can neglect the convective term in (2.7). This simplifies the modeling of the wet-chemical etching process, as the governing equations now only involve the diffusion equation and the moving boundary equation. In the next subsections we present the algorithm and simulation results for diffusion-controlled etching in two and three spatial dimensions of the computational domain.

6.4.1 Algorithm for the simulations

For a diffusion-controlled etching process, the diffusion equation and the moving boundary equation have to be solved simultaneously in each time interval $I_n = (t_n, t_{n+1})$, which increases the complexity of the simulation. In [56, 66] a choice is made to solve these equations decoupled during each time level. In this thesis, we

solve both equations simultaneously by conducting an iteration process. First, the moving boundary equation is solved to obtain the new position of the etching surface. The initial concentration used in the moving boundary equation is the one computed in the previous time step. Then, the diffusion equation is solved in the computational domain with the updated boundary position, which also provides a new concentration for the moving boundary equation. This iteration process is continued until the position of the etching surface at the new time level is obtained. The main steps in simulating diffusion-controlled wet-chemical etching are summarized in the following algorithm.

Algorithm 6.1 Algorithm for simulating diffusion-controlled wet-chemical etching.

(1) At the start of the computation in the time interval I_n, set $c_h^{(0)} = c^n$ and $\bar{x}_s^{(0)} = \bar{x}_s^n$, the concentration and the cavity surface points, respectively, from the previous time interval.

(2) Set the maximum iteration count $maxit$ and stopping criterion ϵ.

(3) Do for each iteration $i = 1, 2, \ldots, maxit$:

   (i) For all points $\bar{x}_{s,j}^{(i-1)}, j = 1, \ldots, N_s$, with N_s the number of points at the etching surface:
   Solve (6.2) with $c_s = c_h^{(i-1)}$ for each Cartesian component of the etching surface points to obtain $\bar{x}_{s,j}^{(i)}$.

   (ii) Compute the maximum in the change of the boundary position:

$$x_{s,max}^{(i)} = \max_j |\bar{x}_{s,j}^{(i)} - \bar{x}_{s,j}^{(i-1)}|,$$

   and compute the ratio $r_s^{(i)} = |x_{s,max}^{(i)} - x_{s,max}^{(i-1)}|/x_{s,max}^{(i)}$.

   (iii) Move the coordinates of the etching surface to the new position $\bar{x}_s^{(i)}$.

   (iv) If $r_s^{(i)} < \epsilon$, stop the iteration. If not, continue the iteration procedure.

   (v) Solve (2.7) in the new coordinates to obtain $c_h^{(i)}$.

(4) The position of the etching surface at t_{n+1} is now equal to $\bar{x}_s^{n+1}$.

(5) Update the mesh and refine the elements if the mesh becomes too coarse due to the boundary movement.

(6) Solve (2.7) with the new coordinates $\bar{x}_s^{n+1}$ to obtain c_h^{n+1}, the space-time DG solution of the etchant concentration in the time interval I_n.

6.4.2 Diffusion-controlled etching of a slit

We discuss here the simulation results for the diffusion-controlled etching of a slit. The description for this model problem follows the discussion in [43, 66].

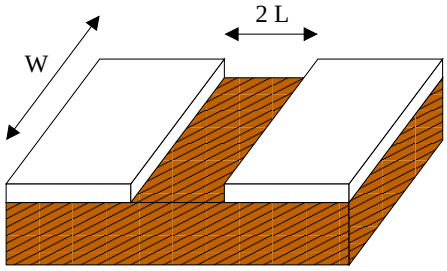

Figure 6.3: A slit to be etched.

Consider a slit of width $2L$ and length W shown in Fig. 6.3, which needs to be etched in a flat plate. Assuming that the length is much larger than the width, the problem can be considered in two spatial dimensions (see Fig. 6.4). The thickness of the mask is assumed to be very small compared to the width of the slit and is taken to be zero in the computational domain. The concentration of the etchant throughout the computational domain Ω_t is governed by the diffusion equation, given in (2.1), neglecting the convective term.

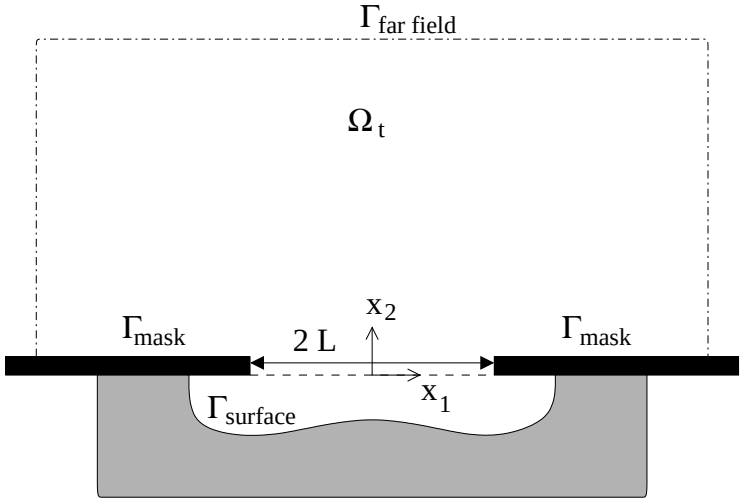

Figure 6.4: Computational domain.

The initial and boundary conditions for this problem are formulated as follows. We assume that initially the flow domain is filled with the etchant. During etching, the concentration on the far field boundary $\Gamma_{\text{far field}}$ is kept equal to the initial concentration. In addition, it is assumed that the fluid can not flow through the mask Γ_{mask}. Note that this condition also applies to the boundary under the mask. The boundary condition on Γ_{surface} is governed by the chemical reaction at this surface (see Section 2.2). Using the following reference values: L the half width of the slit, C the initial etchant concentration, and D the diffusion coefficient, the initial and boundary conditions are described in dimensionless form as:

$$\begin{aligned} c &= 1 && \text{in } \Omega \text{ at } t = 0, \\ c &= 1 && \text{on } \Gamma_{\text{far field}}, \\ \overline{\nabla} c \cdot \bar{n} &= 0 && \text{on } \Gamma_{\text{mask}}, \\ \overline{\nabla} c \cdot \bar{n} &= -\mathrm{Sh}\, c && \text{on } \Gamma_{\text{surface}}, \end{aligned}$$

with Sh the Sherwood number defined in (2.10). The boundary surface Γ_{surface} moves with the velocity described by (6.1).

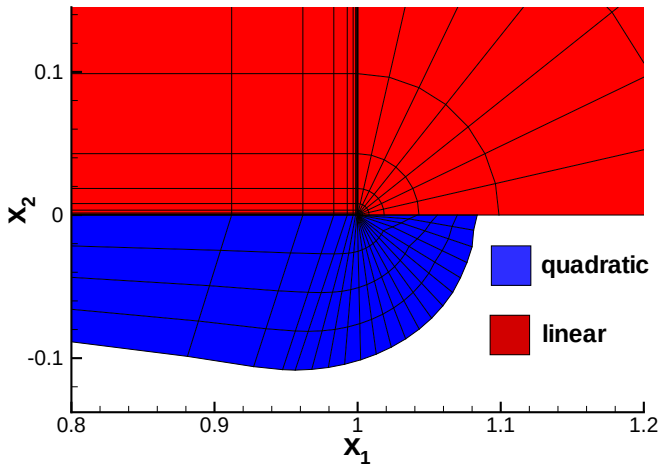

Figure 6.5: Space-time elements near the mask edge and their corresponding polynomial degrees. Etching parameters: Sh = 1000, $\beta = 100$.

First, we choose a Sherwood number Sh = 1000 as an example of an etching process where the surface reaction is very fast (Sh $\to \infty$). During the simulation, we fix the number of elements to 976 elements, the grid inside the computational domain

is remeshed during the simulations, in particular near the cavity surface and on the far field boundary, to follow the shape of the cavity and to accommodate the boundary condition at the far field boundary. Different polynomial degrees are assigned to the space-time elements. Quadratic polynomials are used as basis functions for elements near the cavity surface and the mask, while linear polynomials are used as basis functions for elements in other parts of the computational domain. This choice is based on the preliminary results obtained for simulations of 1D Stefan problems, see [58] for more details. The mesh near the mask edge and the polynomial degrees are shown in Fig. 6.5.

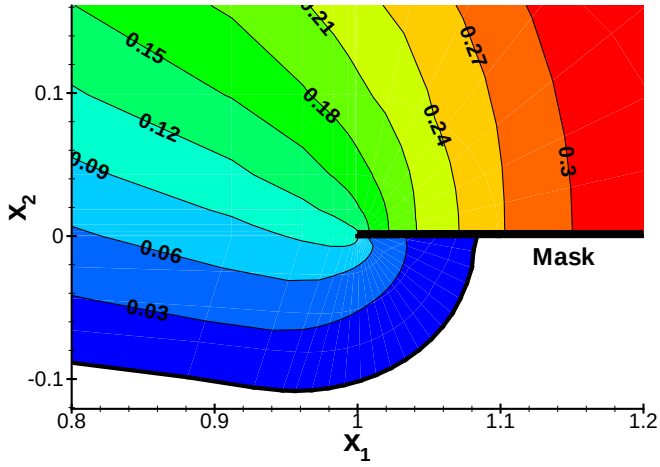

Figure 6.6: Contour of etchant concentration near the mask at time $t = 10$. Etching parameters: $\mathrm{Sh} = 1000$, $\beta = 100$.

The contour plot of the etchant concentration near the mask edge at time level $t = 10$ is shown in Fig. 6.6. The strength of the concentration gradients near the mask in Fig. 6.6 confirm the result from the analytical approach discussed in [46], Figure 5.A. This steep gradients are due to the corner singularities, we refer to [33] for the mathematical theory of this topic. The shape of the cavity surface during time evolution is shown in Fig. 6.7. This figure shows how the shape of the cavity is changing in time. Due to the fast surface reaction in the etching process, initially a bulge is formed near the corner of the mask. Later, when the flow domain under the mask is large enough, this bulge vanishes, i.e. the final shape becomes convex. This phenomenon is described in [43], and is confirmed by our simulation results.

When the Sherwood number goes to infinity, an asymptotic solution of the shape of

the etching surface was given in [43]. A comparison between the numerical simulation results and the asymptotic solution in [43] is shown in Fig. 6.8. This figure shows a good agreement between the numerical simulation and the asymptotic solution.

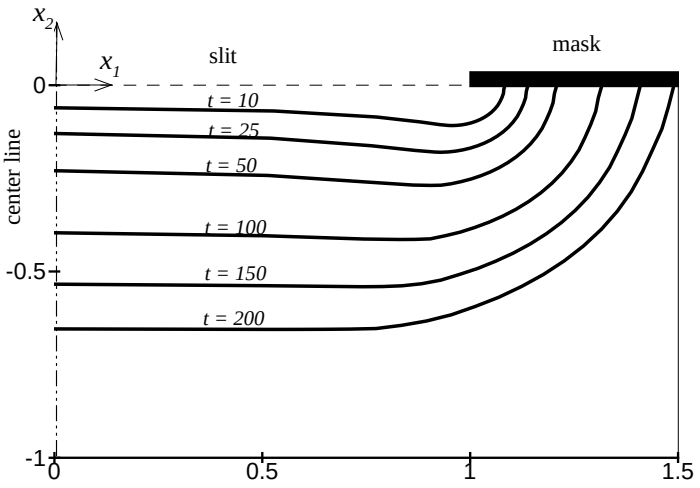

Figure 6.7: Shape of the etching cavity during time evolution for diffusion-controlled etching of a slit. Etching parameters: Sh = 1000, $\beta = 100$.

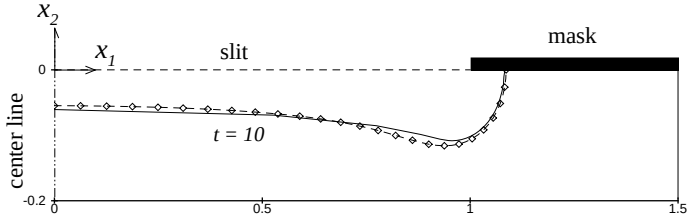

Figure 6.8: Comparison between numerical results (solid line) and asymptotic solution [43] ($\diamond$ symbol) at $t = 10$ with parameter Sh = 1000, $\beta = 100$.

Next, we perform a simulation for a Sherwood number Sh = 1, which is an example of a case where the surface reaction proceeds slowly compared to the transport of the etchant. Here the kinetics controls the transport process and the concentration is nearly the same everywhere. For small values of the Sherwood number, the bulge phenomenon is less pronounced and the boundary moves slower than for large values of the Sherwood number, as shown in Fig. 6.9.

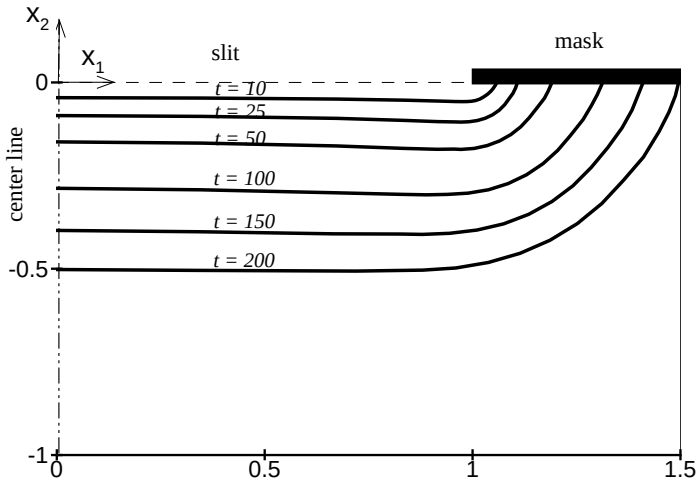

Figure 6.9: Shape of the etching cavity during time evolution for diffusion-controlled etching of a slit. Etching parameters: Sh = 1, $\beta = 100$.

6.4.3 Diffusion-controlled etching of a circular hole

In this section we discuss the simulation results for diffusion-controlled etching of a circular hole, as an example of wet-chemical etching in three spatial dimensions.

We consider a circular hole with radius L which needs to be etched in a flat plate, see Fig. 6.10 for a view of the hole in the $x_1 - x_2$ plane. Similar to the model in Section 6.4.2, we assume here that the thickness of the mask is very small compared to the radius of the circle and is taken to be zero in the computational domain.

If we take the cross section $P - Q$ in Fig. 6.10, the computational domain is similar to the sketch in Fig. 6.4. The concentration of the etchant throughout the computational domain is governed by the diffusion equation, given by (2.1) neglecting the convective term. Using the following reference values: L the radius of the circular

hole at the mask, C the initial etchant concentration, and D the diffusion coefficient, the initial and boundary conditions follow the model discussed in Section 6.4.2.

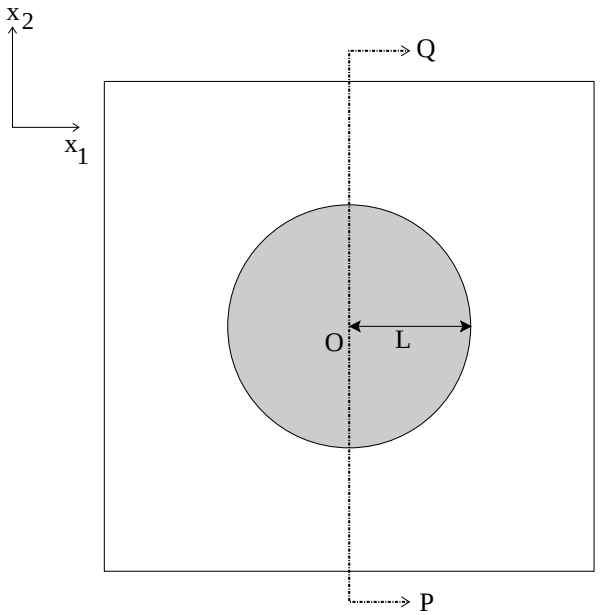

Figure 6.10: Circular hole to be etched in the $x_1 - x_2$ plane.

We conduct the simulation for a Sherwood number Sh = 1000 and parameter $\beta = 100$ as an example of an etching process where the surface reaction is very fast. We use 6816 elements and similar to the simulation of etching of a slit presented in Section 6.4.2, two different polynomial degrees are assigned to the elements. For elements near the cavity surface and the mask, quadratic polynomials are used, while far away from the mask, we use linear polynomials.

The shape of the cavity at two different times is shown in Fig. 6.11 and Fig. 6.13. Fig. 6.11 shows the shape of the cavity at $t = 10$ when the bulge is still present, while Fig. 6.13 shows the shape of the cavity at $t = 100$ when the bulge vanishes and the shape of the hole becomes convex. The etchant concentration inside the etching cavity at time levels $t = 10$ and $t = 100$ is shown in Figs. 6.12 and 6.14.

The shape of the cavity during time revolution at the cross section $P - Q$ is shown in Fig. 6.15. We observe in Fig. 6.15 that first the shape behaves similar to the etching of a slit. Initially a bulge is formed near the corner of the mask and later this bulge disappears when the flow domain under the mask is large enough and the shape becomes convex.

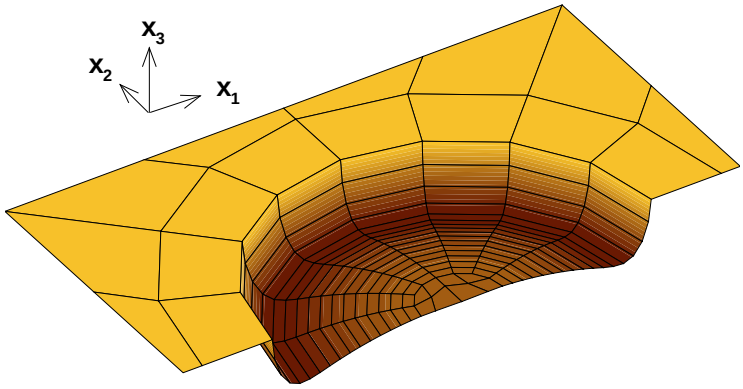

Figure 6.11: Shape of the etching cavity of a circular hole under diffusion-controlled etching at $t = 10$. Etching parameters: Sh $= 1000$, $\beta = 100$.

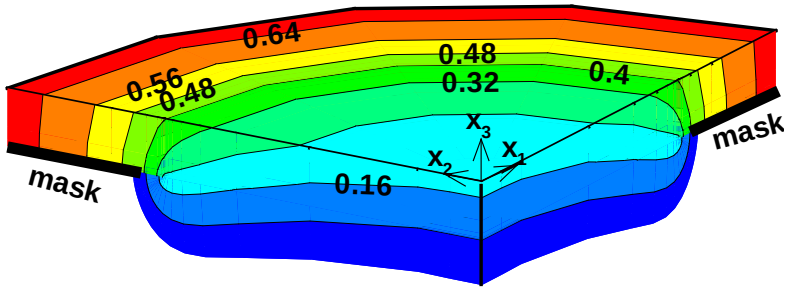

Figure 6.12: Etchant concentration inside the etching cavity of a circular hole under diffusion-controlled etching at $t = 10$. Etching parameters: Sh $= 1000$, $\beta = 100$.

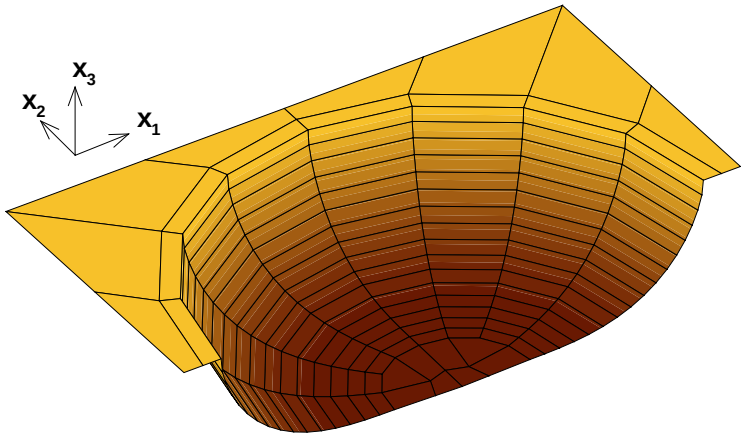

Figure 6.13: Shape of the etching cavity of a circular hole under diffusion-controlled etching at $t = 100$. Etching parameters: Sh $= 1000$, $\beta = 100$.

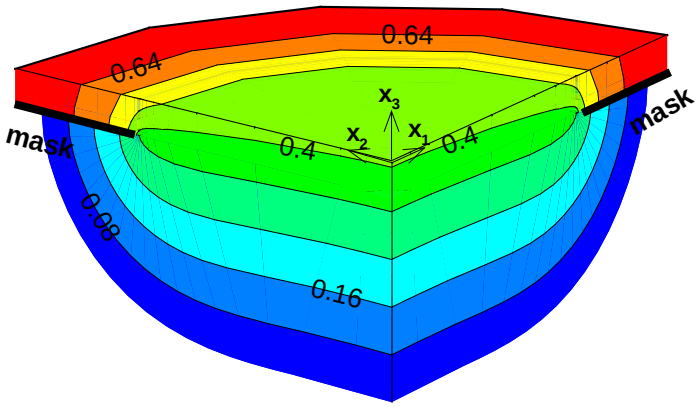

Figure 6.14: Etchant concentration inside the etching cavity of a circular hole under diffusion-controlled etching at $t = 100$. Etching parameters: Sh $= 1000$, $\beta = 100$.

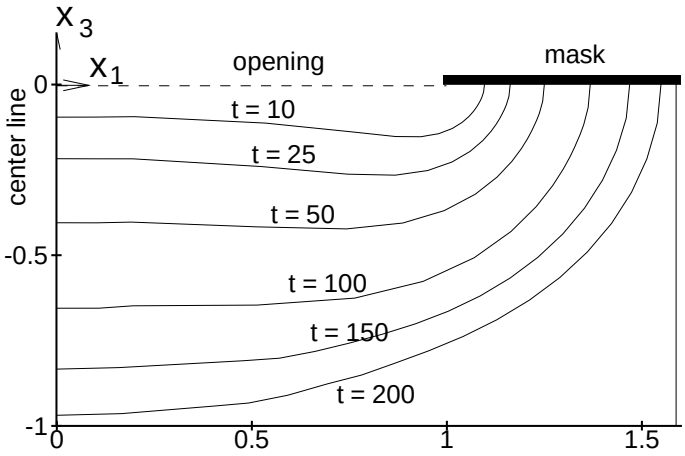

Figure 6.15: Shape of the etching cavity during time evolution for diffusion-controlled etching of a circular hole at the cross section $P - Q$. Etching parameters: Sh = 1000, $\beta = 100$.

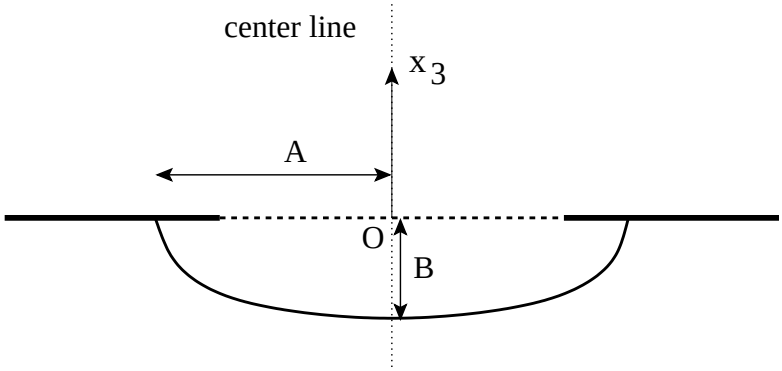

Figure 6.16: Geometrical sketch of hole in $x_1 - x_3$ plane.

We consider now the values of the side movement and depth of the hole (distances A and B in Fig. 6.16) during time evolution. In Fig. 6.17 the values for A and B, scaled with $Z = (\frac{3\,t}{\pi\,\beta})^{1/3}$, are shown. In [46] it is shown that both A/Z and B/Z tend to one, and the results from the simulations seem to confirm this.

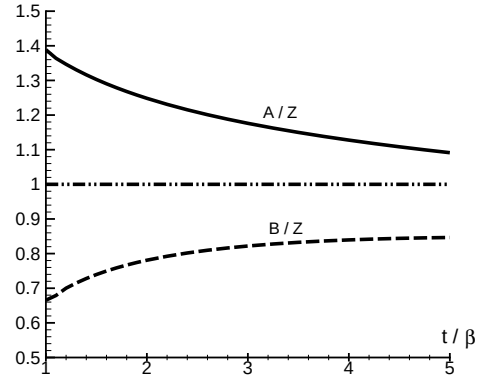

Figure 6.17: Comparison between A/Z and B/Z, with A the half width, B the depth of the cavity, and $Z = (\frac{3\,t}{\pi\,\beta})^{1/3}$, during time evolution for diffusion-controlled etching of a circular hole. Etching parameters: Sh = 1000, $\beta = 100$.

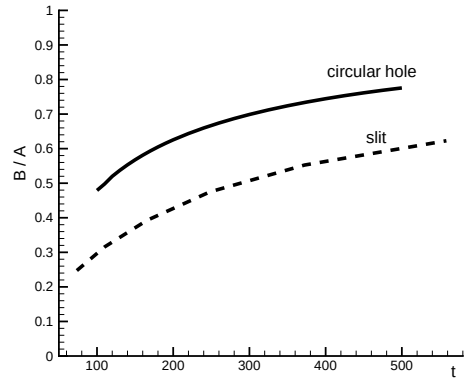

Figure 6.18: Ratio between A and B, with A the half width and B the depth of the cavity, during the time evolution of diffusion-controlled etching of a circular hole and a slit, shown in Figs. 6.7 and 6.15. Etching parameters: Sh = 1000, $\beta = 100$.

The ratio between the depth of the cavity and the side movement, both for the etching of a slit and a hole, will also go to one as time goes to infinity, as discussed

in [46]. The numerical simulations show a similar behavior, but for the slit it takes longer to approach a ratio equal to one than for the hole, as shown in Fig. 6.18. This phenomenon is also observed during experiments and in [66], but a definite conclusion based on numerical simulations will require a much longer simulation time due to the slow growth of the etching cavity.

6.5 Convection-dominated wet-chemical etching

When the Péclet number Pe is large, the concentration of the etchant is influenced by the fluid flow and the etching process is considered convection-dominated. The velocity field u in the advection-diffusion equation (2.7) can be modeled at several levels of complexity. As a simple model, the velocity can be described explicitly. In more complex models, the velocity is governed by the Stokes equations (2.15) or even by the incompressible Navier-Stokes equations. In this section we apply the first two modeling levels of the velocity field for the etching process of a slit.

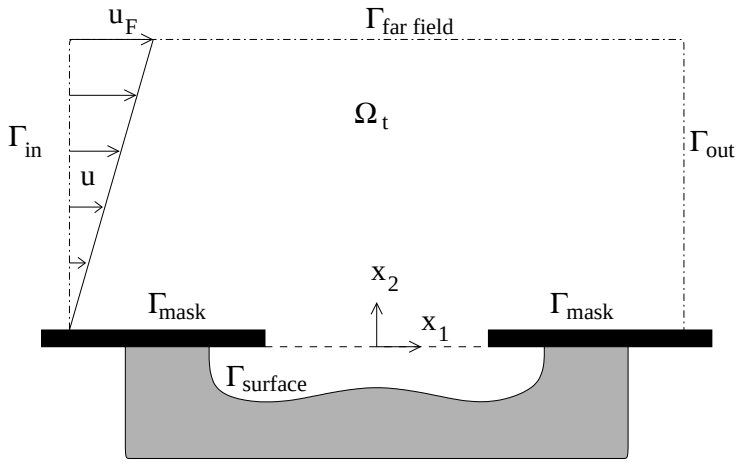

Figure 6.19: Computational domain of convection-dominated etching of a slit.

6.5.1 Convection-dominated etching with a prescribed velocity field

First, we discuss simulation results for convection-dominated etching of a slit when the velocity field is prescribed. The concentration of the etchant is governed by the advection-diffusion equation and the etching surface moves with the velocity determined from the moving boundary equation. The algorithm for the simulation of convection-dominated etching with a prescribed velocity field is similar to Algorithm 6.1, only now we solve the advection-diffusion equation with the convective term.

Consider the sketch of the computational domain in Fig. 6.19. Here we assume that the flow enters the computational domain from the left. Using the same reference values as in Section 6.4.2, the initial and boundary conditions in dimensionless form are:

$$\begin{aligned} c &= 1 && \text{in } \Omega \text{ at } t = 0, \\ c &= 1 && \text{on } \Gamma_{\text{in}}, \\ \overline{\nabla} c \cdot \bar{n} &= 0 && \text{on } \Gamma_{\text{mask}}, \Gamma_{\text{far field}}, \Gamma_{\text{out}}, \\ \overline{\nabla} c \cdot \bar{n} &= -\text{Sh}\, c && \text{on } \Gamma_{\text{surface}}. \end{aligned}$$

We prescribe the velocity field u with functions that resemble the approximate behavior of the fluid flow in the domain. First, we assume that the velocity field has nonzero values only in the region above the mask. The Cartesian components u_i, $i = 1, 2$ of the velocity field u have the following profile:

$$\begin{cases} u_1 = u_F x_2, & u_2 = 0, \quad \text{for } x_2 > 0, \quad \text{with } u_F > 0 \\ u_1 = 0, & u_2 = 0, \quad \text{for } x_2 \leq 0. \end{cases} \tag{6.3}$$

A simple nondimensionalization procedure shows that u_F is proportional to

$$u_F = \frac{D}{L^2},$$

with D the diffusion coefficient and L the half width of the slit. In a typical wet-chemical etching process, the coefficient D is of the order 10^{-9} and L of the order 10^{-5}. Hence, we assume that the value of u_F is of the order 10.

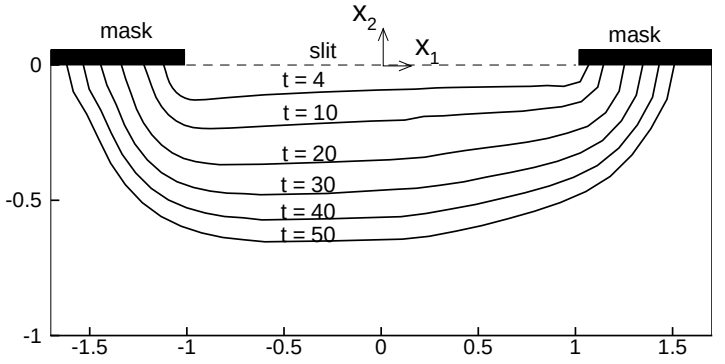

Figure 6.20: Shape of the etching cavity during time evolution for convection-dominated etching of a slit with zero fluid velocity inside the cavity. Etching parameters: Sh = 1000, $\beta = 100$, Pe = 100.

We perform the numerical simulation for a Péclet number Pe = 100 and a Sherwood number Sh = 1000. We use 724 elements, the polynomial degrees assigned to each element are similar to the simulation presented in Section 6.4.2. The resulting shape of the cavity is shown in Fig. 6.20. We can clearly see the non-symmetric evolution of the shape due to the fluid flow. As the flow comes from the left, the concentration of the etchant is higher on the left side, compared to the right side. Meanwhile, due to the fast reaction at the moving surface, the concentration along this surface is equal to zero. Hence the gradient of the concentration on the left side of the cavity is higher than on the right side and, since the movement of the cavity boundary depends linearly on the magnitude of the gradient of the concentration at the boundary, the boundary on the left side moves (etches) faster than on the right side. For small times this is indeed confirmed by the numerical simulations in, e.g. [29, 56].

For longer times, however, it is known from [29] that the non-symmetry becomes of a different character: the right side becomes deeper and our approximation does not capture this phenomenon. Of course this can be understood physically, because for longer times there should be a flow from left to right within the cavity which effectively transports the etchant material to the right, and as a consequence starts to speed up the etching process in the right part of the cavity.

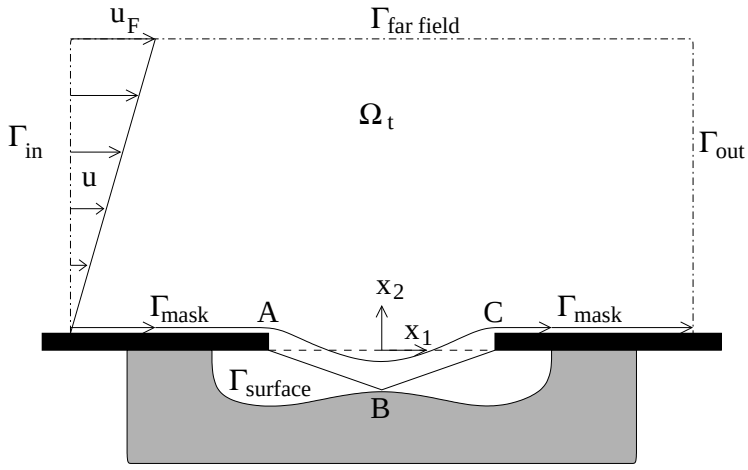

Figure 6.21: Fluid velocity profile u above the mask and into the cavity.

In order to model this behavior of the fluid flow, we apply a refined (but still very simple) approximation of the velocity field u. We define the velocity field as being non-zero above the mask, but also extend it into the cavity. This is accomplished by assuming that the streamline at Γ_{surface} moves down from the left mask edge point A

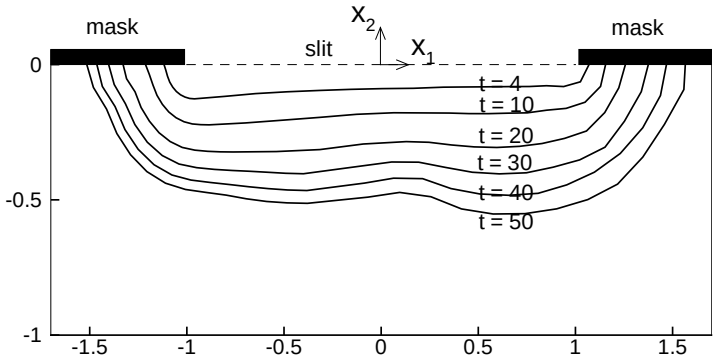

Figure 6.22: Shape of the etching cavity during time evolution for convection-dominated etching of a slit with a non-zero velocity field inside the cavity. Etching parameters: Sh = 1000, $\beta = 100$, Pe = 100.

to the point B in the center of the cavity boundary and up to right mask edge C (see Fig. 6.21). We assume that the velocity has a linear profile in the vertical direction and is constant above $\Gamma_{\text{far field}}$.

The result of this simulation is shown in Fig. 6.22. This figure shows qualitatively a behavior that compares well with numerical solutions which also involve a full simulation of the (Navier)-Stokes equations, e.g. [56, 57]. However, for longer simulation times, we need more accurate information on the velocity field inside the cavity. In the next section we discuss simulation results where the velocity field is governed by the Stokes equations.

6.5.2 Fully coupled convection-dominated etching using the Stokes equations

We consider now the case when the velocity field inside and outside the etching cavity is governed by the Stokes equations. The computational domain for convection-dominated etching when the fluid flow is modeled with the Stokes equations is the same as shown in Fig. 6.19. We assume that the acid flow enters from the left into the domain, and the same reference values are used here as in Section 6.4.2.

First, we discuss the Stokes equations. We denote by u_1 and u_2 the Cartesian components of the velocity field u. Along the cavity surface and on the mask, both velocity components are equal to zero. The velocity component u_1 has a linear profile on the inflow boundary Γ_{in}, while u_2 is kept zero. On the far field boundary, the velocity component u_1 has a constant value while u_2 is equal to zero. On the outflow boundary Γ_{out} we have a Neumann boundary condition. The initial and boundary

conditions in dimensionless form for the Stokes equation are presented as follows.

$$\begin{aligned}
u_1 &= u_F x_2 & u_2 &= 0 \quad \text{in } \Omega \text{ at } t = 0,\\
u_1 &= u_F x_2 & u_2 &= 0 \quad \text{on } \Gamma_{\text{in}},\\
u_1 &= 0 & u_2 &= 0 \quad \text{on } \Gamma_{\text{mask}}, \Gamma_{\text{surface}},\\
u_1 &= u_F & u_2 &= 0 \quad \text{on } \Gamma_{\text{far field}},\\
\overline{\nabla} u_1 \cdot \bar{n} &= 0 & \overline{\nabla} u_2 \cdot \bar{n} &= 0 \quad \text{on } \Gamma_{\text{out}}.
\end{aligned}$$

The initial and boundary conditions for the advection-diffusion equation for the etchant concentration follow the description given in Section 6.5.1.

Since now the equations are fully coupled, in each time interval we need to solve these equations iteratively. The main steps in the simulations of convection-dominated wet-chemical etching coupled with the Stokes equations are summarized in the following algorithm.

Algorithm 6.2 Algorithm for simulating convection-dominated etching coupled with the Stokes equations.

(1) At the start of the computation in the time interval I_n, set $c_h^{(0)} = c^n$, $u_h = u^n$ and $\bar{x}_s^{(0)} = \bar{x}_s^n$, the concentration, velocity field, and cavity surface points, respectively, from the previous time interval.

(2) Set the maximum iteration count $maxit$ and stopping criterion ϵ.

(3) Do for each iteration $i = 1, 2, \ldots, maxit$:

   (i) For all points $\bar{x}_{s,j}^{(i-1)}, j = 1, \ldots, N_s$, with N_s the number of points at the etching surface:
   Solve (6.2) with $c_s = c_h^{(i-1)}$ for each Cartesian component of the etching surface points to obtain $\bar{x}_{s,j}^{(i)}$.

   (ii) Compute the maximum in the change of the boundary position:

$$x_{s,max}^{(i)} = \max_j |\bar{x}_{s,j}^{(i)} - \bar{x}_{s,j}^{(i-1)}|,$$

   and compute the ratio $r_s^{(i)} = |x_{s,max}^{(i)} - x_{s,max}^{(i-1)}| / x_{s,max}^{(i)}$.

   (iii) Move the coordinates of the etching surface to the new position $\bar{x}_s^{(i)}$.

   (iv) If $r_s^{(i)} < \epsilon$, stop the iteration. If not, continue the iteration procedure.

   (v) Solve (2.7) in the new coordinates to obtain $c_h^{(i)}$.

(4) The position of the etching surface at t_{n+1} is now equal to $\bar{x}_s^{n+1}$.

(5) Update the mesh and refine the elements if the mesh becomes too coarse due to the boundary movement.

(6) Solve (2.15) with the new coordinates $\bar{x}_s^{n+1}$ to obtain u_h^{n+1}, the space-time DG solution of the velocity field in the time interval I_n.

(7) Solve (2.7) with the new coordinates $\bar{x}_s^{n+1}$ and the velocity field u_h^{n+1} to obtain c_h^{n+1}, the space-time DG solution of the etchant concentration in the time interval I_n.

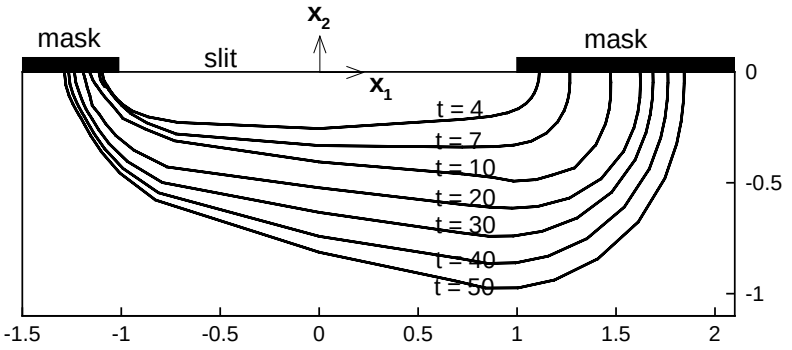

Figure 6.23: Shape of the etching cavity during time evolution for convection-dominated etching of a slit coupled with the Stokes equations for the velocity field inside the cavity. Etching parameters: Sh = 1000, $\beta = 100$, Pe = 100, Re = 1.

We perform the numerical simulation for a Péclet number Pe = 100, a Reynolds number Re = 1, and a Sherwood number Sh = 1000. The resulting shape of the cavity is shown in Fig. 6.23. This figure shows the non-symmetric evolution of the shape of the etching cavity already noticed in the simulations discussed in Section 6.5.1, using the advection-diffusion equation with a non-zero velocity field inside the cavity. In the beginning, the movement of the cavity boundary is faster on the left-hand side than on the right-hand side, as the acid flow comes from the left. As soon as the cavity becomes large enough, the acid also flows into the cavity refreshing the concentration levels. This can be seen in Figs. 6.24-6.25, which show the velocity and concentration contours inside the cavity at time $t = 50$. As a result the boundary on the right-hand side of the cavity moves faster than on the left-hand side. The main reason for this is that the transport of the etchant into the cavity increases the gradient of the etchant concentration near the cavity surface, in particular at the right-hand side. This stimulates the etching process and the cavity grows significantly faster than during diffusion-controlled etching, compare for instance Figs. 6.7 and 6.23.

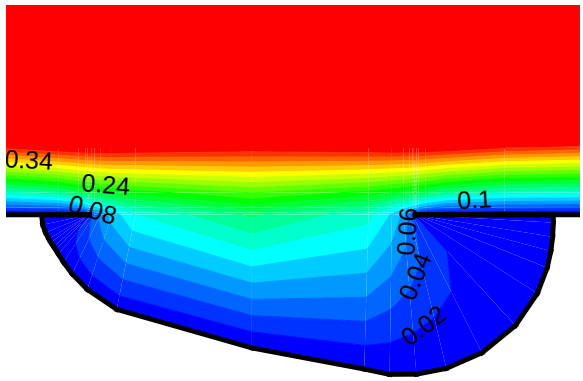

Figure 6.24: Absolute value of the velocity vector inside and above the etching cavity of a slit under convection-dominated etching at $t = 50$. Etching parameters: Sh $=$ 1000, $\beta = 100$, Pe $= 100$, Re $= 1$.

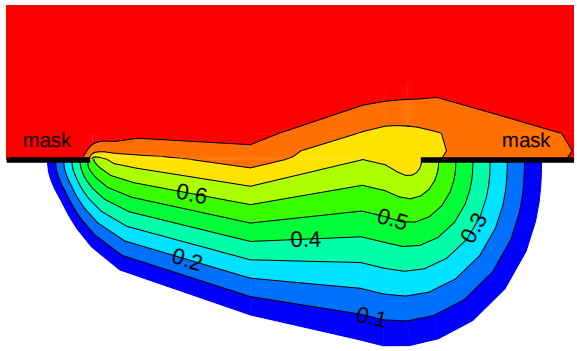

Figure 6.25: Etchant concentration inside the etching cavity of a slit under convection-dominated etching at $t = 50$. Etching parameters: Sh $= 1000$, $\beta = 100$, Pe $=$ 100, Re $= 1$.

Solving the Stokes equations for the acid flow results in a more realistic model for the transport of the etchant and gives a more accurate description of the shape of the cavity during time evolution. Note that for the choices of the parameters Re $= 1$ and

Pe = 100, the divergence of the velocity field during the simulation is not so negative. Hence the condition (4.41) in Section (4.5) is fulfilled during the computation. However, for larger Reynolds number, we can not guarantee condition (4.41) anymore unless the post-projection is used such as the one discussed in [24].

Chapter 7

Conclusions and Future Research

7.1 Conclusions

In this thesis space-time Discontinuous Galerkin (DG) finite element methods for the equations describing transport phenomena in wet-chemical etching processes have been developed, analyzed, and tested on real applications. In particular, we presented a space-time DG method for the advection-diffusion equation for the etchant concentration in the acid fluid and the incompressible Navier-Stokes equations describing the flow of the acid fluid. The capability of these newly developed methods is demonstrated for different types of wet-chemical etching processes. Here we present the main conclusions.

First, a space-time DG method for the advection-diffusion equation in a time-dependent computational domain has been presented. Based on a study of the DG discretizations for second-order elliptic partial differential equations, the discretization for the diffusive term in the advection-diffusion equation follows the method proposed by Bassi and Rebay. A detailed analysis is given to provide stability conditions and to prove the uniqueness of the solution of the DG discretization in a time-dependent domain. In addition, detailed error estimates are provided and supported with numerical simulations which show optimal convergence.

Also, a space-time DG method for the incompressible Navier-Stokes equations has been developed. For this method, the algorithm proposed by Bassi and Rebay for the discretization of the viscous term is combined with the Local Discontinuous Galerkin (LDG) method for the discretization of the incompressibility condition and the pressure stabilization, which has been developed by Cockburn and his coworkers. A detailed analysis is provided to prove the stability of the space-time DG method when using a pressure stabilization operator. The accuracy of the space-time DG method applied to the Stokes equations is studied using numerical experiments.

The space-time discretizations are well suited to deal with problems with moving boundaries which require deforming meshes. The capabilities of the space-time DG

methods for the simulation of wet-chemical etching have been demonstrated using different models. For this purpose special techniques were developed to generate the initial mesh for the space-time computations. The numerical simulations of diffusion-controlled etching of a slit and a circular hole show good agreement with the predictions obtained with analytical techniques. Moreover, the numerical simulations can give a complete description of the etching cavity during time evolution, something that the analytical approach is not capable of.

The numerical simulations of convection-dominated etching of a slit coupled with the Stokes equations give a detailed description of the transport phenomena in wet-chemical etching, including the flow of the acid fluid inside the cavity. These fully coupled simulations of convection-dominated etching clearly show the effect of the transport of the etchant inside the cavity on the shape of the cavity which grows much faster than under diffusion-controlled etching, but also looses symmetry.

7.2 Recommendations for future research

Here we present several recommendations for future research.

The first recommendation is related to *hp*-adaptation. From experience with the simulations of wet-chemical etching, we observe that an adaptation strategy is important in order to further improve the robustness and accuracy of the numerical simulations for wet-chemical etching processes. Making use of *hp*-adaptation, we can reduce the number of elements and the degrees of freedom of the linear system resulting from the discretization while maintaining the same level of accuracy. This will reduce the computing time needed for the simulations. An additional adaptation strategy should also be included in the moving boundary equation to remesh the cavity surface resulting from the simulations.

Further study is also needed in the development of the space-time DG discretization for the incompressible Navier-Stokes equations, in particular regarding the pressure stabilization operator and the linear solvers for the resulting linear system.

Regarding the problems in wet-chemical etching, it is worth to investigate the shape of the cavity near sharp corners, where the underetching behaves differently than at other parts of the mask edge. Further study should also be pursued in the direction of anisotropic wet-chemical etching and on modeling multiple chemical reactions at the cavity surface as this phenomena also occurs in experiments. A further validation of the simulation model with the experiments presently being conducted will also require significant attention. Finally, improving mask designs using inverse methods and the analysis techniques developed in this project will reduce the time necessary to control the etching process and improve the accuracy of the objects to be produced.

Appendix A

Algebraic System for the Space-Time DG Discretizations

A.1 Algebraic system for the advection-diffusion equation

In this section we present the algebraic equations for the space-time DG discretization of the advection-diffusion equation in the space-time slab $\mathcal{E}^n$, which was discussed in Section 4.4.2. We introduce the polynomial approximations $c_h \in \mathcal{W}_h^{(p_t,p_s)}$ in each space-time element $\mathcal{K}_j$ as follows:

$$c_h(x) = \sum_{n=0}^{N_j} \hat{C}_{n,\mathcal{K}_j} \psi_{n,\mathcal{K}_j}(x), \tag{A.1}$$

with $\psi_{n,\mathcal{K}_j} \in \mathcal{Q}_{p_{t,\mathcal{K}},p_{s,\mathcal{K}}}(\hat{\mathcal{K}})$, where $\mathcal{Q}_{p_{t,\mathcal{K}},p_{s,\mathcal{K}}}(\hat{\mathcal{K}})$ is defined in Section 4.3.2, and $N_j = (p_{t,\mathcal{K}_j}+1)(p_{s,\mathcal{K}_j}+1)^d$. Similar expressions are used for the test functions $w \in \mathcal{W}_h^{(p_t,p_s)}$.

A.1.1 Algebraic system for the diffusive part

We recall the formulation of the bilinear form for the diffusive part, given in (4.32):

$$\begin{aligned} a_d(c_h, w) = &\sum_{\mathcal{K}\in\mathcal{T}_h^n} \int_{\mathcal{K}} D\overline{\nabla}_h c_h \cdot \overline{\nabla}_h w \, \mathrm{d}\mathcal{K} \\ &- \sum_{S\in\mathcal{S}_{ID}^n} \int_S \left(D\langle\!\langle c_h \rangle\!\rangle \cdot \{\!\{ \overline{\nabla}_h w \}\!\} + D\{\!\{ \overline{\nabla}_h c_h \}\!\} \cdot \langle\!\langle w \rangle\!\rangle \right) \mathrm{d}S \\ &- \sum_{S\in\mathcal{S}_{ID}^n} \eta_{\mathcal{K}} \int_S D\{\!\{ \bar{r}_S([\![c_h]\!]) \}\!\} \cdot \langle\!\langle w \rangle\!\rangle \, \mathrm{d}S + \sum_{S\in\mathcal{S}_M^n} \int_S \alpha c_h w \, \mathrm{d}S, \end{aligned} \tag{A.2}$$

and the diffusive part of the linear form (4.37):

$$\ell_d(w) = -\sum_{S\in\mathcal{S}_D^n}\int_S g_D D\bar{n}\cdot\overline{\nabla}_h w \,\mathrm{d}S - \sum_{S\in\mathcal{S}_D^n}\eta_{\mathcal{K}}\int_S D\bar{r}_S(\mathcal{P}g_D n)\cdot\bar{n}w \,\mathrm{d}S + \sum_{S\in\mathcal{S}_M^n}\int_S g_M w \,\mathrm{d}S. \tag{A.3}$$

Note that the terms involving the lifting operator $\bar{r}_S$ are written as face integrals for simpler implementation.

First, we describe an approximation to the local lifting operator $\bar{r}_S(\llbracket c_h \rrbracket)$. This approximation is derived in [59]. We consider the local lifting operator r_S on $S \in \cup_n \mathcal{S}_I^n$. If we replace the functions κ in (4.5) with $\langle\!\langle c_h \rangle\!\rangle$ and use the fact that the local lifting operator r_S has nonzero values only in the elements $\mathcal{K}_i$ and $\mathcal{K}_j$ that share the face S, we obtain the following relation for the spatial part of the local lifting operator $\bar{r}_S$:

$$\int_{\mathcal{K}_i}\bar{r}_{S,i}(\langle\!\langle c_h \rangle\!\rangle)\cdot\bar{\varphi}_i \,\mathrm{d}\mathcal{K} + \int_{\mathcal{K}_j}\bar{r}_{S,j}(\langle\!\langle c_h \rangle\!\rangle)\cdot\bar{\varphi}_j \,\mathrm{d}\mathcal{K} = -\frac{1}{2}\int_S (c_{h,i}\bar{n}_i + c_{h,j}\bar{n}_j)\cdot(\bar{\varphi}_i + \bar{\varphi}_j)\,\mathrm{d}S, \quad \forall\varphi_i,\varphi_j \in \Upsilon_h^{(p_t,p_s)}. \tag{A.4}$$

Since (A.4) holds for any $\varphi_i, \varphi_j \in \Upsilon_h^{(p_t,p_s)}$, we have in element $\mathcal{K}_i$:

$$\int_{\mathcal{K}_i}\bar{r}_{S,i}(\langle\!\langle c_h \rangle\!\rangle)\cdot\bar{\varphi}_i \,\mathrm{d}\mathcal{K} = -\frac{1}{2}\int_S c_{h,i}\bar{n}_i\cdot\bar{\varphi}_i \,\mathrm{d}S - \frac{1}{2}\int_S c_{h,j}\bar{n}_j\cdot\bar{\varphi}_i \,\mathrm{d}S. \tag{A.5}$$

A similar expression is obtained for the lifting operator $\bar{r}_{S,j}$ in element $\mathcal{K}_j$.

We approximate the local lifting operator $\bar{r}_S$ and the test functions $\bar{\varphi}$ in element $\mathcal{K}_i$ as:

$$\bar{r}_{S,i} = \sum_{m=0}^{N_i}\hat{R}_{m,\mathcal{K}_i}\psi_{m,\mathcal{K}_i}(x), \qquad \varphi_i = \sum_{l=0}^{N_i}\hat{P}_{l,\mathcal{K}_i}\psi_{l,\mathcal{K}_i}(x). \tag{A.6}$$

We then introduce the following matrices: $A_i \in \mathbb{R}^{N_i\times N_i}$, $L_{ij}^k \in \mathbb{R}^{N_i\times N_j}$, defined as:

$$(A_{nm})_i = \int_{\mathcal{K}_i}\psi_{n,\mathcal{K}_i}\psi_{m,\mathcal{K}_i}\,\mathrm{d}\mathcal{K}, \quad (L_{nm})_{ij}^k = \int_S \psi_{n,\mathcal{K}_i}\psi_{m,\mathcal{K}_j}n_{\mathcal{K}_j}^k \,\mathrm{d}S,$$

where i, j refer to the element indices, and n^k, with $k = 1,\ldots,d$ is the k-th component of the space-time normal vector n on face S. We also introduce the coefficients: $\hat{R}_i^k \in \mathbb{R}^{N_i}$, $\hat{C}_i \in \mathbb{R}^{N_i}$, defined as:

$$\hat{R}_i^k = (\hat{R}_{0,\mathcal{K}_i}^k \ldots \hat{R}_{N_i,\mathcal{K}_i}^k), \quad \hat{C}_i = (\hat{C}_{0,\mathcal{K}_i}\ldots\hat{C}_{N_i,\mathcal{K}_i}),$$

with $\hat{R}_i^k$ the vector with the expansion coefficients of $\bar{r}_{S,i}$ and $\hat{C}_i$ the vector with the expansion coefficients of c_h. Introducing (A.1) and (A.6) into (A.5) and using the

notations just described, we obtain the following relation for the coefficients $\hat{R}_i^k$:

$$\hat{R}_i^k = -\frac{1}{2}A_i^{-1}L_{ii}^k\hat{C}_i - \frac{1}{2}A_i^{-1}L_{ij}^k\hat{C}_j,$$

and the k-th component of the spatial part of the lifting operator $\bar{r}_{S,i}$ can be written as:

$$\bar{r}_{S,i}^k = -\frac{1}{2}\sum_{m=0}^{N_i}\left(A_i^{-1}L_{ii}^k\hat{C}_i\right)\psi_{m,\mathcal{K}_i} - \frac{1}{2}\sum_{m=0}^{N_i}\left(A_i^{-1}L_{ij}^k\hat{C}_j\right)\psi_{m,\mathcal{K}_i}.$$

Now we consider the lifting operator on $S \in \cup_n \mathcal{S}_D^n$, given in (4.7). We introduce the vector: $G_j^k \in \mathbb{R}^{N_j}$, defined as:

$$(G_n)_j^k = \int_S g_D \psi_{n,\mathcal{K}_j} n_{\mathcal{K}_j}^k \, \mathrm{d}S.$$

Following a similar approach as before, we obtain the following relation for the coefficients of the k-th component of $\bar{r}_S$ on $S \in \cup_n \mathcal{S}_D^n$, with S a face on the boundary of $\mathcal{K}_j$:

$$\hat{R}_j^k = -A_j^{-1}G_j^k.$$

The k-th component of the spatial part of the lifting operator $\bar{r}_{S,j}$, related to a face $S \in \mathcal{S}_D^n$, can be written as:

$$\bar{r}_{S,j}^k = -\sum_{m=0}^{N_j}\left(A_j^{-1}G_j^k\right)\psi_{m,\mathcal{K}_j}.$$

We now discretize each term in (A.2) and (A.3). For this purpose, we introduce the vectors: $F_j \in \mathbb{R}^{N_j}$, $Q_j \in \mathbb{R}^{N_j}$, and the matrices: $D_j \in \mathbb{R}^{N_j \times N_j}$, $C_{ij} \in \mathbb{R}^{N_i \times N_j}$, $R_{ij} \in \mathbb{R}^{N_i \times N_j}$, defined as:

$$\begin{aligned}
(F_n)_j &= \int_S g_D D\bar{n}_{\mathcal{K}_j} \cdot \overline{\nabla}_h \psi_{n,\mathcal{K}_j} \, \mathrm{d}S, \\
(Q_n)_j &= \int_S g_M \psi_{n,\mathcal{K}_j} \, \mathrm{d}S, \\
(D_{nm})_j &= \int_{\mathcal{K}_i} D\overline{\nabla}_h \psi_{n,\mathcal{K}_j} \cdot \overline{\nabla}_h \psi_{m,\mathcal{K}_j} \, \mathrm{d}\mathcal{K}, \\
(C_{nm})_{ij} &= \int_S D\overline{\nabla}_h \psi_{n,\mathcal{K}_i} \cdot \bar{n}_{\mathcal{K}_j} \psi_{m,\mathcal{K}_j} \, \mathrm{d}S, \\
(R_{nm})_{ij} &= \int_S \alpha \psi_{n,\mathcal{K}_i} \psi_{m,\mathcal{K}_j} \, \mathrm{d}S,
\end{aligned}$$

and a slight extension for L_{ij}^k:

$$(L_{nm})_{ij,D}^k = \int_S \psi_{n,\mathcal{K}_i} \psi_{m,\mathcal{K}_j} (D\bar{n}_{\mathcal{K}_j})^k \, \mathrm{d}S.$$

Next, we describe the algorithm for assembling the linear system $M \in \mathbb{R}^{N\times N}$ related to the bilinear form (A.2) and the right hand side $R \in \mathbb{R}^N$ related to (A.3), with $N = \sum_{\mathcal{K}_j\in\mathcal{T}_h^n} N_j$.

Algorithm A.1 Algorithm for constructing the linear system for the diffusive part of the advection-diffusion equation.

- Initialize M to zero.
- Loop over all elements $\mathcal{K}_j \in \mathcal{T}_h^n$:

$$M_{jj} \leftarrow M_{jj} + D_j.$$

- Loop over all faces $S \in \mathcal{S}_I^n$, where S is the face shared by the elements $\mathcal{K}_i$ and $\mathcal{K}_j$:

$$\begin{aligned}
M_{ii} &\leftarrow M_{ii} - \frac{1}{2}\big(C_{ii} + C_{ii}^T\big) + \frac{1}{4}\eta_{\mathcal{K}}\big(\sum_k L_{ii,D}^k A_i^{-1} L_{ii}^k - \sum_k L_{ij,D}^k A_j^{-1} L_{ji}^k\big),\\
M_{ij} &\leftarrow M_{ij} - \frac{1}{2}\big(C_{ij} + C_{ji}^T\big) + \frac{1}{4}\eta_{\mathcal{K}}\big(\sum_k L_{ii,D}^k A_i^{-1} L_{ij}^k - \sum_k L_{ij,D}^k A_j^{-1} L_{jj}^k\big),\\
M_{ji} &\leftarrow M_{ji} - \frac{1}{2}\big(C_{ji} + C_{ij}^T\big) - \frac{1}{4}\eta_{\mathcal{K}}\big(\sum_k L_{ji,D}^k A_i^{-1} L_{ii}^k - \sum_k L_{jj,D}^k A_j^{-1} L_{ji}^k\big),\\
M_{jj} &\leftarrow M_{jj} - \frac{1}{2}\big(C_{jj} + C_{jj}^T\big) - \frac{1}{4}\eta_{\mathcal{K}}\big(\sum_k L_{ji,D}^k A_i^{-1} L_{ij}^k - \sum_k L_{jj,D}^k A_j^{-1} L_{jj}^k\big).
\end{aligned}$$

- Loop over all faces $S \in \mathcal{S}_D^n$, where S is a face on the boundary $\partial\mathcal{K}_j$:

$$\begin{aligned}
M_{jj} &\leftarrow M_{jj} - \big(C_{jj} + C_{jj}^T\big) + \eta_{\mathcal{K}}\big(\sum_k L_{jj,D}^k A_j^{-1} L_{jj}^k\big),\\
R_j &\leftarrow R_j - F_j + \eta_{\mathcal{K}}\big(\sum_k L_{jj,D}^k A_j^{-1} G_j^k\big).
\end{aligned}$$

- Loop over all faces $S \in \mathcal{S}_M^n$, where S is a face on the boundary $\partial\mathcal{K}_j$:

$$\begin{aligned}
M_{jj} &\leftarrow M_{jj} + R_{jj},\\
R_j &\leftarrow R_j + Q_j.
\end{aligned}$$

Here $\eta_{\mathcal{K}}$ is the stabilization parameter in each element $\mathcal{K}$ which is chosen such that $\eta_{\mathcal{K}} > N_f$, with N_f the number of faces on each element $\mathcal{K}$, which guarantees the stability of the space-time DG discretization, see Section 4.5 for the proof.

A.1.2 Algebraic system for the advective part

In this section we discuss the algebraic system for the advective part. To simplify the implementation, we consider the bilinear form $a_a(\cdot,\cdot)$ and the advective part of $\ell(\cdot)$ in a slightly different setting than given in (4.36) and (4.37), respectively. The upwind flux is now written in its usual form, instead of the one given in (4.19). In the space-time slab $\mathcal{E}^n$, the bilinear form $a_a(\cdot,\cdot)$ is written in the following form:

$$\begin{aligned} a_a(c_h, w) = &- \sum_{\mathcal{K}\in\mathcal{T}_h^n} \int_{\mathcal{K}} c_h \frac{\partial w}{\partial t} \,\mathrm{d}\mathcal{K} - \sum_{\mathcal{K}\in\mathcal{T}_h^n} \int_{\mathcal{K}} u c_h \cdot \overline{\nabla}_h w \,\mathrm{d}\mathcal{K} \\ &+ \sum_{S\in\mathcal{S}_I^n} \int_S c_h^a (u - u_g) \cdot \langle\!\langle w \rangle\!\rangle \,\mathrm{d}S + \sum_{\mathcal{K}\in\mathcal{T}_h^n} \int_{K_j^{n+1}} c_h w \,\mathrm{d}K \\ &+ \sum_{S\in\mathcal{S}_{MDSp}^n} \int_S (u - u_g) \cdot \bar{n} c_h w \,\mathrm{d}S, \end{aligned} \tag{A.7}$$

where c_h^a is either $c_{h,i}$ or $c_{h,j}$, depending on the direction of the flux on the face $S \in \mathcal{S}_I^n$, with S the face shared by the elements $\mathcal{K}_i$ and $\mathcal{K}_j$. If $(u-u_g)\cdot\bar{n}_i \geq 0$ with $\bar{n}_i$ the spatial part of the space-time normal vector n_i at $\partial\mathcal{K}_i$ then we choose $c_h^a = c_{h,i}$, while if $(u-u_g)\cdot\bar{n}_i < 0$ then $c_h^a = c_{h,j}$. The advective part of $\ell(\cdot)$ is written as:

$$\ell_a(w) = - \sum_{S\in\cup_n\mathcal{S}_{DBSm}^n} \int_S g_D (u - u_g)\cdot\bar{n} w \,\mathrm{d}S + \sum_{\mathcal{K}\in\mathcal{T}_h^n} \int_{K_j^n} c_h^{n-1} w \,\mathrm{d}K, \tag{A.8}$$

with c_h^{n-1} the solution c_h in the previous space-time slab $\mathcal{E}^{n-1}$. At $t = 0$ the solution c_h^{n-1} is replaced with c_0.

To discretize (A.7)-(A.8) we introduce the following vectors: $H_j \in \mathbb{R}^{N_j}$, $B_j \in \mathbb{R}^{N_j}$, and the matrices: $T_j \in \mathbb{R}^{N_j\times N_j}$, $V_j \in \mathbb{R}^{N_j\times N_j}$, $P_j \in \mathbb{R}^{N_j\times N_j}$, $E_{ij} \in \mathbb{R}^{N_i\times N_j}$, defined as:

$$\begin{aligned} (H_n)_j &= \int_S g_D (u - u_g)\cdot\bar{n}_{\mathcal{K}_j}\psi_{n,\mathcal{K}_j} \,\mathrm{d}S, \\ (B_n)_j &= \int_{K_j^n} c_h^{n-1}\psi_{n,\mathcal{K}_j} \,\mathrm{d}K, \\ (T_{nm})_j &= \int_{\mathcal{K}_j} \frac{\partial\psi_{n,\mathcal{K}_j}}{\partial t}\psi_{m,\mathcal{K}_j} \,\mathrm{d}\mathcal{K}, \\ (V_{nm})_j &= \int_{\mathcal{K}_j} \overline{\nabla}_h\psi_{n,\mathcal{K}_j}\cdot u\psi_{m,\mathcal{K}_j} \,\mathrm{d}\mathcal{K}, \\ (P_{nm})_j &= \int_{K_j^{n+1}} \psi_{n,\mathcal{K}_j}\psi_{m,\mathcal{K}_j} \,\mathrm{d}K, \\ (E_{nm})_{ij} &= \int_S (u - u_g)\cdot\bar{n}_{\mathcal{K}_i}\psi_{n,\mathcal{K}_i}\psi_{m,\mathcal{K}_j} \,\mathrm{d}S. \end{aligned}$$

Now we describe the algorithm for assembling the linear system M related to (A.7) and the vector R related to (A.8).

Algorithm A.2 Algorithm for constructing the linear system for the advective part of the advection-diffusion equation.

- Loop over all elements $\mathcal{K}_j \in \mathcal{T}_h^n$:

$$M_{jj} \leftarrow M_{jj} - T_j - V_j + P_j,$$
$$R_j \leftarrow R_j + B_j.$$

- Loop over all faces $S \in \mathcal{S}_I^n$, where S is the face shared by the elements $\mathcal{K}_i$ and $\mathcal{K}_j$:

  - If $(u - u_g) \cdot \bar{n}_i \geq 0$, with $\bar{n}_i$ the spatial part of the space-time normal vector n_i at $\partial\mathcal{K}_i$:

$$M_{ii} \leftarrow M_{ii} + E_{ii},$$
$$M_{ji} \leftarrow M_{ji} + E_{ji}.$$

  - If $(u - u_g) \cdot \bar{n}_i < 0$:

$$M_{ij} \leftarrow M_{ij} + E_{ij},$$
$$M_{jj} \leftarrow M_{jj} + E_{jj}.$$

- Loop over all faces $S \in \mathcal{S}_D^n$, where S is a face on the boundary $\partial\mathcal{K}_j$:

  - If $(u - u_g) \cdot \bar{n}_j \geq 0$:

$$M_{jj} \leftarrow M_{jj} + E_{jj}.$$

  - If $(u - u_g) \cdot \bar{n}_j < 0$:

$$R_j \leftarrow R_j - H_j.$$

- Loop over all faces $S \in \mathcal{S}_M^n$, where S is a face on the boundary $\partial\mathcal{K}_j$:

$$M_{jj} \leftarrow M_{jj} + E_{jj}.$$

A.2 Algebraic system for incompressible flows

In this section we present the algebraic equations for the space-time DG discretization of the Oseen equations in the space-time slab $\mathcal{E}^n$, discussed in Sections 5.4.2-5.4.3.

The approximations $u_h \in V_h^{(p_t,p_s)}$, $p_h \in \mathcal{Q}_h^{(p_t,p_s)}$ in each space-time element $\mathcal{K}_j$ are defined as follows:

$$u_h(x) = \sum_{n=0}^{N_j^u} \hat{U}_{n,\mathcal{K}_j} \psi_{n,\mathcal{K}_j}(x),$$
$$p_h(x) = \sum_{n=0}^{N_j^p} \hat{P}_{n,\mathcal{K}_j} \psi_{n,\mathcal{K}_j}(x), \tag{A.9}$$

with $\psi_{n,\mathcal{K}_j} \in \mathcal{Q}_{p_t,\mathcal{K},p_s,\mathcal{K}}(\hat{\mathcal{K}})$, where $\mathcal{Q}_{p_t,\mathcal{K},p_s,\mathcal{K}}(\hat{\mathcal{K}})$ is defined in Section 4.3.2, and N_j^u, N_j^p the number of polynomial coefficients for u_h and p_h, respectively. Similar expressions are used for the test functions $v \in V_h^{(p_t,p_s)}$ and $q \in \mathcal{Q}_h^{(p_t,p_s)}$.

A.2.1 Algebraic system for the diffusive and convective parts

First, we recall the bilinear form $\mathcal{A}_h(\cdot,\cdot)$, given in (5.41), but written in the following form:

$$\begin{aligned}\mathcal{A}_h(u_h, v) = &\sum_{\mathcal{K}\in\mathcal{T}_h^n} \int_{\mathcal{K}} \nu \overline{\nabla}_h u_h : \overline{\nabla}_h v \, \mathrm{d}\mathcal{K} \\ &- \sum_{S\in\cup_n \mathcal{S}_{ID}^n} \int_S \left(\nu \langle\!\langle u_h \rangle\!\rangle : \{\!\{ \overline{\nabla}_h v \}\!\} + \nu \{\!\{ \overline{\nabla}_h u_h \}\!\} : \langle\!\langle v \rangle\!\rangle \right) \mathrm{d}S \\ &+ \sum_{S\in\cup_n \mathcal{S}_{ID}^n} \eta_{\mathcal{K}}^u \int_S \nu \bar{\mathcal{L}}_S(\langle\!\langle u_h \rangle\!\rangle) : \langle\!\langle v \rangle\!\rangle \, \mathrm{d}S,\end{aligned} \tag{A.10}$$

and the corresponding linear form $F_h(\cdot)$, given in (5.44):

$$\begin{aligned}F_h(v) = &- \sum_{S\in\cup_n \mathcal{S}_D^n} \int_S \nu g_D \otimes \bar{n} : \overline{\nabla}_h v \, \mathrm{d}S \\ &+ \sum_{S\in\cup_n \mathcal{S}_D^n} \eta_{\mathcal{K}}^u \int_S \nu \bar{\mathcal{L}}_S(\mathcal{P} g_D \otimes \bar{n}) : v \otimes \bar{n} \, \mathrm{d}S + \sum_{S\in\cup_n \mathcal{S}_N^n} \int_S \nu g_N \cdot v \, \mathrm{d}S.\end{aligned} \tag{A.11}$$

These forms are the space-time DG discretization for the diffusive terms in the Oseen equations. Comparing the form A_h with the form a_d in Section A.1.1, we notice that the form A_h is an extension of the form a_d to the vector functions. Hence, all terms discussed for the algebraic equations generated by a_d can be used for the l-th component of u_h by replacing the diagonal terms in the diffusion coefficient matrix D with the viscosity coefficient ν and setting the other contributions equal to zero, and replacing the function g_M on the face $S \in \mathcal{S}_N^n$ with g_N. The same applies for the form ℓ_d in Section A.1.1 and F_h.

For the definition of the linear system for the l-th component of u_h, given by (A.10)-(A.11), we introduce the matrix $M^l \in \mathbb{R}^{N^u \times N^u}$ and the vector $R^l \in \mathbb{R}^{N^u}$,

where $N^u = \sum_{\mathcal{K}_j \in \mathcal{T}_h^n} N_j^u$. The algorithm for assembling the linear system M^l and the vector R^l then follows Algorithm A.1.

Next, we recall the trilinear form $\mathcal{O}_h(\cdot,\cdot;\cdot)$ given in (5.40), but reformulated in ALE form, as follows:

$$\begin{aligned}\mathcal{O}_h(u_h, v; w) = &- \sum_{\mathcal{K}\in\mathcal{T}_h^n} \int_{\mathcal{K}} u_h \cdot \frac{\partial v}{\partial t} \,\mathrm{d}\mathcal{K} - \sum_{\mathcal{K}\in\mathcal{T}_h^n} \int_{\mathcal{K}} u_h \otimes w : \overline{\nabla}_h v \,\mathrm{d}\mathcal{K} \\ &+ \sum_{\mathcal{K}\in\mathcal{T}_h^n} \int_{K_j^{n+1}} u_h v \,\mathrm{d}K + \sum_{S\in\mathcal{S}_I^n} \int_S u_h^a \otimes (w - u_g) : \langle\!\langle v \rangle\!\rangle \,\mathrm{d}S \\ &+ \sum_{S\in\mathcal{S}_{Dp}^n} \int_S u_h \otimes (w - u_g) : v \otimes \bar{n} \,\mathrm{d}S \\ &+ \sum_{S\in\mathcal{S}_N^n} \int_S u_h \otimes (w - u_g) : v \otimes \bar{n} \,\mathrm{d}S, \end{aligned} \tag{A.12}$$

with u_g the mesh velocity introduced in Section 4.4.2. The solution u_h^a is either $u_{h,i}$ or $u_{h,j}$, depending of the direction of the flux on a face $S \in \mathcal{S}_I^n$, where S is the face shared by the elements $\mathcal{K}_i$ and $\mathcal{K}_j$. If $(u-u_g)\cdot\bar{n}_i \geq 0$ with $\bar{n}_i$ the spatial par of the space-time normal vector n_i at $\partial\mathcal{K}_i$ then we choose $u_h^a = u_{h,i}$, while if $(u - u_g)\cdot\bar{n}_i < 0$ then $u_h^a = u_{h,j}$. The corresponding linear form $N_h(\cdot)$, given in (5.43), is now formulated in ALE form as follows:

$$N_h(v) = - \sum_{S\in\cup_n\mathcal{S}_{Dm}^n} \int_S g_D \otimes (w - u_g) : v \otimes \bar{n} \,\mathrm{d}S + \sum_{\mathcal{K}\in\mathcal{T}_h^n} \int_{K_j^n} u_h^{n-1} \cdot v \,\mathrm{d}S, \tag{A.13}$$

where u_h^{n-1} denotes the solution in the previous space-time slab $\mathcal{E}^{n-1}$, and at $t = 0$ this solution is replaced with the initial solution u_0.

Similar to the diffusive part, we also recognize that the form $\mathcal{O}_h$ is an extension to vector functions of the form a_a. Hence, all terms discussed for the algebraic equations generated by a_a can be used for each component of u_h in $\mathcal{O}_h$ by replacing the advective field u in each term with the velocity field w. The same applies for the form ℓ_a in Section A.1.2 and N_h. The algorithm for assembling the linear system M^l for $\mathcal{O}_h$ and the right hand side R^l for N_h follows directly from Algorithm A.2.

A.2.2 Algebraic system for the pressure term and incompressibility constraint

First, we recall the bilinear form $\mathcal{B}_h$, given in (5.42), which is related to the space-time DG discretization of the pressure term and the incompressibility constraint in the Oseen equations:

$$\mathcal{B}_h(p_h, v) = - \sum_{\mathcal{K}\in\mathcal{T}_h^n} \int_{\mathcal{K}} p_h \overline{\nabla}_h \cdot v \,\mathrm{d}\mathcal{K} + \sum_{S\in\cup_n\mathcal{S}_{ID}^n} \int_S \{\!\{p_h\}\!\} \langle\!\langle v \rangle\!\rangle \,\mathrm{d}S. \tag{A.14}$$

To discretize the l-th component of v in (A.14) we introduce the following matrices: $W_j^l \in \mathbb{R}^{N_j^u \times N_j^p}$ and $Z_{ij}^l \in \mathbb{R}^{N_i^u \times N_j^p}$:

$$(W_{nm})_j^l = \int_{\mathcal{K}} \frac{\partial \psi_{n,\mathcal{K}_j}}{\partial x_l} \psi_{m,\mathcal{K}_j} \, \mathrm{d}\mathcal{K},$$
$$(Z_{nm})_{ij}^l = \int_S n_{\mathcal{K}_i}^l \psi_{n,\mathcal{K}_i} \psi_{m,\mathcal{K}_j} \, \mathrm{d}S.$$

Next, we consider the linear forms G_h and H_h, given in (5.45) and in (5.54), respectively:

$$G_h(v) = \sum_{\mathcal{K} \in \mathcal{T}_h^n} \int_{\mathcal{K}} f \cdot v \, \mathrm{d}\mathcal{K} - \sum_{S \in \cup_n \mathcal{S}_N^n} \int_S p_N v \cdot \bar{n} \, \mathrm{d}S, \tag{A.15}$$

$$H_h(q) = - \sum_{S \in \cup_n \mathcal{S}_D^n} \int_S g_D \cdot \bar{n} q \, \mathrm{d}S. \tag{A.16}$$

To discretize each component of v in (A.15)-(A.16), we introduce the following vectors: $F_{j,f}^l \in \mathbb{R}^{N_j^u}$, $P_j^l \in \mathbb{R}^{N_j^p}$, and $T_j \in \mathbb{R}^{N_j^p}$:

$$(F_n)_{j,f}^l = \int_{\mathcal{K}_j} f^l \psi_{n,\mathcal{K}_j} \, \mathrm{d}\mathcal{K},$$
$$(P_n)_j^l = \int_S p_N \psi_{n,\mathcal{K}_j} n_{\mathcal{K}_j}^l \, \mathrm{d}S,$$
$$(T_n)_j = \int_S g_D \cdot \bar{n}_{\mathcal{K}_j} \psi_{n,\mathcal{K}_j} \, \mathrm{d}S,$$

with f^l the l-th component of the force vector f.

For the l-th component of v in (A.14)-(A.15), we introduce a matrix $M_B^l \in \mathbb{R}^{N^u \times N^p}$ and vectors $R_B^l \in \mathbb{R}^{N^u}$, $R_C \in \mathbb{R}^{N^p}$, where $N^p = \sum_{\mathcal{K}_j \in \mathcal{T}_h^n} N_j^p$. The algorithm for assembling the linear system M_B^l related to (A.14) and the right hand sides R_B^l and R_C related to (A.15) and (A.16), respectively, can now be summarized as follows.

Algorithm A.3 Algorithm for constructing the linear system for the pressure contribution in the Oseen equations.

- Initialize M_B^l to zero.
- Loop over all elements $\mathcal{K}_j \in \mathcal{T}_h^n$:

$$M_{jj,B}^l \leftarrow M_{jj,B}^l - W_j^l,$$
$$R_{j,B}^l \leftarrow R_{j,B}^l + F_{j,f}^l.$$

- Loop over all faces $S \in \mathcal{S}_I^n$, where S is the face shared by the elements $\mathcal{K}_i$ and $\mathcal{K}_j$:

$$\begin{aligned} M_{ii,B}^l &\leftarrow M_{ii,B}^l + Z_{ii}^l, \\ M_{ij,B}^l &\leftarrow M_{ij,B}^l + Z_{ij}^l, \\ M_{ji,B}^l &\leftarrow M_{ji,B}^l + Z_{ji}^l, \\ M_{jj,B}^l &\leftarrow M_{jj,B}^l + Z_{jj}^l. \end{aligned}$$

- Loop over all faces $S \in \mathcal{S}_D^n$, where S is a face on the boundary $\partial\mathcal{K}_j$:

$$\begin{aligned} M_{jj,B}^l &\leftarrow M_{jj,B}^l + Z_{jj}^l, \\ R_{j,C} &\leftarrow R_{j,C} + T_j. \end{aligned}$$

- Loop over all faces $S \in \mathcal{S}_N^n$, where S is a face on the boundary $\partial\mathcal{K}_j$:

$$R_{j,B}^l \leftarrow R_{j,B}^l + P_j^l.$$

A.2.3 Algebraic system for the stability term

Two types of stabilization terms are considered in Section (A.2.3). First, we consider the stabilization term with the jump, given in (5.52):

$$\mathcal{C}_h^{(1)}(p_h, q) = \sum_{S \in \cup_n \mathcal{S}_I^n} \int_S \gamma \langle\!\langle p_h \rangle\!\rangle \cdot \langle\!\langle q \rangle\!\rangle \, \mathrm{d}S. \tag{A.17}$$

In order to discretize this term, we introduce the following matrix: $Y_{ij} \in \mathbb{R}^{N_i^p \times N_j^p}$, with:

$$(Y_{nm})_{ij} = \int_S \gamma \bar{n}_{\mathcal{K}_i} \cdot \bar{n}_{\mathcal{K}_j} \psi_{n,\mathcal{K}_i} \psi_{n,\mathcal{K}_j} \, \mathrm{d}S. \tag{A.18}$$

We then construct a matrix $M_C^{(1)} \in \mathbb{R}^{N^p \times N^p}$ related to the stabilization operator in (A.17) as follows.

Algorithm A.4 Algorithm for constructing the linear system for the stabilization term $\mathcal{C}_h^{(1)}$.

- Initialize $M_C^{(1)}$ to zero.
- Loop over all faces $S \in \mathcal{S}_I^n$, where S is shared by the elements $\mathcal{K}_i$ and $\mathcal{K}_j$:

$$\begin{aligned} M_{ii,C}^{(1)} &\leftarrow M_{ii,C}^{(1)} + Y_{ii}, \\ M_{ij,C}^{(1)} &\leftarrow M_{ij,C}^{(1)} + Y_{ij}, \\ M_{ji,C}^{(1)} &\leftarrow M_{ji,C}^{(1)} + Y_{ji}, \\ M_{jj,C}^{(1)} &\leftarrow M_{jj,C}^{(1)} + Y_{jj}. \end{aligned}$$

Next, we consider the stabilization term with the lifting operator, given by (5.53):

$$\mathcal{C}_h^{(2)}(p_h, q) = \sum_{S \in \cup_n \mathcal{S}_I^n} \int_S \alpha \{\!\{ \bar{\mathcal{L}}_S(\langle\!\langle p_h \rangle\!\rangle) \}\!\} \cdot \langle\!\langle q \rangle\!\rangle \, \mathrm{d}S. \tag{A.19}$$

The lifting operator $\bar{\mathcal{L}}_S(\langle\!\langle p_h \rangle\!\rangle)$ has a similar expression as the lifting operator $\bar{r}_S$ in Section A.1.1, only the sign is different, and we do not discuss this operator in detail. The linear system $M_C^{(2)} \in \mathbb{R}^{N^p \times N^p}$ related to the stabilization operator in (A.19) is constructed as follows:

Algorithm A.5 Algorithm for constructing the linear system for the stabilization term $\mathcal{C}_h^{(2)}$.

- Initialize $M_C^{(2)}$ to zero.
- Loop over all faces $S \in \mathcal{S}_I^n$, where S is the face shared by the elements $\mathcal{K}_i$ and $\mathcal{K}_j$:

$$\begin{aligned}
M_{ii,C}^{(2)} &\leftarrow M_{ii,C}^{(2)} - \frac{1}{4}\alpha\Big(\sum_k L_{ii}^k A_i^{-1} L_{ii}^k - \sum_k L_{ij}^k A_j^{-1} L_{ji}^k\Big),\\
M_{ij,C}^{(2)} &\leftarrow M_{ij,C}^{(2)} - \frac{1}{4}\alpha\Big(\sum_k L_{ii}^k A_i^{-1} L_{ij}^k - \sum_k L_{ij}^k A_j^{-1} L_{jj}^k\Big),\\
M_{ji,C}^{(2)} &\leftarrow M_{ji,C}^{(2)} + \frac{1}{4}\alpha\Big(\sum_k L_{ji}^k A_i^{-1} L_{ii}^k - \sum_k L_{jj}^k A_j^{-1} L_{ji}^k\Big),\\
M_{jj,C}^{(2)} &\leftarrow M_{jj,C}^{(2)} + \frac{1}{4}\alpha\Big(\sum_k L_{ji}^k A_i^{-1} L_{ij}^k - \sum_k L_{jj}^k A_j^{-1} L_{jj}^k\Big).
\end{aligned}$$

With the discretizations for all terms in the Oseen equations defined in the Algorithms A.1-A.5, we can present now the complete linear system:

$$\begin{pmatrix} M^1 & \dots & \mathbb{O} & M_B^1 \\ \vdots & \ddots & \vdots & \vdots \\ \mathbb{O} & \dots & M^d & M_B^d \\ (M_B^1)^T & \dots & (M_B^d)^T & M_C^{(i)} \end{pmatrix} \begin{pmatrix} u_h^1 \\ \vdots \\ u_h^d \\ p_h \end{pmatrix} = \begin{pmatrix} R^1 + R_B^1 \\ \vdots \\ R^d + R_B^d \\ R_C \end{pmatrix} \tag{A.20}$$

Appendix B

Anisotropic Interpolation Error Estimates

B.1 Preliminaries

In this appendix, we derive in more detail the anisotropic interpolation error estimates discussed in Section 4.6.1. The derivations follow the analysis in [31], but are extended to general dimensions, such that they can be applied in the analysis of the space-time discretization.

First, we recall the construction of the space-time elements $\mathcal{K}$ introduced in Section 4.3.2. Each space-time element $\mathcal{K}$ is the image of a fixed master element $\hat{\mathcal{K}}$, with $\hat{\mathcal{K}}$ an open unit hypercube in $\mathbb{R}^{d+1}$. We define in $\hat{\mathcal{K}}$ reference coordinates $\hat{x} = (\hat{x}_0, \hat{x}_1, \ldots, \hat{x}_d)$. The space-time element $\mathcal{K}$ is constructed via two mappings $F_{\mathcal{K}}$ and $Q_{\mathcal{K}}$, where $F_{\mathcal{K}} : \hat{\mathcal{K}} \to \tilde{\mathcal{K}}$ is an affine mapping and $Q_{\mathcal{K}} : \tilde{\mathcal{K}} \to \mathcal{K}$ is a (regular enough) diffeomorphism (see Fig. 4.2). The element $\tilde{\mathcal{K}}$ is defined with respect to the coordinates $\tilde{x} = (\tilde{x}_0, \tilde{x}_1, \ldots, \tilde{x}_d)$. We denote by $h_i, i = 1, \ldots, d$ the edge length of $\tilde{\mathcal{K}}$ in the x_i direction, and $\triangle_n t$ the edge length in the x_0 direction. The boundaries $\partial\hat{\mathcal{K}}_i, \partial\tilde{\mathcal{K}}_i, \partial\mathcal{K}_i$ denote the boundary face with respectively the $\hat{x}_i, \tilde{x}_i$, and x_i coordinate constant.

We also recall the definition of anisotropic Sobolev spaces given in Section 4.3.2. Note that the definition of anisotropy is restricted to the case where the Sobolev index can be different for the temporal and spatial variables. All spatial variables have, however, the same index.

Definition B.1 Let (s_t, s_s) be a pair of non-negative integers, where s_t, s_s correspond to the temporal and spatial Sobolev index, respectively. The anisotropic Sobolev space of order (s_t, s_s) on an element $\tilde{\mathcal{K}}$ is defined as

$$H^{(s_t,s_s)}(\tilde{\mathcal{K}}) := \{w \in L^2(\tilde{\mathcal{K}}) : \partial^{\gamma_t}\partial^{\gamma_s} w \in L^2(\tilde{\mathcal{K}}) \text{ for } 0 \leq \gamma_t \leq s_t, 0 \leq |\gamma_s| \leq s_s\},$$

while on an element $\mathcal{K}$, the anisotropic Sobolev space is defined as

$$H^{(s_t,s_s)}(\mathcal{K}) := \{w \in L^2(\mathcal{K}) : w \circ Q_{\mathcal{K}} \in H^{(s_t,s_s)}(\tilde{\mathcal{K}})\}.$$

Next, we introduce the spaces of polynomials associated with the finite element spaces given in Section 4.3.2.

Definition B.2 Let $\hat{I} \equiv (-1,1)$ and $\hat{\mathcal{K}} \equiv (-1,1)^{d+1}$. On the interval $\hat{I}$ we define the space of polynomials $P_p(\hat{I})$ by

$$P_p(\hat{I}) := \text{span}\{\hat{x}^i : i = 0,\dots,p\}.$$

Furthermore, we define the anisotropic tensor-product polynomial space $\mathcal{Q}_{p_{t,\mathcal{K}},p_{s,\mathcal{K}}}(\hat{\mathcal{K}})$ by

$$\begin{aligned}\mathcal{Q}_{p_{t,\mathcal{K}},p_{s,\mathcal{K}}}(\hat{\mathcal{K}}) :=& P_{p_{t,\mathcal{K}}}(\hat{I}) \otimes \underbrace{P_{p_{s,\mathcal{K}}}(\hat{I}) \otimes \ldots \otimes P_{p_{s,\mathcal{K}}}(\hat{I})}_{d\times} \\ =& \text{span}\{\hat{x}_0^i \hat{x}_1^{m_1} \ldots \hat{x}_d^{m_d} : i = 0,\dots,p_{t,\mathcal{K}}; m_1,\dots,m_d = 0,\dots,p_{s,\mathcal{K}}\},\end{aligned}$$

where $p_{t,\mathcal{K}}, p_{s,\mathcal{K}}$ are local polynomial degrees, in time and space, respectively.

We introduce a one-dimensional L^2 projection operator in the following definition.

Definition B.3 Let $\hat{u} \in L^2(\hat{I})$ and let $P_p(\hat{I})$ be the space of polynomials on $\hat{I}$ of degree p or less. We define the L^2 projection operator

$$\hat{\pi}_p : L^2(\hat{I}) \to P_p(\hat{I}),$$

by

$$\hat{\pi}_p \hat{u}(x) := \sum_{n=0}^{p} a_n L_n(x),$$

where

$$a_n = \frac{2n+1}{2} \int_I \hat{u}(x) L_n(x)\ \mathrm{d}x,$$

with L_n the Legendre polynomial of degree n defined on $\hat{I}$. It is easy to show that the linear operator $\hat{\pi}_p$ is idempotent with norm $\|\hat{\pi}_p\|_{L^2(\hat{I})\to P_p(\hat{I})} = 1$.

The following lemma, which is taken from [31] (Lemmas 3.2, 3.3, and 3.5), states several one-dimensional estimates.

Lemma B.4 *Let $\hat{u} \in H^{k+1}(\hat{I})$, with integer $k \geq 0$. Let $\hat{\pi}_p\hat{u}$ be the L^2-projection of $\hat{u}$ onto $P_p(\hat{I})$, $p \geq 0$. Then for every integer s, with $0 \leq s \leq \min(p+1, k+1)$, we have the estimates:*

$$\|\hat{u} - \hat{\pi}_p\hat{u}\|_{0,\hat{I}} \leq \Phi_1(p+1,s)\|\hat{u}^{(s)}\|_{0,\hat{I}}, \tag{B.1}$$

with $\hat{u}^{(s)} = \frac{d^s \hat{u}}{dx^s}$*, and for every integer* t*, with* $0 \leq t \leq \min(p, k)$*:*

$$\|\hat{\pi}_p \hat{u}' - (\hat{\pi}_p \hat{u})'\|_{0,\hat{I}} \leq C_p^{L^2} \Phi_1(p,t) \|\hat{u}^{(t+1)}\|_{0,\hat{I}}, \tag{B.2}$$

where the parameter $C_p^{L^2}$ *depends on* p*, with* $C_0^{L^2} = 0$*,* $C_1^{L^2} = 36/15$*, and* $C_p^{L^2} = \sqrt{2p+2}$*, and a prime denotes differentiation. Moreover, we have*

$$\|\hat{u}' - (\hat{\pi}_p \hat{u})'\|_{0,\hat{I}} \leq (1 + C_p^{L^2}) \Phi_1(p,t) \|\hat{u}^{(t+1)}\|_{0,\hat{I}}, \tag{B.3}$$

with $\Phi_1(p,s) := \left(\frac{\Gamma(p-s+1)}{\Gamma(p+s+1)}\right)^{\frac{1}{2}}$*, and* Γ *the gamma function, see for instance [1]. At the boundary of* $\hat{I}$*, we have the following estimate:*

$$|\hat{u} - \hat{\pi}_p \hat{u}(\pm 1)| \leq \frac{\Phi_1(p,t)}{\sqrt{2p+1}} \|\hat{u}^{(t+1)}\|_{0,\hat{I}}. \tag{B.4}$$

We also introduce the projection operator $\hat{\mathcal{P}} : L^2(\hat{\mathcal{K}}) \to \mathcal{Q}_{p_{t,\mathcal{K}}, p_{s,\mathcal{K}}}(\hat{\mathcal{K}})$.

Definition B.5 Let $\hat{\mathcal{K}} \equiv (-1,1)^{d+1}$. We define the L^2-projection operator

$$\hat{\mathcal{P}} : L^2(\hat{\mathcal{K}}) \to \mathcal{Q}_{p_{t,\mathcal{K}}, p_{s,\mathcal{K}}}(\hat{\mathcal{K}}),$$

by

$$\hat{\mathcal{P}} := \hat{\pi}^0_{p_t} \hat{\pi}^1_{p_s} \dots \hat{\pi}^d_{p_s},$$

where $\hat{\pi}^0_{p_t}, \hat{\pi}^1_{p_s}, \dots, \hat{\pi}^d_{p_s}$ denote the one-dimensional L^2 projection given in Definition B.3. The superscripts $0, 1, \dots, d$ refer to the coordinate direction in which the one-dimensional projection is applied.

In the following lemma, we present a trace inequality for an anisotropic element. This lemma is a direct extension from [31], Lemma A.1, to a space-time discretization in $d+1$ dimensions.

Lemma B.6 *Let* $\tilde{u} \in H^{(k_t,k_s)}(\tilde{\mathcal{K}})$ *with* $k_t, k_s \geq 1$*,* $\tilde{\mathcal{K}}$ *an axiparallel element, with* $\triangle_n t, h_1, \dots, h_d$ *the length of its edges. Then the following trace inequality holds:*

$$\|\tilde{u}\|^2_{0,\partial\tilde{\mathcal{K}}_i} \leq \frac{2}{h_i} \|\tilde{u}\|^2_{0,\tilde{\mathcal{K}}} + 4 \|\tilde{u}\|_{0,\tilde{\mathcal{K}}} \|\tilde{\partial}_i \tilde{u}\|_{0,\tilde{\mathcal{K}}},$$

for $i = 0, \dots, d$*, and* $h_0 = \triangle_n t$*.*

The next lemma, which provides scaling identities between Sobolev seminorms on the reference element $\hat{\mathcal{K}}$ and on the axiparallel element $\tilde{\mathcal{K}}$, will be needed for deriving estimates on a space-time element $\mathcal{K}$. This lemma is a direct extension from [31], Lemma A.3, to a space-time discretization in $d+1$ dimensions.

Lemma B.7 *Let $\tilde{u} \in H^{(k_t,k_s)}(\tilde{\mathcal{K}})$, and $\tilde{\mathcal{K}}$ an axiparallel element with $\triangle_n t, h_1, \ldots, h_d$ the length of its edges. On element $\tilde{\mathcal{K}}$, the following scaling identity holds for $0 \leq l \leq k_t$, $0 \leq m_1, \ldots, m_d \leq k_s$:*

$$\|\hat{\partial}_0^l \hat{\partial}_1^{m_1} \ldots \hat{\partial}_d^{m_d} \hat{u}\|_{0,\hat{\mathcal{K}}}^2 = \Big(\frac{\triangle_n t}{2}\Big)^{2l-1} \Big(\frac{h_1}{2}\Big)^{2m_1-1} \ldots \Big(\frac{h_d}{2}\Big)^{2m_d-1} \|\tilde{\partial}_0^l \tilde{\partial}_1^{m_1} \ldots \tilde{\partial}_d^{m_d} \tilde{u}\|_{0,\tilde{\mathcal{K}}}^2,$$

where $\hat{u} := \tilde{u} \circ F_{\mathcal{K}}$ and $\hat{\partial}_i, \tilde{\partial}_i$ denote the partial derivatives in respectively the $\hat{x}_i$ and $\tilde{x}_i$ coordinate directions. On the part of the element boundary $\partial\tilde{\mathcal{K}}_i$ with $i = 1, \ldots, d$, we have:

$$\|\hat{\partial}_0^l \hat{\partial}_1^{m_1} \ldots \hat{\partial}_d^{m_d} \hat{u}\|_{0,\partial\hat{\mathcal{K}}_i}^2 = \Big(\frac{\triangle_n t}{2}\Big)^{2l-1} \Big(\frac{h_i}{2}\Big) \Big(\frac{h_1}{2}\Big)^{2m_1-1} \ldots \Big(\frac{h_d}{2}\Big)^{2m_d-1} \|\tilde{\partial}_0^l \tilde{\partial}_1^{m_1} \ldots \tilde{\partial}_d^{m_d} \tilde{u}\|_{0,\partial\tilde{\mathcal{K}}_i}^2, \tag{B.5}$$

and on the boundary $\partial\tilde{\mathcal{K}}_0$ we have:

$$\|\hat{\partial}_0^l \hat{\partial}_1^{m_1} \ldots \hat{\partial}_d^{m_d} \hat{u}\|_{0,\partial\hat{\mathcal{K}}_0}^2 = \Big(\frac{\triangle_n t}{2}\Big)^{2l} \Big(\frac{h_1}{2}\Big)^{2m_1-1} \ldots \Big(\frac{h_d}{2}\Big)^{2m_d-1} \|\tilde{\partial}_0^l \tilde{\partial}_1^{m_1} \ldots \tilde{\partial}_d^{m_d} \tilde{u}\|_{0,\partial\tilde{\mathcal{K}}_0}^2. \tag{B.6}$$

B.2 Interpolation error estimates on the reference element

In this section we discuss the interpolation error estimates on the reference element $\hat{\mathcal{K}}$. The first two lemmas are extensions to a space-time discretization in $d+1$ dimensions of the result given in [31], Lemma 3.7.

Lemma B.8 *Let $\hat{u} \in H^{(k_t+1,k_s+1)}(\hat{\mathcal{K}})$ and $k_t, k_s \geq 0$. Let $\hat{\mathcal{P}}\hat{u}$ be the L^2-projection of $\hat{u}$ onto $\mathcal{Q}_{p_{t,\mathcal{K}},p_{s,\mathcal{K}}}(\hat{\mathcal{K}})$. Then we have an estimate*

$$\|\hat{u} - \hat{\mathcal{P}}\hat{u}\|_{0,\hat{\mathcal{K}}} \leq \Phi_1(p_{s,\mathcal{K}} + 1, s_{\mathcal{K}}) \sum_{i=1}^{d} \|\hat{\partial}_i^{s_{\mathcal{K}}} \hat{u}\|_{0,\hat{\mathcal{K}}} + \Phi_1(p_{t,\mathcal{K}} + 1, s_{0,\mathcal{K}}) \|\hat{\partial}_0^{s_{0,\mathcal{K}}} \hat{u}\|_{0,\hat{\mathcal{K}}}, \tag{B.7}$$

with $0 \leq s_{\mathcal{K}} \leq \min(p_{s,\mathcal{K}} + 1, k_s + 1)$ and $0 \leq s_{0,\mathcal{K}} \leq \min(p_{t,\mathcal{K}} + 1, k_t + 1)$.

Proof . We show the proof for $d = 3$. The proof for other dimensions is similar. Using the tensor product nature of the projection operator, we decompose $\hat{u} - \hat{\mathcal{P}}\hat{u}$ as

$$\hat{u} - \hat{\mathcal{P}}\hat{u} = \hat{u} - \hat{\pi}_{p_t}^0 \hat{u} + \hat{\pi}_{p_t}^0 \Big(\hat{u} - \hat{\pi}_{p_s}^1 \hat{u} + \hat{\pi}_{p_s}^1 \big(\hat{u} - \hat{\pi}_{p_s}^2 \hat{u} + \hat{\pi}_{p_s}^2 (\hat{u} - \hat{\pi}_{p_s}^3 \hat{u}) \big) \Big),$$

and apply the triangle inequality to obtain

$$\begin{aligned} \|\hat{u} - \hat{\mathcal{P}}\hat{u}\|_{0,\hat{\mathcal{K}}} \leq & \|\hat{u} - \hat{\pi}_{p_t}^0 \hat{u}\|_{0,\hat{\mathcal{K}}} + \|\hat{\pi}_{p_t}^0 (\hat{u} - \hat{\pi}_{p_s}^1 \hat{u})\|_{0,\hat{\mathcal{K}}} \\ & + \|\hat{\pi}_{p_t}^0 \hat{\pi}_{p_s}^1 (\hat{u} - \hat{\pi}_{p_s}^2 \hat{u})\|_{0,\hat{\mathcal{K}}} + \|\hat{\pi}_{p_t}^0 \hat{\pi}_{p_s}^1 \hat{\pi}_{p_s}^2 (\hat{u} - \hat{\pi}_{p_s}^3 \hat{u})\|_{0,\hat{\mathcal{K}}}. \end{aligned}$$

Since the projection operators $\hat{\pi}^0_{p_t}, \hat{\pi}^1_{p_s}, \hat{\pi}^2_{p_s}, \hat{\pi}^3_{p_s}$ are bounded with norm equal to one, we then obtain:

$$\|\hat{u} - \hat{\mathcal{P}}\hat{u}\|_{0,\hat{\mathcal{K}}} \leq \sum_{i=1}^{3} \|\hat{u} - \hat{\pi}^i_{p_s}\hat{u}\|_{0,\hat{\mathcal{K}}} + \|\hat{u} - \hat{\pi}^0_{p_t}\hat{u}\|_{0,\hat{\mathcal{K}}}.$$

Using Fubini's theorem to separate the integrals in the norms on the right-hand side into a product of one dimensional integrals and applying (B.1) to each term completes the proof. □

Lemma B.9 *Let $\hat{u} \in H^{(k_t+1,k_s+1)}(\hat{\mathcal{K}})$ and $k_t, k_s \geq 0$. Let $\hat{\mathcal{P}}\hat{u}$ be the L^2-projection of $\hat{u}$ onto $\mathcal{Q}_{p_{t,\mathcal{K}},p_{s,\mathcal{K}}}(\hat{\mathcal{K}})$. Denoting the partial derivative in the $\hat{x}_i$ direction as $\hat{\partial}_i$, for $i = 1, \ldots, d$, we have the following estimate:*

$$\begin{aligned}\|\hat{\partial}_i(\hat{u} - \hat{\mathcal{P}}\hat{u})\|_{0,\hat{\mathcal{K}}} \leq & (1 + C^{L^2}_{p_{s,\mathcal{K}}})\Phi_1(p_{s,\mathcal{K}}, t_{\mathcal{K}})\|\hat{\partial}_i^{t_{\mathcal{K}}+1}\hat{u}\|_{0,\hat{\mathcal{K}}} \\ & + \Phi_1(p_{s,\mathcal{K}}+1, q_{\mathcal{K}}) \sum_{j=1, j\neq i}^{d} \|\hat{\partial}_j^{q_{\mathcal{K}}}\hat{\partial}_i\hat{u}\|_{0,\hat{\mathcal{K}}} \\ & + \Phi_1(p_{t,\mathcal{K}}+1, q_{0,\mathcal{K}})\|\hat{\partial}_0^{q_{0,\mathcal{K}}}\hat{\partial}_i\hat{u}\|_{0,\hat{\mathcal{K}}}, \end{aligned} \tag{B.8}$$

with $0 \leq q_{\mathcal{K}} \leq \min(p_{s,\mathcal{K}}+1, k_s)$, $0 \leq q_{0,\mathcal{K}} \leq \min(p_{t,\mathcal{K}}+1, k_t)$, and $0 \leq t_{\mathcal{K}} \leq \min(p_{s,\mathcal{K}}, k_s)$.

Proof . We show the proof for $d = 3$ and $i = 1$. The proof for the other coordinate directions and dimensions is similar. We have:

$$\|\hat{\partial}_1(\hat{u} - \hat{\mathcal{P}}\hat{u})\|_{0,\hat{\mathcal{K}}} \leq \|\hat{\partial}_1\hat{u} - \hat{\mathcal{P}}(\hat{\partial}_1\hat{u})\|_{0,\hat{\mathcal{K}}} + \|\hat{\mathcal{P}}(\hat{\partial}_1\hat{u}) - \hat{\partial}_1\hat{\mathcal{P}}\hat{u}\|_{0,\hat{\mathcal{K}}} = T_1 + T_2.$$

Using Lemma B.8 with $\hat{u}$ replaced by $\hat{\partial}_1\hat{u}$, the term T_1 is bounded as follows

$$\begin{aligned} T_1 \leq & \Phi_1(p_{s,\mathcal{K}}+1, t_{\mathcal{K}})\|\hat{\partial}_1^{t_{\mathcal{K}}+1}\hat{u}\|_{0,\hat{\mathcal{K}}} + \Phi_1(p_{s,\mathcal{K}}+1, q_{\mathcal{K}}) \sum_{j=2,3} \|\hat{\partial}_j^{q_{\mathcal{K}}}\hat{\partial}_1\hat{u}\|_{0,\hat{\mathcal{K}}} \\ & + \Phi_1(p_{t,\mathcal{K}}+1, q_{0,\mathcal{K}})\|\hat{\partial}_0^{q_{0,\mathcal{K}}}\hat{\partial}_1\hat{u}\|_{0,\hat{\mathcal{K}}}. \end{aligned}$$

Using the commutativity of $\hat{\partial}_1$ with $\hat{\pi}^0_{p_t}, \hat{\pi}^2_{p_s}, \hat{\pi}^3_{p_s}$ and the fact that $\hat{\pi}^0_{p_t}, \hat{\pi}^2_{p_s}, \hat{\pi}^3_{p_s}$ are idempotent, we have for the term T_2:

$$T_2 = \|\hat{\pi}^3_{p_s}\hat{\pi}^2_{p_s}\hat{\pi}^0_{p_t}(\hat{\pi}^1_{p_s}(\hat{\partial}_1\hat{u}) - \hat{\partial}_1\hat{\pi}^1_{p_s}\hat{u})\|_{0,\hat{\mathcal{K}}} \leq \|\hat{\pi}^1_{p_s}(\hat{\partial}_1\hat{u}) - \hat{\partial}_1\hat{\pi}^1_{p_s}\hat{u}\|_{0,\hat{\mathcal{K}}}.$$

Then, using (B.2) and Fubini's theorem we have

$$T_2 \leq C^{L^2}_{p_{s,\mathcal{K}}}\Phi_1(p_{s,\mathcal{K}}, t_{\mathcal{K}})\|\hat{\partial}_1^{t_{\mathcal{K}}+1}\hat{u}\|_{0,\hat{\mathcal{K}}}.$$

Adding the terms T_1 and T_2, and noting that $\Phi_1(p_{s,\mathcal{K}}+1, t_{\mathcal{K}}) \leq \Phi_1(p_{s,\mathcal{K}}, t_{\mathcal{K}})$, the result follows. □

Next, we present an interpolation error estimate on the boundary of the reference element $\partial\hat{\mathcal{K}}$. This estimate is an extension of the result given in [31], Lemma 3.8, to a space-time discretization in $d+1$ dimensions.

Lemma B.10 *Let $\hat{u} \in H^{(k_t+1,k_s+1)}(\hat{\mathcal{K}})$ with integers $k_t, k_s \geq 0$. Let $\hat{\mathcal{P}}\hat{u}$ be the L^2-projection of $\hat{u}$ onto $\mathcal{Q}_{p_{t,\mathcal{K}},p_{s,\mathcal{K}}}(\hat{\mathcal{K}})$. Denoting with $\partial\hat{\mathcal{K}}_i$ that part of $\partial\hat{\mathcal{K}}$ where $\hat{x}_i = \pm 1$, we have for $i = 1, \ldots, d$ the following estimate:*

$$\begin{aligned}
\|\hat{u} - \hat{\mathcal{P}}\hat{u}\|_{0,\partial\hat{\mathcal{K}}_i} \leq & \frac{\Phi_1(p_{s,\mathcal{K}}, t_{\mathcal{K}})}{\sqrt{2p_{s,\mathcal{K}}+1}} \|\hat{\partial}_i^{t_{\mathcal{K}}+1}\hat{u}\|_{0,\hat{\mathcal{K}}} \\
& + \sqrt{3}\Phi_1(p_{s,\mathcal{K}}+1, s_{\mathcal{K}}) \sum_{j=1,j\neq i}^{d} \|\hat{\partial}_j^{s_{\mathcal{K}}}\hat{u}\|_{0,\hat{\mathcal{K}}} \\
& + \big(\sqrt{2} + \frac{1}{\sqrt{2p_{s,\mathcal{K}}+1}}\big)\Phi_1(p_{s,\mathcal{K}}+1, q_{\mathcal{K}}) \sum_{j=1,j\neq i}^{d} \|\hat{\partial}_j^{q_{\mathcal{K}}}\hat{\partial}_i\hat{u}\|_{0,\hat{\mathcal{K}}} \\
& + \sqrt{3}\Phi_1(p_{t,\mathcal{K}}+1, s_{0,\mathcal{K}}) \|\hat{\partial}_0^{s_{0,\mathcal{K}}}\hat{u}\|_{0,\hat{\mathcal{K}}} \\
& + \big(\sqrt{2} + \frac{1}{\sqrt{2p_{s,\mathcal{K}}+1}}\big)\Phi_1(p_{t,\mathcal{K}}+1, q_{0,\mathcal{K}}) \|\hat{\partial}_0^{q_{0,\mathcal{K}}}\hat{\partial}_i\hat{u}\|_{0,\hat{\mathcal{K}}}, \qquad \text{(B.9)}
\end{aligned}$$

while on $\partial\hat{\mathcal{K}}_0$, which is the part of $\partial\hat{\mathcal{K}}$ where $\hat{x}_0 = \pm 1$, we have the estimate:

$$\begin{aligned}
\|\hat{u} - \hat{\mathcal{P}}\hat{u}\|_{0,\partial\hat{\mathcal{K}}_0} \leq & \frac{\Phi_1(p_{t,\mathcal{K}}, t_{0,\mathcal{K}})}{\sqrt{2p_{t,\mathcal{K}}+1}} \|\hat{\partial}_0^{t_{0,\mathcal{K}}+1}\hat{u}\|_{0,\hat{\mathcal{K}}} \\
& + \sqrt{3}\Phi_1(p_{s,\mathcal{K}}+1, s_{\mathcal{K}}) \sum_{i=1}^{d} \|\hat{\partial}_i^{s_{\mathcal{K}}}\hat{u}\|_{0,\hat{\mathcal{K}}} \\
& + \big(\sqrt{2} + \frac{1}{\sqrt{2p_{t,\mathcal{K}}+1}}\big)\Phi_1(p_{s,\mathcal{K}}+1, q_{\mathcal{K}}) \sum_{i=1}^{d} \|\hat{\partial}_i^{q_{\mathcal{K}}}\hat{\partial}_0\hat{u}\|_{0,\hat{\mathcal{K}}}, \qquad \text{(B.10)}
\end{aligned}$$

with $0 \leq s_{\mathcal{K}} \leq \min(p_{s,\mathcal{K}}+1, k_s+1)$, $0 \leq s_{0,\mathcal{K}} \leq \min(p_{t,\mathcal{K}}+1, k_t+1)$, $0 \leq q_{\mathcal{K}} \leq \min(p_{s,\mathcal{K}}+1, k_s)$, $0 \leq s_{0,\mathcal{K}}, q_{0,\mathcal{K}} \leq \min(p_{t,\mathcal{K}}+1, k_t)$, $0 \leq t_{\mathcal{K}} \leq \min(p_{s,\mathcal{K}}, k_s)$, and $0 \leq t_{0,\mathcal{K}} \leq \min(p_{t,\mathcal{K}}, k_t)$.

Proof . We show the proof for $d = 3$ and $i = 1$. The proof for the other coordinate directions and dimensions is similar. We decompose the projector $\hat{\mathcal{P}}$ as:

$$\hat{\mathcal{P}} = \hat{\pi}_{p_s}^1 \hat{\pi}^m,$$

with $\hat{\pi}^m = \hat{\pi}_{p_t}^0 \hat{\pi}_{p_s}^2 \hat{\pi}_{p_s}^3$. Using the triangle inequality, we have:

$$\|\hat{u} - \hat{\mathcal{P}}\hat{u}\|_{0,\partial\hat{\mathcal{K}}_1} \leq \|\hat{u} - \hat{\pi}_{p_s}^1\hat{u}\|_{0,\partial\hat{\mathcal{K}}_1} + \|\hat{\pi}_{p_s}^1(\hat{u} - \hat{\pi}^m\hat{u})\|_{0,\partial\hat{\mathcal{K}}_1} = A_1 + A_2.$$

For the term A_2, we proceed as follows. We define $w = \hat{u} - \hat{\pi}^m\hat{u}$ and write $\hat{\pi}_{p_s}^1 w = w + (\hat{\pi}_{p_s}^1 w - w)$. Then, using (B.4) with $t = 0$, we obtain

$$\begin{aligned}
A_2 &\leq \|w\|_{0,\partial\hat{\mathcal{K}}_1} + \|w - \hat{\pi}_{p_s}^1 w\|_{0,\partial\hat{\mathcal{K}}_1}, \\
&\leq \|w\|_{0,\partial\hat{\mathcal{K}}_1} + \frac{1}{\sqrt{2p_{s,\mathcal{K}}+1}} \|\hat{\partial}_1 w\|_{0,\hat{\mathcal{K}}}, \\
&= A_{21} + A_{22}.
\end{aligned}$$

Using the trace inequality, given in Lemma B.6, and the arithmetic-geometric mean inequality, we then obtain for the term A_{21}:

$$\begin{aligned} A_{21} &\leq \left(\|w\|^2_{0,\hat{\mathcal{K}}} + 4\|w\|_{0,\hat{\mathcal{K}}}\|\hat{\partial}_1 w\|_{0,\hat{\mathcal{K}}}\right)^{\frac{1}{2}}, \\ &\leq \left(\|w\|^2_{0,\hat{\mathcal{K}}} + 2\|w\|^2_{0,\hat{\mathcal{K}}} + 2\|\hat{\partial}_1 w\|^2_{0,\hat{\mathcal{K}}}\right)^{\frac{1}{2}}, \end{aligned}$$

and using the fact that $\sqrt{a+b} \leq \sqrt{a} + \sqrt{b}$, we have:

$$A_{21} \leq \sqrt{3}\|w\|_{0,\hat{\mathcal{K}}} + \sqrt{2}\|\hat{\partial}_1 w\|_{0,\hat{\mathcal{K}}}.$$

Adding up all terms together, we then obtain:

$$\begin{aligned} \|\hat{u} - \hat{\mathcal{P}}\hat{u}\|_{0,\partial\hat{\mathcal{K}}_1} \leq & \|\hat{u} - \hat{\pi}^1_{p_s}\hat{u}\|_{0,\partial\hat{\mathcal{K}}_1} + \sqrt{3}\|\hat{u} - \hat{\pi}^m\hat{u}\|_{0,\hat{\mathcal{K}}} \\ & + \left(\sqrt{2} + \frac{1}{\sqrt{2p_{s,\mathcal{K}}+1}}\right)\|\hat{\partial}_1(\hat{u} - \hat{\pi}^m\hat{u})\|_{0,\hat{\mathcal{K}}}. \end{aligned}$$

We use (B.4) for the first term and Lemma B.8 with respect to $\hat{\pi}^m$ for the second term. For the third term, we first observe that $\hat{\partial}_1(\hat{u} - \hat{\pi}^m\hat{u}) = \hat{\partial}_1\hat{u} - \hat{\pi}^m\hat{\partial}_1\hat{u}$. Further application of Lemma B.8 with $\hat{u}$ replaced by $\hat{\partial}_1\hat{u}$ and $\hat{\mathcal{P}}$ with $\hat{\pi}^m$ completes the proof.

The proof for the estimate on the boundary $\partial\hat{\mathcal{K}}_0$ is analogous. □

B.3 Interpolation error estimates on the space-time element

In this section we derive interpolation error estimates on a space-time element $\mathcal{K}$. First, we define the projection operators on $\tilde{\mathcal{K}}$ and $\mathcal{K}$, respectively, using the mappings $F_{\mathcal{K}}$ and $Q_{\mathcal{K}}$, see also [31], Section 3.1.3.

Definition B.11 Let $\tilde{u} : \tilde{\mathcal{K}} \to \mathbb{R}$ and $u : \mathcal{K} \to \mathbb{R}$ and assume there exist one-to-one and invertible mappings $F_{\mathcal{K}} : \hat{\mathcal{K}} \to \tilde{\mathcal{K}}, Q_{\mathcal{K}} : \tilde{\mathcal{K}} \to \mathcal{K}$. We define the L^2-projection operator $\tilde{\mathcal{P}}$ on $\tilde{\mathcal{K}}$ by the relation

$$\tilde{\mathcal{P}}\tilde{u} := (\hat{\mathcal{P}}(\tilde{u} \circ F_{\mathcal{K}})) \circ F^{-1}_{\mathcal{K}}, \quad \forall \tilde{u} \in L^2(\tilde{\mathcal{K}}),$$

where, as before, $\hat{\mathcal{P}}$ denotes the L^2-projector on the reference element $\hat{\mathcal{K}}$. Moreover, we define the L^2-projection operator $\mathcal{P}$ on $\mathcal{K}$ by

$$\mathcal{P}u := (\tilde{\mathcal{P}}(u \circ Q_{\mathcal{K}})) \circ Q^{-1}_{\mathcal{K}}, \quad \forall u \in L^2(\mathcal{K}).$$

We denote by $J_{Q_{\mathcal{K}}}$ the Jacobian matrix of the mapping $Q_{\mathcal{K}}$ and introduce the following notations:

$$\begin{aligned} C_{Q_{\mathcal{K}}} &:= \|\det J_{Q_{\mathcal{K}}}\|^{\frac{1}{2}}_{0,\infty,\tilde{\mathcal{K}}}, \\ C'_{Q_{\mathcal{K}}} &:= \|(\det J_{Q_{\mathcal{K}}})^{-1}\|^{\frac{1}{2}}_{0,\infty,\tilde{\mathcal{K}}}, \\ C^{mn}_{Q_{\mathcal{K}}} &:= \|\det J_{Q_{\mathcal{K}}\setminus mn}\|_{0,\infty,\tilde{\mathcal{K}}}, \\ C^{\partial_i}_{Q_{\mathcal{K}}} &:= \|\det(J_{\partial\mathcal{K}_i})\|^{\frac{1}{2}}_{0,\infty,\tilde{\mathcal{K}}}, \end{aligned}$$

with $J_{Q_\mathcal{K}\setminus mn}$ the submatrix of $J_{Q_\mathcal{K}}$ obtained by deleting the m-th row and n-th column and $J_{\partial\mathcal{K}_i}$ the surface measure of the boundary $\partial\mathcal{K}_i$.

First, we extend the interpolation estimates in Lemma B.8 to functions defined on $\mathcal{K}$.

Lemma B.12 *Assume that $\mathcal{K}$ is a space-time element in $\mathbb{R}^{d+1}$ constructed via two one-to-one and invertible mappings $Q_\mathcal{K}$, $F_\mathcal{K}$, with $F_\mathcal{K} : \hat{\mathcal{K}} \to \tilde{\mathcal{K}}$ and $Q_\mathcal{K} : \tilde{\mathcal{K}} \to \mathcal{K}$. Assume also that $h_i, i = 1, \ldots, d$ is the edge length of $\tilde{\mathcal{K}}$ in the x_i direction, and $\triangle_n t$ the edge length in the x_0 direction. Let $u \in H^{(k_t+1,k_s+1)}(\mathcal{K})$, with $k_t, k_s \geq 0$, and $\mathcal{P}$ be the L^2 projection of u on $\mathcal{K}$. Then we have the following estimate:*

$$\begin{aligned}\|u - \mathcal{P}u\|_{0,\mathcal{K}} \leq & C_{Q_\mathcal{K}} \Phi_1(p_{s,\mathcal{K}} + 1, s_\mathcal{K}) \sum_{i=1}^{d} \Big(\frac{h_i}{2}\Big)^{s_\mathcal{K}} \|\tilde{\partial}_i^{s_\mathcal{K}} u\|_{0,\tilde{\mathcal{K}}} \\ & + C_{Q_\mathcal{K}} \Phi_1(p_{t,\mathcal{K}} + 1, s_{0,\mathcal{K}}) \Big(\frac{\triangle_n t}{2}\Big)^{s_{0,\mathcal{K}}} \|\tilde{\partial}_0^{s_{0,\mathcal{K}}} u\|_{0,\tilde{\mathcal{K}}}, \end{aligned} \tag{B.11}$$

with $0 \leq s_\mathcal{K} \leq \min(p_{s,\mathcal{K}} + 1, k_s + 1)$ and $0 \leq s_{0,\mathcal{K}} \leq \min(p_{t,\mathcal{K}} + 1, k_t + 1)$.

Proof . First, using the definition of the projection operators $\mathcal{P}$ and $\tilde{\mathcal{P}}$, we have the following bound:

$$\|u - \mathcal{P}u\|_{0,\mathcal{K}} \leq C_{Q_\mathcal{K}} \|\tilde{u} - \tilde{\mathcal{P}}\tilde{u}\|_{0,\tilde{\mathcal{K}}} \leq C_{Q_\mathcal{K}} C_{F_\mathcal{K}} \|\hat{u} - \hat{\mathcal{P}}\hat{u}\|_{0,\hat{\mathcal{K}}},$$

with

$$C_{F_\mathcal{K}} = \Big(\frac{\triangle_n t}{2}\Big)^{\frac{1}{2}} \Big(\frac{h_1}{2}\Big)^{\frac{1}{2}} \cdots \Big(\frac{h_d}{2}\Big)^{\frac{1}{2}}.$$

Using Lemma B.8 and the scaling identities given in Lemma B.7, we have:

$$\begin{aligned}\|u - \mathcal{P}u\|_{0,\mathcal{K}} \leq & C_{Q_\mathcal{K}} \Phi_1(p_{s,\mathcal{K}} + 1, s_\mathcal{K}) \sum_{i=1}^{d} \Big(\frac{h_i}{2}\Big)^{s_\mathcal{K}} \|\tilde{\partial}_i^{s_\mathcal{K}} u\|_{0,\tilde{\mathcal{K}}} \\ & + C_{Q_\mathcal{K}} \Phi_1(p_{t,\mathcal{K}} + 1, s_{0,\mathcal{K}}) \Big(\frac{\triangle_n t}{2}\Big)^{s_{0,\mathcal{K}}} \|\tilde{\partial}_0^{s_{0,\mathcal{K}}} u\|_{0,\tilde{\mathcal{K}}},\end{aligned}$$

for $0 \leq s_\mathcal{K} \leq \min(p_{s,\mathcal{K}}+1, k_s+1)$ and $0 \leq s_{0,\mathcal{K}} \leq \min(p_{t,\mathcal{K}}+1, k_t+1)$. This completes the proof. □

Next, we extend the interpolation estimates in Lemma B.9 to functions defined on $\mathcal{K}$.

Lemma B.13 *Assume that $\mathcal{K}$ is a space-time element in $\mathbb{R}^{d+1}$ constructed via two one-to-one and invertible mappings $Q_\mathcal{K}$, $F_\mathcal{K}$, with $F_\mathcal{K} : \hat{\mathcal{K}} \to \tilde{\mathcal{K}}$ and $Q_\mathcal{K} : \tilde{\mathcal{K}} \to \mathcal{K}$. Assume also that $h_i, i = 1, \ldots, d$ is the edge length of $\tilde{\mathcal{K}}$ in the x_i direction, and $\triangle_n t$ the edge length in the x_0 direction. Let $u \in H^{(k_t+1,k_s+1)}(\mathcal{K})$, with $k_t, k_s \geq 0$, and $\mathcal{P}$ be the L^2 projection of u on $\mathcal{K}$. Then we have the following estimate:*

$$\|\partial_i(u - \mathcal{P}u)\|_{0,\mathcal{K}} \leq \alpha^{ii} M_i + \sum_{j \neq i} \alpha^{ij} M_j, \tag{B.12}$$

where:

$$\begin{aligned} M_i =&(1+C^{L^2}_{p_{s,\mathcal{K}}})\Phi_1(p_{s,\mathcal{K}},t_{\mathcal{K}})\Big(\frac{h_i}{2}\Big)^{t_{\mathcal{K}}}\|\tilde{\partial}_i^{t_{\mathcal{K}}+1}u\|_{0,\tilde{\mathcal{K}}}\\ &+\Phi_1(p_{s,\mathcal{K}}+1,t_{\mathcal{K}}+1)\sum_{j=1,j\neq i}^{d}\Big(\frac{h_j}{2}\Big)^{t_{\mathcal{K}}+1}\|\tilde{\partial}_j^{t_{\mathcal{K}}+1}\tilde{\partial}_i u\|_{0,\tilde{\mathcal{K}}}\\ &+\Big(\frac{\triangle_n t}{2}\Big)^{t_{0,\mathcal{K}}+1}\Phi_1(p_{t,\mathcal{K}}+1,t_{0,\mathcal{K}}+1)\|\tilde{\partial}_0^{t_{0,\mathcal{K}}+1}\tilde{\partial}_i u\|_{0,\tilde{\mathcal{K}}}, \end{aligned}$$

for $i=\{1,\dots,d\}$, *with* $\alpha^{ii}=\sqrt{2}C^{ii}_{Q_{\mathcal{K}}}C^{'}_{Q_{\mathcal{K}}}$, $\alpha^{mn}=\sqrt{2}C^{mn}_{Q_{\mathcal{K}}}C^{'}_{Q_{\mathcal{K}}}, m\neq n$, *and* $0\leq t_{\mathcal{K}}\leq \min(p_{s,\mathcal{K}},k_s)$, $0\leq t_{0,\mathcal{K}}\leq\min(p_{t,\mathcal{K}},k_t)$, .

Proof . Using the chain rule and the arithmetic-geometric mean inequality, we obtain:

$$\begin{aligned}\|\partial_i(u-\mathcal{P}u)\|^2_{0,\mathcal{K}}\leq&2\int_{\mathcal{K}}\Big(\tilde{\partial}_i((u-\mathcal{P}u)\circ Q_{\mathcal{K}})\circ Q_{\mathcal{K}}^{-1}\frac{\partial\tilde{x}_i}{\partial x_i}\Big)^2\,\mathrm{d}\mathcal{K}\\ &+4\sum_{j=1,j\neq i}^{d}\int_{\mathcal{K}}\Big(\tilde{\partial}_j((u-\mathcal{P}u)\circ Q_{\mathcal{K}})\circ Q_{\mathcal{K}}^{-1}\frac{\partial\tilde{x}_j}{\partial x_i}\Big)^2\,\mathrm{d}\mathcal{K}.\end{aligned}$$

Using the mapping $Q_{\mathcal{K}}^{-1}$ from $\mathcal{K}$ to $\tilde{\mathcal{K}}$ we then obtain:

$$\|\partial_i(u-\mathcal{P}u)\|_{0,\mathcal{K}}\leq\sqrt{2}C^{'}_{Q_{\mathcal{K}}}C^{ii}_{Q_{\mathcal{K}}}\|\tilde{\partial}_i(\tilde{u}-\tilde{\mathcal{P}}\tilde{u})\|_{0,\tilde{\mathcal{K}}}+2C^{'}_{Q_{\mathcal{K}}}\sum_{j=1,j\neq i}^{d}C^{ij}_{Q_{\mathcal{K}}}\|\tilde{\partial}_j(\tilde{u}-\tilde{\mathcal{P}}\tilde{u})\|_{0,\tilde{\mathcal{K}}}.$$

Now we want to estimate the term $\|\tilde{\partial}_i(\tilde{u}-\tilde{\mathcal{P}}\tilde{u})\|_{\tilde{\mathcal{K}}}$, for $i=1,\dots,d$. Using the change of variables from $\tilde{u}$ to $\hat{u}$, Lemma B.9 and the scaling identities given in Lemma B.7, we obtain:

$$\begin{aligned}\|\tilde{\partial}_i(\tilde{u}-\tilde{\mathcal{P}}\tilde{u})\|_{0,\tilde{\mathcal{K}}}\leq&(1+C^{L^2}_{p_{s,\mathcal{K}}})\Phi_1(p_{s,\mathcal{K}},t_{\mathcal{K}})\Big(\frac{h_i}{2}\Big)^{t_{\mathcal{K}}}\|\tilde{\partial}_i^{t_{\mathcal{K}}+1}u\|_{0,\tilde{\mathcal{K}}}\\ &+\Phi_1(p_{s,\mathcal{K}}+1,t_{\mathcal{K}}+1)\sum_{j=1,j\neq i}^{d}\Big(\frac{h_j}{2}\Big)^{t_{\mathcal{K}}+1}\|\tilde{\partial}_j^{t_{\mathcal{K}}+1}\tilde{\partial}_i u\|_{0,\tilde{\mathcal{K}}}\\ &+\Big(\frac{\triangle_n t}{2}\Big)^{t_{0,\mathcal{K}}+1}\Phi_1(p_{t,\mathcal{K}}+1,t_{0,\mathcal{K}}+1)\|\tilde{\partial}_0^{t_{0,\mathcal{K}}+1}\tilde{\partial}_i u\|_{0,\tilde{\mathcal{K}}}.\end{aligned}$$

This completes the proof. □

Finally, we derive an estimate on the boundary of element $\partial\mathcal{K}$.

Lemma B.14 *Assume that* $\mathcal{K}$ *is a space-time element in* $\mathbb{R}^{d+1}$ *constructed via two one-to-one and invertible mappings* $Q_{\mathcal{K}}$, $F_{\mathcal{K}}$, *with* $F_{\mathcal{K}}:\hat{\mathcal{K}}\to\tilde{\mathcal{K}}$ *and* $Q_{\mathcal{K}}:\tilde{\mathcal{K}}\to\mathcal{K}$. *Assume also that* $h_i, i=1,\dots,d$ *is the edge length of* $\tilde{\mathcal{K}}$ *in the* x_i *direction, and* $\triangle_n t$ *the edge length in the* x_0 *direction. Let* $u\in H^{(k_t+1,k_s+1)}(\mathcal{K})$, *with* $k_t,k_s\geq 0$ *and*

$\mathcal{P}$ be the L^2 projection of u on $\mathcal{K}$. On the boundaries $\partial\mathcal{K}_i, i = 1, \ldots, d$ we have the following estimate:

$$\|u - \mathcal{P}u\|_{0,\partial\mathcal{K}_i} \leq C_{Q_\mathcal{K}}^{\partial_i} M_i^\partial, \tag{B.13}$$

where

$$\begin{aligned}
M_i^\partial =& \frac{\Phi_1(p_{s,\mathcal{K}}, t_\mathcal{K})}{\sqrt{2p_{s,\mathcal{K}}+1}} \Big(\frac{h_i}{2}\Big)^{t_\mathcal{K}+\frac{1}{2}} \|\tilde{\partial}_i^{t_\mathcal{K}+1} u\|_{0,\tilde{\mathcal{K}}} \\
&+ \sqrt{3}\Big(\frac{h_i}{2}\Big)^{-\frac{1}{2}} \Phi_1(p_{s,\mathcal{K}}+1, s_\mathcal{K}) \sum_{j=1, j\neq i}^{d} \Big(\frac{h_j}{2}\Big)^{s_\mathcal{K}} \|\tilde{\partial}_j^{s_\mathcal{K}} u\|_{0,\tilde{\mathcal{K}}} \\
&+ \Big(\frac{h_i}{2}\Big)^{\frac{1}{2}} \big(\sqrt{2} + \frac{1}{\sqrt{2p_{s,\mathcal{K}}+1}}\big) \Phi_1(p_{s,\mathcal{K}}+1, q_\mathcal{K}) \sum_{j=1, j\neq i}^{d} \Big(\frac{h_j}{2}\Big)^{q_\mathcal{K}} \|\tilde{\partial}_j^{q_\mathcal{K}} \tilde{\partial}_i u\|_{0,\tilde{\mathcal{K}}} \\
&+ \sqrt{3}\Big(\frac{h_i}{2}\Big)^{-\frac{1}{2}} \Phi_1(p_{t,\mathcal{K}}+1, s_{0,\mathcal{K}}) \Big(\frac{\triangle_n t}{2}\Big)^{s_{0,\mathcal{K}}} \|\tilde{\partial}_0^{s_{0,\mathcal{K}}} u\|_{0,\tilde{\mathcal{K}}} \\
&+ \Big(\frac{h_i}{2}\Big)^{\frac{1}{2}} \big(\sqrt{2} + \frac{1}{\sqrt{2p_{s,\mathcal{K}}+1}}\big) \Phi_1(p_{t,\mathcal{K}}+1, q_{0,\mathcal{K}}) \Big(\frac{\triangle_n t}{2}\Big)^{q_{0,\mathcal{K}}} \|\tilde{\partial}_0^{q_{0,\mathcal{K}}} \tilde{\partial}_i u\|_{0,\tilde{\mathcal{K}}},
\end{aligned}$$

while on the boundary $\partial\mathcal{K}_0$ we have the following estimate:

$$\|u - \mathcal{P}u\|_{0,\partial\mathcal{K}_0} \leq C_{Q_\mathcal{K}}^{\partial_0} M_0^\partial, \tag{B.14}$$

where

$$\begin{aligned}
M_0^\partial =& \frac{\Phi_1(p_{t,\mathcal{K}}, t_{0,\mathcal{K}})}{\sqrt{2p_{t,\mathcal{K}}+1}} \Big(\frac{\triangle_n t}{2}\Big)^{t_{0,\mathcal{K}}+\frac{1}{2}} \|\tilde{\partial}_0^{t_{0,\mathcal{K}}+1} u\|_{0,\tilde{\mathcal{K}}} \\
&+ \sqrt{3}\Big(\frac{\triangle_n t}{2}\Big)^{-\frac{1}{2}} \Phi_1(p_{s,\mathcal{K}}+1, s_\mathcal{K}) \sum_{i=1}^{d} \Big(\frac{h_i}{2}\Big)^{s_\mathcal{K}} \|\tilde{\partial}_i^{s_\mathcal{K}} u\|_{0,\tilde{\mathcal{K}}} \\
&+ \Big(\frac{\triangle_n t}{2}\Big)^{\frac{1}{2}} \big(\sqrt{2} + \frac{1}{\sqrt{2p_{t,\mathcal{K}}+1}}\big) \Phi_1(p_{s,\mathcal{K}}+1, q_\mathcal{K}) \sum_{i=1}^{d} \Big(\frac{h_i}{2}\Big)^{q_\mathcal{K}} \|\tilde{\partial}_i^{q_\mathcal{K}} \tilde{\partial}_0 u\|_{0,\tilde{\mathcal{K}}},
\end{aligned}$$

with $0 \leq s_\mathcal{K} \leq \min(p_{s,\mathcal{K}}+1, k_s+1)$, $0 \leq s_{0,\mathcal{K}} \leq \min(p_{t,\mathcal{K}}+1, k_t+1)$, $0 \leq q_\mathcal{K} \leq \min(p_{s,\mathcal{K}}+1, k_s)$, $0 \leq q_{0,\mathcal{K}} \leq \min(p_{t,\mathcal{K}}+1, k_t)$, and $0 \leq t_\mathcal{K} \leq \min(p_{s,\mathcal{K}}, k_s)$, $0 \leq t_{0,\mathcal{K}} \leq \min(p_{t,\mathcal{K}}, k_t)$.

Proof . First, using the change of variables, we have:

$$\|u - \mathcal{P}u\|_{0,\partial\mathcal{K}_i} \leq C_{Q_\mathcal{K}}^{\partial_i} \|\tilde{u} - \tilde{\mathcal{P}}\tilde{u}\|_{0,\partial\tilde{\mathcal{K}}_i}, \quad \text{for } i = 0, 1, \ldots, d.$$

Then, using Lemma B.10 and the scaling identities on the boundary $\partial\tilde{\mathcal{K}}_i, i = 1, \ldots, d$, given in Lemma B.7, we have:

$$\|\tilde{u} - \tilde{\mathcal{P}}\tilde{u}\|_{0,\partial\tilde{\mathcal{K}}_i} \leq M_i^\partial,$$

while on the boundary $\partial\tilde{\mathcal{K}}_0$ we obtain:

$$\|\tilde{u} - \tilde{\mathcal{P}}\tilde{u}\|_{0,\partial\tilde{\mathcal{K}}_0} \leq M_0^{\partial}.$$

This completes the proof. □

Bibliography

[1] M. Abramowitz & I.A. Stegun, *Handbook of Mathematical Functions*, Dover Publications, New York, 1972.

[2] M. Ainsworth & B. Senior, An Adaptive Refinement Strategy for *hp*-Finite Element Computations, *Appl. Num. Math.*, **26**, 165-178, 1998.

[3] D.N. Arnold, An Interior Penalty Finite Element Method with Discontinuous Elements, *SIAM J. Num. Anal.*, **19** (4), 742-760, 1982.

[4] D.N. Arnold, F. Brezzi, B. Cockburn, & L.D. Marini, Unified Analysis of Discontinuous Galerkin Methods for Elliptic Problems, *SIAM J. Num. Anal.*, **39** (5), 1749-1779, 2002.

[5] F. Bassi, S. Rebay, G. Mariotti, S. Pedinotti, & M. Savini, A High-Order Accurate Discontinuous Finite Element Method for Inviscid and Viscous Turbomachinery Flows, in *Proceedings of 2nd European Conference on Turbomachinery, Fluid Dynamics and Thermodynamics*, Technologisch Instituut, Antwerpen, Belgium, 99-108, 1997.

[6] F. Bassi & S. Rebay, A High-Order Accurate Discontinuous Finite Element Method for the Numerical Solution of the Compressible Navier-Stokes Equations, *J. Comput. Phys.*, **131**, 267-279, 1997.

[7] F. Bassi & S. Rebay, Numerical Evaluation of Two Discontinuous Galerkin Methods for the Compressible Navier-Stokes Equations, *Int. J. Numer. Meth. Fluids*, **40**, 197-207, 2002.

[8] F. Bassi, A. Crivellini, D.A. Di Pietro, & S. Rebay, An Artificial Compressibility Flux for the Discontinuous Galerkin Solution of the Incompressible Navier-Stokes Equations, submitted to *J. Comput. Phys.*, 2005.

[9] C.E. Baumann & J.T. Oden, A Discontinuous *hp* Finite Element Method for Convection-Diffusion Equations, *Comput. Methods Appl. Engrg.*, **175**, 311-341, 1999.

[10] C.E. Baumann & J.T. Oden, A Discontinuous *hp* Finite Element Method for the Euler and Navier-Stokes Equations, *Int. J. Numer. Meth. Fluids*, **31**, 79-95, 1999.

[11] S.C. Brenner & L.R. Scott, *The Mathematical Theory of Finite Element Methods*, 2nd ed., Springer-Verlag, 2002.

[12] F. Brezzi, G. Manzini, D. Marini, P. Pietra, & A. Russo, Discontinuous Galerkin Approximations for Elliptic Problems, *Numer. Methods Partial Differential Eq.*, **16**, 365-378, 2000.

[13] F. Brezzi, L.D. Marini, & E. Süli, Discontinuous Galerkin Methods for First-Order Hyperbolic Problems, *Math. Models Methods Appl. Sci.*, **14** (12), 1893-1903, 2004.

[14] P. Castillo, B. Cockburn, I. Perugia, & D. Schötzau, Local Discontinuous Galerkin Methods for Elliptic Problems, *Commun. Numer. Meth. Engng*, **18**, 69-75, 2002.

[15] B. Cockburn & P.A. Gremaud, Error Estimates for Finite Element Methods for Nonlinear Conservation Laws, *SIAM. J. Num. Anal.*, **33**, 522-554, 1996.

[16] B. Cockburn & C.W. Shu, The Local Discontinuous Galerkin Method for Time-Dependent Convection-Diffusion Systems, *SIAM. J. Num. Anal.*, **35** (6), 2440-2463, 1998.

[17] B. Cockburn, Discontinuous Galerkin Methods for Convection Dominated Problems, in *High-Order Methods for Computational Physics*, T. Barth & H. Deconink (editors), Springer-Verlag, 1999.

[18] B. Cockburn, G. Karniadakis, & C.W. Shu, *Discontinuous Galerkin Methods. Theory, Computation and Applications*, Springer-Verlag, 2000.

[19] B. Cockburn & C.W. Shu, Runge Kutta Discontinuous Galerkin Method for Convection-Dominated Problems, *J. Sci. Comput.*, **6** (3), 173-261, 2001.

[20] B. Cockburn, G. Kanschat, I. Perugia, & D. Schötzau, Superconvergence of the Local Discontinuous Galerkin Method for Elliptic Problems on Cartesian Grids, *SIAM J. Numer. Anal.*, **39** (1), 264-285, 2002.

[21] B. Cockburn, G. Kanschat, D. Schötzau, & C. Schwab, Local Discontinuous Galerkin Methods for the Stokes Systems, *SIAM J. Numer. Anal.*, **40** (1), 319-343, 2002.

[22] B. Cockburn, G. Kanschat, & D. Schötzau, The Local Discontinuous Galerkin Method in Incompressible Fluid Flow, in *Proceedings of Fifth World Congress on Computational Mechanics V*, 2002.

[23] B. Cockburn, G. Kanschat, & D. Schötzau, The Local Discontinuous Galerkin Method for the Oseen Equations, *Math. Comput.*, **73**, 569-593, 2004.

[24] B. Cockburn, G. Kanschat, & D. Schötzau, A Locally Conservative LDG Method for the Incompressible Navier-Stokes Equations, *Math. Comput.*, **74**, 1067-1095, 2004.

[25] R.M.J. van Damme & J.J. Sudirham, *Optimal hp Adaptive Methods for Discontinuous Galerkin methods*, in preparation.

[26] L. Demkowicz, W. Rachowicz, & Ph. Devloo, A Fully Automatic *hp*-Adaptivity, *J. Sci. Comput.*, **17** (1-4), 117-142, 2002.

[27] L. Demkowicz, *Projection-Based Interpolation*, internal report **ICES 04-03**, 2004.

[28] J. Jr. Douglas & T. Dupont, Interior Penalty Procedures for Elliptic and Parabolic Galerkin Methods, in *Lecture Notes in Physics*, **58**, Springer-Verlag, 1976.

[29] C.H. Driesen, *Simulation of Convection-Driven Wet-Chemical Etching*, PhD Thesis, University of Twente, 1999.

[30] K.J. Fidkowski & P.F. Fischer, *A Discontinuous Galerkin Multigrid Method for the Incompressible Navier-Stokes Equations*, internal report, Dept. Aerospace Engineering, Massachusetts Institute of Technology, 2004.

[31] E.H. Georgoulis, *Discontinuous Galerkin Methods on Shaped-Regular and Anisotropic Meshes*, PhD Thesis, Christ Church, University of Oxford, 2003.

[32] V. Girault & P.-A. Raviart, *Finite Element Methods for Navier-Stokes Equations. Theory and Algorithms*, Springer-Verlag, 1986.

[33] P. Grisvard, *Elliptic Problems in Nonsmooth Domains*, Pitman Advanced Pub. Program, 1985.

[34] W. Gui & I. Babuška, The h, p, and hp Versions of the Finite Element Method in 1 Dimension, Part I. The Error Analysis of the p-Version, *Numer. Math.*, **49**, 577-612, 1986.

[35] W. Gui & I. Babuška, The h, p, and hp Versions of the Finite Element Method in 1 Dimension, Part II. The Error Analysis of the h- and hp Versions, *Numer. Math.*, **49**, 613-657, 1986.

[36] W. Gui & I. Babuška, The h, p, and hp Versions of the Finite Element Method in 1 Dimension, Part III. The Adaptive hp Version, *Numer. Math.*, **49**, 659-683, 1986.

[37] J. Haneveld, H. Jansen, E. Berenschot, N. Tas, & M. Elwenspoek, Wet-Anisotropic Etching for Fluidic 1D Nanochannels, *J. Micromech. Microeng.*, **13**, S62-S66, 2003.

[38] P. Houston, C. Schwab, & E. Süli, Discontinuous hp-Finite Element Methods for Advection-Diffusion-Reaction Problems, *SIAM J. Numer. Anal.*, **39** (6), 2133-2163, 2002.

[39] P. Houston, B. Senior, & E. Süli, Sobolev Regularity Estimation for hp-Adaptive Finite Element Methods, in *Numerical Mathematics and Advanced Applications*, F. Brezzi, A. Buffa, S. Corsaro, & A. Murli (editors), Springer-Verlag, 619-644, 2003.

[40] P. Houston, D. Schötzau, & T.P. Wihler, hp-Adaptive Discontinuous Galerkin Finite Element Methods for the Stokes Problem, in *Proceedings of European Congress in Applied Sciences and Engineering (ECCOMAS)*, Jyvaskyla, Finland, 2004.

[41] J. Jaffre, C. Johnson, & A. Szepessy, Convergence of the Discontinuous Galerkin Finite Element Method for Hyperbolic Conservation Laws, *Math. Models Methods Appl. Sci.*, **5**, 367, 1995.

[42] H.K. Kuiken, Etching: A Two-Dimensional Mathematical Approach, *Proc. R. Soc. Lond. A.*, **392**, 199-225, 1984.

[43] H.K. Kuiken, Etching Through A Slit, *Proc. R. Soc. Lond. A*, **396**, 95-117, 1984.

[44] H.K. Kuiken, J.J. Kelly, & P.H.L. Notten, Etching Profiles at Resist Edges Part I. Mathematical Models for Diffusion-Controlled Cases, *J. Electrochem. Soc.*, **133** (6), 1217-1226, 1986.

[45] H.K. Kuiken, Mathematical Modelling of Etching Processes, in *Free Boundary Problems: Theory and Applications*, K.H. Hoffmann & J. Sprekels (editors), Longman Scientific & Technical, 1990.

[46] H.K. Kuiken, A Mathematical Model for Wet-Chemical Diffusion-Controlled Mask Etching through a Circular Hole, *J. Eng. Math.*, **45**, 75-90, 2003.

[47] M. Madou, *Fundamentals of Microfabrication*, CRC Press, 1997.

[48] MEMSnet, Etching Processes, http://www.memsnet.org/mems/processes/etch.html.

[49] W. Rachowicz, D. Pardo, & L. Demkowicz, *Fully Automatic hp-Adaptivity in Three Dimensions*, internal report **ICES 04-22**, 2004.

[50] R. Rannacher, *Error Control in Finite Element Computations*, internal report **21/98**, Institut für Angewandte Mathematik, Universität Heidelberg, 1998.

[51] W.H. Reed & T.R. Hill, *Triangular Mesh Methods for the Neutron Transport Equation*, Technical report **LA-UR-73-479**, Los Alamos Scientific Laboratory, Los Alamos, NM, 1973.

[52] B. Riviere, M.F. Wheeler, & V. Girault, Improved Energy Estimates for Interior Penalty, Constrained and Discontinuous Galerkin Methods for Elliptic Problems. Part I., *Comput. Geosci.*, **3**, 337-360, 1999.

[53] B. Riviere & M.F. Wheeler, A Posteriori Error Estimates for a Discontinuous Galerkin Method Applied to Elliptic Problems, *Comput. Math. Appl.*, **46**, 141-164, 2003.

[54] D. Schötzau, C. Schwab, & A. Toselli, Mixed *hp*-DGFEM for Incompressible Flows, *SIAM J. Numer. Anal.*, **40** (6), 2171-2194, 2003.

[55] D. Schötzau, C. Schwab, & A. Toselli, *Mixed hp-DGFEM for Incompressible Flows III : Pressure Stabilization*, internal report **2002-25**, Seminar for Applied Mathematics, ETH Zurich, 2002.

[56] C.B. Shin & D.J. Economou, Effect of Transport and Reaction on the Shape Evolution of Cavities during Wet Chemical Etching, *J. Electrochem. Soc.*, **136** (7), 1997-2004, 1989.

[57] C.B. Shin & D.J. Economou, Forced and Natural Convection Effects on the Shape Evolution of Cavities during Wet Chemical Etching, *J. Electrochem. Soc.*, **138** (2), 527-538, 1991.

[58] J.J. Sudirham, *Discontinuous Galerkin Method for Diffusion Problems*, unpublished report, Department of Applied Mathematics, University of Twente, 2002.

[59] J.J. Sudirham, J.J.W. van der Vegt, & R.M.J. van Damme, *A Study on Discontinuous Galerkin Finite Element Methods for Elliptic Problems*, internal report **1690**, Department of Applied Mathematics, University of Twente, 2003.

[60] J.J. Sudirham, R.M.J. van Damme, & J.J.W. van der Vegt, Space-Time Discontinuous Galerkin Method for Wet-Chemical Etching of Microstructures, in *Proceedings of European Congress in Applied Sciences and Engineering (ECCOMAS)*, Jyvaskyla, Finland, 2004.

[61] J.J. Sudirham, J.J.W. van der Vegt, & R.M.J. van Damme, Space-Time Discontinuous Galerkin Method for Advection-Diffusion Problems on Time-Dependent Domains, accepted for publication in *Appl. Num. Math.*, 2005.

[62] J.J. Sudirham, J.J.W. van der Vegt, & R.M.J. van Damme, *Space-Time Discontinuous Galerkin Method for the Incompressible Navier-Stokes Equations*, in preparation.

[63] V. Thomee, *Galerkin Finite Element Methods for Parabolic Problems*, Springer-Verlag, 1997.

[64] J.J.W. van der Vegt & H. van der Ven, Space-Time Discontinuous Galerkin Finite Element Method with Dynamic Grid Motion for Inviscid Compressible Flows, Part I. General Formulation, *J. Comput. Phys.*, **182**, 546-585, 2002.

[65] H. van der Ven & J.J.W. van der Vegt, Space-Time Discontinuous Galerkin Finite Element Method with Dynamic Grid Motion for Inviscid Compressible Flows, Part II. Efficient Flux Quadrature, *Comput. Methods Appl. Engrg.*, **191**, 4747-4780, 2002.

[66] C. Vuik & C. Cuvelier, Numerical Solution of an Etching Problem, *J. Comput. Phys.*, **59**, 247-263, 1985.

[67] M. F. Wheeler, An Elliptic Collocation-Finite Element Method with Interior Penalties, *SIAM J. Numer. Anal.*, **15**, 152-161, 1978.

Acknowledgements

It has been a little more than four years since I started my PhD study which resulted in this thesis. During those years of study, there are many people that have contributed in different ways to the completion of this thesis and I would like to express my sincere thanks to them.

First, I would like to express my sincere gratitude to my first supervisor and my promoter, Jaap van der Vegt, for giving me the opportunity to work on this project as well as for his supervision, patience and understanding. His help encouraged me to work on some theoretical analysis, which is a new thing for me. I also would like to thank him for carefully reading the draft of this thesis. I would like to express my sincere thanks to my second supervisor, Ruud van Damme, for his guidance. I can always discuss with him for the help on computer programs and numerical simulations. Our small discussions gave me confident to carry on with my work. I also thank him for the *samenvatting* and help on the cover. It is nice to have supervisors with whom you can discuss many things, including non-scientific matters.

My sincere thanks go to Prof. Miko Elwenspoek and Prof. Henk Kuiken for nice project meetings as well as their willingness to be members of my graduation committee. I also would like to thank Prof. Piet Hemker, Prof. Barry Koren, and Guido Kanschat, for their willingness to be members of my graduation committee. Financial support from STW for the project and the printing is greatly appreciated. I also would like to thank Leo Kastanje from STW and other users' committee members for nice meetings that we had.

I enjoy very much working in MPCM group. In particular I would like to thank my officemates Satyendra, Joris, Lars, and Yan for a nice and enjoyable working place and for helping me with computer-related problems. I will remember Lars' home-made cakes and Joris' introduction to classical music and clarinet. I will always treasure my friendship with Helen, Monika, and Jaqueline, full with laughs, sharing stories, and nice talks. My thanks go to David, Pablo, Sena, Nathan, Hadi, Kiran, Chris, and other members of the group for the help, nice talks and lunches. Thank you to Vijaya for letting me use part of his C++ code as a base of my program which results in some of the numerical simulations presented in Chapter 6. My special thanks to Marielle for helping me with administrative matters and for constant invitations for

joining group lunch everyday.

Being away from my country, I am grateful to have nice friendship from many Indonesian friends in PPIE, IMEA, Anugrah, and IAMSN. In particular I would like to thank Sri Nurdiati for the friendship that we have.

My special gratitude and love are directed to my mother and my father for their love, constant prayers, and understanding. Their support give me the strength to complete this thesis. My grateful thanks go to my brothers and sisters for their love, prayers, and support, especially to Mas Kemal, Mbak Vera, and Kevin, for their hospitality during my very frequent visits to Wageningen. I also want to thank my parents-in-law for their love and prayers. Last but not least, I would like to express my special gratitude and love to my husband, for his love, prayers, patience, and understanding. His support and companion are essential in the completion of this thesis.

Ringkasan

Etching merupakan tahap penting dalam produksi struktur mikro, dimana pola dipindahkan ke bahan dengan mengikis sebagian dari bahan tersebut. Dalam penerapan di industri, zat kimia cair digunakan untuk melarutkan bahan dan karena itu proses ini disebut *wet-chemical etching*. Pengangkutan zat kimia cair dan zat hasil pelarutan selama proses *etching* merupakan hal yang penting untuk diperhatikan agar diperoleh pola yang diinginkan. Namun demikian, sangat sulit untuk mengontrol proses *etching*. Simulasi numerik kemudian digunakan untuk mempelajari fenomena pengangkutan tersebut. Karena fenomena dan geometri dari struktur mikro yang kompleks, proses *wet-chemical etching* memerlukan teknik numerik yang dapat digunakan untuk elemen yang berubah bentuk, untuk mengakomodir pergerakan dari batas rongga yang dihasilkan oleh *etching*.

Di dalam tesis ini dibahas kelas dalam metoda numerik elemen hingga, yang disebut *space-time discontinuous Galerkin (DG)*, untuk menjelaskan fenomena pengangkutan dalam aliran fluida yang tidak dapat dimampatkan. Metoda ini, yang secara bersamaan mendiskretisasi persamaan matematik dalam ruang dan waktu, memberikan fleksibilitas yang dibutuhkan elemen yang berubah bentuk terhadap waktu. Khususnya dalam tesis ini, dikembangkan metoda *space-time DG* untuk persamaan konveksi-difusi, yang mengatur konsentrasi dari zat kimia, dan persamaan Navier-Stokes untuk aliran fluida yang tidak dapat dimampatkan, yang memodelkan aliran dari zat kimia di dalam dan di luar rongga *etching*. Analisa terperinci untuk stabilitas dari metoda baru dan beberapa hasil simulasi sederhana untuk mempelajari ketelitian dari metoda baru juga dibahas dalam tesis ini.

Kemampuan metoda baru didemonstrasikan untuk beberapa proses *wet-chemical etching*. Pertama dibahas proses *etching* yang dikontrol oleh difusi: *etching* pada celah, sebagai contoh kasus dalam dua dimensi, dan *etching* pada lubang berbentuk lingkaran. Kasus kedua diselesaikan tanpa memanfaatkan pengetahuan mengenai simetri sumbu rotasi, ini dilakukan untuk menunjukkan bahwa simulasi untuk kasus *etching* dalam tiga dimensi dapat dimungkinkan dengan menggunakan metoda numerik yang baru. Untuk kasus sederhana, hasil simulasi menunjukkan kesesuaian dengan hasil yang diperoleh secara analitik. Selain itu, simulasi numerik memberikan gambaran lengkap mengenai bentuk rongga *etching* sepanjang proses berlangsung.

Hasil simulasi untuk proses *etching* pada celah yang dikontrol oleh konveksi, yang digabungkan dengan persamaan Stokes untuk memodelkan aliran zat kimia cair, memberikan gambaran terperinci mengenai fenomena pengangkutan dari *wet-chemical etching* dalam rongga *etching*.